Preparation and Characterization of Mg-based Hydrogen Storage Materials

W. Peter Kalisvaart

Samenstelling van de promotiecommissie:

prof. dr. P.J. Lemstra	Technische Universiteit Eindhoven, *voorzitter*
prof. dr. P.H.L. Notten	Philips Research Laboratories Eindhoven Technische Universiteit Eindhoven, *promotor*
dr. H.T. Hintzen	Technische Universiteit Eindhoven, *copromotor*
prof. dr. R.P. Griessen	Vrije Universiteit Amsterdam
prof. dr. R.A. van Santen	Technische Universiteit Eindhoven
dr. M. Latroche	CNRS Thiais
dr. F.A. de Bruijn	Technische Universiteit Eindhoven
dr. B.A. Boukamp	Technische Universiteit Twente

CIP-DATA LIBRARY TECHNISCHE UNIVERSITEIT EINDHOVEN

Kalisvaart, W. Peter

Preparation and Characterization of Mg-based Hydrogen Storage Materials/by W. Peter Kalisvaart. –Eindhoven : Technische Universiteit Eindhoven, 2008.

Proefschrift. -ISBN 978-90-386-1487-8
NUR 913

Trefwoorden: Elektrochemie / batterijen / waterstofopslag / Magnesium legeringen / neutronendiffractie / kernspinresonantie / metastabiele materialen / mechanisch legeren

Subject headings: Electrochemistry / batteries / hydrogen storage / Magnesium alloys / neutron diffraction / nuclear magnetic resonance / metastable materials / mechanical alloying

Cover design: Oranje Vormgevers

Printed by Eindhoven University press

This research has been financially supported by NWO within the framework of the Sustainable Hydrogen Program of Active Chemical Technologies for Sustainability (ACTS)

Preparation and Characterization of Mg-based Hydrogen Storage Materials

PROEFSCHRIFT

ter verkrijging van de graad van doctor aan de
Technische Universiteit Eindhoven, op gezag van de
Rector Magnificus, prof.dr.ir. C.J. van Duijn, voor een
commissie aangewezen door het College voor
Promoties in het openbaar te verdedigen
op dinsdag 2 december 2008 om 16.00 uur

door

Willem Peter Kalisvaart

geboren te Terneuzen

Dit proefschrift is goedgekeurd door de promotor:

prof.dr. P.H.L. Notten

Copromotor:
dr. H.T. Hintzen

Dankwoord

Bij een proefschrift mag een uitgebreid dankwoord aan alle mensen die een bijdrage aan het promotieonderzoek hebben geleverd natuurlijk niet ontbreken.

Allereerst noem ik uiteraard mijn promotor prof. dr. Peter H.L. Notten, die het ruim 4 jaar geleden heeft aangedurft een pas afgestudeerd studentje, die toch wel erg gewend was aan het feit dat dingen hem (te) makkelijk af gingen, op een lastig AIO-project te zetten. Dankzij zijn stimulans tot het leggen van contacten met andere onderzoekers en het verkennen van nieuwe onderzoeksrichtingen is dit proefschrift uiteindelijk geworden zoals het hier nu ligt. De kans om zelf onderzoeksvoorstellen te schrijven en publicaties te reviewen laten het vertrouwen in eigen oordeel en kunnen enorm groeien, ook al ben je dan op dat moment een relatieve nieuwkomer in een vakgebied. Ik hoop dat ik dit in mijn verdere werk zal kunnen vasthouden en dat in de toekomst nog veel promovendi van Peter zullen leren!

Verder wil ik prof. dr. P.J. Lemstra, dr. H.T. Hintzen, prof. dr. R.P. Griessen, prof. dr. R.A. van Santen, dr. Michel Latroche, dr. F.A. de Bruijn en dr. B.A. Boukamp bedanken dat zij deel uit wilden maken van mijn promotie-commissie.

Voor een vruchtbare samenwerking speciaal dank aan (in willekeurige volgorde): Michel Latroche, Fermin Cuevas, Bob Bowman jr., Mark Conradi *et al*., Pieter Magusin, Subramanian Srinivasan, Brian Pauw, Shu Xia Tao, Tonek Jansen, Albert Bosch, Ludo Froyen. To Michel and Fermin I would like to say that I very much appreciated the chance to work with you at your lab in Thiais and at the ILL in Grenoble. I hope the feeling was mutual.

Een promotie-onderzoek kent vele ups en downs, maar gelukkig waren een aantal mensen altijd bereikbaar voor raad en daad. Allereerst bedank ik Rogier Niessen, in de eerste plaats voor het beantwoorden van 1001 'domme' vragen over electrochemie. Ook was hij een toonbeeld van hoe het leven van een AIO niet altijd over rozen gaat en hoe jezelf vastbijten in een ('loodzwaar') probleem uiteindelijk succes zal opleveren. Verder mogen Wilco Keur, Harrie van Hal en Daniëlle Beelen zeker niet onvermeld blijven. Zij stonden altijd klaar voor de nodige experimentele ondersteuning bij het maken van de Magnesiumlegeringen, evenals Geert van Limpt en later Emiel van Thiel. Harry Wondergem, René Bakker, Peter Graat en Chenjun Duan waren van onschatbare waarde als XRD-analisten en aan hen ben ik dan ook zeer veel dank verschuldigd. Het aantal metingen dat zij in de afgelopen 4 jaar hebben verricht is bijna niet te tellen. Jos Oudenhoven, Jiang Zhou, Loic Baggetto, Alexander Ledovskikh en Paul Vermeulen bedank ik voor de stimulerende wetenschappelijke discussies, maar vooral voor de gezellige tijd die we als kamergenoten op het werk en tijdens etentjes en aansluitende drinkgelagen in de Trafalgar Pub hebben gehad. Ook de schakers van WLC en de korfballers van Attila mogen zeker niet onvernoemd blijven. De broodnodige afleiding in de vorm van geestelijke of lichamelijke inspanning waren dankzij hen ook altijd voorhanden.

Omdat goed wetenschappelijk onderzoek een hoop geld kost wil ik NWO/ACTS bedanken voor de financiering van dit project. Verder wil ik de groepsleiders bij Philips Research bedanken, omdat ook zij de nodige middelen ter beschikking hebben gesteld.

Ondanks het grote aantal namen dat hierboven is genoemd, blijft promoveren, en dan met name het afronden van je proefschrift, een tamelijk individualistische bezigheid. Vrienden en familie snappen weinig tot niets van waar je mee bezig bent, maar het besef dat ze heel trots zullen zijn als naast 'meneer de ingenieur' (maar je mag nog gewoon Peter zeggen hoor, oma...) ook de 'Herr Doctor'-titel is behaald is toch een extra motivatie om door te gaan. Mijn ouders bedank ik nog in het bijzonder voor het geduld waarmee ze de vele nietszeggende antwoorden op hun goedbedoelde vragen over de voortgang van het onderzoek hebben verdragen. Mocht ik nu toch nog mensen zijn vergeten; ook jullie, bedankt!

Eindhoven, Oktober 2008 Peter Kalisvaart

Table of contents

1 Introduction

1.1 Energy demands and availability

Nowadays, the use of portable electronic equipment is still increasing tremendously. The continuous rise in the amount of built-in functionality of e.g. mobile phones, makes the power consumption of these devices ever higher. This puts very high demands on the portable energy source that is used for a particular application with regard to operating time of the equipment, cycle life etc.

On a larger scale, the availability of energy is also becoming an ever increasingly important issue. Traditional energy sources such as fossil fuels are not infinitely available and the resulting emissions are environmentally unfriendly. The use of hydrogen produced in a sustainable manner, such as solar power, as an energy carrier has been proposed as a possible solution to these problems[1]. Stored hydrogen can be used in two forms; as a gas in e.g. PEM fuel cells[2] or electrochemically in rechargeable Nickel-MetalHydride (NiMH) batteries[3], which can be used in portable applications or in Hybrid Electric Vehicles (HEVs)[4].

At present, a number of different technologies are used to store gaseous hydrogen. It can be stored under very high pressures in containers, as a liquid at cryogenic temperatures, physisorbed on large surface area materials such as activated carbons and Metal-Organic-Frameworks or in the form of reversible metal hydrides (MHs)[5]. For a hydrogen storage technology to be viable, it must store at least 6 weight % of hydrogen as stated in the U.S. Department of Energy (DoE) target for 2010[6].

Since the discovery of hydrogen absorption by palladium in 1866[7], metal hydrides have been intensively studied. They can be classified in three groups depending on the character of the metal-hydrogen bond[8]; covalent hydrides such as SnH_4 and AlH_3, ionic hydrides such as NaH and MgH_2 and interstitial hydrides such as $PdH_{0.7}$ and $LaNi_5H_6$. A remarkable characteristic of a large number of metal hydrides is that the volumetric hydrogen density is actually larger than that of liquid hydrogen, which has a density of 70.8 kg/m^3. Of the interstitial hydrides, AB_5-type ($LaNi_5$-based) and AB_2-type ($(Zr,Ti)(Cr,Mn,Ni)_2$-based) alloys have been optimized for use in rechargeable batteries[9].

1.2 Rechargeable NiMH battery concept

In a rechargeable battery, both the electrochemical reaction at the positive electrode and the negative electrode are reversible. Ions are transported through the electrolyte, while electrons move through the external circuit (*e.g.* a mobile phone). Nowadays, three types of rechargeable battery are in widespread use: NiCd, NiMH and Li-ion, although NiCd is slowly going out of use because of the toxicity of Cd. Fig. 1 depicts a schematic of a NiMH battery together with the basic electrode reactions (next page):

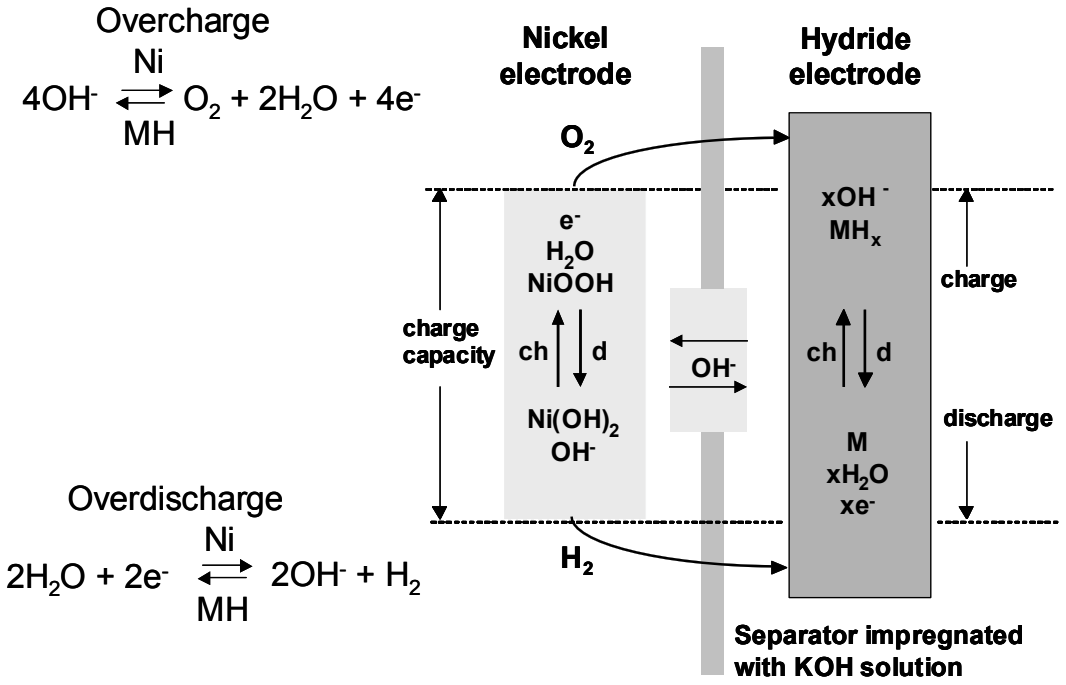

Fig. 1: Schematic overview of the chemistry of a rechargeable NiMH battery

The positive and negative electrodes are electrically insulated from each other by a seperator and together are rolled into a cylinder-shaped stack. Both the electrodes and separator are impregnated with an electrolyte to facilitate the transport of ions between the electrodes. NiCd and NiMH are alkaline batteries where the electrolyte is a concentrated aqueous solution of KOH and LiOH. For both NiCd and NiMH batteries, the positive electrode reaction is:

$$Ni(OH)_2 + OH^- \underset{d}{\overset{ch}{\rightleftarrows}} NiOOH + H_2O + e^- \qquad (1.1)$$

For the NiMH battery the negative electrode reaction is:

$$M + xH_2O + xe^- \underset{d}{\overset{ch}{\rightleftarrows}} MH_x + xOH^- \qquad (1.2)$$

During overcharge and overdischarge, side reactions occur, which are also indicated in Fig. 1. The hydrogen and oxygen gas that is generated is recombined at the MH electrode and is, in principle, not harmful to the battery if the state of over(dis)charge does not persist for too long. A disadvantage of Ni-MH batteries, however, is that the use of an aqueous electrolyte limits the maximum battery voltage to ~1.4 V.

The other type of rechargeable battery that is nowadays in widespread use in portable electronics, is the Li-ion battery. In Li-ion batteries, positive Li^+ ions are transported through the electrolyte instead of negative OH^- ions. The electrolyte consists of a Li-salt, $LiPF_6$ or $LiClO_4$, dissolved in an organic solvent at a concentration of ~1M. The negative electrode is graphite, the positive electrode material is a layered oxide such as $LiCoO_2$. The electrode reactions:

$$LiCoO_2 \underset{discharge}{\overset{charge}{\rightleftarrows}} Li_{1-x}CoO_2 + xLi^+ + xe^- \qquad (1.3)$$

$$6C + xLi^{+} + xe^{-} \underset{discharge}{\overset{charge}{\rightleftarrows}} Li_xC_6 \qquad (1.4)$$

In a Li-ion battery, the reaction products of electrolyte decomposition are not recombined at the other electrode, contrary to the NiMH battery. Overcharge and overdischarge will therefore result in irreversible damage.

All three types of rechargeable battery have their own specific advantages and disadvantages. Environmental concerns as well as a 30-50% lower energy density compared to NiMH, have caused Ni-Cd batteries to be gradually replaced by either NiMH or Li-ion batteries. NiMH has the advantage of intrinsic safety and relatively low cost. The good resistance to overcharge and overdischarge, especially compared to Li-ion, makes them most suitable for applications where multiple cells need to be used in parallel or in series when higher voltages and currents are needed in, for instance, HEVs. However, the aqueous electrolyte limits the voltage of an individual cell to 1.2-1.5 V. Li-ion batteries on the other hand, contain organic electrolytes and have a much higher average discharge voltage of ~3.7 V. As a result, the energy density in Wh/kg or Wh/l is higher for Li-ion than for Ni-MH[10], despite a lower storage capacity in mAh/g, which is the reason why portable electronics almost exclusively use Li-ion batteries nowadays.

1.3 The Hydrogen-driven Fuel Cell

The hydrogen stored in Metal Hydrides can also be released via the gas phase to be used in a fuel cell. A schematic picture of a PEM (Proton Exchange Membrane) fuel cell is shown in Fig. 2:

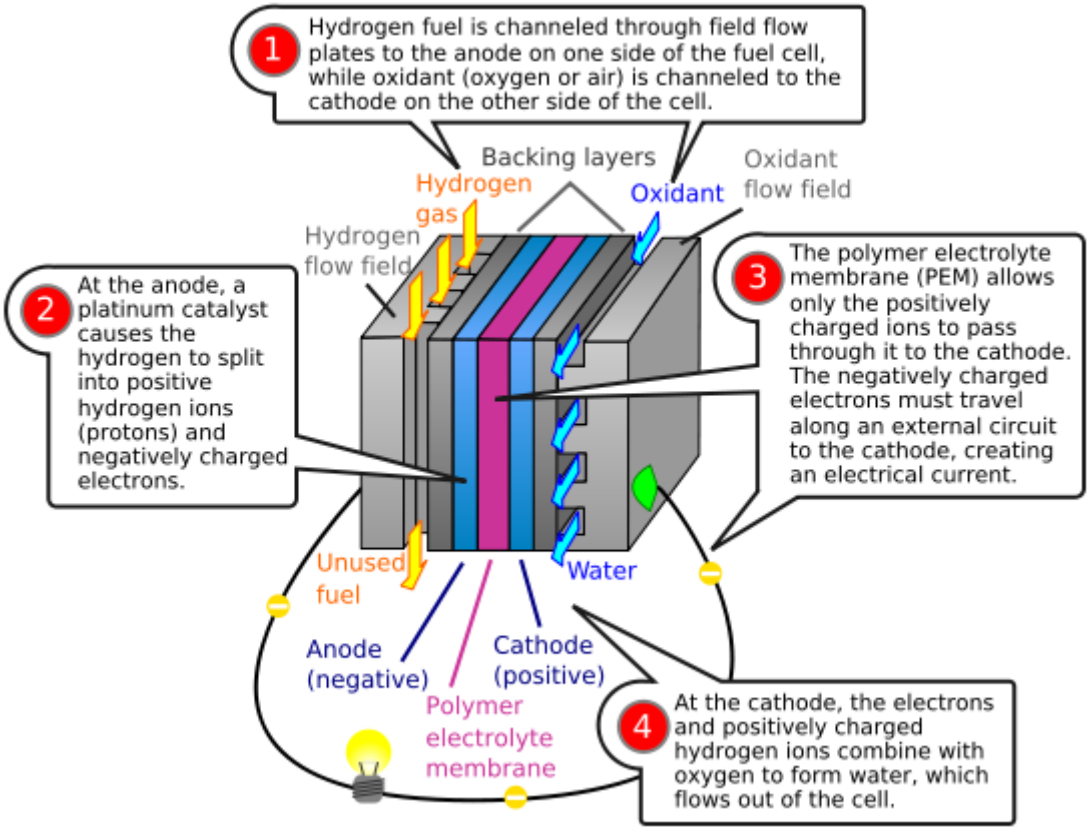

Fig. 2 : Schematic overview of a hydrogen-driven PEM fuel cell[11]

The chemical reactions taking place inside a fuel cell are very simple; on one side, H_2 gas is converted into protons and electrons:

$$H_2(g) \xrightarrow{Pt} 2H^+ + 2e^- \qquad (1.5)$$

At the counter-electrode, oxygen gas (air) is recombined with the electrons and protons to form water:

$$O_2(g) + 4H^+ + 4e^- \longrightarrow 2H_2O \qquad (1.6)$$

As in the alkaline rechargeable battery, the electrons move through an external circuit driving *e.g.* an electric engine in a car and the ions (H^+) move through the Proton Exchange Membrane (PEM) to the other electrode.

Even though the hybrid car, which is already in commercial use, uses alkaline NiMH batteries as its hydrogen storage medium, the hydrogen-driven fuel cell is envisioned as the power source for future-generation hydrogen-powered cars. There are several reasons for this:

- The positive electrode in NiMH batteries consists mainly of Ni and is quite heavy. A fuel cell uses oxygen from the air and does not require another storage material as a counter-electrode. A fuel cell car, would, compared to a battery-powered vehicle, need to carry only the negative electrode.
- Batteries contain a liquid electrolyte. Especially a strongly alkaline aqueous environment is quite aggressive and a large number of potential hydrogen storage materials are simply too reactive with water to be applied in NiMH batteries. Gas-phase storage media do not suffer from this limitation and the range of candidate materials is therefore much larger for fuel-cell powered vehicles as compared to hybrid or all-electric cars.
- There are limits to the rate at which a battery can be recharged. If a battery is recharged too fast, oxygen and hydrogen gas are generated at the cost of water in NiMH batteries, while Li-ion batteries will suffer irreversible damage. In a fuel-cell powered car, the hydrogen *storage* tank can be separately optimized to be recharged with hydrogen as fast as possible, without affecting the properties of the energy *conversion* device. This puts fuel-cell powered vehicles at a distinct advantage compared to all-electric vehicles, as short refueling times are very important for mobile applications.

Because, the 'classic' AB_5-type hydrides store only 1.2 wt.% of hydrogen, these materials are not a viable option for use in a fuel-cell powered vehicle. In order to compete with Li-ion batteries in portable electronics, the energy density needs to be increased as well. Therefore, hydride-forming materials with a higher gravimetric capacity are actively searched for nowadays. Of the metal hydrides, MgH_2 has the highest gravimetric capacity (7.6 wt.%), but suffers from a number of practical shortcomings, such as slow ab-and desorption kinetics and low equilibrium gas pressure. Therefore, the goal of the present work is overcome the aforementioned problems by alloying of magnesium and to gain a more fundamental insight into the hydrogen storage properties of magnesium and its alloys.

1.4 Scope of this thesis

In Chapter 2, a theoretical introduction is given about the electrochemical methods, specifically applied to hydrogen storage materials, used in the present work. More specifically, constant-current charging and discharging, galvonastatic intermittent titration technique and impedance spectroscopy are introduced. Furthermore, the experimental details on alloy and electrode preparation and the experimental electrochemical setup will be described. Diffraction techniques, Nuclear Magnetic Resonance and Density Functional theory will also be introduced in sufficient detail so that the reader is able to understand how the results, discussed in subsequent chapters, have been obtained.

Chapter 3 provides a general overview of hydrogen storage materials. Complex hydrides, nitride-based materials and interstitial metal hydrides are introduced and some general characteristics of interstitial hydrides are described. Subsequently, four classes of Transition Metal based interstitial metal hydrides, AB_5, AB_2, superlattice alloys and Vanadium-based solid solution alloys are reviewed based on a number of key properties: hydrogen storage capacity, crystallographic structure and suitability for use in practical gas-phase or electrochemical storage systems. The fifth class of materials that will be discussed are Magnesium-based alloys. MgH_2 contains twice as much hydrogen (7.6 wt.%) as the Transition Metal-based hydrides. Unfortunately, MgH_2 suffers from a number of shortcomings such as slow sorption kinetics and low equilibrium pressure that will also be discussed in chapter 3. Thin films of Mg alloyed with Rare-Earth metals exhibit interesting optical properties as well as improved hydrogenation kinetics. As an introduction to the work on Mg-Sc alloys and hydrides described in chapters 4 and 5, a preliminary experimental study on Mg-Y bulk alloys is presented and compared to previous investigations on Mg-RareEarth thin films.

In chapter 4, an elaborate comparative study between MgSc thin films and bulk materials is presented. The electrochemical, thermodynamic and crystallographic properties of both systems are investigated and compared. The aim of this work is to investigate whether the thin films can function as a model system for bulk materials. If this is indeed the case, then thin films can be used to search for promising alloy compositions, which can subsequently be 'translated' into a bulk material.

In chapter 5, findings on the more fundamental properties of MgSc alloys and hydrides are presented using neutron diffraction, Nuclear Magnetic Resonance and Density Functional Theory calculations. Neutron diffraction has a distinct advantage over X-Ray diffraction, because the position of hydrogen (deuterium) atoms inside the crystal lattice can be resolved. Nuclear Magnetic Resonance provides information on the chemical (nearest-neighbor) environment of the hydrogen atoms and in this way acts as a more local structure probe compared to diffraction techniques. Density functional theory calculations will be used to determine the structure preference of the ternary hydride for either the rutile structure of pure MgH_2 or the fluorite structure of pure ScH_2 and the results of the calculations are compared to the experimental findings from chapter 4.

Because Sc is very expensive, suitable (*i.e.* cheaper) replacements have to be found. In chapter 6, the synthesis of Mg-Ti based alloys by ball-milling is described. The electrochemical, thermodynamic and crystallographic properties of the resulting alloys are investigated and compared with thin films. The same as for Mg-Sc, neutron diffraction, NMR and DFT studies were carried out on these materials, providing a more fundamental insight in their properties.

2

Theory

Abstract

This chapter gives a brief overview of the basic theory behind the characterization methods used in this thesis. The reactions relevant to electrochemical hydrogen storage are described and the electrochemical characterization methods are introduced. Subsequently, the preparative methods for Mg-based alloys by casting and ball-milling and of test electrodes for electrochemical measurements and the experimental setup are described. The remainder of the chapter describes the aspects of X-ray diffraction, Nuclear Magnetic Resonance and Density Functional Theory calculations that are relevant to the experimental work on hydrogen storage alloys.

2.1 Introduction

The present chapter describes the underlying principles of electrochemical hydrogen storage. The relevant electrochemical hydrogen storage reactions will be described and three electrochemical characterization techniques, namely Constant-Current (CC) measurements, Galvanostatic Intermittent Titration Technique (GITT) and Electrochemical Impedance Spectroscopy (EIS), will be introduced. A description of the experimental electrochemical setup and the experimental details of alloy synthesis by casting and ball-milling and of electrode preparation for electrochemical measurements is also included. In the remainder of the chapter, the basic aspects of X-ray diffraction (XRD), Nuclear Magentic Resonance (NMR) and Density Functional Theory (DFT) that are most relevant to the work presented in this thesis are introduced to a level that is sufficient to understand how the results in chapters 3-6 have been obtained and how they can be interpreted.

2.2. Electrochemical hydrogen storage

2.2.1 Relevant reactions

A hydrogen storage material can be loaded with hydrogen in two different ways. One possibility is via the gas-phase, which will be discussed further in chapter 3. The other option is electrochemical hydrogen storage, which takes place in a battery. The relevant reactions are listed below and are depicted schematically in Fig. 3.

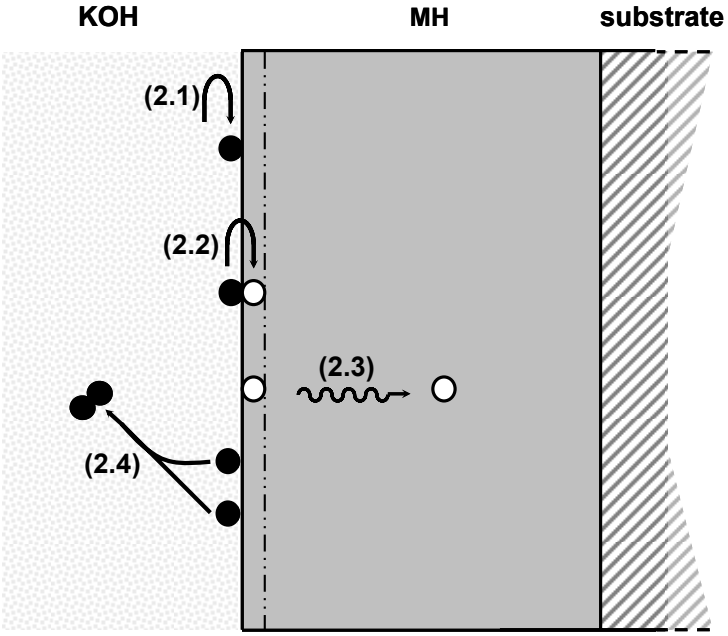

Fig. 3: Schematic drawing of a planar MH electrode. The relevant electrode reactions such as the charge transfer and hydrogen recombination reactions are indicated at their appropriate locations with the same labels as used in the text.

The first step can be represented by the following reaction equation

$$M + H_2O + e^- \underset{disch\,arg\,e}{\overset{ch\,arg\,e}{\rightleftharpoons}} MH_{ad} + OH^- \qquad (2.1)$$

This reaction is known as the Volmer reaction where water is reduced to hydroxyl ions and hydrogen atoms that are adsorbed at the materials' surface. This adsorbed hydrogen then becomes absorbed inside the material in the layer just below the surface, forming *subsurface* hydrogen or H_{ss}

$$MH_{ad} \rightleftarrows MH_{ss} \qquad (2.2)$$

From the subsurface layer, the hydrogen then diffuses further into the bulk of the material, becoming absorbed hydrogen H_{abs}

$$MH_{ss} \rightleftarrows MH_{abs} \qquad (2.3)$$

The adsorbed hydrogen atoms can also recombine to form hydrogen gas in the so-called *Tafel reaction*

$$2\,MH_{ads} \rightleftarrows 2\,M + H_2(g) \qquad (2.4)$$

Hydrogen gas can also be formed in a reaction involving electron transfer, the so-called *Heyrovsky reaction*

$$H_2O + MH_{ads} + e^- \rightleftarrows H_2(g) + OH^- \qquad (2.5)$$

However, the contribution of this reaction is generally considered to be negligible compared to the Tafel mechanism[12].

2.2.2 Constant-Current (CC) measurements

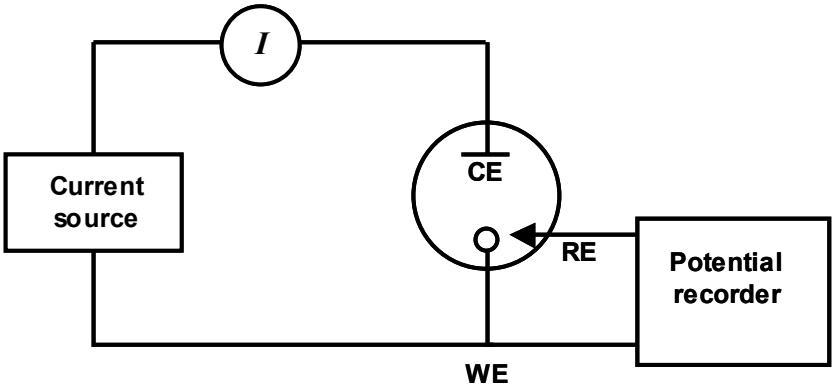

Fig. 4: Schematic overview of the electrochemical experimental setup.

In a galvanostatic experiment, a predetermined, constant current is applied to the working electrode (WE) consisting of the material to be studied and the resulting potential of the WE *versus* a reference electrode (RE) is measured. A simplified scheme of the experimental setup is shown in Fig. 4. This type of experiment is also called *chronopotentiometry* as it records the potential over time. Fig. 5 shows the possible response of the working electrode potential to an applied constant charging current at t = 0. In this example, there is one well-defined potential region where the hydrogen storage reactions (*(2.1)-(2.3)*) take place (region I).

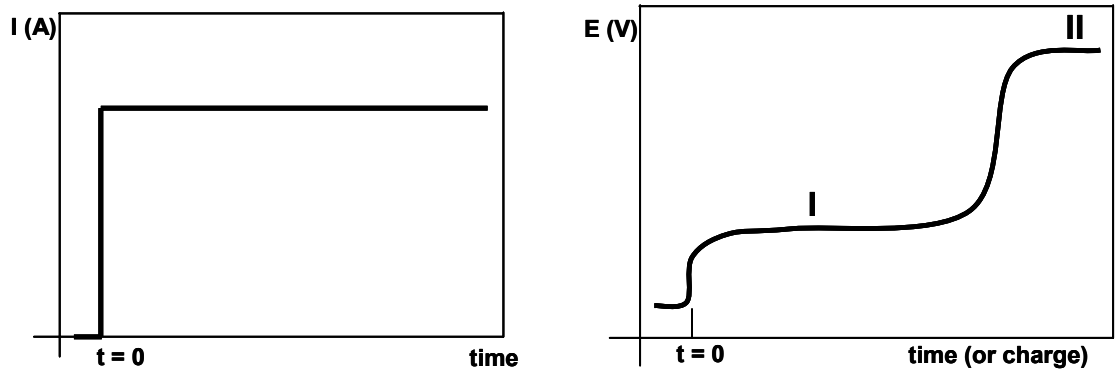

Fig. 5: An applied constant current starting at t = 0 (left) and a possible potential response of the working electrode during charge (right)

The applied current will drive reactions involving electron transfer at the electrode surface; reaction *(2.1)*. It can be seen in this charge-transfer reaction that 1 transferred electron corresponds to 1 stored H atom. The amount of absorbed hydrogen can be determined, simply by integrating the current over time. Therefore, electrochemically determined capacities are most often reported in mAh/g. For conversion to weight%, the following relation is used:

$$1\,mAh = 10^{-3}\,C/s * 3600\,s = 3.6\,C;\; 3.6\,C \cong \frac{3.6\,C}{96485\,C/mol} * 1.008\,g/mol = 3.76 * 10^{-5}\,g$$

Thus, 1 mAh/g is equivalent to 0.00376 wt.%, or 1 wt.% corresponds to 265 mAh/g. Because currents can be very accurately measured, electrochemical determination of the storage capacity is much more precise than by gas-phase measurements, especially during discharge.

When the material approaches its maximum hydrogen content, the potential will start to change towards that of region II. Here, the storage reactions *(2.2)* and *(2.3)* no longer take place and the formation of adsorbed hydrogen is exclusively followed by recombination of the hydrogen atoms to H_2 gas (reaction *(2.4)*). Therefore, near the end of the charging step, some inaccuracy is introduced in the amount of absorbed hydrogen, as not all the transferred charge is converted to absorbed hydrogen.

2.2.3 Galvanostatic Intermittent Titration Technique (GITT)

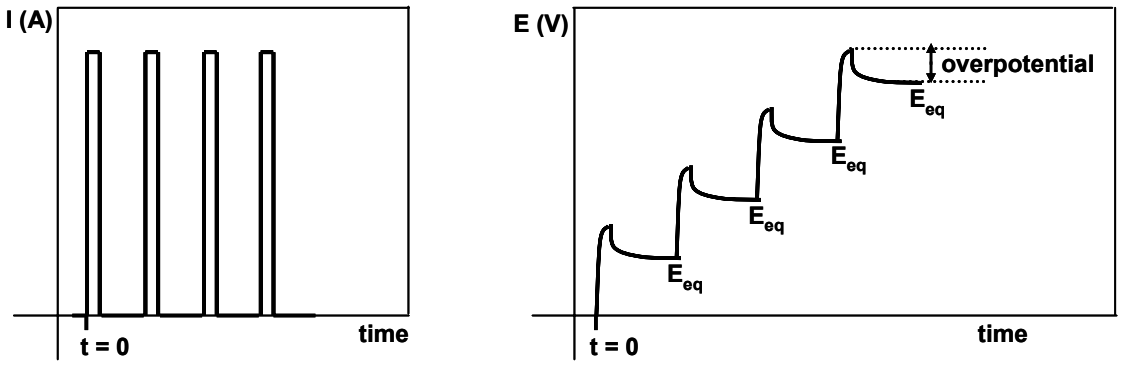

Fig. 6: Alternately applied current pulses and resting periods (left) and the possible potential response of the working electrode (right) during a GITT measurement.

To obtain equilibrium data of an electrochemical system, in this case a hydride-forming material, a technique most often abbreviated as GITT is used. In order to obtain equilibrium potentials, no current should be flowing through the system. Therefore, short current pulses

are alternated with relaxation periods as is shown in Fig. 6. When a short current pulse is applied, reaction *(2.1)* will proceed, storing a small amount of hydrogen. As a consequence, the equilibrium potential after relaxation will differ from the one measured at $t = 0$. The current pulses and relaxation periods are subsequently repeated until the active material is completely charged with hydrogen. The equilibrium potentials recorded at the end of the relaxation periods each correspond to a certain concentration of hydrogen inside the material and an electrochemical equilibrium curve is obtained, which is equivalent to a pressure-composition isotherm (see Chapter 3).

The equilibrium hydrogen pressure and the equilibrium electrode potential can be converted into one another. In general, the chemical potential of hydrogen in a hydride forming material $\mu_{H,MH}$ is linked to that of hydrogen in the gas-phase ($\mu_{H_2,g}$) via[13]

$$\mu_{H,MH} = \frac{1}{2}\mu_{H_2,g} = \frac{1}{2}\mu^0_{H_2,g} + \frac{1}{2}RT\ln\left(\frac{P_{H_2}}{P_{ref}}\right) \qquad (2.6)$$

where $\mu^0_{H_2}$ is the standard chemical potential of hydrogen gas, which is set to 0 by convention. Furthermore, $\mu_{H,MH}$ is linked to the electrode potential by[14]

$$\mu_{MH} = -FE^{eq}_{MH} \qquad (2.7)$$

where F is Farday's constant (96485.3 C/mol) and E^{eq}_{MH} is expressed versus the standard hydrogen electrode (SHE)

$$2H^+ + 2e^- \overrightarrow{\leftarrow} H_2(g) \qquad (2.8)$$

in a 1M acidic solution. However, in alkaline media, the potential of the working electrode is usually monitored *versus* an Hg/HgO reference electrode. The Hg/HgO redox couple in an alkaline solution is represented by the following reaction

$$Hg + 2OH^- \overrightarrow{\leftarrow} HgO + H_2O + 2e^- \qquad (2.9)$$

At an OH^- concentration of 1M, this reaction has a potential *vs.* SHE of +98 mV[15]. The hydrogen electrode in alkaline medium can be written as

$$2H_2O + 2e^- \overrightarrow{\leftarrow} H_2(g) + 2OH^- \qquad (2.10)$$

The equilibrium potential of this redox reaction obviously has the same pH dependence as the Hg/HgO couple and the potential *vs.* SHE is –0.828 V at pH 14[16]. This means that the potential *vs.* Hg/HgO that corresponds to 1 bar of H_2 pressure is, within certain concentration limits, independent of the pH at –0.926V. However, all electrochemical measurements presented in this thesis are done in 6M KOH solution, which is so concentrated that a small correction for the activity coefficients of all involved species has to be made. In the remainder of the work, the following relation will therefore be used

$$E_{MH}^{eq} = -0.931 - \frac{RT}{2F}\ln\left(\frac{P_{H_2}}{P_{ref}}\right) \qquad (2.11)$$

It can be seen in this equation that measuring the potential with mV accuracy enables the determination of the equilibrium pressure to within $1/30^{th}$ of a pressure decade, which is a much higher accuracy than that which can be attained in gas-phase experiments.

2.2.4 Electrochemical Impedance Spectroscopy

The principle of EIS is to impose a small alternating potential (E_{ac}) on an electrochemical system in equilibrium at potential E_{eq} at a certain frequency ω and to measure the current response of the system as a result of this perturbation. The amplitude E_m of the perturbation should be kept small, typically 5 mV, to preserve linearity of the system.

$$E = E_{eq} + E_{ac} = E_{eq} + E_m \sin(\omega t) \qquad (2.12)$$

By varying the frequency ω over several orders of magnitude (typically between 10^5 and 10^{-3} Hz), information can be obtained on the electrochemical reactions *(2.1)-(2.4)*. If the amplitude E_m is kept small, the response of the resulting current i_{ac} will be linear. For a pure resistance *R,* $E = iR$ and the resulting current is given by

$$i_{ac} = \frac{E_{ac}}{R} = \frac{E_m}{R}\sin(\omega t) \qquad (2.13)$$

Subsequently, the impedance Z is defined as

$$Z = \frac{E_{ac}}{i_{ac}} = R \qquad (2.14)$$

For a capacitor C, the current response i_C to an alternating potential signal is given by

$$i_C = C\frac{dE}{dt} = i_{ac} = CE_m\omega\cos(\omega t) = CE_m\omega\sin(\omega t + \pi/2)\,. \qquad (2.15)$$

It is clear that the current response for a capacitor is phase shifted by 90^o with respect to the applied potential signal. To take this into account, a complex impedance is defined, consisting of a real and imaginary part. The potential *E* is now written as

$$E = E_{eq} + E_{ac} = E_{eq} + E_m e^{(j\omega t)} \qquad (2.16)$$

Where $j=\sqrt{-1}$ and $e^{(j\omega t)} = \cos(\omega t) + j\sin(\omega t)$. Substituting this expression for *E* into Eq. *(2.15)* yields the following equation for the impedance

$$Z_C = \frac{E_{ac}}{i_{ac}} = \frac{E_m e^{(j\omega t)}}{CE_m j\omega e^{(j\omega t)}} = \frac{1}{j\omega C} = -\frac{j}{\omega C}\,. \qquad (2.17)$$

When a redox reaction takes place at an electrode/electrolyte interface, the total current is the sum of the double layer charging current i_{dl} and a Faradaic current i_{Far} which corresponds to the charge transfer reaction *(2.1)* yielding

$$i_{tot} = i_{dl} + i_{Far} = C_{dl}\frac{dE}{dt} + i_{Far} \qquad (2.18)$$

The impedance Z_{Far} associated with this reaction is the charge-transfer resistance R_{ct}. The addition of two currents is equivalent to putting their resistances in parallel, resulting in Eq. *(2.19)* for the total impedance

$$Z_{tot} = \left(\frac{1}{Z_C} + \frac{1}{Z_{reaction}}\right)^{-1} = \left(j\omega C_{dl} + \frac{1}{R_{ct}}\right) = \frac{R_{ct}\left(1 - j\omega C_{dl} R_{ct}\right)}{1 + \omega^2 {C_{dl}}^2 {R_{ct}}^2} \qquad (2.19)$$

Usually, the results of an impedance measurement are depicted as an *impedance spectrum*, where $-Z_{Im}$ is plotted *versus* Z_{Re} for each value of ω, which is also known as a Nyquist plot. When the impedance is described by Eq. *(2.19)* and plotted in this way, it has the shape of a semicircle. However, in a real electrochemical setup, there will always be a small ohmic resistance R_s of the electrolyte solution in series with the two parallel impedances of the double layer and the charge transfer resistance. This shifts the semicircle along the real axis over a distance corresponding to R_s. An electrochemical system can thus be 'translated' to an equivalent electronic circuit, which in this case consists of a resistance (= electrolyte) arranged in series with a parallel arrangement of a capacitor (= electrical double layer) and a resistance (= charge transfer reaction). The circuit and resulting Nyquist plot are shown in Fig. 7.

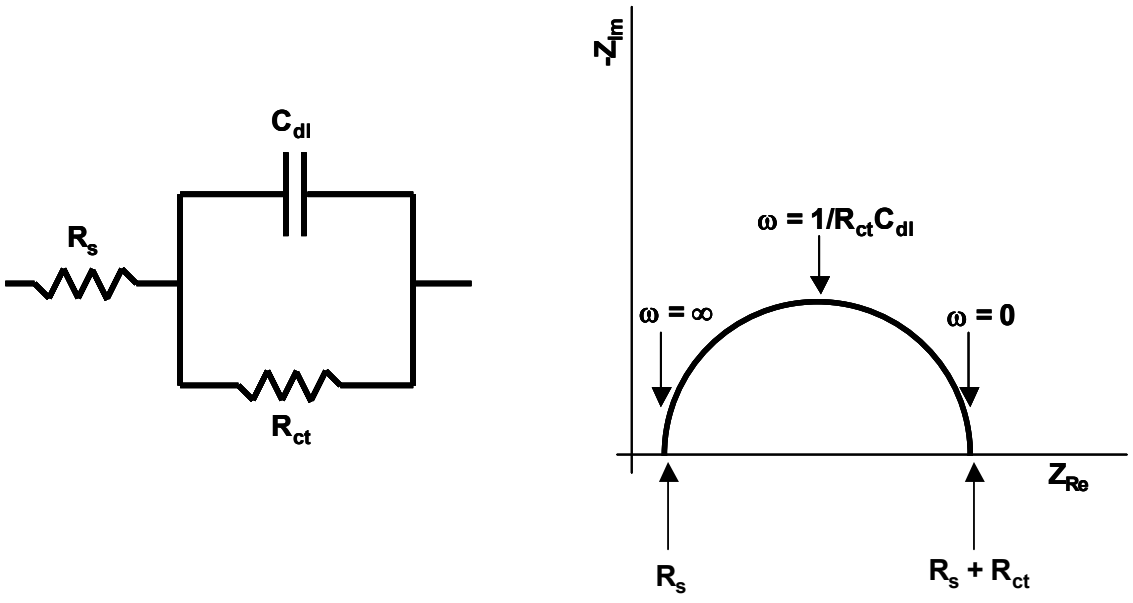

Fig. 7: Equivalent circuit representing an electrode immersed in an electrolyte where a reaction takes place at the electrode/electrolyte interface and the resulting Nyquist plot.

Apart from the charge transfer reaction, bulk diffusion of hydrogen will also play a role in the electrochemical response of a practical system. Semi-infinite diffusion of an active species

can be described by a *Warburg* element (*W*). Using Fick's laws, the Warburg diffusion element can be described as follows[17]

$$W = \sigma \frac{1}{\sqrt{\omega}} - j\sigma \frac{1}{\sqrt{\omega}} \qquad (2.20)$$

The constant σ is given by

$$\sigma = \frac{RT}{n^2 F^2 \sqrt{2}} \left[\frac{1}{c_{ox}^{bulk} \sqrt{D_{ox}}} + \frac{1}{c_{red}^{bulk} \sqrt{D_{red}}} \right], \qquad (2.21)$$

where the subscripts *ox* and *red* stand for the oxidized and reduced form of the species, respectively, c^{bulk} stands for the bulk concentration of the species in the solid and *D* denotes the diffusion coefficients in the solid. Equation *(2.20)* shows that the real and imaginary part of the Warburg impedance are equal. In a Nyquist plot, this will result in a straight line with a constant phase angle of 45° for all frequencies. It has to be noted, however, that this description holds only for semi-infinite diffusion in a flat plate electrode where only one face is in contact with the electrolyte such as the one shown in Fig. 3.

The value for R_{ct} as obtained from the Nyquist plot in Fig. 7 is inversely proportional to the rate constant of the charge transfer reaction in equilibrium. The value of *W* is directly linked to the diffusion coefficient of the active species. At high ω, the Warburg impedance plays no role as diffusion can not keep up with the rapid changes in the potential. In this frequency range, the system is under kinetic control. At lower frequencies, diffusion is fast enough and the system can become diffusion-controlled. The complete equivalent circuit including bulk diffusion and the resulting Nyquist plot are shown in Fig. 8. The equivalent circuit is also known as the *Randles equivalent circuit.*

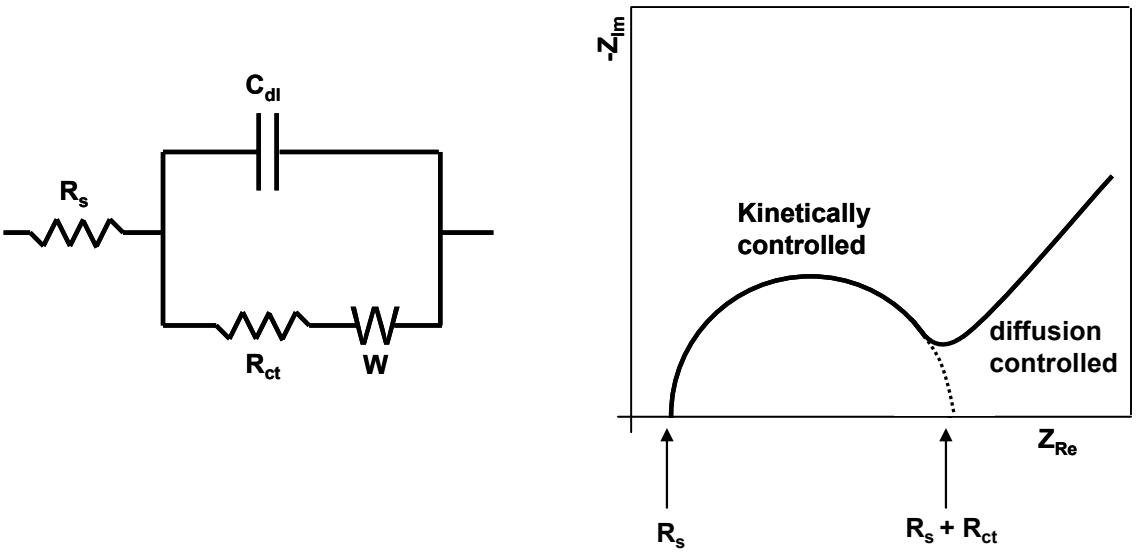

Fig. 8: The Randles equivalent circuit and a typical Nyquist plot showing the Warburg impedance.

It should be noted that, according to Eq. *(2.20)*, both the real and imaginary part of the Warburg impedance go to infinity as ω approaches 0. Of course, this does not happen, because at very low frequency, the assumption of semi-infinite diffusion is no longer valid.

Eventually, the real part of the impedance will approach a limit value, which is a measure for the total overpotential during constant-current flow (see Fig. 6).

2.3 Alloy and electrode preparation

Fig. 9: From left to right: Mg rod and Sc pieces, Mo crucible with lid, sealed Mo crucible, ingot after removal of Mo crucible, file to shave off small metal pieces to make working electrodes, mold to press active material and metal powder into a pellet, electrode holder with pellet fixed at the end by a shrink sleeve.

The present work deals with Mg-based alloys with generally >50 at.% Mg. This presents some preparative challenges, because Mg has a relatively low melting point (650^{o}C) and is also a rather volatile metal. The high vapor pressure of Mg will lead to evaporation losses, contamination of equipment etc. if the Mg is not properly contained. A practical 'trick' to overcome these problems has been developed and is depicted in Fig. 9. A cylindrical piece of Mg metal is put into a matched cylindrical Mo-crucible, together with the alloying element(s). A circular lid is then fixed on top using an arc-melter, hermetically sealing the reactants inside the crucible. The mixture can now be fired to above the boiling point of Mg (1090^{o}C) without problems. After quenching the crucible in water and an annealing step, the Mo-crucible is then removed from around the cylindrical ingot at the bottom. To make a test electrode, the ingot is filed down to small flakes and the fraction <50 micrometers is mixed with Ni or Ag powder, pressed into a small pellet and fixed onto a metal rod (also Ni or Ag) by means of a shrink sleeve.

Instead of melting the constituent metals to form an alloy, other preparation methods are also used in this thesis. Ball-milling is a non-equilibrium room-temperature technique to synthesize alloys from elements that are not miscible by standard methods. In the present work, two types of mill have been used; a low-energy Uni Ball-Mill type II and a Spex 8000 shaker mill. Both are depicted in Fig. 10.

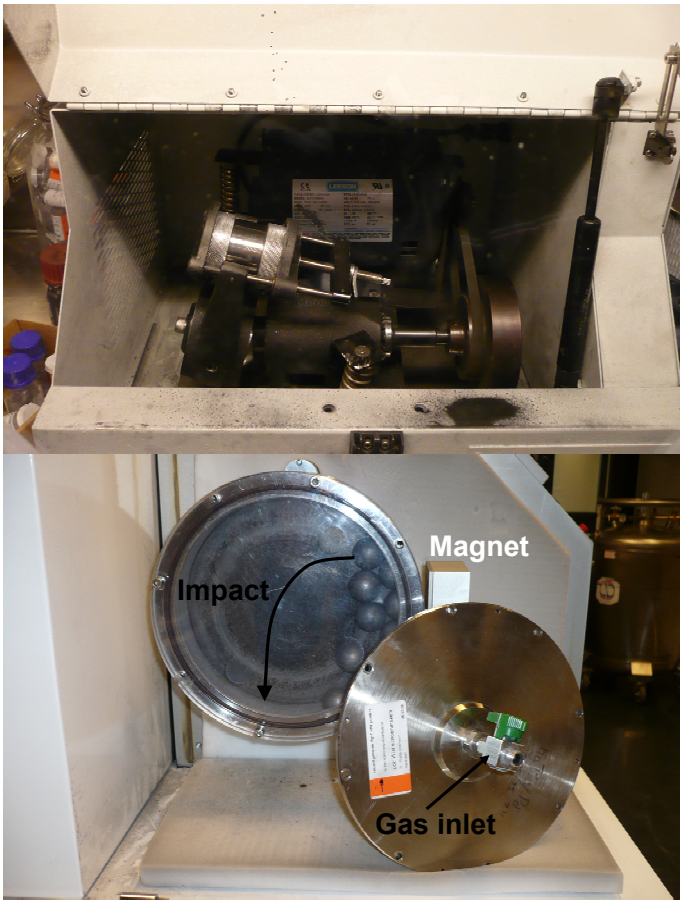

Fig. 10: A Spex 8000M shaker mill (top) and an Uni-Ball Mill type II (bottom). The impact mechanism is visualized for the Uni-Ball Mill through a transparent cover. The lid actually used during milling with a gas inlet in the middle is shown on the right-hand side.

In the Spex shaker mill, the vial makes both left-to-right and back-and-forth motion, inducing an extremely chaotic movement of the powder and balls inside the vial. The rotation speed of the electric engine is, at 1425 rpm, very high, which makes the milling process highly energetic. In the Uni Ball-Mill, impact between the powder and the balls is achieved by magnetic attrition of the steel balls along the side of the wheel until they drop back down to the bottom, trapping the powder underneath. The milling energy is, generally, much lower compared to the Spex; the rotation speed is usually no higher than 100-200 rpm. Through the gas-inlet in the metal cover, up to 7 bars of gas (hydrogen) pressure can be applied.

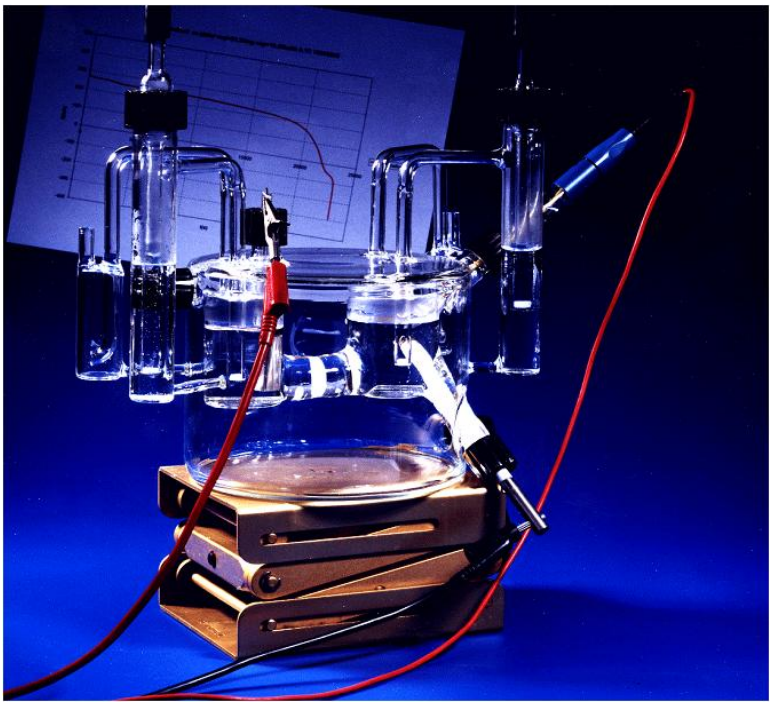

Fig. 11: Photograph of the experimental setup used for electrochemical measurements on powder electrodes.

A picture of the experimental electrochemical setup is shown in Fig. 11. All electrochemical measurements described in this thesis were performed using this 3-electrode setup, consisting of a working electrode (bottom right), a counter electrode (left) and a Pb-free[18] Hg/HgO reference electrode (top right). The setup is continuously flushed with Ar gas to remove any oxygen that is dissolved in the electrolyte. This is necessary because the oxygen reduction reaction

$$O_2(aq) + 2H_2O + 4e^- \rightleftarrows 4OH^- \qquad (2.22)$$

also consumes electrons that can be supplied either by an applied current during charging or by oxidation of the metal hydride during discharge or a resting period (see reaction *(2.1)*). This will lead to overestimation of the absorption capacity and underestimation of the discharge capacity in an electrochemical experiment.

2.4 Crystallography and diffraction

2.4.1 Basic principles

In a crystalline solid, the atoms are arranged in a regular pattern that periodically repeats itself in 3 dimensions: the *crystal lattice.* The *unit cell* is the smallest possible unit that can describe the overall structure of the solid by repeated translation in the direction of its unit cell vectors given by the angles α, β and γ, over a distance given by its *lattice parameters* a, b and c. A schematic picture of a unit cell is given in Fig. 12. The angles and lattice parameters are indicated in the figure. Seven different crystal systems can be distinguished by their specific relations between the lattice parameters a, b and c and the angles between them and these are summarized in Table 1.

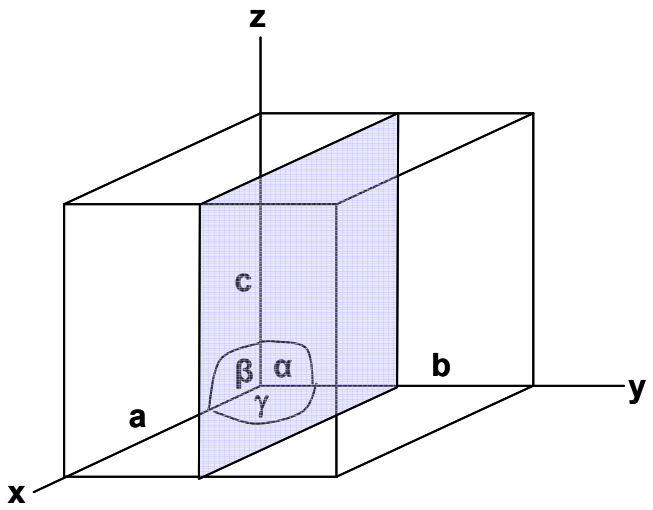

Fig. 12: Schematic picture of a crystallographic unit cell. The shaded area represents a (0 2 0) plane. The lattice parameters a, b and c and the angles between the unit cell axes α, β and γ are also indicated.

Table 1: relations between cell parameters and angles for the seven crystal systems; triclinic, monoclinic, orthorhombic, tetragonal, trigonal, hexagonal and cubic

Crystal system	Cell axes	Angles
Triclinic	$a \neq b \neq c$	$\alpha \neq \beta \neq \gamma \neq 90^o$
Monoclinic	$a \neq b \neq c$	$\alpha = \gamma = 90^o\ \beta \neq 90^o$
Orthorombic	$a \neq b \neq c$	$\alpha = \beta = \gamma = 90^o$
Tetragonal	$a = b \neq c$	$\alpha = \beta = \gamma = 90^o$
Trigonal	$a = b = c$	$\alpha = \beta = \gamma \neq 90^o$
Hexagonal	$a = b \neq c$	$\alpha = \beta = 90^o\ \gamma = 120^o$
Cubic	$a = b = c$	$\alpha = \beta = \gamma = 90^o$

Within a unit cell, crystallographic planes can be identified by their set of so-called *Miller indices (h k l)*, where *h k* and *l* are the reciprocals of the intersections of the crystal plane with each of the axes. The (0 2 0) plane, for instance, intersects the y-axis at a distance b/2 from the origin and is parallel to the y and z-axis as depicted in Fig. 12. For orthogonal crystals (*i.e.* orthorhombic, tetragonal and cubic) the spacing *d* between two crystallographic planes with Miller indices (*hkl*) is given by

$$\frac{1}{d_{hkl}^2} = \frac{h^2}{a^2} + \frac{k^2}{b^2} + \frac{l^2}{c^2} \qquad (2.23)$$

which, for a cubic crystal simplifies to

$$\frac{1}{d_{hkl}^2} = \frac{h^2 + k^2 + l^2}{a^2} \qquad (2.24)$$

where the (110), (011) and (101) planes have the same d-spacing, contrary to *e.g.* an orthorhombic system.

When a powdered sample of a crystalline solid is irradiated with (electromagnetic) radiation of a certain wavelength λ as a function of the angle of incidence θ, a diffraction pattern can be recorded. For each group of crystallographic planes with Miller indices (hkl)

and corresponding d-value, a peak will appear at an angle of incidence θ where the *Bragg law* for constructive interference between two electromagnetic waves:

$$n\lambda = 2d_{hkl}\sin\theta \qquad (2.25)$$

is satisfied. Thus, the *positions* of the reflections in the diffraction pattern, give information about the *shape* and the *size* of the unit cell.

2.4.2 The structure factor

Where the atoms are actually located *inside* the unit cell is derived from the *intensity* of the reflections. The intensity I of a reflection is proportional to the square of the absolute value of the structure factor F_{hkl} which is defined as

$$F_{hkl} = \sum_{1}^{N} f_n\left(\cos 2\pi[hu+kv+lw] + i\sin 2\pi[hu+kv+lw]\right)$$

and (2.26)

$$I \propto \left|F_{hkl}\right|^2$$

where u, v and w are the coordinates of the atoms expressed as fractions of the unit cell axes and f_n is the scattering power, or form factor, of each of the atoms present in the unit cell. The scattering power of an atom is, for X-Rays, directly proportional with the number of electrons around the atomic nucleus and also strongly dependent on θ. Thus, heavy elements scatter very strongly and are readily resolved in X-Ray diffraction, whereas lighter elements are more difficult to detect.

Because these structures are very important for the present work, the body-centered-cubic (bcc) and face-centered-cubic (fcc) lattice will be briefly discussed in more detail.

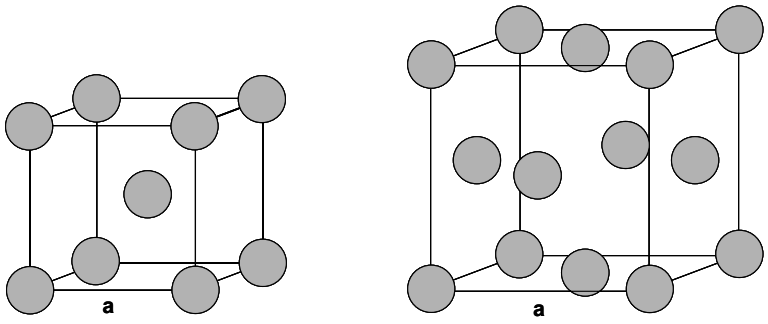

Fig. 13: Body-centered-cubic (left) and face-centered-cubic (right) unit cell with lattice parameter a. The bcc cell contains 2 atoms, one at (0, 0, 0) and one at (½, ½, ½); the fcc cell has 4 atoms at (0, 0, 0), (½, ½, 0), (0, ½, ½) and (½, 0, ½)

The bcc unit cell depicted on the left-hand side of Fig. 13. The atoms on the cube´s 8 corners are shared by 8 adjacent unit cells. Therfore, the unit cell therefore contains two atoms at fractional coordinates (0, 0, 0) and (½, ½, ½). Substituting these coordinates into the equation for the structure factor gives

$$F_{hkl} = f_n\left[1+\cos\pi(h+k+l)\right] =$$
$$2f_n \text{ for } h+k+l = even \qquad (2.27)$$
$$0 \text{ for } h+k+l = odd$$

Thus, in the diffraction pattern of a bcc-structured solid, the reflections for which the sum of the indices is odd are *necessarily absent*.

The fcc unit cell on the right-hand side of Fig. 13 contains 4 atoms at (0, 0, 0); (½, 0, ½); (½, ½, 0) and (0, ½, ½). The result for the structure factor is now:

$$F_{hkl} = f_n[(1+\cos 2\pi(h+k)+\cos 2\pi(k+l)+\cos 2\pi(h+l)] =$$
$$4f_n \text{ for h, k and l all even or all odd} \qquad (2.28)$$
$$0 \text{ for mixed h, k and l}$$

Compared to a primitive cubic lattice (with only one atom at (0, 0, 0) and $F_{hkl} = f_n$ for any h, k, l), the diffraction patterns of a bcc and fcc structured solid exhibit fewer diffraction peaks. Especially an fcc structure has a very typical signature with two peaks close together, alternating with a single reflection as shown in Fig. 14.

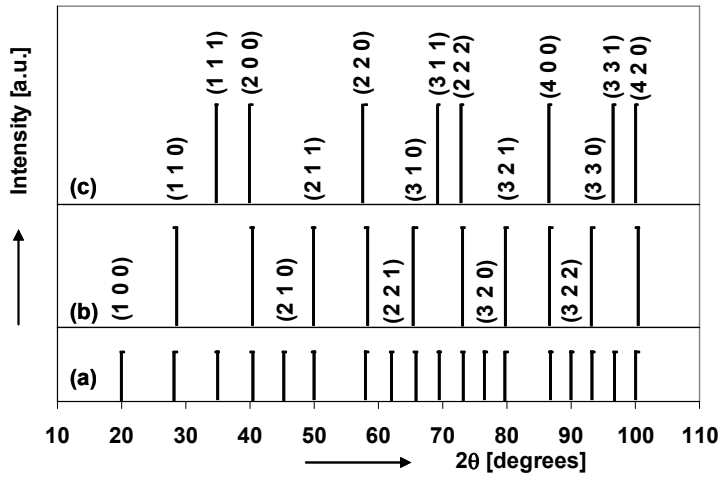

Fig. 14: 'Fingerprint' diffraction patterns of a primitve (a), body-centered (b) and face-centered (c) cubic crystal lattice.

In principle, a powder with sufficiently small particle size and sufficiently large crystallite size will exhibit a diffraction pattern that resembles the ones depicted above. However, in practice, diffraction lines are always somewhat broadened due to instrumental and thermal effects. Furthermore, reduction of the crystallite size and internal stresses (induced by, for instance, hydrogenation or cold-deformation of the material) will lead to additional broadening. Below a few tens of nanometers, the effect of the grain size will be dominant and can be quantified by the Scherrer formula

$$L = \frac{0.9\lambda}{B\cos\theta} \qquad (2.29)$$

where L is the coherence length or crystallite size in Ångstrom, B is the full-width-at-half-maximum (FWHM) of the peak in radians.

2.4.3 Vegard's law

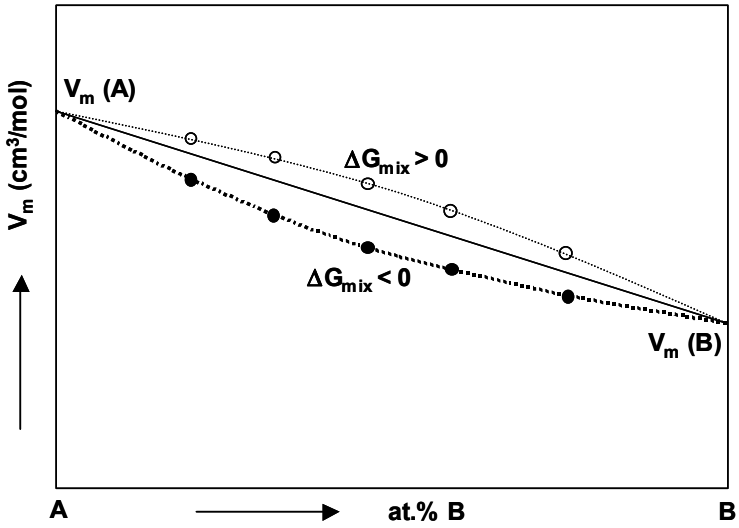

Fig. 15: Illustration of Végards' law. Upon formation of a solid solution of A and B, the resulting mixture will have a molar volume intermediate between that of A and B themselves. For systems with negative heats of mixing, there will generally be a slight negative deviation from linearity, whereas positive deviations can occur for systems with positive heat of mixing.

Végards' law is not so much a law as it is a rule-of-thumb. It states that the volume per mole of atoms of a substitutional solid solution of 2 (or more) elements or compounds will lie between the molar volumes of the constituents. If both constituents and the resulting solid solution have the same crystal structure, a comparison of the molar volumes of the elemental solids can predict the volume change upon changing the molar ratio. If this is not the case, then the effective atomic radii as derived from the unit cell volume of the elemental solids have to be used. A perfectly linear relation is almost never found in practice. In general, a slightly negative deviation from linearity will occur for mixtures with a negative free energy of mixing, whereas a positive deviation is indicative for a tendency of the system to segregate into the end-members (*i.e.* positive free energy of mixing). This is schematically illustrated in Fig. 15.

For solid solutions formed between two compounds (*e.g.* hydrides), the situation is a bit more complicated and the resulting volume harder to predict. However, when an increase (or decrease) in mol% of the element or compound with the larger molar volume also causes the volume of the resulting solid solution to increase (or decrease) monotonously, then the system can still be said to obey Vegard's law, even if all the crystal structures are different. Changes in molar volume thus found by diffraction techniques are generally regarded as very strong evidence that a solid solution has been formed.

2.5 Nuclear Magnetic Resonance [19]

Many atomic nuclei have a magnetic moment and respond to an applied magnetic field. Conveniently, all three hydrogen isotopes are NMR-active and can be studied with this technique. When ^{1}H nuclei are brought into a magnetic field, a small energy difference between parallel and anti-parallel alignment results, which is proportional to the field strength B_0:

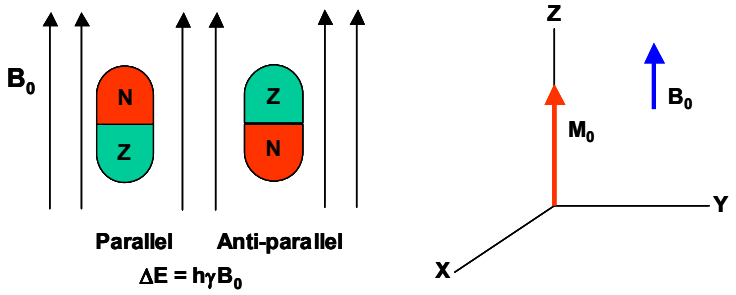

Fig. 16: Orientation of nuclear spins in an applied magnetic field B_0. The energy difference ΔE between parallel and anti-parallel orientation is given as $h\gamma B_0$, where h is Plancks constant, B_0 is the applied magnetic field in T and γ is the gyromagnetic ratio.

As a consequence, a (small) population difference between parallel and anti-parallel alignment arises, giving the sample a net magnetization M_0 parallel to B_0, as is depicted on the right-hand side of Fig. 16. The proportionality constant γ is called the *gyromagnetic ratio*, which is isotope-specific. The gyromagnetic ratio for ^{1}H is the highest of all elements, 42.57 MHz/T. A sample containing hydrogen will absorb electromagnetic radiation with a frequency equal to γB_0, which is the so-called *Larmor frequency* ν_L, and is typically in the radio-frequency range. *E.g.* a field strength of 11.7 T, which is commonly used in commercial NMR equipment, results in a ^{1}H resonance frequency of 500 MHz.

However, the specific resonance frequency of any particular nucleus depends not on the externally applied field, but on the *effective field* B_{eff} *at the position of this nucleus*

$$B_{eff} = B_0(1-\sigma) \qquad (2.30)$$

The quantity σ is called the shielding tensor, which is influenced by the atoms in the nearest-neighbor shell in the crystal lattice and/or the type of lattice site it occupies. NMR can thus be used as a local structure-probe, providing structural information on much shorter length scales than *e.g.* X-Ray or Neutron Diffraction. Chemically different nuclei are distinguishable by their so-called *chemical shift* δ with respect to a reference compound, which is assigned zero chemical shift. In the case of ^{1}H, ^{2}H, ^{13}C and ^{29}Si, TetraMethylSilane (TMS) is commonly used as a reference compound and the expression for chemical shift is

$$\delta = \frac{\nu_L - \nu_{REF}}{\nu_{REF}} * 10^6 \qquad (2.31)$$

where the value of δ is expressed in ppm (parts per million). This is the most convenient way to express the chemical shift as this is a field-independent quantity.

The simplest way to measure the chemical shifts in the sample is illustrated in Fig. 17. An on-resonance RF pulse will rotate the magnetization over an angle θ, which is proportional to the duration of the pulse (τ) and its amplitude (B_1). Because the specific resonance frequencies are not known beforehand, the excitation pulse must contain a sufficient bandwidth around the ^{1}H resonance frequency of TMS. A 90^o pulse rotates the magnetization vector into the xy plane where it will start to rotate around the z-axis at the Larmor frequency. This rotation, also called *precession*, induces an AC signal in the detection coil, from which the chemical shift spectrum of the sample can be obtained by Fourier transformation.

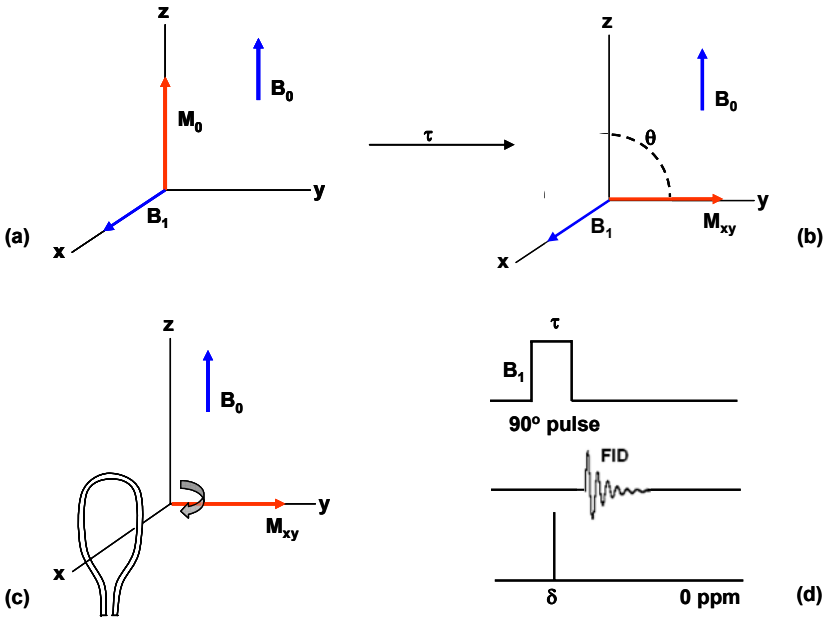

Fig. 17: Graphical representation of the measurement of a free induction decay (FID) to obtain the chemical shift spectrum. A 90° pulse (B_1, τ) rotates the magnetization into the xy plane (b). Precession of the magnetization around the z-axis induces an ac signal in the detection coil (c) which decays to zero over time. Fourier transformation of the FID signal yields the specific ^{1}H resonance frequency (d)

While the chemical shift can be used to probe the chemical environment of a nucleus and provides 'static' information, the dynamics of hydrogen interaction with the crystal lattice and other hydrogen atoms can also be studied by NMR. After the magnetization vector has been rotated into the xy-plane as illustrated in Fig. 17, it will slowly return to its original position along the +z axis. The characteristic time constant of this recovery process is denoted T_1 and is called the *spin-lattice relaxation time*. Fig. 18 (a)-(d) (next page) illustrates a common way to measure T_1 by an inverse-recovery sequence. First, the samples' magnetization is rotated over 180° from the '+z' to the '-z' direction (a). A short time after the 180° pulse, the magnitude of the magnetization in the –z direction has decreased (b) and a 90° pulse is applied, which turns the magnetization into the xy-plane (c) and generates a free induction decay (d). The amplitude (*S*) of the signal *at the start of the acquisition time (S_0)* is governed by the following equation

$$S = S_0(1 - 2e^{-TI/T_1}) \qquad (2.32)$$

where TI is the time between the 180° and 90° pulses. By varying TI, T_1 can be determined.

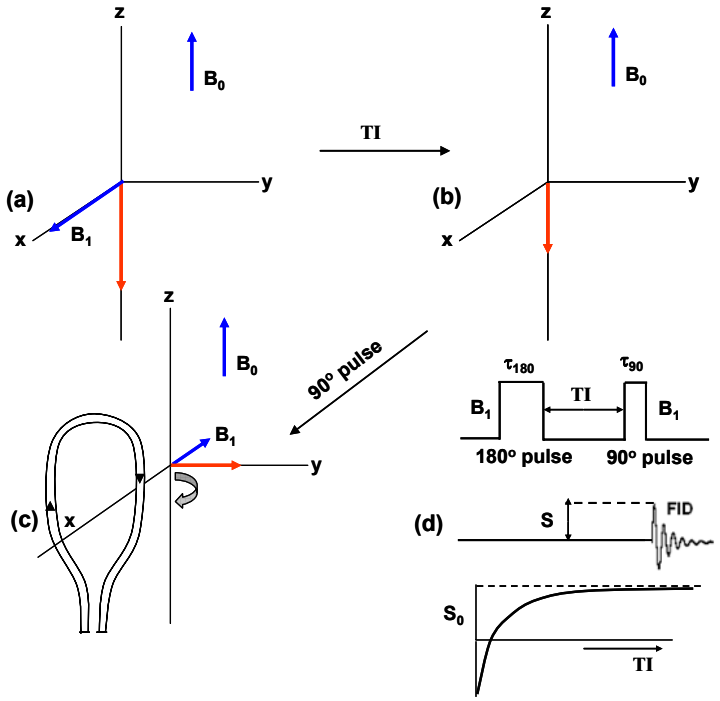

Fig. 18: Pulse sequence of an inverse-recovery measurement of the spin-lattice relaxation time T_1.

$T_{1\rho}$ is the spin-lattice relaxation time in the rotating frame of reference. In this case, the B_1 field is not switched off, after a 90° pulse (see Fig. 17). Instead it is phase-shifted by 90° so that it is lying parallel to the nuclear magnetization along the y-axis. A sufficiently strong B_1 field forces the magnetization vectors of spins with different resonance frequencies to remain aligned in the xy-plane. This is called spin-locking; in a frame of reference rotating at ν_L, the magnetization appears stationary. As B_1 will be much smaller than B_0, the magnetization decays, with a characteristic time constant $T_{1\rho}$. After the B_1 field is switched off, a FID is recorded. The value of $T_{1\rho}$ can be determined by measuring the amplitude at the start of the FID as a function of the duration of the spin-locking pulse.

After a 90° pulse, the magnetization in the xy-plane, or *transverse magnetization*, and thus the signal amplitude in the FID, decays with a characteristic time constant T_2^* according to

$$M_{xy} = M_{xy0} e^{t/T_2^*} \qquad (2.33)$$

where M_{xy0} is the transverse magnetization immediately after the 90° pulse. T_2^* will always be (much) shorter than T_1 especially in solids. There are two factors contributing to T_2*, one of which is variations in the local field B_{loc} due to differences in chemical environment and small inhomogeneities in B_0. The other is interaction between spins, involving energy transfer between hydrogen atoms in close proximity to each other. Phase coherence of the transverse magnetization is lost during this process, leading to a 'pure' T_2 effect. This is the reason why T_2 is called the *spin-spin relaxation time*. A way to measure T_2, a so-called spin-echo sequence, is illustrated in Fig. 19.

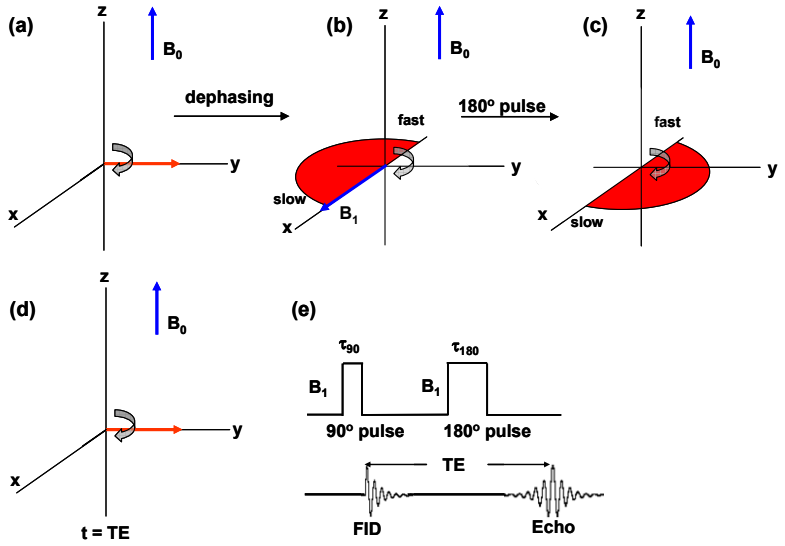

Fig. 19: Spin-Echo sequence to measure the spin-spin relaxation time T_2

After a 90° pulse, the spins start to dephase due to differences in precession frequency (*i.e.* chemical shift) and spin-spin relaxation, (a-b). Subsequently, a 180° pulse is applied around the x-axis, after which the slower-moving spins will be 'overtaken' by the faster-moving spins resulting in refocusing of the magnetization (d) and a peak in the signal; the 'echo' (e). However, only the magnetization losses that were caused by differences in precession frequency are refocused. Therefore, the maximum signal strength in the echo will decrease with increasing time between the 90 and 180° pulses due to spin-spin interactions. The relation between the maximum signal amplitude *S* in the echo and T_2 is given by

$$S = S_0 e^{-TE/T_2} \qquad (2.34)$$

where the *EchoTime TE* is the time between the end of the 90° pulse and the maximum in the echo. T_2 can now be determined by measuring S as a function of TE.

T_1, $T_{1\rho}$ and T_2 can be used to study hydrogen motion rates in liquids and solids. T_1 is most sensitive to hydrogen motions near the Larmor frequency. As a consequence, T_1 will show a minimum as a function of temperature, at the point where the correlation time τ_c associated with hydrogen motion multiplied by the larmor frequency is approximately equal to 1. The temperature dependence of T_2 is different from that of T_1. At low temperatures, and hence low hydrogen motion rate, T_2 remains almost constant, but above a certain temperature it will start to increase. This can be understood from the fact that T_2 is a measure of the time scale of spin-spin interactions between the hydrogen atoms. When the hydrogen mobility increases, these interactions become weaker, resulting in an increase of T_2 above a certain temperature. At hydrogen hopping rates comparable to the so-called "nutation frequency", *i.e.* the Larmor frequency *in the B_1 field,* a minimum in $T_{1\rho}$ will occur. Because the Larmor frequency in B_1 is much lower ($\gamma_H B_1 << \gamma_H B_0$), in the kHz range rather than MHz, the minimum occurs at much lower temperatures. The temperature dependencies of T_1, $T_{1\rho}$ and T_2 are depicted schematically in Fig. 20 and will be used to study hydrogen motion rates in chapter 5.

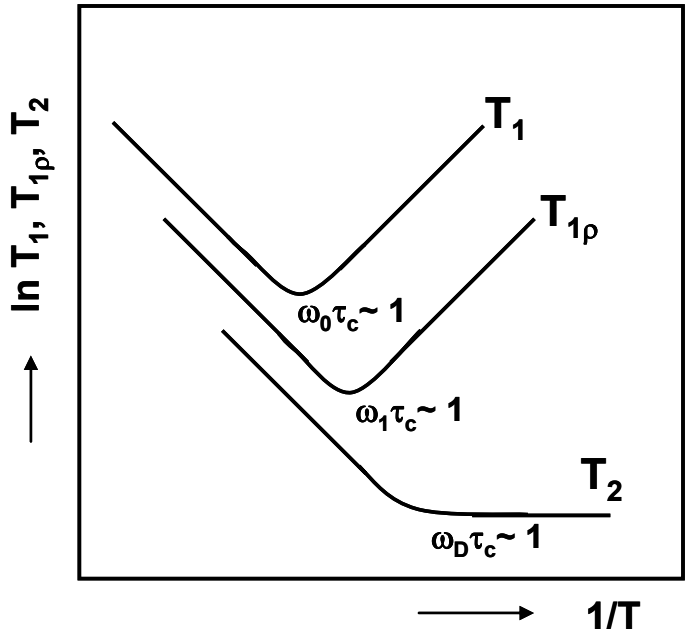

Fig. 20: Schemcatic representation of the temperature dependence of three types of relaxation time. The minima in the $T_{1(\rho)}$ and the onset of the increase in T_2 correspond to characteristic hydrogen motion rates.

2.6 Density Functional Theory

Density Functional Theory, or DFT, is a quantum mechanical theory used in physics and chemistry to investigate the ground state of many-body systems such as crystalline solids. The practical implementation of DFT has been made possible through the Hohenberg-Kohn theorems and Kohn-Sham equations, which will be briefly discussed below.

Hohenberg and Kohn[20] proved that for an interacting electron gas in an external potential $\upsilon(r)$ (*e.g.* an electronic potential exerted by the atomic nuclei in a solid) there exists a unique functional $F[n(r)]$ of the electron density $n(r)$ such that the total energy

$$E = \int \upsilon(r) n(r) dr + F[n(r)] \qquad (2.35)$$

attains its minimum value for a density $n(r)$ that is the ground-state electron density associated with the external potential $\upsilon(r)$. They furthermore proved that the density that yields this minimum value is the single-particle ground-state density. The functional $F[n(r)]$ includes the kinetic energy, the electron-electron electrostatic repulsion and the exchange and correlation energy E_{xc} which denotes the non-coulombic interactions between electrons.

The Hohenberg-Kohn theorems can be put into practice using the Kohn-Sham equations[21]. They showed how the ground state energy of a many-body system could be obtained by solving the following set of one-electron equations self-consistently. The total electric potential $\varphi(r)$ that an electron experiences is given by

$$\varphi(r) = \upsilon(r) + \int \frac{n(r')}{|r - r'|} dr' \qquad (2.36)$$

where the second term on the right-hand side is the electron-electron repulsion term. The exchange and correlation contribution $\mu_{xc}(n)$ is given by

$$\mu_{xc}(n) = \frac{d(n\varepsilon_{xc}(n))}{dn} \qquad (2.37)$$

where ε_{xc} is the exchange and correlation energy per electron. The Shrödinger equation for a single electron is now given by

$$\left\{-\frac{1}{2}\nabla^2 + [\varphi(r) + \mu_{xc}(n(r))]\right\}\psi_i(r) = \varepsilon_i\psi_i(r) \qquad (2.38)$$

where $\psi_i(r)$ is the single-electron wavefunction and ε_i its energy. For a system of N electrons:

$$n(r) = \sum_{i=1}^{N} |\psi_i(r)|^2 \qquad (2.39)$$

The electron density *n(r)* and the corresponding energies ε_i can be obtained by solving Eq. *(2.36)-(2.39)* self-consistently. The problem with this approach is that nobody knows exactly what the exchange and correlation energy looks like for an inhomogeneous electron gas. However, good approximations are available based on E_{xc} of a homogeneous free electron gas, which can be calculated exactly.

The Vienna Ab-initio Simulation Package (VASP)[22], which uses the Perdew and Wang '91 (PW91) generalized gradient approximation for the exchange and correlation potential[23], has been used to perform the DFT calculations. The program uses periodic boundary conditions, which means it requires only a single unit cell as input and then treats it as an infinite system, and plane-wave basis sets to describe the electron density distribution around each ion in a crystal lattice. From these basis sets, an initial guess for *n(r)* is constructed. Subsequently, the electrostatic contribution and exchange-correlation contribution to the energy are calculated from Eq. *(2.36)* and *(2.37)* and a new wavefunction $\psi_i(r)$ is calulated from Eq. *(2.38)*. This wavefunction is then used to calculate a new electron density from *(2.39)*. This procedure is repeated until *n(r)* and $\psi_i(r)$ do not change anymore.

The procedure as described above yields the electronic ground state for a given configuration of the nuclei. The program subsequently checks whether there are forces acting on the atoms, which would indicate that the volume is not yet optimal. The atomic positions are then adjusted in the direction that will decrease the total energy. Because this changes υ(r), the iterative solution of Eq. *(2.36)-(2.39)* has to be repeated to find the electronic ground state again.

In the way described above, it is possible to calculate the reaction enthalpy of virtually any reaction for which no experimental data are known by calculating the total energies of the reactants and reaction products. In chapters 5 and 6, DFT will be used to calculate the hydrogenation enthalpies of Mg-alloy hydrides and to compare the energies, and thus relative stablities, of different crystallographic modifications of the hydride.

3

Overview of hydrogen storage materials

Abstract

An overview of the state-of-the-art in hydrogen storage materials is given. Complex hydrides and nitride-based materials are briefly described based on their crystal structure, storage capacity and the biggest challenges that must be overcome before they can be practically applied. The interstitial metal hydrides are discussed in greater detail. An introduction about their general properties is given and four application areas of metal hydrides are briefly described. Subsequently, four classes of interstitial metal hydrides, AB_5-type alloys, AB_2 type materials, Superlattice alloys and Vanadium-based solid solutions are described, based on their hydrogen storage capacity, crystallographic properties of the alloys and hydrides and the optimization of the alloy's composition for application in either gas-phase or electrochemical storage applications. The optimization of AB_5-type alloys for application in NiMH batteries is further advanced than for any of the other materials that are discussed, but a drawback is the rather low gravimetric storage capacity (1.2 wt.%). For the Superlattice alloys, a 10% increase in capacity compared to AB_5 for an AA-size battery has been demonstrated with comparable cycle life. Of the Transition Metal-based alloys, the Vanadium solid solutions have the highest reversible capacity at practically accessible temperatures and pressures of up to 2.3 wt.%. Magnesium has a sufficiently high gravimetric storage capacity for fuel cell applications (7.6 wt.%), but suffers from very slow ab-and desorption kinetics due to severe diffusion limitations through its hydride. Combining Mg with Rare-Earth metals in thin film form induces some interesting optical phenomena as well as a vast improvement in the ab-and desorption rates. Prelimenary experiments with bulk Mg-Y and Mg-Sc alloys and hydrides showed the same improvements in the kinetics as those found for thin films. These results are briefly discussed as an introduction to the work described in subsequent chapters.

3.1 Introduction

A large number of elements interact with hydrogen, forming hydrides. In this chapter, four categories of hydrides will be discussed and their hydrogen storage properties evaluated for application in fuel cells and/or Ni-MH batteries:

1) Complex hydrides
2) Nitride based materials
3) Interstitial hydrides
4) Magnesium-based materials

The first two are potentially very high-capacity materials for gas-phase storage, with the lightest representative of complex hydrides, $LiBH_4$, containing over 18 wt.% of hydrogen and nitride-based materials also storing over 10 wt.%. The interstitial hydrides are the most intensively studied class of hydrides for application in Nickel-MetalHydride batteries. As the application of NiMH batteries in Hybrid Electric Vehicles is highly topical at this moment, the AB_5, AB_2 and Vanadium-based materials will be elaborately reviewed regarding their crystal structure, storage capacity and electrochemical properties. The fourth class, the Mg-based materials, is currently under intense investigation, both as gas-phase and electrochemical storage medium. Pure MgH_2 has a reversible storage capacity of 7.6 wt.%, but suffers from various shortcomings, which will be discussed later.

3.2 Complex hydrides

The most famous examples of this class of hydrides are sodium borohydride ($NaBH_4$) and sodium alanate ($NaAlH_4$). In $NaAlH_4$, the hydrogen is covalently bonded to Al in a negatively charged AlH_4^- tetrahedron, where Na^+ acts as the counterion. The orthorhombic unit cell containing 4 formula units is depicted in Fig. 21:

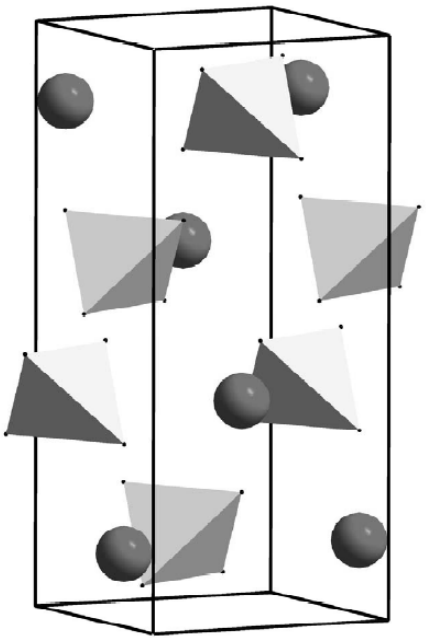

Fig. 21: Crystal structure of $NaAlH_4$. The unit cell contains 4 formula units in a tetragonal structure, consisting of covalent AlH_4^- tetrahedral and Na^+ counterions.

$NaAlH_4$ releases hydrogen according to the following reaction scheme[24]:

$$3\ NaAlH_4 \overset{\leftarrow}{\rightarrow} Na_3AlH_6 + 2\ Al + 3\ H_2 \qquad (3.1)$$

$$2\ Na_3AlH_6 \overset{\leftarrow}{\rightarrow} 6\ NaH + 2\ Al + 3\ H_2 \qquad (3.2)$$

The first step takes place at 1 bar hydrogen pressure at 306 K and releases 3.7 wt% hydrogen, the second step an additional 1.8 wt.%. This 5.5 wt% is still below the DOE target of 6.0 wt% for 2010. Other problems include the need for a catalyst (*e.g.* Ti) in order to make the dehydrogenation reaction reversible and also the rather extreme conditions needed for re-absorption despite the use of a catalyst because of the macroscopic phase separation into NaH and Al. Another problem is deactivation of the Ti catalyst. Because free Al metal is formed upon dehydrogenation at elevated temperature a Ti-Al alloy will be formed, which has been shown to decrease the catalytic activity of the Ti[25] as well as decreasing the intrinsic capacity of the system as Al is 'leaking' away from the alanate compound. Because Al is one of the most reactive metals in terms of intermetallic-formation, it is highly unlikely that alternative metal catalysts will eliminate this problem.

Although the borohydrides have a significantly higher hydrogen content than the alanates, up to 18 wt.% for $LiBH_4$, their practical application is severely hindered by high desorption temperatures and poor reversibility. The latter is illustrated by the fact that synthesizing $LiBH_4$ from its elements is very difficult, but can nevertheless be achieved by ball-milling a Li/B mixture with a high excess of Li under 60 bars of hydrogen[26]. The same is true for $Mg(BH_4)_2$ and $Ca(BH_4)_2$, where, after desorption to $Mg(Ca)H_2$ and B, only 5-6 wt.% of hydrogen can be resorbed, under rather extreme conditions, while more than 8.5 wt.% is theoretically expected[27, 28].

3.3 Nitride-based materials

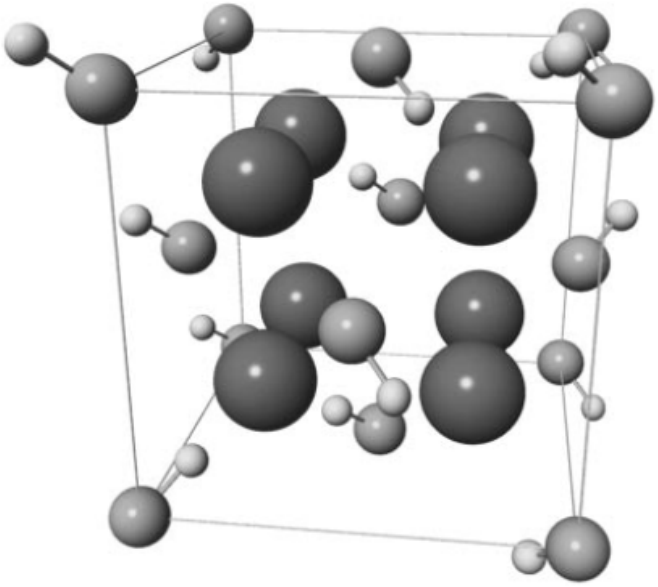

Fig. 22: Crystal structure of Li_2NH[29]

It was recently found that some light-weight metal nitrides are also able to reversible ab-and desorb large amounts of hydrogen. In 2002, it was found by Chen *et al.*[30] that Li_3N can absorb two hydrogen molecules to from a mixture of LiH and $LiNH_2$. This mixture could release the hydrogen without formation of ammonia, contrary to pure $LiNH_2$, according to the following reaction:

$$LiNH_2 + 2LiH \longleftrightarrow Li_3N + 2H_2 \qquad (3.3)$$

The reversible hydrogen content is 11.5 wt.% based on Li_3N, which is quite high compared to *e.g.* the alanates. Unfortunately, the complete release of the hydrogen requires temperatures in excess of 300°C, which is too high for practical application. Xiong *et al.* investigated a series of $Mg(NH_2)_2$-LiH mixtures prepared by ball-milling[31]. It was found that using 3 molar equivalents of LiH suppressed the formation of ammonia during desorption as compared to an equimolar mixture. The total reversible capacity was approximately 5 wt.% at 220°C. The equilibrium pressure of the material equaled ~50 bars at the same temperature, which would make it quite a suitable option for mobile hydrogen storage at room temperature. Luo *et al.* reported similar effects for a mixture of $LiNH_2$ and MgH_2[32]. However, the reversible hydrogen content of these systems is, at 5 wt.%, much lower than the 11.5 wt.% that Li_3N can theoretically store.

Another option to adjust the hydrogenation properties is to make a composite material with a different hydrogen storage compound. Pinkerton *et al*. synthesized a ternary compound of $LiBH_4$ and $LiNH_2$ by ball milling with nominal composition $Li_3BN_2H_8$[33]. The amount of desorbed hydrogen was more than 10 wt.% above 250°C. However, the desorption was found to be exothermic and it would therefore be very difficult to rehydrogenate the resulting material.

The nitride-based materials are quite promising candidates for practical hydrogen storage systems. Although the operating temperatures are still too high, application of a suitable catalyst may bring down the reaction temperatures further. A way to adjust the equilibrium pressure has already been demonstrated, although the capacity was decreased by a large amount, and it is therefore not unlikely that the operating temperatures and pressures can be adjusted to ambient conditions.

3.4 Interstitial metal hydrides

3.4.1 General properties of interstitial hydrides

The by far most intensively studied group of metal hydrides are the interstitial hydrides. In an interstitial hydride, hydrogen molecules first dissociate on the surface forming atomic, adsorbed hydrogen. The H-atoms subsequently diffuse into the material, where they end up inside ‘holes’ in the metal host-structure called interstitial sites. Depending on the applied temperature and hydrogen pressure, the hydrogen concentration in these compounds can vary continuously, contrary tot the compex hydrides.

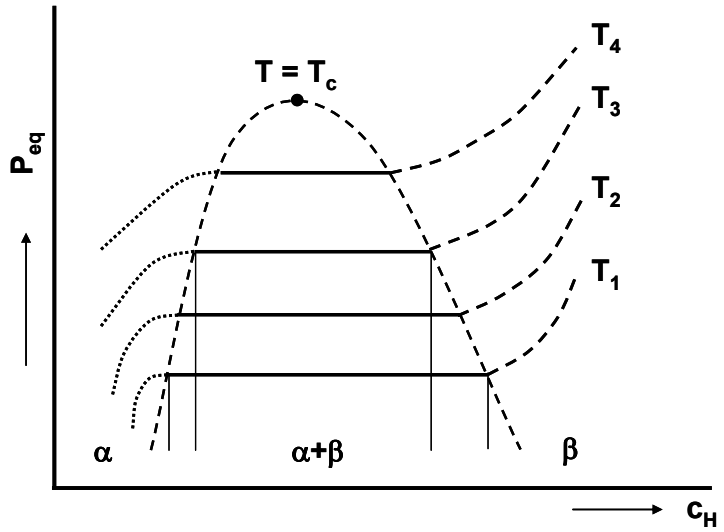

Fig. 23: General shape of pressure-composition isotherms of an interstitial metal hydride as a function of temperature

The storage capacity and thermodynamic properties of an interstitial metal hydride are characterised by the so-called Pressure-Composition Isotherm, or PCI-curve. Basically, this curve depicts which external hydrogen pressure has to be applied to store a certain amount of hydrogen inside the material or at which pressure the hydrogen is available when extracting it from the material. Ideally, a PCI curve of an interstitial metal hydride looks like the ones depicted in Fig. 23. At low hydrogen concentrations, the equilibrium pressure gradually increases as the hydrogen concentration is increased. There is only a single hydride phase at this stage, which is called the *α - phase.* At a certain critical hydrogen concentration x_α, a new phase with a higher hydrogen concentration x_β will be formed. When the total hydrogen concentration is between x_α and x_β the equilibrium pressure stays constant and is called the plateau pressure. This pressure increases with temperature as is also shown in Fig. 23 according to the Van 't Hoff relation[34]:

$$\ln\frac{P_{eq}}{P_0} = \frac{\Delta H_f}{RT} + \frac{\Delta S^{\phi}}{R} \qquad (3.4)$$

When the total hydrogen concentration equals x_β, the α-phase has completely disappeared and the hydride consists of a single phase once more. Further increase of the hydrogen content now once again leads to a gradual increase in equilibrium pressure in the so-called *β-solid solution region*. The miscibility-gap, will become ever narrower as the temperature is increased, until at the so-called critical temperature T_c, the plateau will completely vanish.

Applications of metal hydrides

Metal hydrides can be used for various purposes, depending on the nature of the hydride. This section gives a short overview of the fields in which MHs can be used. It is by no means exhaustive, but the most interesting applications are highlighted:

- **Hydrogen storage**

    1. Electrochemical hydrogen storage in interstitial hydrides is currently used in rechargeable alkaline Ni-MH batteries. The most commonly used

materials are AB_5-type and AB_2-type alloys. Increasing efforts are being made to optimize these materials for use in battery packs of Hybrid Electric Vehicles (HEVs).

2. Stored hydrogen in metal hydrides or complex hydrides can also be released as a gas and subsequently be used to produce electricity in a fuel cell. In this case, the hydrogen storage material replaces a high-pressure vessel or liquid hydrogen-tank as the portable hydrogen source for *e.g.* fuel-cell driven cars.

- **Heat storage**

  Metal hydrides essentially have a double function as energy stores. The stored hydrogen can be desorbed and subsequently burned to water to release -242 kJ/mol, but upon hydride *formation* a lot of heat is released to the surroundings. The formation enthalpy of *e.g.* MgH_2 is –77 kJ/mol H_2, which is about 30% of the energy content of the hydrogen. Another thing to keep in mind is that after combustion or conversion in a fuel cell, the hydrogen has been converted into water vapor and has to be regenerated. When hydrides are used as heat stores, the same amount of hydrogen can be re-used cycle after cycle. The basic idea is that waste heat from an industrial process can be used to desorb hydrogen from a high-temperature hydride such as MgH_2, which is subsequently absorbed by a hydride with a higher dissociation pressure that is maintained at ambient temperature. This process is reversed when there is a heat demand on the side of the low-pressure hydride, where the hydrogen is then resorbed, which releases the stored heat back to the surroundings. A more extensive description of such a system using Ni-doped MgH_2 and a $TiMn_2$ based alloy can be found in a study by Bogdanovic *et al.*[35]

- **'Smart windows'**

  Rare-earth thin films were shown to be optically active upon changing the hydrogen content. In the metallic as well as in the dihydride form, these films are shiny and reflective. However, in 1996 at the VU in Amsterdam, it was discovered that the trihydrides of Rare-Earth metals are semiconducting and, as a consequence, transparent to a large part of the visible spectrum[86]. This optical change is easily reversible by changing the surrounding hydrogen pressure. Later it was discovered by van der Sluis *et al.* at Philips Research Laboratories that Mg-RE alloy thin films exhibit an additional optical state in which the film becomes black and highly absorbing, additionally achieving color-neutrality in the transparent state[88]. These different optical states could be used to tune *e.g.* the amount of sunlight entering office buildings, saving energy costs for heating and/or cooling.

- **Hydrogen sensors**

  The large changes in optical and electrical properties of metal hydride thin films upon hydrogenation can be used to detect the presence of hydrogen in the surrounding air. Kumar and Malhotra used a Pd-capped Sm thin film as a hydrogen sensor, based on resistivity measurements[36]. A very low detection

limit and short response time were achieved for detection of hydrogen in ambient atmosphere. However, a disadvantage of electrical sensing is the risk of inducing sparks at the detection point and that the detectors occupy a lot of space. Therefore, sensors making use of optical properties are currently under development. A very elegant application of this principle has recently been demonstrated by Slaman *et al.*[37]. Using an optical fiber, with a thin film of MgTi, a material which will be discussed in detail in chapter 6, deposited on the end, the large changes in reflectance upon hydrogenation can be detected from the backside of the film and used as an indicator for the presence of hydrogen in the surrounding atmosphere. The detection limit is, at 15% of the lower explosion boundary, sufficiently low and the response time and reversibility are excellent.

For on-board storage of hydrogen gas (Hydrogen storage option 2) the target energy density for 2010 is 6 wt.% as formulated by the Department of Energy (DoE)[6] For Hybrid Electric Vehicles, different criteria apply, mainly because a battery pack in a hybrid car has a much narrower operating range, typically between 40 and 60% of its nominal capacity, and has to be able to deliver or accept very high currents during acceleration of the vehicle or recovery of braking energy. An extensive review of on the requirements set by both the DoE and the Partnership for the Next Generation of Vehicles (PNGV) and the suitability of the available battery technologies for application in HEVs based on these criteria is given by Nelson[38].

In the remainder of the chapter, different classes of interstitial hydrides will be discussed and their potential for application as hydrogen storage materials will be evaluated both for electrochemical application in Ni-MH batteries as well as gas-phase storage for fuel-cells.

3.4.2 AB_5 type materials

The by far most-researched materials forming interstitial hydrides are the AB_5-type alloys. These materials have excellent ab-and desorption kinetics, even at room-temperature and relatively mild (close to ambient) pressure conditions, but a disadvantage is the relatively low gravimetric storage capacity of only 1-1.5 wt.%. However, the alloys have proven to be very suitable as anode materials in NiMH batteries and nowadays, most commercial Ni-MH rechargeable batteries use AB_5 type alloys as the negative electrode. 'A' represents a metal with a very high affinity for hydrogen, in this case a rare-earth metal. 'B' is a metal with a low affinity for hydrogen, *i.e.* late 3d transition metals such as Ni. The 'parent' compound in this respect is $LaNi_5$, whose remarkable hydrogenation properties were first described by Van Vught *et al.* in 1970[39]. The material has a plateau pressure of 1.7 bar at room-temperature and can, in principle, be charged to $LaNi_5H_6$ corresponding to ~1.4 wt% or 372 mAh/g between 0 and ~3 bars hydrogen pressure.

3.4.2.1 Crystal structure of the alloys and hydrides

$LaNi_5$ and most of its related compounds crystallize in the $CaCu_5$ structure, which is depicted in Fig. 24. Both the La-atoms and Ni-atoms form hexagonal arrays, where the Ni-atoms are located in the top-and basal plane and in a plane exactly in the middle. The basic repeating unit of the structure is also indicated in Fig. 24, but the structure is more easily visualized using the representation with 7 La-atoms in the basal and top planes. It has to be noted that there is also a Ni atom in the middle of each of the 6 side faces. There is only 1 site for the rare-earth atom, namely the 1a-site. The Ni-sites in the basal and top-planes are called '2c'-sites whereas the Ni-sites in the middle-plane are denoted as '3g'.

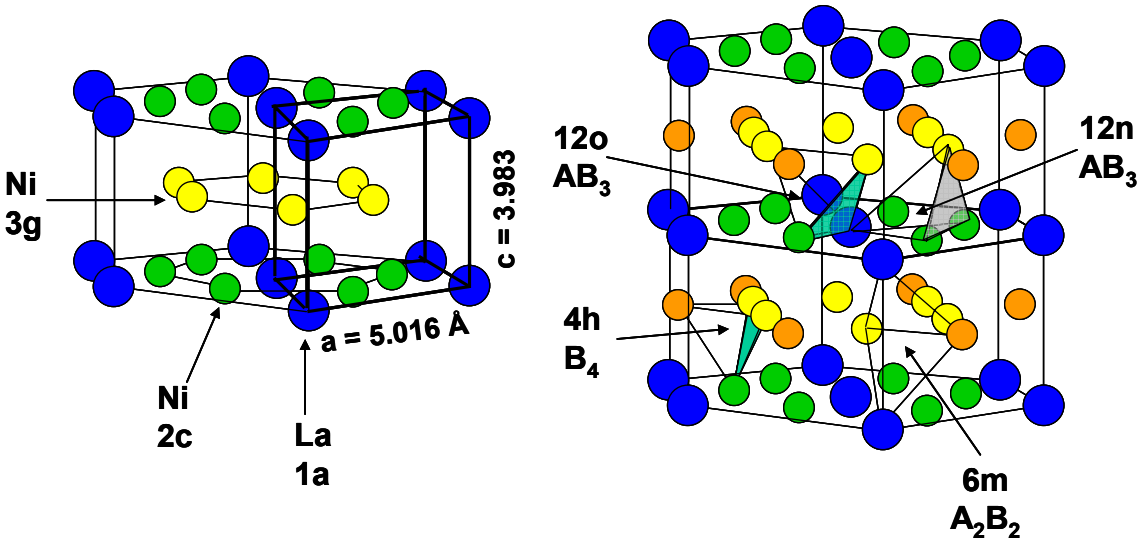

Fig. 24 : Crystal structure of $LaNi_5$; hexagonal unit cell (left) and two stacked unit cells with the interstitial sites for hydrogen indicated by arrows (right)

The crystal structure of the metal host-lattice is generally preserved upon hydrogenation. Several types of tetrahedral interstices can be identified within the structure with different metal co-ordination: A_2B_2, AB_3 (2 types) or B_4 and these are also indicated in Fig. 24[40, 41, 42] Upon hydrogenation, the A_2B_2 sites are filled first, followed by the AB_3 sites (12n before 12o). The occupation of the B_4 sites remains low, even for a fully loaded hydride.

3.4.2.2 Hydriding properties

Gas-phase storage

The plateau pressure, at ~2 bars at room-temperature, is close to ideal for fuel-cell applications. Furthermore, the plateau region is 5.5 H/f.u. wide, which means that the compound releases the major part of its hydrogen within a very narrow pressure window. This is very advantageous as it would allow a system using this material as a storage medium to operate at a near-constant pressure. The gravimetric capacity is, however, much lower than the required 6 wt.%, only 1.4%. The volumetric capacity, based on the volume of the unhydrided metal alloy, is 142 kgH_2/m^3, which is much larger than liquid hydrogen. However, such a wide plateau region means a large difference in H-concentration between the α and β-phase and hence a large so-called *discrete lattice expansion.* Upon crossing the plateau region, the material expands over 20% and the total expansion is 24.5%. Taking this expansion into account and assuming the most efficient packing of spherical hydride particles (74%), the maximum theoretical capacity of a hydrogen tank using $LaNi_5$ is 84.5 kg/m^3, which is only slightly above liquid H_2.

Electrochemical storage

The properties of unsubstituted $LaNi_5$ are far from ideal for battery-applications. The plateau pressure of about 2 bar limits the effective capacity in an aqueous environment, although in a sealed battery, the pressure can rise to ~15 bar, which allows the full capacity to be used. However, a high partial hydrogen pressure inside the battery will lead to a high self-discharge rate at the Ni-electrode reducing the shelf-life of the battery[43].

Much more so than for gas-phase storage, the high discrete expansion of the material leads to severe problems in alkaline environments. Cracking of the particles exposes fresh surface to the electrolyte leading to corrosion of the active material and rapid capacity decay. In view of the above, modifications to the alloy composition for electrochemical applications have aimed to both decrease the plateau pressure and the discrete lattice expansion.

3.4.2.3 Modifications to the alloy composition

In general, the equilibrium pressure of a hydride depends on the hydrogen affinity of the constituent elements, but also on the volume of the interstitial sites and hence to the total molar volume of the material. Since Ni is the smallest transition metal with a molar volume of only 6.6 cm^3, almost any substitution on the Ni-sites lead to a decrease in plateau pressure. The relation between $\ln P_{eq}$ and the unit cell volume for the case of AB_5-type materials is depicted in Fig. 25 for substitutions on the Ni-site. For substitution by elements with hydrogen affinity comparable to Ni, such as Al, Mn and Co, the relation is almost perfectly linear[44, 45, 46].

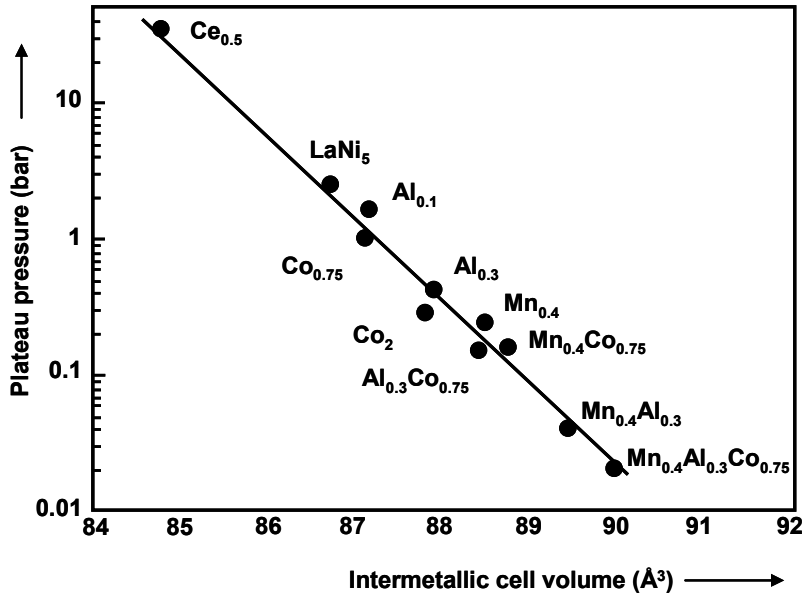

Fig. 25 : Correlation between $\ln(P_{eq})$ and the unit cell volume of $LaNi_5$-type alloys. Note the almost perfectly linear relationship for substituting elements with comparable hydrogen affinity to Ni (Al, Co and Mn) or La (Ce).

Substitution of Ni by Co also had a profound effect on the cycling stability of the material. $LaNi_4Co$ has 2 plateau regions during hydrogen absorption[47], forming an intermediate γ-phase. The lattice expansions associated with the α-γ and γ-β transitions are much smaller than the 20% of $LaNi_5$ resulting in a much improved cycling stability. Eventually, the composition converged towards the tri-substituted compound $LaNi_{3.55}Mn_{0.4}Al_{0.3}Co_{0.75}$, which, in equilibrium, has a single plateau about 3 H/f.u. wide with a large β-branch, a total capacity of 325 mAh/g (slightly more than 5 H/f.u. at 1 bar) and about 10% discrete expansion going from $LaNi_{3.55}Mn_{0.4}Al_{0.3}Co_{0.75}H_{0.6}$ to $LaNi_{3.55}Mn_{0.4}Al_{0.3}Co_{0.75}H_{3.4}$[47]. The only remaining issue was that Co was now an important constituent of the alloy, but also rather expensive.

An alternative approach is to adapt the stoichiometry of the alloy. Above 995°C $LaNi_5$ has a homogeneity-domain ranging from $LaNi_{\sim 4.8}$ to $LaNi_{\sim 5.4}$ at 1270°C. In 1994, Notten *et al.* showed that the cycling stability of unsubstituted $LaNi_5$ was significantly improved for Cu-substituted non-stoichiometric compositions[48]. Using *in-situ* diffraction techniques, the

increase in the stoichiometry was found to result in a much reduced discrete lattice expansion and eventually the disappearance of the two-phase coexistence region when the stoichiometry was higher than 5.4[49]. This can be viewed as a 'critical composition' equivalent to the critical temperature in Fig. 23. Analysis of line-broadening effects in neutron diffraction showed that the internal stress inside the material was significantly decreased by the smaller discrete expansion[50].

Unfortunately, the equilibrium pressure of the $LaNi_{5+x}$ and $LaNi_{4+x}Cu$ compounds is significantly increased[48, 51], thereby reducing the available capacity in electrochemical applications. The same substitutions that were effective for bringing down the equilibrium pressure of $LaNi_5$ can also be used for the over-stoichiometric compounds. However, the maximum capacity of a multi-substituted $MmNi_4Mn_{0.4}Al_{0.3}Co_{0.35}$ alloy was found to be only 270 mAh/g[52] (as derived from gas-phase loading at 1 bar), which is significantly lower than for the stoichiometric $LaNi_{3.55}Mn_{0.4}Al_{0.3}Co_{0.75}$.

The AB_5-type alloys used nowadays have compositions very similar to $LaNi_{3.55}Mn_{0.4}Al_{0.3}Co_{0.75}$ with some minor modifications. MischMetal, a mixture of rare-earths rather than pure La is used for economical reasons, along with small additions of *e.g.* Si to further improve the corrosion resistance. The capacity of the alloys is around 320 mAh/g[53].

3.4.3 AB_2 Laves phase alloys

AB_2 type Laves phase alloys have also been extensively investigated for application in Ni-MH batteries. Again, A represents an element with a high affinity for hydrogen; Zr, Ti or a mixture of both and B later transition metals from V to Ni. The gravimetric capacity of this type of alloy is generally quite a bit higher than that of AB_5, reaching 1.8-2.8 wt.%. The same type of problems that had to be solved for AB_5 type alloys such as adjusting the plateau pressure and improving the cycling stability also had to be dealt with here. In this respect, the development of AB_5-type alloys is a lot further advanced than that of AB_2-type alloys.

3.4.3.1 Crystal structure of the alloys and hydrides

There are three types of Laves phase, which are just different stacking arrangements of the structural unit shown in Fig. 26: the hexagonal C14, cubic C15 and hexagonal C36. $MgZn_2$, $MgCu_2$ and $MgNi_2$ are prototypical compounds of each of the structure types, respectively.

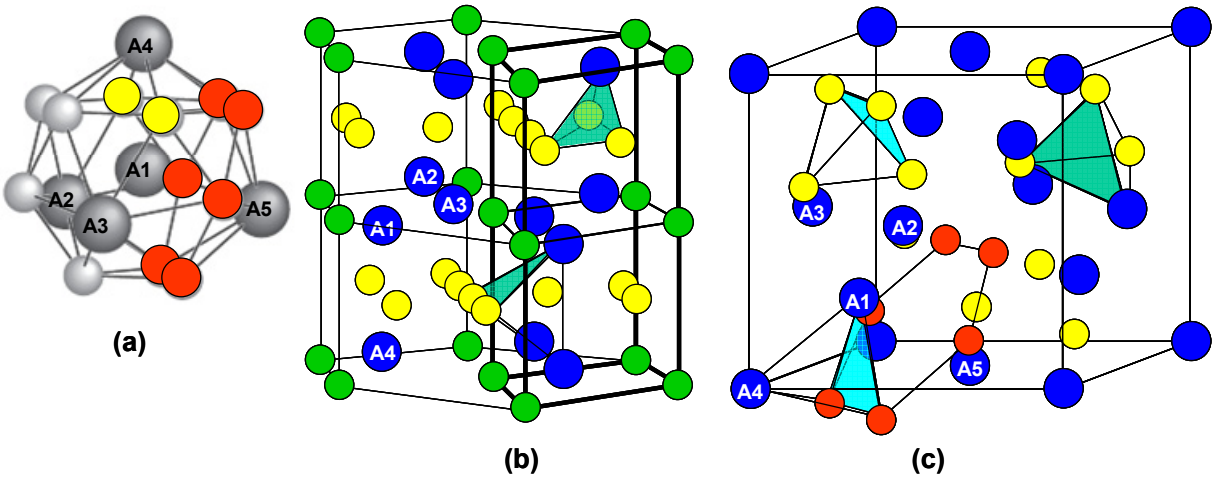

Fig. 26: Crystal structure of AB_2 Laves phase alloys. (a): basic building block, (b): hexagonal C14 structure, (c): cubic C15 structure

The C14 and C15 structure-types are shown in Fig. 26. In the hexagonal C14 Laves phase type, (part of) the basic building block is easily recognizable as is shown in Fig. 26 along with the basic repeating unit of the structure. $ZrMn_2$ and $TiMn_2$ belong to this structure type, along with high-temperature modifications of $ZrCr_2$ and $TiCr_2$.

In the case of the cubic C15 structure type, the basic building block from Fig. 26 (a) is a bit more difficult to recognize, but with 2 extra B-atoms just below the bottom plane, the A-tetrahedron and the hexagon of B-atoms between atom A1 and A5 can be depicted. The structure can be viewed as a face-centered cubic arrangement of the A-atoms where half the tetrahedral sites are also occupied by A-atoms in a 'staggered' arrangement. The B-atoms form tetrahedra around the empty tetrahedral sites in the A-sublattice. ZrV_2 and the low-temperature modifications of $ZrCr_2$ and $TiCr_2$ belong to this structure type.

The crystal structure of the alloys is generally preserved upon hydrogenation. Available sites for hydrogen have, similar to the AB_5-type alloys, A_2B_2, AB_3 or B_4 coordination. In Fig. 26 (a) and (b), both a A_2B_2 and a AB_3 site are indicated. Except in alloys where both constituents have rather high hydrogen affinity, such as ZrV_2 only the A_2B_2 sites are filled.

3.4.3.2 Hydriding properties

Gas-phase storage

Table 2 summarizes the hydrogenation characteristics of a number of binary AB_2 type alloys. Note that '$C_{electrochemical}$' is simply the capacity in H/f.u. expressed in mAh/g and not an experimentally obtained value in an electrochemical setup:

Table 2 : Capacities in H/f.u. and mAh/g for a number of different AB_2 type alloys. Structure type is given between brackets, plateau pressure is given at the temperature indicated between the brackets[9].

	$C_{solid\text{-}gas}$ (H/f.u.)	P_{max} (bar), T (^oC)	$C_{electrochemical}$ (mAh/g)	$P_{plateau}$ (bar) (T(^oC))
ZrV_2 (C15)	5.4	1, 25	750	$<10^{-8}$ (50)
$ZrCr_2$ (C15)	3.8	1, 25	520	0.01 (50)
$ZrMn_2$ (C14)	3.6	8, 25	480	0.1 (50)
$TiCr_{1.9}$ (C14)	3.5	14, -78	640	0.2 (-78)
$TiMn_{1.6}$ (C14)	2	20, 20	390	12 (20)

Cubic C15 $ZrCr_2$ has a gravimetric capacity of 1.94 wt.%, which is considerably higher than for the AB_5-type alloys. The theoretical maximum volumetric capacity is 114 kgH_2/m^3 based on $ZrCr_2D_{3.8}$ and a = 7.658 Å for the fully charged material, which is in fact equal to $LaNi_5$. For $ZrMn_2$ these values are 1.79wt.% and 128 kg/m^3 based on $ZrMn_2H_{3.6}$ and 189 $Å^3$ cell volume (a=5.48 A, c=8.931 A).

A number of AB_2-type alloys have, potentially, an even higher capacity. For instance, ZrV_2 can be charged to $ZrV_2H_{5.4}$ at pressures up to 1 bar at RT, which corresponds to 2.80 wt.%. However, the plateau pressure of this particular alloy is extremely low; below 10^{-8} bars at 50^{o}C. On the other end, $TiCr_2$ has a plateau pressure of more than 0.1 bar at –78^{o}C, so the range of hydride stabilities in this class of alloys is very large, providing a lot of possibilities to adjust the equilibrium pressure by making appropriate substitutions.

Once again Ni, as the smallest transition metal, appears to be a key element in adjusting the equilibrium pressure of the material. The same as for AB_5-type alloys, the inverse relation between unit-cell volume and equilibrium pressure also holds for AB_2 type alloys for substitutions between elements with comparable hydrogen affinity. A study by Fujitani *et al.*

revealed a linear relation between cell volume and equilibrium pressure for Co, Fe and V substitution in $ZrMn_2$[54].

3.4.3.3 Optimization of the properties

Alloy decrepitation by the same mechanism as for AB_5-type alloys will decrease the intrinsic capacity of the alloys in the course of cycling as a result of progressive corrosion. Neutron diffraction studies by Joubert *et al.*[55] and Fruchart *et al.*[56] showed that the total volume expansion upon full deuteration is ~20%, approximately the same as for unsubstituted $LaNi_5$, for $ZrCr_2$ and ZrV_2 alloys. Even though this is no different from the problems facing AB_5-type alloys, the high oxidation sensitivity of the A-elements, Zr and Ti, makes the behavior of these materials much worse than that of the AB_5 materials.

Not only does alloy oxidation decrease the capacity, oxidic layers at the alloy surface also slow down the activation of the material. Where AB_5-type materials need only a few cycles to reach their maximum capacity, single-phase AB_2 alloys often need several dozen. Therefore, adjustments to the alloy composition have both aimed to improve the cycle life and the activation behavior of the alloy.

Joubert *et al.* investigated the Zr-Cr-Ni system for application in NiMH batteries and concluded that the activation behavior of the alloys was much improved by precipitation of binary ZrNi-phases[57]. They concluded that these precipitates acted as catalysts at the alloy surface and having good corrosion resistance themselves, 'shortcutted' the oxide layer, preserving the surface catalytic activity for hydrogen absorption. However, a study by Yang *et al.* on a series of multi-substituted $Zr(Ni,Mn)_{2\text{-}2.2}$ alloys showed some evidence to the contrary. All of the compositions studied had secondary ZrNi phases at their grain boundaries, but the activation behavior seemed most strongly influenced by the Ni/V ratio, where alloys with a ratio between 2 and 3 showed much slower activation compared to alloys where this ratio was higher than 5[58]. Alternatively, Sun *et al.* studied the effects of adding a rare-earth element, La or Ce, to a V and Cr-substituted Zr(Ni,Mn)-based alloy. The LaNi and CeNi-phases that were formed also had beneficial effect on the activation behavior, similar to ZrNi[59].

An interesting alternative approach was recently demonstrated by Matsuoka and Tamura[60]. Mechanical milling of $Zr_{0.9}Ti_{0.1}Mn_{0.5}Co_{0.1}Cr_{0.1}V_{0.2}Ni_{1.1}$ with 1 wt.% of Mg or Al powder decreased the activation period from more than 20 cycles to less than 5. Milling without additives was also effective[61], although milling times should be limited to 1 h or less. This was ascribed to an enlargement of the surface area by the ball-milling treatment and the reaction of the additives with the electrolyte, creating electrocatalytically active surface sites and enlarging the surface area even further. Addition of Mg or Al appeared to be equally effective. If this method turns out to be generally applicable, the activation performance of the AB_2 phase itself is no longer a concern and the alloys would only have to be optimized for capacity and cycle life. This could increase the storage capacity in practical applications, which is now limited to ~350 mAh/g (1.32 wt.%).

3.4.4 Superlattice alloys

In the La-Ni phase diagram, 3 intermetallic phases are present between 75 and 80 at.% Ni, $LaNi_3$, La_2Ni_7 and La_5Ni_{19}, which corresponds to a stoichiometry between 3 and almost 4. Interest in the hydrogen storage properties of these alloys increased when ternary alloys with AB_2C_9 stoichiometry (A = Rare-earth Y or Ca, B = Alkaline-earth, C = late transition metal) were discovered. A reversible storage capacity of ~0.95 H/M between 10 and 0.1 bar at 283 K was reported by Kadir *et al.* for a partially Ca-substituted $(LaMgCa)Ni_3$ alloy[62]. The

compound can be viewed as $(La_{0.66}Ca_{0.33})(Mg_{0.66}Ca_{0.33})_2Ni_9$, for which a capacity of 0.95 H/M corresponds to about 440 mAh/g.

3.4.4.1 Crystal structure of the alloys

The crystal structure of these alloys is quite complicated. It consists of a periodic stacking of AB_2 and AB_5 units, with either rombohedral or hexagonal symmetry and different periodicity. The La/Mg, as well as the (La,Mg)/Ni ratio can be varied. Varying the La/Mg ratio leads to mixed occupation of the A sites in the AB_2 units, whereas changes in the (La+Mg)/Ni ratio change the periodicity of the stacking and often lead to multiphase materials. An elaborate study of the effects of substitutions on the crystal structure and stacking periodicity was conducted by Ozaki *et al.*[63] A multi-substituted La-Mg-Ni-Co-Mn-Al alloy with Rhombohedral 1(AB_2):4(AB_5) stacking showed the best performance.

3.4.4.2 Hydrogenation properties

For fuel-cell applications, the gravimetric capacity of these alloys is still too low. Interest in the electrochemical storage properties was also generally lacking because of the high corrosion sensitivity of the Mg-containing compounds, until a breakthrough was achieved by Kohno *et al* in 2000. It was reported that $La_{0.7}Mg_{0.3}Ni_{2.8}Co_{0.5}$ ($AB_{3.3}$) could store up to 410 mAh/g[64]. The equilibrium pressure is approximately 1 bar at 60°C, which means the battery voltage is comparable to AB_5 type materials. Cycle life was not extensively investigated, but also comparable to a Mm-based AB_5 type alloy over the first 30 cycles.

Yasuoka *et al.* investigated a Mm-based $AB_{3.3}$ type alloy and compared its performance with the $La_{0.7}Mg_{0.3}Ni_{2.8}Co_{0.5}$ composition investigated by Kohno. Optimization of the Mm/Mg ratio and using Al as a Ni-substitute instead of Co improved the cycling stability from about 60% of the original capacity after 200 cycles to more than 80% after 600 cycles. $Mm_{0.83}Mg_{0.17}Ni_{3.1}Al_{0.2}$ was shown to have about 10% higher gravimetric capacity and improved cycle life compared to a selected AB_5-type material for AA and AAA-sized cells[65]. This is the best performance of this alloy type in electrochemical applications reported to this date.

3.4.5 TiV-based bcc solid solution alloys

Yet another class of hydrogen storage alloys that is being investigated as hydrogen storage materials are the V-based solid solution alloys. In electrochemical studies, the overall compositions of investigated alloys resemble those of AB_2, but with an elevated V-content, resulting in dual-phase alloys containing both the V-based phase and a Laves phase. These alloys have potentially very high *absorption* capacities although the reported reversible capacity rarely exceeds 400 mAh/g, or ~1.5 wt.%. Remaining issues concerning the cycling stability of these alloys have not yet been satisfactorily solved for electrochemical applications. For gas-phase applications, these alloys have the advantage that the equilibrium pressure can easily be tuned by varying the V/Ti ratio and the addition of more 3d-elements.

3.4.5.1 Crystal structure of the alloys and hydrides

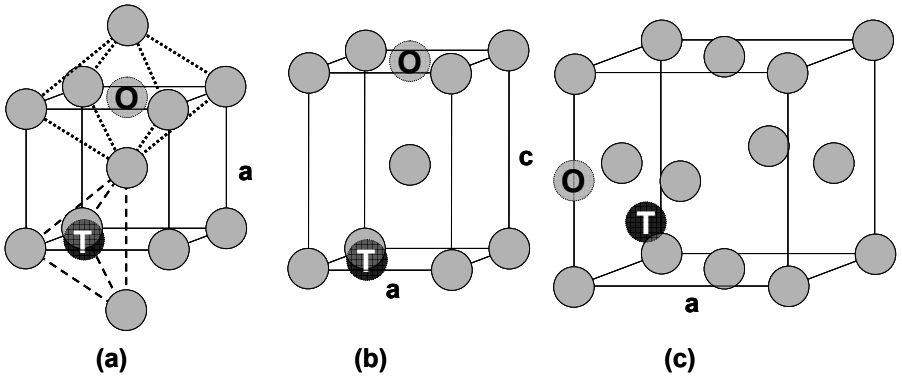

Fig. 27: Metal host structures of V-based alloy hydrides. Vanadium metal has a bcc structure (a), $VH_{\sim 1}$ has an intermediate body-centered-tetragonal (bct) structure (b) and the dihydride VH_2 has a face-centered-cubic (fcc) structure (c).

Vanadium metal has a body-centered-cubic (bcc) structure, which is shown on the left side of Fig. 27. Above 880°C it has complete mutual solid solubility with Ti, retaining the bcc structure. Additional elements are soluble to some extent in the bcc-phase, which makes it possible to adjust the equilibrium hydrogen pressure of this phase. Upon hydrogenation, the metal host structure undergoes a number of crystallographic transformations, depending on the Ti/V ratio. Pure Vanadium first transforms from a bcc to a body-centered-tetragonal (bct) structure upon filling the lattice with hydrogen. At higher Ti contents, the structure transforms directly from a bcc to a face-centered-cubic[66, 67] (fcc) structure, but this is also strongly influenced by the presence of more alloying elements[68]. The fcc and bct structures are also shown in Fig. 27 (b and c).

There are two types of interstitials available for the hydrogen atoms; Tetrahedral and Octahedral sites. Both are indicated with 'T' and 'O' respectively in all three crystallographic modifications of the hydride in Fig. 27. For clarity the O-and T-site have been drawn in different planes, but it is obvious that for the bcc and bct structures, 4 tetrahedral interstitials are located very close around each O-site. At low H/M ratio, most of these will be empty, which enables very fast hydrogen diffusion through the metal lattice. In fact, the dilute bcc hydrides VH_y ($y < 0.68$) and NbH_y have the highest diffusion rates known for metal-hydride systems, exceeding 10^{-5} cm^2/s at 160 °C[69] for VH_y. Neutron-scattering experiments revealed that hydrogen preferably occupies the T-sites in Ti-rich alloys and O-sites are preferred for V-rich compositions in the bcc or bct monohydride phase[66]. In the fully hydrogenated state, $(Ti,V)H_2$ assumes an fcc-structure with all T-sites fully occupied.

3.4.5.2 Hydrogenation characteristics

Gas-phase storage

A Ti-V based solid solution can store a large amount of hydrogen. Both Ti and V can form a dihydride which means the absorption capacity should be between 4.18 (pure Ti) and 3.93 wt.% (pure V). VH_2 has a lattice parameter of 4.27 Å, from which a total volumetric hydrogen density of 172 kg/m^3 can be calculated. This is the highest total volumetric and gravimetric density of all the alloys discussed so far. However, only the monohydride-dihydride transformation is reversible at accessible pressures at room-temperature.

The $VH_{\sim 1}$-$VH_{\sim 2}$ transition has an equilibrium pressure of 1 bar at 12°C, but the equilibrium pressure drastically goes down upon alloying with Ti and Zr, which form much

more stable hydrides than V. Other elements such as Fe, Al, Si, Cr, Co, Mn and Ni are soluble to some extent in the bcc-phase, which enables fine-tuning of the plateau pressure. Kagawa *et al*. preformed an extensive study on these substituted Ti-V alloys and found that generally ~1 H/M is reversible at 333 K between 10 bar to 10 mbar[70].

Challet *et al.* performed an extensive diffraction study on $(Ti_{0.355}V_{0.645})_{100-x}M_x$ (M = Mn, Fe and x = 7, 14) alloys and quantified the H/M ratios where the crystallographic transformations take place as well as the concurrent volume changes[68]. $(Ti_{0.355}V_{0.645})_{86}Fe_{14}$ showed the highest reversible capacity at room-temperature, 1.97 wt.%, which increased to 2.31 wt.% at 100°C. After one activation cycle, this alloy absorbed its maximum capacity of 1.84 H/M at 20 bars within 40 seconds at room-temperature. The volume changes during hydrogenation were found to be very large for this alloy type. Upon transforming from bcc to bct, the alloy expands 10%, followed by more than 22% going from bct to fcc. The total volume increase was found to be more than 35% for all the investigated compositions.

The deuterium sites were resolved for the 'Mn-7' deuteride by neutron diffraction. This alloy did not have the intermediate bct-phase and it was found that deuterium occupies O and T-sites to approximately equal extent in the bcc-phase and exclusively fills the T-sites in the fcc-phase. A quite remarkable finding was that the bcc-fcc coexistence region was quite narrow, between 0.85 and 1.26 D/M, but the discrete expansion was very large, 24%. Subsequently, although there is an additional 0.62 D/M absorbed, the volume hardly increases anymore. This behavior is completely different from *e.g.* the AB_5-type materials, where the discrete expansion decreases accordingly with the plateau width and the hydride expands further in the β-branch.

Electrochemical storage

Electrochemically, the (Ti,V)-phase does not absorb hydrogen in alkaline media, due to the absence of electrocatalytic activity. Therefore, additional elements are included in order to precipitate an electrocatalytic phase. Iwakura *et al.*[71] investigated ternary Ti-V-Ni compositions and found that a $TiV_{2.1}Ni_{0.3}$ alloy consisted of a bcc V-based solid solution, a bcc TiNi-based phase and a small amount of Ti_2Ni-type phase. The alloy could charge ~1050 mAh/g and discharge ~540 (equivalent to 3.92 and 2.01 wt.%, respectively), which are among the highest capacities ever reported for this alloy type. The large difference between these two values is caused by the low equilibrium voltage of the alloy at hydrogen contents below 1 H/M. This was found to be around -0.7 V *vs.* Hg/HgO (10^{-7} bar) by Tsukahara *et al.* for $Ti_{22}V_{66}Ni_{12}$[72]. Instead of a TiNi-based secondary phase, a secondary Laves phase can also be precipitated, as was already mentioned. A study by Zhang *et al.*[73] showed that addition of ~11 at% Ni to TiV_3 together with small amounts of Hf, Mn and Cr resulted in a secondary phase with C14 Laves-phase structure. The maximum capacity of this alloy was 400 mAh/g.

3.4.5.3 Optimization of the (electrode) properties

Until now, the cycling stability of these alloys has been quite unsatisfactory, despite numerous studies on the effects of substitutions on the electrochemical properties. This may be due to the enormous lattice expansions these materials undergo upon hydrogen loading, although Kagawa *et al.* mentioned to have observed 'no tendency to become finer powders' for pure $V_{0.9}Ti_{0.1}$[70]. Apparently, the material is able to withstand very large deformations without breaking. However, even during gas-phase cycling a substantial decline of the capacity was reported for $V_{0.9}Ti_{0.1}$ and $(V_{0.9}Ti_{0.1})_{0.95}Fe_{0.05}$ after more than 100 cycles, while a Cr-substituted compound showed much better performance[70].

In all electrochemical studies conducted on these materials, the electrocatalytic phase and the V-based main phase were formed from a homogeneous melt. The Laves-phases that are formed in this way generally have high V–content, which is known from studies on AB_2 alloys to be unfavorable. Furthermore, the potentially superior capacity of the V-based phase is often not utilized[74, 75], although an initial capacity over 500 mAh/g was reported by Yin and Zhao for $TiV_{1.1}Mn_{0.9}Ni_{0.4}$. However, the cycling stability was very poor in this case[76].

In view of the above, it may be a better option to separately optimize the V-based phase for optimum capacity at ambient temperatures and pressures and (gas-phase) cycling stability. Combination with a catalytic phase, such as the optimal AB_2-type phase $ZrNi_{1.2}Mn_{0.6}V_{0.2}Cr_{0.05}Co_{0.05}$[60], can be realized by *e.g.* ball-milling. This enables separate variation of the composition of each phase and of their relative amounts, while in a conventional synthesis by casting both are dictated by the overall composition of the alloy. This would combine the good electrocatalytic properties of an AB_2-type material with the superior storage capacity of the V-based material. It is therefore reasonable to state that there is quite some unexplored potential for the V-based alloys and that they are certainly worthy of further investigation.

Summary Transition Metal-based hydride forming materials.

AB_5-type materials are the most intensively investigated and best optimized materials regarding cycling stability in alkaline media and equilibrium pressure, but the gravimetric capacity falls far short of the requirements for mobile fuel-cell applications. For Ni-MH batteries, these materials are still the preferred choice. AB_2-type materials are potentially better gravimetrically, especially in gas-phase applications, but in the optimization process for use as battery materials a relatively larger part of the capacity is sacrificed compared to AB_5. The V-based solid solutions can absorb up to 4 wt.%, but the reversible part at accessible pressures is no larger than 2.3 wt.% in the temperature range below 100°C, which means the gravimetric capacity is still too low for mobile applications in PEM fuel-cell vehicles. However, it has been shown that the available capacity at ambient pressures can be adjusted by adding third (or possibly fourth) elements, which leaves open the possibility that the capacity of these alloys will be improved further.

3.5 Mg-based materials

The alloys that have been discussed until now, with exception of the V-based alloys, have intrinsic hydrogen storage capacities below 2 wt.%. The AB_5-type alloys have been widely applied in rechargeable batteries and are still the first choice for hybrid vehicles because of their good tolerance for overcharge and overdischarge. However, for gas-phase storage for on-board use in *e.g.* fuel cell driven cars, much higher requirements on the capacity (6 wt.%) have been defined[6]. Therefore, the search for materials with higher gravimetric capacities is continuing and intensifying.

Pure Mg has a very high gravimetric capacity (7.6 wt.%), which is exceeded only by some complex hydrides (*e.g.* $Li/Na(BH_4)$) and the nitride-based materials. A lot of scientific effort has already been invested in MgH_2, which will be discussed in the following sections. First, the properties and practical limitations of pure Mg will be described. Secondly, the effects of alloying Mg with other metals will be discussed and appropriate introduction to the experimental work in Chapter 4-6 will be given.

3.5.1 Pure Mg

Pure Mg has a very high reversible storage capacity, making it in a very attractive hydrogen storage medium in principle. Transformation to MgH_2 stores 7.6 wt.% H, which would translate to 2200 mAh/g Mg, exceeding the absorption capacity of even the V-based alloys by a factor 2. However, a major disadvantage is its extremely slow absorption and desorption kinetics, arising both from diffusion limitations and high oxidation sensitivity of the Mg surface, hindering the dissociation of hydrogen molecules. Besides kinetic limitations, MgH_2 is also very stable, reaching an equilibrium pressure of 1 bar only at 300°C. Numerous studies have aimed to overcome the kinetic limitations by the addition of catalysts to enhance the dissociation rate of hydrogen at the Mg surface and by reducing the particle size to shorten the diffusion length by *e.g.* ball-milling. Despite great experimental efforts to overcome its limitations, practical application of Mg remains problematic.

3.5.1.1 Crystal structure of the metal and its hydride

Mg metal has a hexagonal-close-packed (hcp) structure. Upon hydrogenation, the structure transforms into a so-called rutile structure. The metal lattice has a body-centered-tetragonal structure, the same as for the V-based hydride. The difference is in the arrangement of the hydrogen atoms, which form an octahedron around the central Mg atom (see Fig. 28).

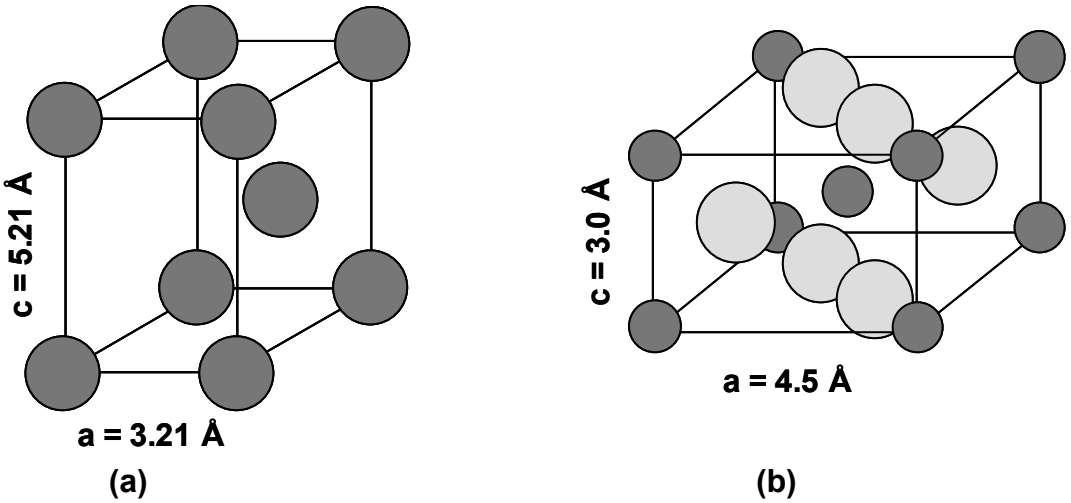

Fig. 28: Crystal structure of hexagonal close packed (hcp) Mg metal (a) and rutile MgH_2 (b).

3.5.1.2 Hydrogenation characteristics

From the lattice parameters of the rutile structure (Fig. 28 (b)) a volumetric hydrogen storage capacity of 82.0 kgH_2/m^3 can be calculated, taking the maximum packing density of spherical hydride particles into account. This is lower than for the TM-based storage alloys, but still sufficiently high regarding the DoE targets. Although MgH_2 also has a very high gravimetric hydrogen content of 7.66 wt.%, its practical application is severely hindered by some of its properties. First of all, its (de)hydrogenation kinetics are extremely slow even at elevated temperatures. A careful study by Vigeholm showed that the hydriding reaction comes to a halt as soon as a closed layer of hydrided material has been formed on the particles' surface[77]. This was evidenced by the curious fact that there was an inverse relation between the applied hydrogen pressure and the reacted fraction at steady state. This showed that the more rapid the hydrogenation reaction is, the sooner a closed hydride layer forms and the sooner further

reaction is blocked. This means that hydrogen diffusion *through* a layer of MgH_2 is extremely slow.

Another problem of MgH_2 is the high stability, which is comparable to Vanadium-monohydride. The enthalpy of formation of MgH_2 is -77 kJ/mole H_2, which corresponds to 1 bar only at 300°C. The catalytic properties of Mg surfaces are also quite poor, because a thin oxide layer will always be present at the surface, hindering the dissociation and adsorption of H_2 molecules onto the metal surface. This, together with the extremely slow bulk diffusion, makes practical application of Mg as a hydrogen storage medium very difficult.

3.5.1.3 Improvement of the hydrogenation properties

The abovementioned problems can be alleviated by:

- Addition of a catalyst
- Shortening the diffusion path by reducing the particle size
- Reducing the stability of the hydride

By far the most effort has been devoted to the first two. They can easily be realized simultaneously by ball-milling, which will reduce both the particle size and the internal grain size and enable mixing of a catalytically active material with the Mg(hydride). The catalyst has the additional advantage of forming a 'shortcut' through the oxide layer, making the resulting material less sensitive to air exposure.

Zaluski *et al.* performed an extensive study on the effects of ball-milling on the H-sorption properties of Mg, both with and without the addition of a catalyst. Reduction of the grain size indeed lead to a significant improvement of the hydrogenation kinetics for powders with the same particle size of ~10 micrometers[78]. Addition of a Pd catalyst further improved the kinetics, but the utilization of the material was always less than the theoretical 7.6 wt.% at 10 bar hydrogen absorption pressure. An exception was formed by a Mg powder milled with Zr and Mn, which absorbed >7 wt.% even at only 190°C. These results suggest that hydrogen diffusion along grain boundaries between MgH_2 grains is very limited and that the distance between free surfaces in contact with hydrogen gas or with a phase with fast H-diffusion (one can expect a $ZrMn_2$-type phase to be formed in the Mg+Zr,Mn system) largely determines the final hydrided fraction. A study by Oelerich *et al.* gave a similar result. Mg ball-milled with a V_2O_5 catalyst showed a much higher initial reaction rate, but the absorption capacity was significantly lower than 7.6 wt.% (even after correction for the added weight of the catalyst)[79]. Remarkably, the oxide was a much more effective catalyst than metallic V. For Nb, similar results were found. Nb_2O_5 is a very effective catalyst[80] and at elevated temperatures, the oxide is more permeable to hydrogen than Nb metal.[81]

An interesting approach was recently demonstrated by Saita *et al.*[82] By reactive Chemical Vapour Deposition of very thin MgH_2 filaments of less than 1 micron thickness, full utilization of the material under equilibrium conditions was achieved. Once again, the self-limiting behavior of MgH_2 manifested itself. An increase in the initial hydrogenation rate by increasing the absorption pressure by a factor 4, decreased the final hydrogen content to ~80% of the theoretical maximum.

So far, only a few ways to decrease the hydrogen *ab*sorption temperature of Mg have been found, the lowering to 190°C for the Mg-(Zr,Mn) composite being the most successful one. However, the most important properties of a hydrogen storage material are, besides storage capacity, its *desorption* temperature and kinetics. Therefore, ways must be found to increase the equilibrium pressure of Mg at ambient temperatures from $\sim 10^{-6}$ bar towards ~1 bar. From first-principles calculations, Wagemans *et al.*[83] found that when a Mg particle

contains less than 10 atoms, the enthalpy of formation of MgH_2 becomes less negative than the bulk value of –77 kJ/mol H_2. In such extremely small particles, the diffusion limitations would disappear as well. Successful preparation of such particles has been reported, but the experimental procedure is rather complicated and the major part of the material still consists of bulk Mg[84, 85].

3.5.2 Mg-RareEarth alloys

In 1995 it was discovered by Huiberts *et al.* that hydrogenated thin layers of Rare-Earth metals exhibit remarkable optical properties[86, 87]. Many Rare-Earth elements can absorb up to 3 hydrogen atoms per metal, but the study of the fundamental materials properties as a function of the hydrogen content has been rather difficult, because bulk metals tend to pulverize upon full hydrogenation. Thin films on the other hand, retain their structural integrity throughout the entire hydriding process. It was discovered that both the as-deposited films and the RE-dihydride are metallic and reflective, whereas further hydrogenation results in a semiconducting, optically transparent state.

Y and La films appear slightly colored in their transparent state; YH_3 is yellowish, while LaH_3 is red. It was subsequently discovered by v.d. Sluis *et al.* that addition of Mg to RE thin films further improves the transparency and also achieves color-neutrality in the transparent state[88]. It was also discovered that these Mg-RE thin films exhibit a third optical state. At intermediate hydrogen contents, the films enter the so-called 'black state', where both the reflection and the transmission are very low.

The origin of this black state has been subject to intense investigation. It was discovered by Giebels *et al.* that pure Mg films also exhibited this black state and it was concluded that the co-existence of very small metallic Mg and insulating MgH_2 grains was responsible for the black state[89]. The optical response of the Mg-RE thin films could be described by considering only Mg and MgH_2 and it was therefore concluded that 'the role of the RE material is to disproportionate the film into small grains of $REH_{2+\varepsilon}$ and Mg during the first hydrogen loading'. However, any direct evidence, *e.g.* from X-Ray diffraction, for the existence of MgH_2 in the fully hydrogenated films was only found for Mg-La[90]. Van der Molen *et al.* found that for Mg_xY_{1-x} the fully hydrogenated film contains an fcc phase for $x > 0.1$[91]. This is unexpected since pure YH_3 has a hexagonal structure. The molar volume of this cubic phase continuously decreased with increasing Mg content. Since MgH_2 has a smaller molar volume than both YH_3 and YH_2, this would be consistent with the view that Mg and Y remain alloyed throughout the entire hydriding process and not with disproportionation. Furthermore, a comparison between an $Mg_{0.4}Y_{0.6}$ alloy thin film and a multilayered system with the same overall composition revealed some clear differences in optical properties between the two[92], again indicating that an alloy behaves differently from a segregated system.

In view of the above, a comparison with a bulk material would be useful. Fig. 29 depicts the X-Ray diffraction patterns of a $Mg_{0.5}Y_{0.5}$ alloy, its hydride synthesized by low-energy mechanical milling under 7 bars of hydrogen and a mixture of MgH_2 and YH_2 milled in Ar for 5 days.

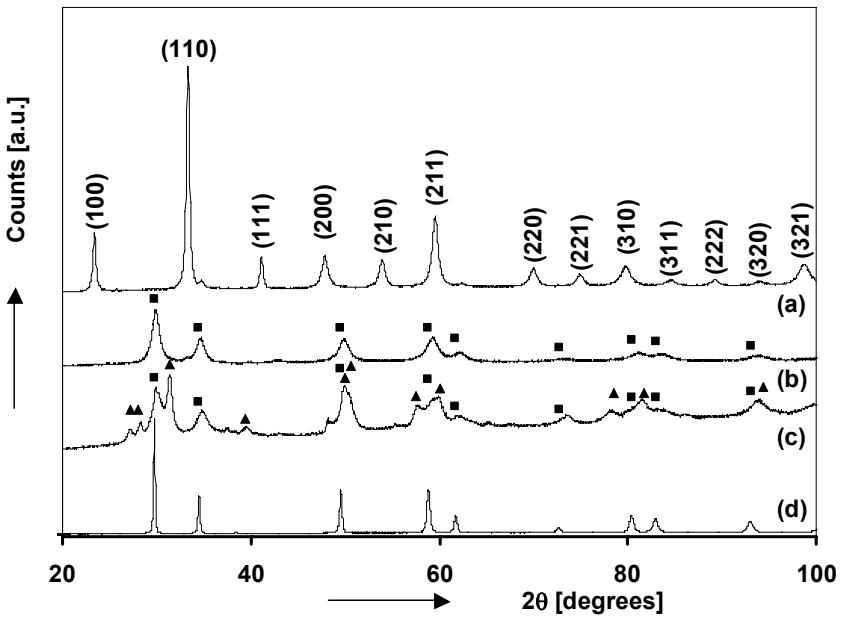

Fig. 29: X-Ray Diffraction patterns of as-cast $Mg_{50}Y_{50}$ alloy (a), $Mg_{50}Y_{50}$ after low-energy milling in 7 bars H_2 (b) and a MgH_2-YH_2 mixture with nominal composition $Mg_{0.65}Y_{0.35}H_2$ milled in Ar for 5 days (c). Pattern (a) indicates a fully ordered CsCl-type structure. Pattern (b) consists of a single fcc phase with a~5.16Å. Pattern (c) is a mixture of a fcc phase and YH_3 (▲). The reference pattern for YH_2 (■) is also marked in the figure and coincides exactly with the peak positions of a home-made sample of YH_2 sample (pattern (d))

The $Mg_{50}Y_{50}$ alloy exhibits a fully ordered CsCl-type structure, as is expected from the equilibrium phase diagram (pattern (a)). Upon hydrogenation by low-energy ball milling, the alloy transforms into a fcc structure, characteristic of YH_2; rutile MgH_2 is not detected. The lattice constant is slightly smaller than that of YH_2, ~5.16 Å, indicating the formation of a ternary, single-phase hydride (b).

When a mixture of the binary hydrides is milled in Ar (pattern (c) in Fig. 29), a slightly contracted YH_2 phase is also detected, while rutile MgH_2 does not seem to be present at all. However, a considerable amount of a hexagonal YH_3-type phase is also found, indicating that some hydrogen can be transferred from MgH_2 to YH_2 during the milling process. Milling was stopped after 5 days, so it is very well possible that the YH_3 phase would disappear upon prolonged milling and that the material would be fully converted into a cubic phase.

The electrochemical response of the $Mg_{0.50}Y_{0.50}$ alloy ball-milled with a small amount of Pd catalyst is depicted in Fig. 30 (next page):

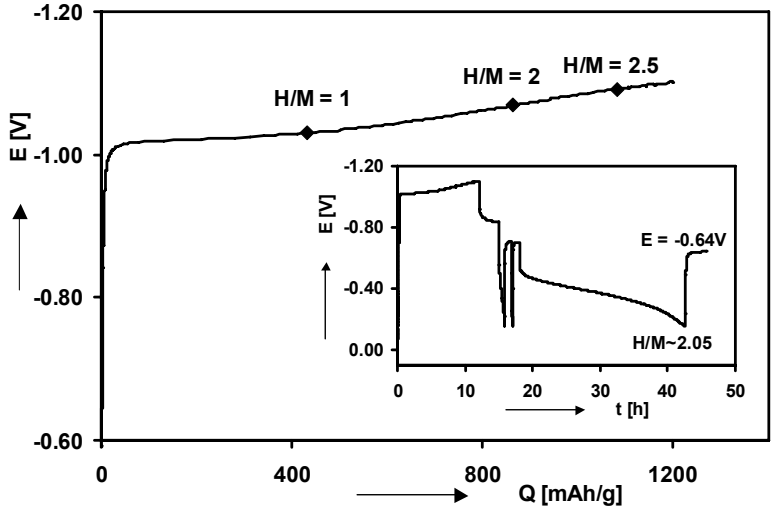

Fig. 30: Electrochemical response of $Mg_{0.50}Y_{0.50}$ alloy ball-milled with 5 at.% Pd. The electrode was charged with 100 mA/g for 12h followed by 2 discharge steps with 50 mA/g and finally a deep-discharge step at 10 mA/g to –0.15V. The entire potential response *vs.* time, including the rest periods, is shown in the inset.

The H/M ratios have been also been indicated along the charging curve. Remarkably enough, it appears to be possible to insert more than the equivalent of 2 H/Mg and 3 H/Y. An overall H/M ratio of 2.5 corresponds to 1080 mAh/g, but even at 1200 mAh/g (2.78 H/M), the potential is still becoming ever more negative, although some hydrogen evolution could be observed near the end. This is an indication that the MgY bulk material does not decompose upon hydrogenation, because in that case, the observed H/M ratio could not be reached without Yttrium absorbing more than 3 H/Y. This is highly unlikely, as the saturated Yttrium hydride is almost always reported as $YH_{3-\delta}$. After charging, the potential relaxes to –0.835 V, which is considerably more positive than –0.931, indicating that the material has not yet reached its maximum hydrogen content. Assuming that the hydrogen concentration at the end of the charging step was 2.7 H/M, then the H/M ratio after the deep-discharge is approximately 2. The equilibrium potential corresponds to a pressure of $\sim 10^{-10}$ bars, which is, as could be expected, intermediate between the plateau pressures of the Mg-MgH_2 and the Y-YH_2 transitions. These observations indicate that the reaction path can be of some influence, but that Mg-Y bulk materials have no tendency to segregate into the binary hydrides.

Ouwerkerk investigated $Mg_{0.7}Sm_{0.3}$ thin films and studied the optical properties as a function of hydrogen content. Hydrogen loading was done electrochemically, which has the big advantage over gas-phase loading that the amount of hydrogen is very accurately known. The maximum hydrogen content was shown to be ~2.3 H/M, which is equivalent to 2 H/Mg and 3 H/Sm. The film could be very rapidly switched between its three optical states, despite the high Mg-content[93]. This result suggested that thin film and/or bulk Mg-RE alloys could combine a high storage capacity with excellent sorption kinetics. Because Sm is chemically similar to La and Y, Sc could be expected to yield similar results as well and would be the most attractive from a gravimetric point of view.

Indeed, it was found by Notten *et al.* that Mg_xSc_{1-x} alloys delivered a high reversible capacity up to 1500 mAh/g for x = 0.80[94]. For Mg contents up to 80 at.%, the kinetics were vastly improved compared to pure Mg. This clearly hinted at a change in the crystal structure of the hydride from rutile to *e.g.* the cubic structure of ScH_2. However, optical measurements on Mg-Sc thin films once again revealed a black state and a segregation model was proposed for this system as well[95]. This assumption was, the same as for Mg-Y, solely based on the

optical properties, as diffraction measurements never showed rutile MgH_2 and the molar volume of the fully charged hydride clearly varied with the Mg-content.

3.6 Thin films versus bulk materials

For the abovementioned reasons, the Mg-Sc system is a very interesting subject for a comparative study between thin films and bulk materials. Some material properties are better studied on a thin film and others on the bulk form of the material, yielding complementary information. The specific (dis)advantages of both systems are listed below:

Thin films

Advantages:

1. Well defined sample geometry with smooth surfaces and interfaces.
2. Diffusion limitations are eliminated when the films are sufficiently thin.
3. Dimensional stability despite large volume changes.
4. *In-situ* measurement of optical properties is relatively easy.
5. The non-equilibrium preparation method (e-beam evaporation or magnetron sputtering) makes it easier to produce metastable compounds.

Disadvantages:

1. Small sample mass and surface area make thin films very susceptible to parasitic influences and poisoning.
2. Characterization by diffraction techniques is generally very difficult because of preferential orientation, thereby reducing the number of visible reflections.
3. Clamping effects can lead to anisotropic volume expansion during hydrogen loading.

Bulk materials

Advantages

1. Larger sample mass, which reduces weighing errors.
2. Larger surface area, which makes them less susceptible to poisoning effects or other parasitic influences.
3. Diffraction patterns of crystalline compounds yield more information, due to random orientation of the grains.
4. Powder is the 'real' form in which the material will eventually be used; both in fuel-cell and battery applications

Disadvantages

1. Powders can have a broad distribution of particle sizes, leading to *e.g.* differences in diffusion length.
2. The surface of the particles is rough and not very well defined.
3. Volume expansion often leads to pulverization of the material; *i.e.* hydrogen embrittlement.
4. Meta-stable compounds are a lot more difficult to manufacture in bulk form, compared to thin films.

The ability to eliminate diffusion limitations makes thin films especially suited to determine the intrinsic storage capacity of a material. This can then be used as the 'target value' to optimize a bulk material. The non-equilibrium preparation technique makes it possible to

quickly search for promising elemental combinations, which can subsequently be synthesized in bulk form. However, the question whether the bulk material will have the same properties in terms of storage capacity, (de)sorption kinetics, equilibrium pressure and crystal structure as the thin film has to be answered. These questions are addressed in the next chapter, where an elaborate comparative study between Mg_xSc_{1-x} thin films and bulk alloys is presented.

4

Hydrogen storage in Mg_xSc_{1-x} alloys: a comparative study between thin films and bulk materials

Abstract

The electrochemical hydrogen storage properties of Mg_xSc_{1-x} alloys are investigated both in thin film and bulk form. A comparison is made between the electrochemical, thermodynamic and structural properties of both systems. It is shown that the electrochemical properties of the thin films and bulk materials strongly resemble one another. For compositions where $x > 0.8$ a sudden decrease in capacity is observed in both cases, which is argued to be due to a structural transformation of the resulting hydride from fluorite to rutile. The formation of a fluorite structure for the bulk hydride was confirmed by X-Ray Diffraction. Both galvanostatic and equilibrium voltage curves show a plateau in the electrode potential, indicative of a phase transition. Partial discharge of a MgSc bulk hydride showed retention of the face-centered cubic host structure. Overall, the thin film materials are able to give a good indication of the electrochemical processes that take place in a simplified 2-dimensional model system. This knowledge can subsequently be used for understanding the bulk system, as bulk and thin film materials complement each other very well.

4.1 Introduction

MgH_2 has a very high reversible storage capacity of 7.6 wt.% hydrogen, but very slow sorption kinetics[78]. However, in the research on switchable mirrors, MgH_2 did find its use in adjusting the optical properties of rare-earth (RE) hydrides[88, 91]. MgH_2 was found to stabilize the cubic modification of the RE-trihydride[91], and to enable the achievement of color-neutrality in the transparent state[88]. Moreover, it was found that Mg-RE thin films could be rapidly switched from the black to the transparent state with the addition of more than 50 at.% Mg[93]. Therefore, it could be expected that bulk Mg-RE alloys with a high magnesium content can store a large amount of hydrogen, while retaining excellent sorption kinetics.

Recently it was shown by Notten *et al.* that Mg alloyed with the lightest element of the class of the rare-earths, Sc, exhibits very high reversible storage capacity of 1500 mAh/g (5.6 wt.%) and good rate capability up to 80 at.% Mg[94]. This was ascribed to the fact that the ternary hydride has a CaF_2-type fluorite crystal structure, which is more favorable than the rutile structure of pure MgH_2. The present chapter provides additional evidence for this assumption based on a more elaborate X-Ray Diffraction study. Electrochemical techniques are used to study the storage capacity, the thermodynamic and kinetic properties of both thin films and bulk materials. From a comparison between MgSc bulk materials and thin films made in this chapter, it is found that thin films are a suitable model system in the search for hydrogen storage materials with favourable properties.

4.2 Experimental

4.2.1 Preparation

4.2.1.1 Thin Films

$Mg_xSc_{(1-x)}$ thin films with a nominal thickness of 200 nm, were deposited on quartz substrates (∅ 20 mm) by means of electron-beam deposition (base pressure $8*10^{-8}$ – $4*10^{-7}$ mbar, depending on the deposition equipment). The Mg content in the films was varied in the range $x = 0.65 – 1$. Cap layers of 10 nm Pd were deposited on top of the thin films. During deposition of the alloys the deposition rates of Mg and Sc were between 0.15 and 0.63 nm s^{-1}. Uniformity of composition throughout the entire film was checked by means of Rutherford Backscattering Spectroscopy (RBS), which showed that the deposition rates were controlled well. The calculation of the hydrogen content in the thin film is purely based on these RBS measurements (accuracy around 1%). As a maximum discrepancy in the hydrogen storage capacity of the Mg-Sc material can occur of at most 3%, no correction is made for the hydrogen stored in the Pd cap layer.

4.2.1.2 Bulk Materials

$Mg_xSc_{(1-x)}Pd_{0.024}$ metal alloys were prepared by weighing the appropriate amounts of starting materials into a Molybdenum crucible, which was then sealed in an arc furnace under a high purity Argon atmosphere. The samples were then heated to 100 ^oC above the liquidus temperature for 1 day, quenched, and subsequently annealed at 450 ^oC for 4 days.

An alternative way to dope the materials with Pd is preparing an undoped MgSc material as described above, followed by ball-milling the material in a Spex 8000 ball-milling apparatus, together with an appropriate amount of Pd powder. First the material was hammered down to pieces smaller than the ball-diameter (~½ inch) after which it was loaded into a 55 ml tungsten carbide-lined vial together with 5 at% Pd powder, 2 wt% stearic acid

and 4 tungsten carbide balls (∅ 11 mm). Ball-to-powder weight ratio was kept at a value of 10:1.

Electrodes for electrochemical characterization were prepared by filing down the alloys into small pieces and passing the resulting powder through a stack of sieves. The powder fraction between 40 and 50 μm was then mixed with Ag powder (Merck, 0.8-1.2 m^2/g) in a weight ratio of 1:5. This mixture was then pressed into pellets (∅ 8 mm) weighing about 150 mg in total, using a pressure of about 400 MPa. Sometimes Ni powder was used instead of Ag, because Ni is also electrocatalytically active and less ductile than Ag.

An alternative way to hydride the bulk metals, which has the advantage of generating much larger sample volumes, is hydriding via the gas phase. This was done by exposing the alloy to hydrogen gas with a pressure of 140 bars at room temperature and subsequently cycling the temperature between 50 and 300 ^oC for 5 to 7 times (heating rate of 100 $^oC/h$). Gas-phase loading under these conditions also works well for MgSc alloys without Pd-catalyst.

4.2.2 Characterization

Structural characterization of all materials was performed on a PANalytical X'PERT-PRO MPD Diffractometer using Cu K_α radiation. Data are collected over a 2θ angular range of 10 tot 120 degrees using a X'Celerator detector. A combination of Scanning Electron Microscopy (SEM) and Energy Dispersive Analysis of X-rays (EDAX) was used to measure phase composition and to check the homogeneity and morphology of the metal alloys.

All electrochemical measurements were carried out in conventional thermostrated three-electrode cells at 25 °C. The details of the experimental setup were already described in section 2.3. The cells contained 6 M KOH aqueous electrolyte and the potential of the working electrode was measured *vs.* a Pb-free[18] Hg/HgO (6M KOH) reference electrode from Koslow Scientific Company. Unless stated otherwise, all potential values are given *vs.* this reference. Galvanostatic measurements and Galvanostatic Intermittent Titration Technique (GITT) were performed using a Maccor M2300 battery tester (Maccor, Tulsa, USA). Electrochemical Impedance Spectroscopy (EIS) was done on an Autolab PGSTAT30 (Ecochemie B.V., Utrecht, the Netherlands). EIS measurements were conducted at equilibrium voltage conditions using an ac amplitude of 5 mV rms and scanning the frequency from 50 kHz to 1 mHz. A non-linear least squares fitting program (EQUIVCRT) was used to analyze the EIS data.

4.3. Results

4.3.1 Structural characterization of the starting materials

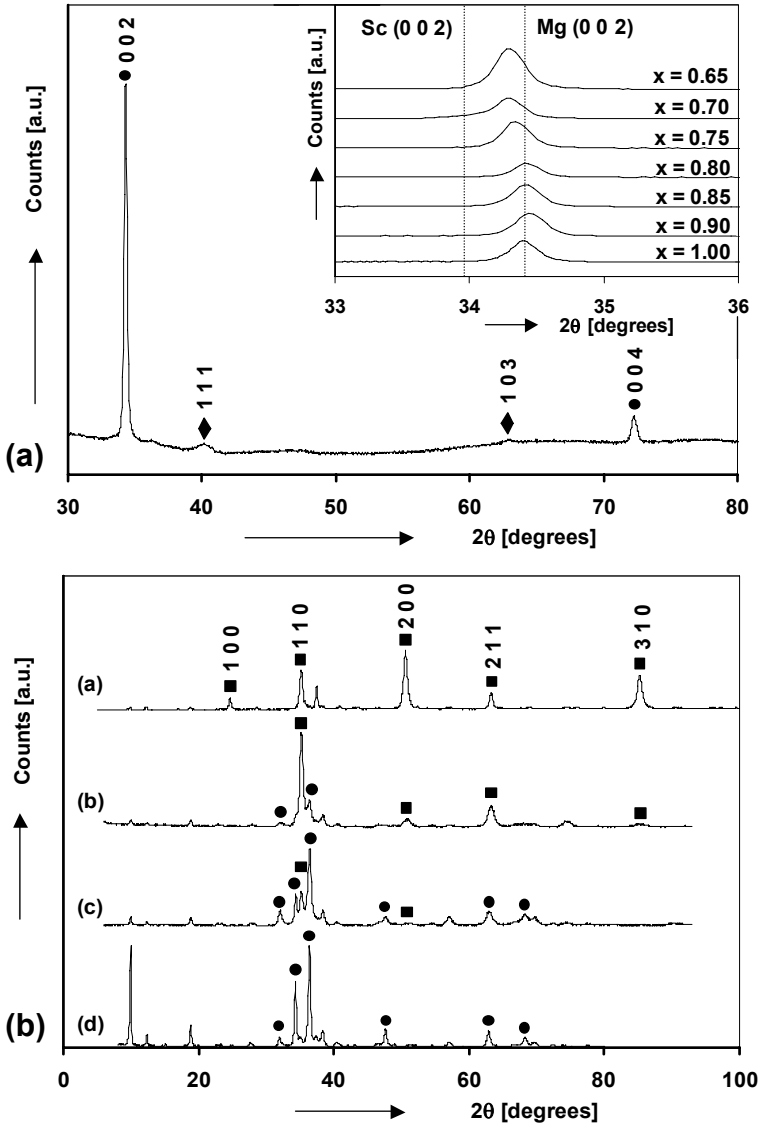

Fig. 31 : X-Ray diffraction patterns of Mg_xSc_{1-x} (x = 0.65 – 1) thin films (a) and $Mg_xSc_{1-x}Pd_{0.024}$ bulk materials (b). The full pattern of a thin film with x = 0.65 is shown in (a), the (0 0 2) reflection as a function of composition is shown in the inset.

Fig. 31 (a) shows the X-ray diffraction pattern of a $Mg_{0.65}Sc_{0.35}$ thin film coated with Pd. The diffraction patterns of all other compositions that were investigated were similar to that shown for x = 0.65. The strongest reflection, the Mg (0 0 2), between 33 and 36° is shown in the inset as a function of alloy composition. Only the reflection belonging to the hexagonal α-Mg structure is found for all compositions. This is strongly different from the equilibrium phase diagram, where a bcc CsCl type solid solution of Sc in Mg is found between 50 and 65 at.% Mg and single-phase α-Mg only beyond 80 at.% Mg[96]. Apparently, it is possible to achieve large solid-solubility extensions by 'freezing' the atoms at room temperature directly from the gas phase. From the diffraction pattern it becomes clear that the sample is strongly oriented in the (002) direction, showing that the crystals are oriented with their c-axis perpendicular to the substrate. From the inset in Fig. 31 (a), a minor, but noticeable, shift in the peak position of the (002) reflection towards larger angles, *i.e.* smaller d-spacings, is

apparent with increasing Mg-content. This is to be expected since Mg has a 7% smaller molar volume than Sc. Additionally, the Pd topcoat is weakly oriented in the (111) direction (see ♦ in Fig. 31 (a)).

In Fig. 31 (b) the X-ray diffraction patterns of the powdered $Mg_xSc_{(1-x)}P_{0.024}$ alloys are shown. For x = 0.65 both the diffraction pattern and the Miller indices for the individual reflections are given (a). For x = 0.65 only the CsCl-type solid solution of Sc in Mg is present. The lattice constant of the material is 3.595 Å. The presence of the (100) reflection indicates that the solid solution is ordered, since in a disordered bcc lattice, reflections for which (h+k+l) is odd are extinguished. For higher Mg-content, x = 0.70 (b) and 0.75 (c), the hexagonal α-Mg structure (•) of magnesium metal also becomes apparent until, at 80 at.% Mg, only the α-Mg structure can be seen (d). This is all in agreement with the bulk phase diagram for the binary Mg-Sc system, which is shown in Fig. 32, and quite different from the thin film case, where the hexagonal Mg-structure with a solid-solution behavior was found for all compositions (see Fig. 31 (a)).

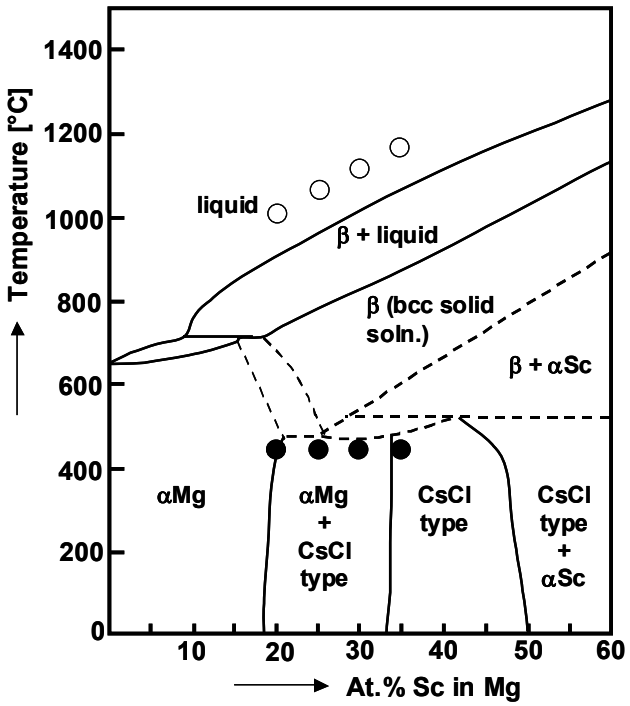

Fig. 32: Equilibrium phase diagram of the Mg-Sc system between 0 and 60 at.% Sc. The compositions studied in bulk form (65-80 at% Mg) are shown as open (firing temperatures) and black (annealing temperaure) dots.

Due to the very different method of preparation, the morphology of the bulk and thin film materials is quite deviating. The thin film samples have a very well-defined layered structure where the Pd topcoat is clearly separated from the Mg-Sc phase. However, as the SEM-pictures in Fig. 33 show, the situation is quite different for the bulk materials.

Photographs of polished cross-sections of $Mg_xSc_{1-x}Pd_{0.024}$ alloys are shown for x = 0.65 (a), x = 0.70 (c) and x = 0.80 (d); Fig. 33 (b) shows the diffraction pattern of $Mg_{0.65}Sc_{0.35}Pd_{0.024}$ once more where the peaks of the catalytic phases are indicated by black dots. From the positions of these peaks, it becomes clear that the Pd is not present in its pure form, but has been alloyed with Mg and Sc.

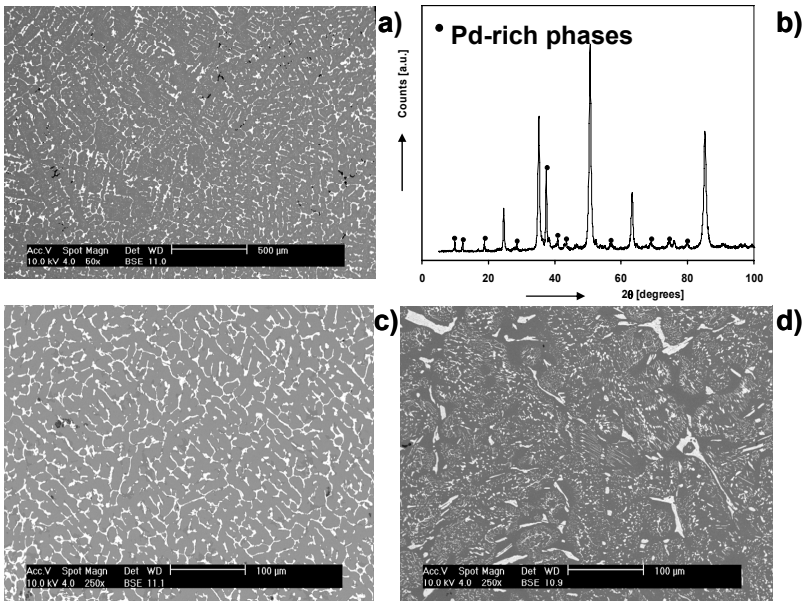

Fig. 33 : SEM micrographs of Mg_xSc_{1-x} bulk alloys: $Mg_{0.65}Sc_{0.35}Pd_{0.024}$ (a), XRD pattern of $Mg_{0.65}Sc_{0.35}Pd_{0.024}$ with reflections of the Pd-rich phases indicated by the black dots (b), $Mg_{0.70}Sc_{0.30}Pd_{0.024}$ (c) and $Mg_{0.80}Sc_{0.20}Pd_{0.024}$ (d)

Instead of the neatly layered structure characteristic of the thin film samples, bulk alloys exhibit a brick-like distribution of the Pd-rich phases for x = 0.65 (a) and 0.70 (c) and a more irregular distribution in the $Mg_{0.8}Sc_{0.2}Pd_{0.024}$ alloy (Fig. 33d). This means that unlike the thin film case, not all the electrochemically active surface will be covered by a catalytically active layer. In the alloy with x = 0.65 two different catalytic phases are present besides the MgSc main phase. One is Sc_2Pd, with some dissolved Mg, which is a Laves phase. The second phase has an approximate composition $Mg_{0.45\text{-}0.55}Sc_{0.38\text{-}0.28}Pd_{0.17}$. In the alloys with x = 0.7, 0.75 and 0.80 only this second phase is present. From the diffraction pattern of $Mg_{0.8}Sc_{0.2}Pd_{0.024}$ in Fig. 31 (d) the structure of this phase was determined to be bcc with a lattice constant of about 17.5 Å.

In materials without Pd, hardly any charge (typically less than 50 mAh/g) can be inserted/extracted into/from the materials. Gas-phase loading is, however, possible at high temperatures and pressures.

4.3.2 Electrochemical characteristics

When Mg-Sc alloys were first described as hydrogen storage materials by Notten *et al.* the overall (de)hydriding reactions were represented as follows[94]:

$$Mg_xSc_{1-x} + (3-x)H_2O + (3-x)e^- \rightarrow Mg_xSc_{1-x}H_{3-x} + (3-x)OH^- \qquad (4.1)$$

Because Mg forms a dihydride and Sc can be both di-and trivalent, the theoretical capacity was assumed to correspond to 2 H/Mg and 3 H/Sc for the initial hydrogenation of the material. Since ScH_2 has a very negative heat of formation (-200 kJ/mole H_2) only 1 H/Sc and 2 H/Mg was assumed to be reversible, according to

$$Mg_xSc_{1-x}H_{3-x} + (x+1)OH^- \leftrightarrow Mg_xSc_{1-x}H_{2-2x} + (x+1)H_2O + (x+1)e^- \qquad (4.2)$$

To investigate the actual storage capacity of the MgSc alloys, both thin film electrodes and bulk materials with similar composition were galvanostatically charged and discharged. The

thin film samples were galvanostatically charged using a current of 0.6 mA (~ 5000 mA/g), discharged with 0.12 mA (~ 1000 mA/g) and deep–discharged with 0.012 mA (~ 100 mA/g). In the thin film case, the same absolute current was always used, corresponding to 40 $\mu A/cm^2$ and 4 $\mu A/cm^2$ for high and low-current discharge, respectively. Therefore, the current density in mA/g is only given as approximate values as they vary slightly, depending on the composition of the Mg-Sc alloy of layers the same thickness. All the bulk materials were electrochemically charged using a current of 250 mA/g, discharged with 50 mA/g and deep-discharged at a current density of 10 mA/g.

Assuming that the material will hydrogenate up to 3 H/Sc may seem a bit simplistic at first sight, because contrary to Y, La and other rare-earth metals, pure Sc only forms a trihydride under GPa pressures and high temperatures. However, as Fig. 34 shows, the first charge of a bulk $Mg_{0.65}Sc_{0.35}Pd_{0.024}$ alloy reaches the theoretical capacity of 1850 mAh/g before the hydrogen evolution reaction becomes dominant. The capacity reached in the discharge and deep-discharge steps is also almost equal to the theoretical one of 1280 mAh/g.

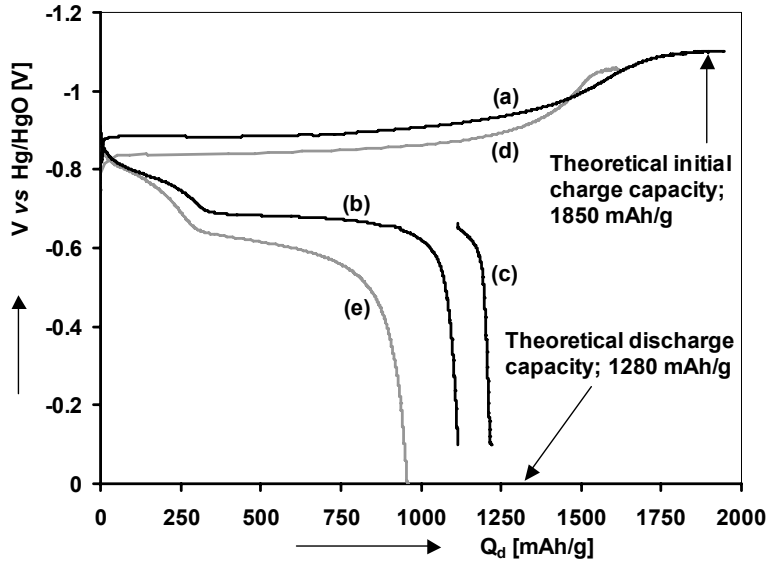

Fig. 34 : First electrochemical charge (250 mA/g, curve (a)), and discharge with 50 mA/g (curve (b)) and 10 mA/g (curve (c)) of a cast and annealed $Mg_{0.65}Sc_{0.35}Pd_{0.024}$ alloy. The theoretical initial charge and discharge capacities are also indicated by the arrows. The charge (100 mA/g) and discharge (50 mA/g) curves of a $Mg_{0.65}Sc_{0.35}$ alloy ball-milled with 5 at.% Pd are shown as curve (d) and (e) respectively.

For the ball-milled alloy, the theoretical charge capacity is ~1710 mAh/g, taking the higher Pd-content into account, which is also reached to within 100 mAh/g before the HER becomes dominant. It is noteworthy, however, that the discharge capacity at 50 mA/g is considerably lower compared to the alloy where the Pd is alloyed with the Mg and Sc.

Discharge curves as a function of composition are shown in Fig. 35 for the thin films (a) and the bulk materials (b) with the highest current density used. The discharge curves of both bulk and thin film materials show very similar shapes. A large plateau region is situated at around – 0.68 V for all compositions, which is indicative of a phase transition. The first part of the discharge curve clearly shows solid solution behavior for high Mg content, but becomes more plateau-like for increasing Sc content. The amount of charge extracted from the material in this region clearly decreases with a decrease in Sc content, for both thin films and bulk materials.

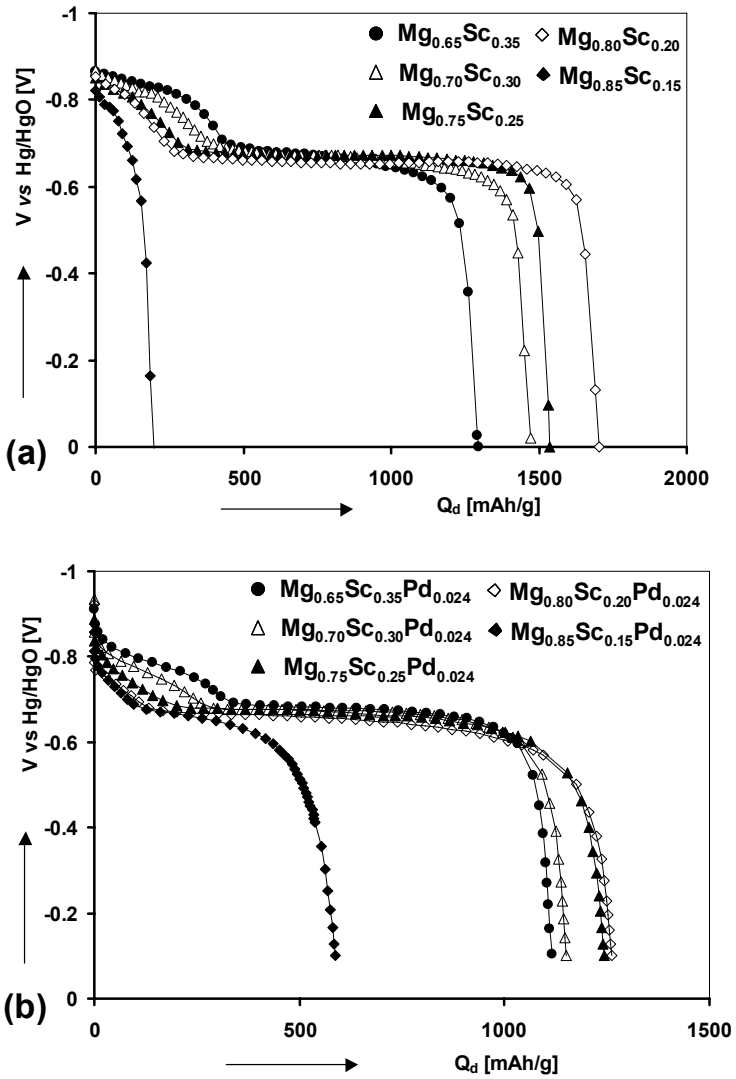

Fig. 35: Constant-Current discharge curves of Pd capped Mg_xSc_{1-x} thin films (a) and $Mg_xSc_{1-x}Pd_{0.024}$ bulk alloys (b) for x = 0.65-0.85. Discharge rate is 1 A/g for the thin films and 50 mA/g for the bulk materials

The discharge capacity as a function of composition is plotted in Fig. 36 for both the discharge at high current (curves (a) and (c)) and deep-discharge (curves (b) and (d)). A similar trend can again be seen for both types of materials. First, an increase in discharge capacity is observed with increasing Mg-content. This is fairly logical, as the material becomes lighter when more Mg is incorporated and due to the fact that two hydrogen atoms can be reversibly adsorbed/desorbed per Mg atom, where Sc is assumed to store only one reversible hydrogen.

Lower discharge capacities for compositions with a Mg-content $x > 0.80$ are observed for the thin films as well as the bulk materials. For the thin film with x = 0.85 it is mostly the rate capability that is affected as the total capacity at low discharge rate is only slightly lower than that for x = 0.80. For the bulk material with the same composition, however, the total capacity has also decreased considerably. Only half of the capacity is reached even at low current compared to x = 0.80. This is believed to be due to a change in crystal structure of the hydride, which will be discussed later.

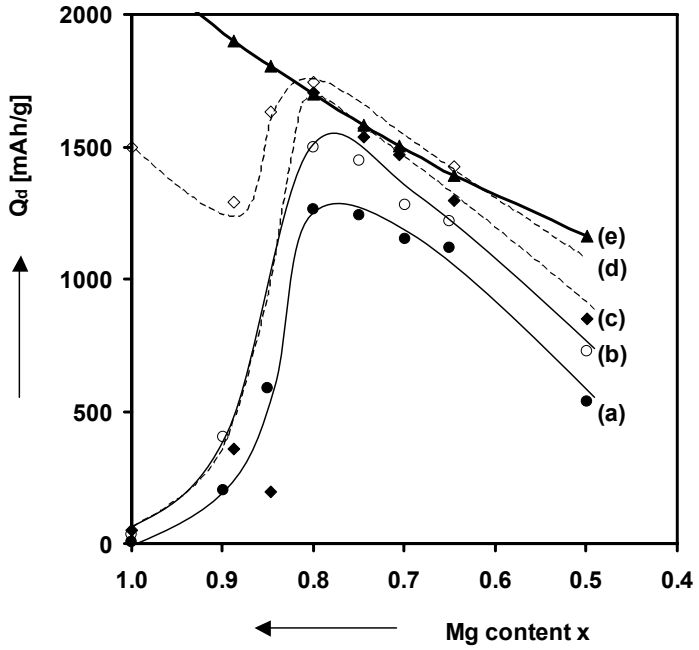

Fig. 36: Discharge capacity of Mg_xSc_{1-x} alloys and thin films for x = 0.5-1. (a): Discharge capacity of bulk materials at 50 mA/g, (b): bulk materials at 10 mA/g, (c): Discharge capacity of thin films at 1000 mA/g, (d): Thin films at 100 mA/g, (e): theoretical discharge capacity based on 2 reversible H/Mg and 1 reversible H/Sc

The absolute discharge capacity of the thin film materials is somewhat higher than their bulk counterparts. This can be explained by the fact that for the thin film materials the amount of extracted charge is directly correlated to the active phase, which consists only of Mg and Sc. For the bulk materials, part of the Mg and Sc is incorporated with Pd into the catalytic phases. The hydriding behavior of these phases is apparently different from that represented by Eqs. (1) and (2), resulting in a lower discharge capacity on a weight-basis of 1495 mAh/g for the bulk case *vs.* 1741 mAh/g for the thin film case (low current) for x = 0.80. Fig. 36 also shows that the rate capability of the thin film materials is better than that of the bulk materials; the current density on weight basis is 10 to 20 times as high, yet still a higher capacity is reached, compared to the bulk materials. This can be explained by the much shorter diffusion length of only 200 nm vs. 20 μm for the bulk materials.

From Fig. 36 it also becomes apparent that the measured capacities for the thin films are very close to the theoretically predicted ones (curve e). So despite the oversimplification of the hydriding behavior of these materials, as expressed by Eq. *(4.1)* and *(4.2)*, the agreement between the predicted and measured capacities is quite good. Note that for the compositions x = 0.65 and x = 0.80 the measured capacity is somewhat higher than the theoretical one, but the difference falls within the stated margin of 3%.

4.3.3 Thermodynamic properties

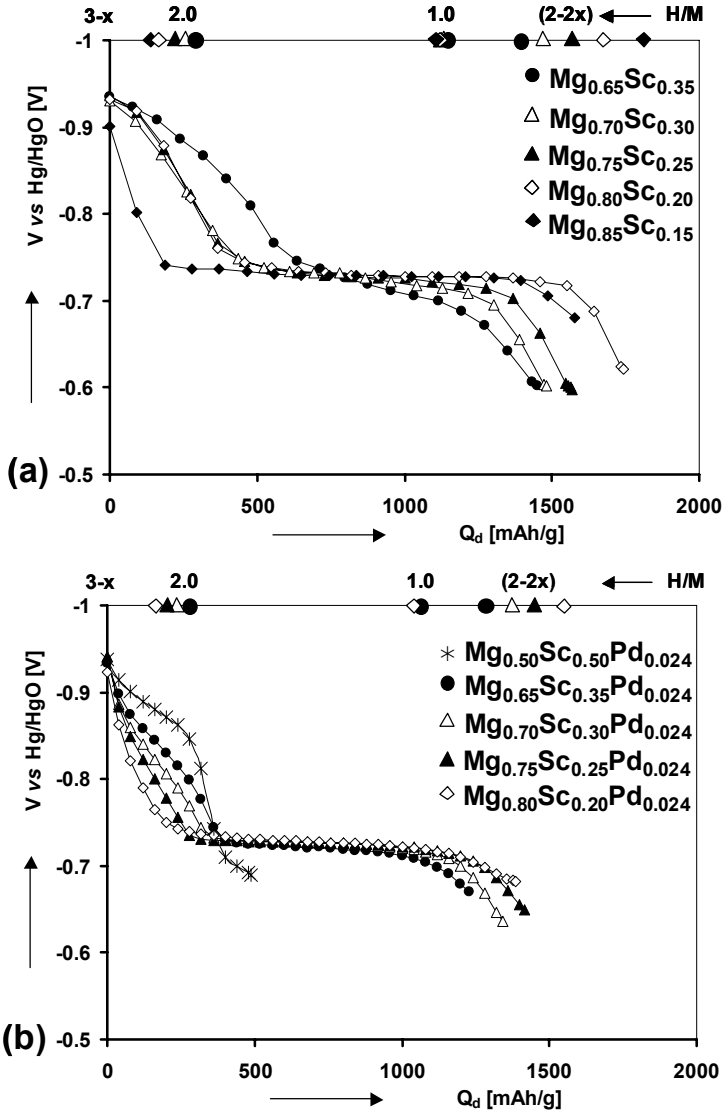

Fig. 37: GITT curves of Mg_xSc_{1-x} thin films (a) and bulk materials (b)

The thermodynamic properties of the MgSc alloys were evaluated by means of GITT. For the thin film materials the GITT measurements were carried out by dividing the total capacity reached with low discharge current (see Fig. 36) into 20 equally large discharge steps. The discharge current used was 0.12 mA (~ 1000 mA/g), but if the kinetics became too slow, the low discharge current of 0.012 mA (~ 100 mA/g) was used for the remainder of the experiment. After each step the electrode was allowed to equilibrate for 1 hour at the end of which the open-circuit voltage (OCV) is assumed to be the equilibrium potential. For the bulk materials a similar approach was used with a much smaller step-size of 10 mAh/g with a current density of 50 mA/g.

The equilibrium voltage curves for the different compositions are shown in Fig. 37, both for thin films (a) and bulk materials (b). On the top x-axis, the H/M ratios are indicated assuming 3 H/Sc and 2 H/Mg in the fully charged state. The plateau voltage is not a strong function of composition, as was already apparent from the constant-current discharge curves in Fig. 35. It can be seen in Fig. 37, however, that the main plateau is more sloping when the alloy is relatively rich in Sc (*i.e.* for $x = 0.65$) and very flat for low Sc concentrations (*i.e.* $x =$

0.85). This is very clear for the thin film samples (Fig. 37 (a)), but looking closely at the isotherms of the bulk materials (Fig. 37 (b)) one can also see that the plateau for x = 0.65 is slightly more sloping than that for x = 0.80. For x = 0.50, the amount of charge extracted before the plateau region is not increased anymore compared to x = 0.65, despite the relatively large change in composition. What is also noteworthy is that between x = 0.85 and x = 0.65, the plateau pressure is constant, but for x = 0.50 the equilibrium potential after the initial solid solution region is approximately 40 mV more positive.

A remarkable difference between the bulk materials and thin films here is that for the bulk materials the amount of charge extracted in the first solid solution part decreases with decreasing Sc content; the same as in the galvanostatic discharge curves, while for the thin films the isotherms for x = 0.70, 0.75 and 0.80 lie on top of each other. The general trend, however, is the same; the amount of charge extracted before the onset of the plateau region decreases with decreasing Sc-content.

The measured equilibrium voltages (E_{eq}) can be converted into an equivalent hydrogen pressure (P_{H_2} , in bar) using the well-known formula, which was already mentioned in Chapter 2:

$$E_{eq} = -\frac{RT}{nF}\ln\frac{P_{H_2}}{P_0} - 0.931 \qquad (4.3)$$

where R is the gas constant, T is the absolute temperature, F is Faraday's constant, n the number of electrons involved in the hydrogen evolution reaction and P_0 is the standard pressure of 1 bar. Note that a potential difference of about 30 mV corresponds to a change in equivalent hydrogen pressure by 1 order of magnitude. Using Eq. *(4.3)*, a plateau voltage of -0.72 to -0.74 V, as exhibited by the MgSc materials presented here, corresponds to an equivalent hydrogen pressure of $7 * 10^{-5}$ to $3.5 * 10^{-4}$ mbar. Using the Van 't Hoff relation[34]:

$$\ln\frac{P_{H_2}}{P_0} = \frac{\Delta H_{tr}}{RT} + \frac{S^0{}_{H_2}}{R} \qquad (4.4)$$

where $S^0{}_{H_2}$ is the standard molar entropy of hydrogen (130.68 $J.mol^{-1}.K^{-1}$) the enthalpy change associated with the phase transition, ΔH_{tr} (mid-plateau), is calculated to be approximately –78 kJ/mole H_2. This value is almost equal to the formation enthalpy of MgH_2.

4.3.4 Electrochemical Impedance Spectroscopy

Both thin film and bulk MgSc materials were galvanostatically hydrogenated to their fully charged state after which they were stepwise discharged. Impedance measurements were carried out after 1 hour of equilibration, which followed each discharge step, thus covering the entire range along the equilibrium voltage curve. The thin film materials were discharged in 20 consecutive steps, using a current of 0.12 mA (~ 1000 mA/g). For the bulk materials the entire discharge process was divided into 25 pulses, using a current of 50 mA/g during each pulse.

From impedance spectroscopy, it is possible to extract information about the separate elementary reaction steps in the hydriding process. The first step is generally considered to be water reduction, leading to a*d*sorbed hydrogen (H_{ad}) and a hydroxyl ion at the electrolyte/catalyst interface

$$H_2O + M + e^- \underset{k_b}{\overset{k_f}{\rightleftarrows}} MH_{ad} + OH^- \qquad (4.5)$$

Then the a*d*sorbed hydrogen is a*b*sorbed into the Pd-topcoat in the case of thin films, or the more complex catalytic phase in the case of bulk materials according to

$$MH_{ad} \underset{k_b}{\overset{k_f}{\rightleftarrows}} MH_{abs,Pd} \qquad (4.6)$$

Eventually hydrogen is stored in the MgSc main phase

$$MH_{abs,Pd} \underset{k_b}{\overset{k_f}{\rightleftarrows}} MH_{abs,MgSc} \qquad (4.7)$$

Thin films are expected to behave as a model system in this respect, because reactions *(4.5)*, *(4.6)* and *(4.7)* occur on clearly defined, flat interfaces, which makes it easier to extract information on the individual reaction steps from the impedance data. Fig. 38 shows a schematic overview of the thin film system, including each elementary reaction step.

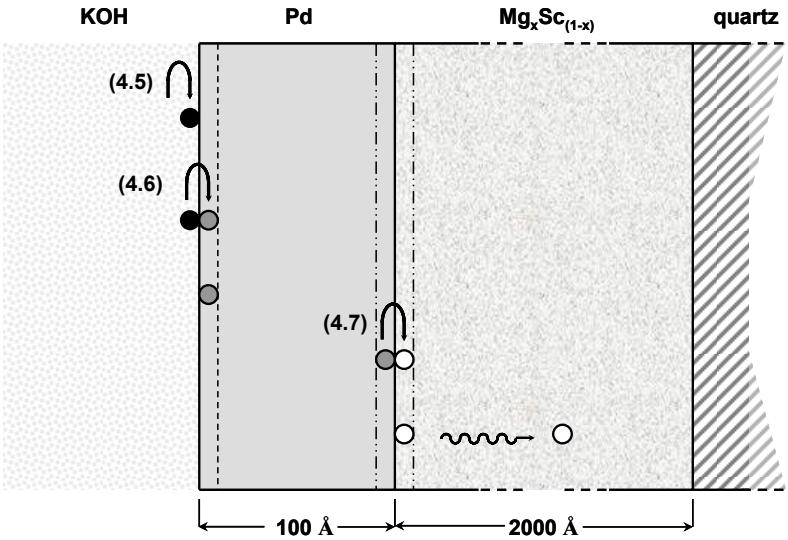

Fig. 38 : Schematic representation of the thin film system showing all elementary reaction steps at the appropriate locations. *(4.5)*: charge transfer reaction forming *ad*sorbed hydrogen at the Pd surface; *(4.6)*: *ad*sorbed hydrogen entering the subsurface layer, becoming *ab*sorbed hydrogen; *(4.7)*: Hydrogen transferring from the Pd topcoat to the MgSc phase and subsequently diffusing into the bulk of the MgSc layer. The diffusion in the Pd topcoat is neglected as it is assumed to be very fast compared to all other reaction steps.

The entire electrochemical reaction scheme (Eqs. *(4.5)- (4.7)*) can be accurately modeled using an equivalent electronic circuit. How this can be done for the thin film system is extensively described in recent work[97]. The appropriate circuit is shown in Fig. 39 (a). The resistance associated with hydrogen absorption into the Pd (Eq. *(4.6)*) was determined to be negligible and is therefore omitted in this scheme. R_{el} represents the Ohmic drop arising from the electrolyte resistance. C_{dl} is the electrical double layer capacity and R_{ct} is the charge transfer resistance associated with reaction *(4.5)*. R_{tr} and C_{tr} represent the transfer of hydrogen from the catalytic layer into the MgSc main phase, *i.e.* reaction *(4.7)*. Finally a Warburg (W) element is included, describing semi-infinite diffusion. The well-known Randles equivalent

circuit, shown in Fig. 39 (b), was used to fit the spectra of the bulk materials for reasons that will become clear shortly.

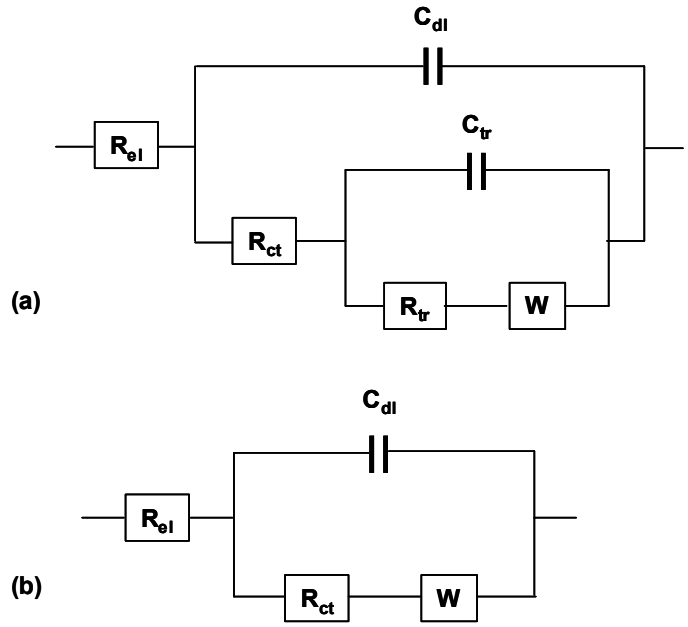

Fig. 39: Equivalent circuits used to fit the impedance spectra of the thin films (a) and the bulk materials (b)

Fig. 40 (a) (thin films) and (b) (bulk) show the complex plane plots (Nyquist plots) for the MgSc materials with x = 0.7 as a function of the normalized hydrogen content in % (curve a-f). The insets show the spectra for the fully discharged state. The fully charged state is defined as 100% and the lowest hydrogen content reached in the measurement is set to 0. For the thin films it can be seen that in the initial stages of discharge only one semicircle and a diffusion-limited region are visible. This semicircle can be modeled by a parallel arrangement of a capacitance and resistance. The double layer capacitance depends only on the electrode surface area and is therefore expected to remain approximately constant throughout the entire discharge process. The capacitance that is obtained by fitting the spectra is indeed constant and therefore the first semicircle is ascribed to the double layer capacity and the charge transfer resistance, R_{ct}. In the final stages of discharge, when the hydrogen content is around and below 10%, a second semicircle becomes clearly visible, although it can already be resolved around 35%. Since the value obtained for the capacitance associated with this semicircle is strongly dependent on the hydrogen content in the films this semicircle has been assigned to reaction *(4.7)*. Both semicircles grow when the hydrogen content decreases, which means that both R_{ct} and R_{tr} increase. Approaching the end of the discharge process R_{tr}, associated with the transfer of hydrogen from the Pd-layer to the MgSc-layer becomes the dominant factor.

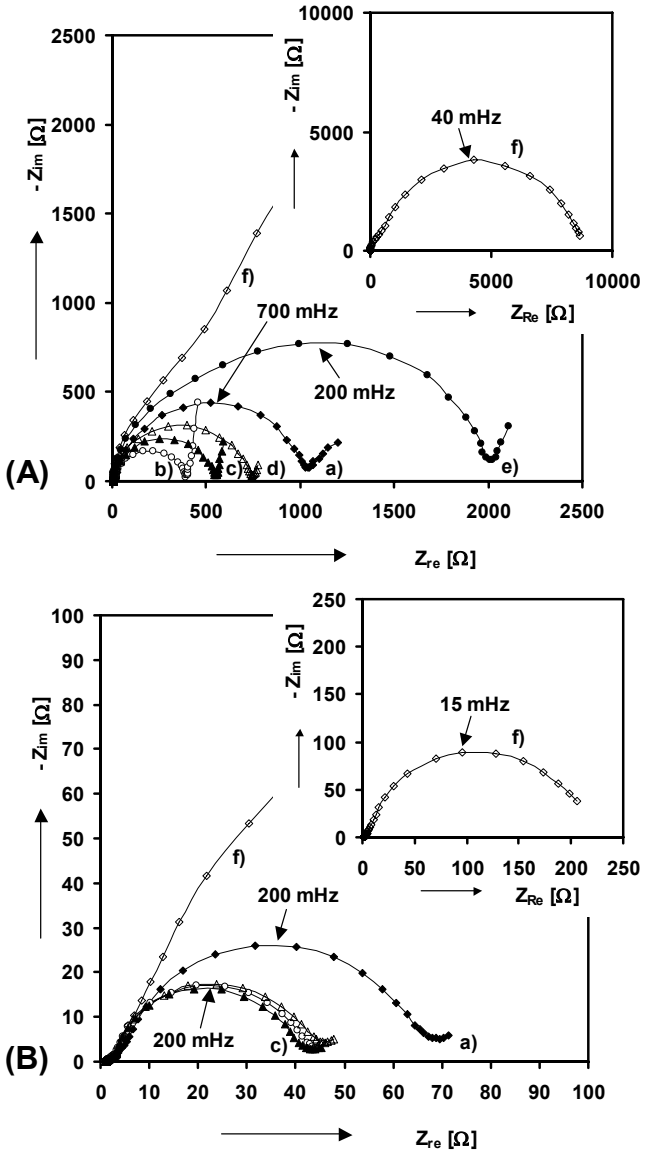

Fig. 40: Impedance spectra of $Mg_{0.70}Sc_{0.30}$ thin film (A) and bulk material (B) for various states of charge; (a): fully charged, (b): 25% discharged, (c): 50% discharged, (d): 75% discharged, (e): 93% discharged, (f): 100% discharged. The inset shows the spectrum for the fully discharged state.

The spectra of the bulk materials on the other hand (see Fig. 40 (b)), consist of only one semicircle and a diffusion line. Because only one semicircle could be resolved throughout the entire discharge process, the spectra of the bulk materials were fitted using the Randles' circuit in Fig. 39 (b). The capacitance derived from this semicircle also remains constant throughout the entire discharge process. Therefore, this semicircle is ascribed to a parallel arrangement of C_{dl} and R_{ct}, the same as for the thin films.

A very important kinetic parameter of a hydrogen storage material is its exchange current density I_0, as this is a measure for its ability to deliver current at high rates. I_0 can be calculated from[98]

$$I_0 = \frac{RT}{R_{ct}F} \qquad (4.8)$$

where R_{ct} is obtained from fitting the spectra in Fig. 40.

I_0 as a function of discharged capacity for the thin films is plotted in Fig. 41. The inset shows I_0 as a function of the equilibrium potential. For the thin films, I_0 is relatively low in the fully charged state, then passes through a maximum and sharply decreases again just before the plateau region and also in the final stages of discharge. The maximum value of I_0 is found at an equilibrium potential of about –0.85 V, corresponding to 2 mbar hydrogen pressure, which is close to the ß-α transition of Pd-hydride.

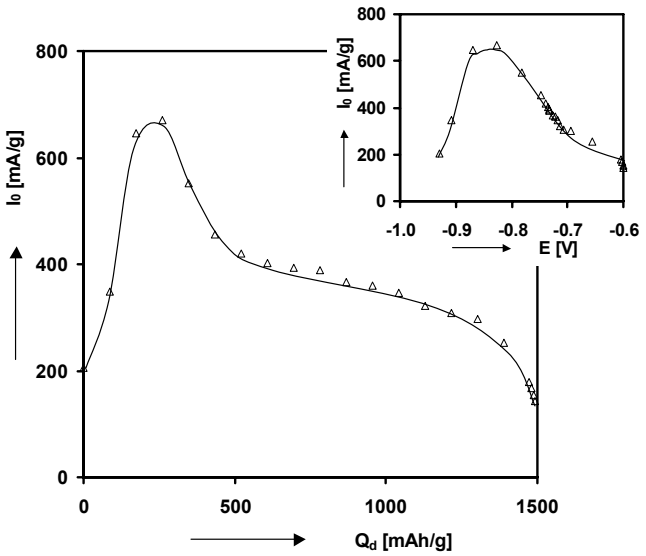

Fig. 41: Values of the exchange current density (I_0) as a function of the hydrogen content and equilibrium potential (inset) for a Pd-capped $Mg_{0.70}Sc_{0.30}$ thin film.

At more positive potentials the exchange current sharply decreases as the Pd-topcoat enters the α-phase and is ever further depleted of hydrogen upon further discharge. A theoretical description of the dependence of the exchange current on the partial hydrogen pressure has been given by Notten *et* al.[99]. Their model predicts a shape of the I_0 *vs.* potential curve that strongly resembles the one that is observed here. The same I_0 *vs.* potential dependence was found for a single Pd layer[97], which means the charge transfer kinetics are completely dominated by the Pd topcoat. Since the Pd layer completely covers the MgSc film this was to be expected.

For the bulk materials the situation is slightly different as can be seen in Fig. 42. Here, an increase in I_0 is also observed in the initial stage of discharge, and in the final stages of discharge there is a decrease to only 4 mA/g in the empty state similar to the thin films. Contrary to the thin film case, however, no sharp maximum in I_0 is found. Instead, the maximum in I_0 is found close to –0.73 V, which is the plateau voltage of the MgSc main phase and at quite a different potential compared to the thin film case. Apparently the alloying of the Pd with Mg and Sc profoundly affects its catalytic properties. The relative difference between the maximum and minimum values for I_0 is about a factor 5, the same as for the thin films.

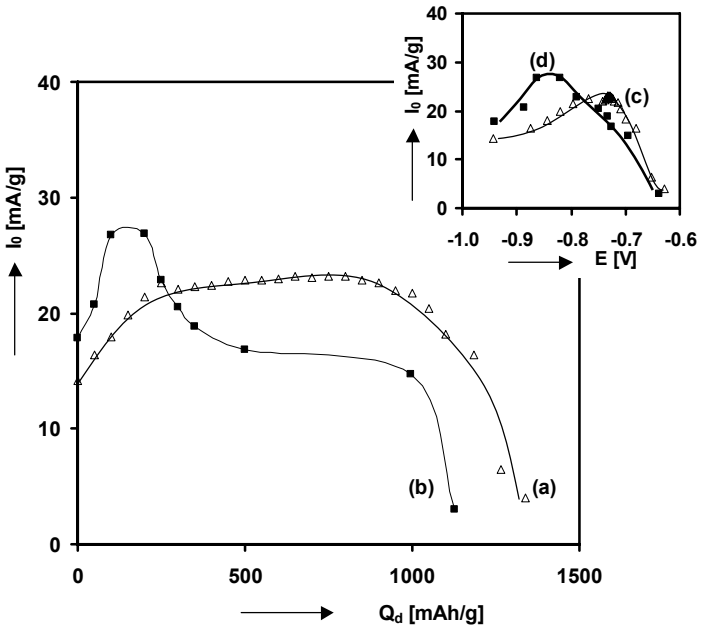

Fig. 42: Exchange current density (I_0) as a function of the hydrogen content and equilibrium potential (inset) for a cast $Mg_{0.70}Sc_{0.30}Pd_{0.024}$ alloy (curves (a) and (c)) and a $Mg_{0.65}Sc_{0.35}$ alloy ball-milled with 5 at% Pd; (b) and (d). Note the much clearer maximum in I_0 for the alloy milled with pure Pd compared to the alloy that was cast with Pd and the similarity with the thin film case in Fig. 41.

Because I_0 is related to the charge transfer reaction, which is a process taking place solely at the electrode surface, the absolute exchange current (in A) should be divided by the electrode surface area, rather than the active mass, to make the comparison between bulk and thin films truly meaningful. For the thin film samples this is straightforward because they have a smooth surface with a geometric surface area of about 3 cm^2. The measured I_0 values in Fig. 41 correspond to 5-30 $\mu A/cm^2$.

Estimating the active surface area of a bulk electrode is not straightforward. It is very likely that the alloy will break up along the boundaries between the Pd-rich and the main MgSc phase, resulting in a considerable surface roughness of the particles. For this reason, assuming smooth spherical particles with an average diameter of 40 μm is not realistic. Therefore, a BET measurement was carried out to determine the specific surface area of the metal filings that were used to make the test electrodes. The specific area was determined to be approximately 2.5 m^2/g, which means the maximum I_0 values for the bulk materials translate to ~1 $\mu A/cm^2$. The catalytic phase will probably not cover the entire surface of the material, but these results show that the charge-transfer reaction is at least a factor 5 slower compared to the thin films, due to the observed alloying of Pd with Mg and Sc.

The response of the alloy that was ball-milled with pure Pd (curves (b) and (d) in Fig. 42) on the other hand, shows much more resemblance to the thin film case. There is now a much clearer maximum in the exchange current density as a function of the discharged capacity and the equilibrium potential. The potential where the maximum occurs is also equal to that of the thin films. Once again, the similarity between the thin film and the bulk system is excellent.

One distinct difference remains, however. From the impedance spectra in Fig. 40, only 1 semicircle was found for the bulk system, whereas for the thin films an additional semicircle was found in the impedance spectra. For the bulk alloy ball-milled with pure Pd, the spectra look similar to those in Fig. 40:

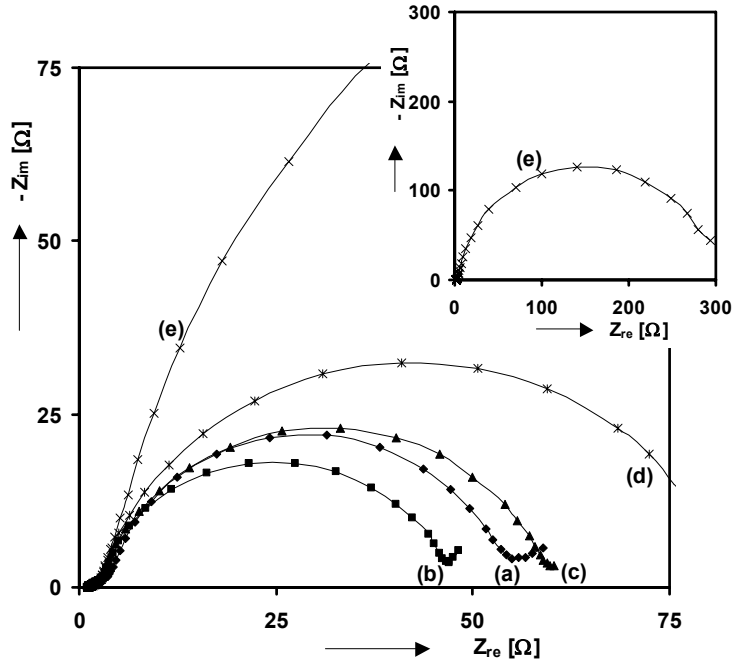

Fig. 43: Impedance spectra of $Mg_{0.65}Sc_{0.35}$ alloy ball-milled with Pd for (a): fully charged, (b): 25% discharged, (c): 50% discharged, (d): 75% discharged and (e): completely discharged

Only 1 semicircle, ascribed to the charge-transfer reaction and the double layer capacitance, is evident in the spectra. A second semicircle that can be ascribed to transfer of hydrogen between the Pd and the MgSc main phase could not be reliably resolved in any of the spectra.

4.3.5 Structure of hydrided materials

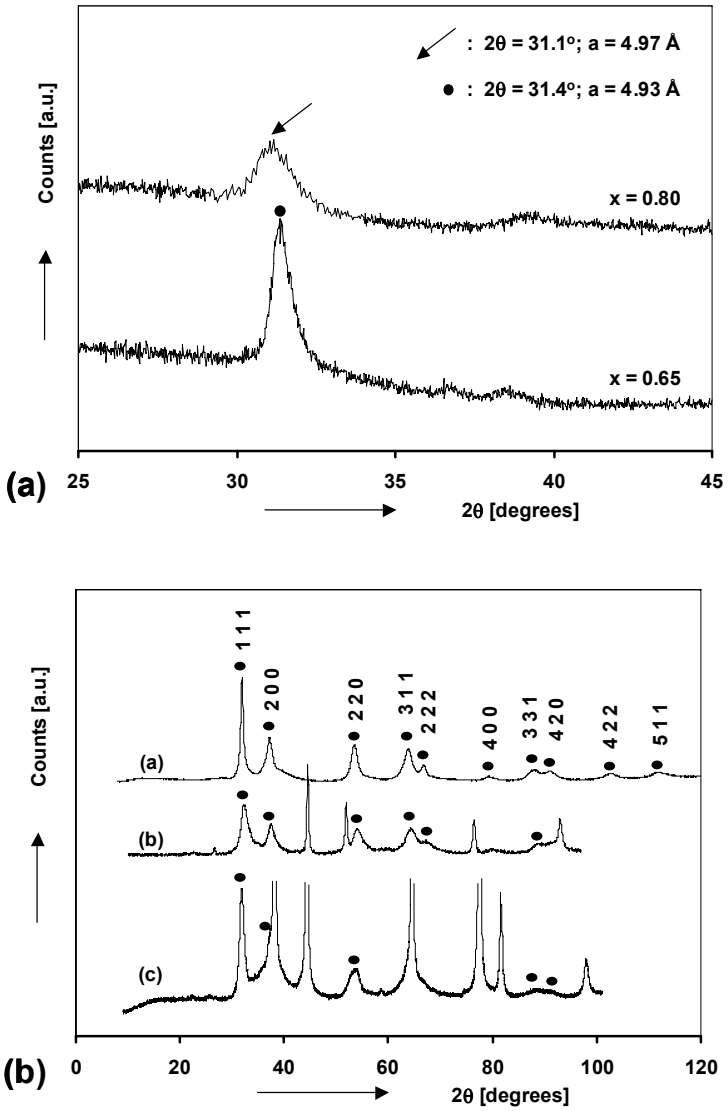

Fig. 44 (a): X-Ray diffraction patterns of fully hydrogenated Pd-capped $Mg_{1-x}Sc_x$ thin films for x = 0.65 and 0.80 and (b) : XRD patterns of fully hydrogenated $Mg_{0.65}Sc_{0.35}Pd_{0.024}$ (pattern (a)), electrochemically charged $Mg_{0.65}Sc_{0.35}Pd_{0.024}$; Ni matrix (pattern (b)) and electrochemically hydrided $Mg_{0.75}Sc_{0.25}Pd_{0.024}$; Ag matrix (pattern (c)).

To determine the structural properties of the hydrided materials, the hydrogenated forms of both the thin films and bulk materials were subjected to XRD analysis. The thin films were measured in-situ by placing them in a hermetically sealed sample-holder with a Be-window, which was equipped with a gas inlet. Hydriding was performed at 0.9 bars H_2 pressure and the results are shown in Fig. 44 (a).

As becomes apparent from this figure, accurate structural measurements are very difficult to perform on thin film samples as the signal-to-background-ratio is rather small, the peaks are very broad and only one peak is clearly visible at 2θ-values between 25 and 45°. Assuming that this single visible reflection arises from the (111) planes of an fcc structure the lattice parameter *a* is about 4.93 Å for x = 0.65. With increasing Mg-content the lattice parameter increases further as evidenced by a shift of the diffraction peak to slightly lower angles. For x = 0.8 a lattice parameter of 4.97 Å can be calculated. The strongest reflection of

MgH_2, which would be at 28°, is absent, indicating that no MgH_2 is formed upon hydrogenation.

Fig. 44 (b) shows the X-ray diffraction patterns of a bulk $Mg_{0.65}Sc_{0.35}Pd_{0.024}$ sample, that has been hydrided via the gas phase (curve a), electrochemically charged $Mg_{65}Sc_{35}P_{0.024}$ in a Ni-matrix after which the Ni-powder was mostly removed with a small magnet (curve b). Now more reflections are visible and the observed pattern is in full agreement with an fcc arrangement of the metal atoms. Again, there is no indication of the presence of MgH_2. The lattice constant of the resulting material, 4.84 Å (curve a), is substantially larger than the literature value for pure ScH_2, which is a = 4.78 Å[100]. Elemental analysis showed the hydrogen content of this material to be about 2.2 H/M, which means that this material was hydrogenated almost to its maximum hydrogen concentration according to reaction *(4.1)*. Curve (c) shows the diffraction pattern of electrochemically charged $Mg_{0.75}Sc_{0.25}Pd_{0.024}$. Because of the larger total volume expansion of Mg-richer compositions, a more ductile Ag matrix had to be used in this case. This has the disadvantage of a larger overlap between the hydride peaks and those of the matrix, but 4 peaks can still be clearly discerned plus a 'shoulder' around 37.5°. The peaks are slightly shifted to smaller angles with respect to curve (b) and the lattice constant was determined to be 4.86 Å, also indicating an increase in the lattice parameter with increasing Mg content, the same as for the thin films.

Fig. 45 shows the (111) reflection of a hydrogenated and completely dehydrogenated thin film with x = 0.65. Gradual desorption is very difficult for thin film samples because of the extremely small amounts of hydrogen contained in the sample, so only the extreme cases (full and empty) could be measured. As was shown in Fig. 44 (a), in the fully charged state, the lattice constant equals 4.93 Å. After desorption, by evacuating and heating the Be sample holder to 150° C, this value has decreased to 4.58 Å, revealing an approximately 25% volume change.

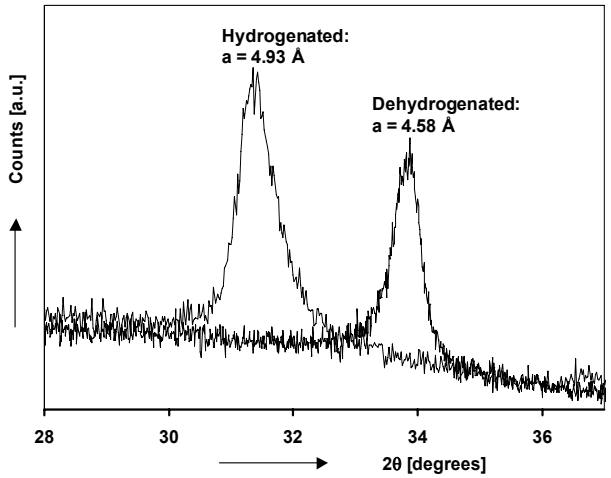

Fig. 45: XRD patterns of fully hydrided (0.9 bar) and dehydrided (vacuum, 150 °C) Pd-capped $Mg_{0.65}Sc_{0.35}$ thin film.

To investigate the phase transition that is occurring in the plateau region, a Pd-free bulk alloy, with x = 0.65, was charged via the gas-phase and then unloaded by heating it in a thermogravimetric analyzer. The complete desorption curve is shown in Fig. 46 (A); the similarity in shape with the electrochemical discharge curve is striking. Slightly more than 4.5 wt.% H was desorbed from the sample, which means the initial hydrogen content was ~2.25 H/M if it is assumed that 2 H/Sc (=0.7 H/M) remain inside the alloy after desorption. Heating was terminated at 3 different temperatures along the TGA curve and the crystal structure of the resulting hydride was determined.

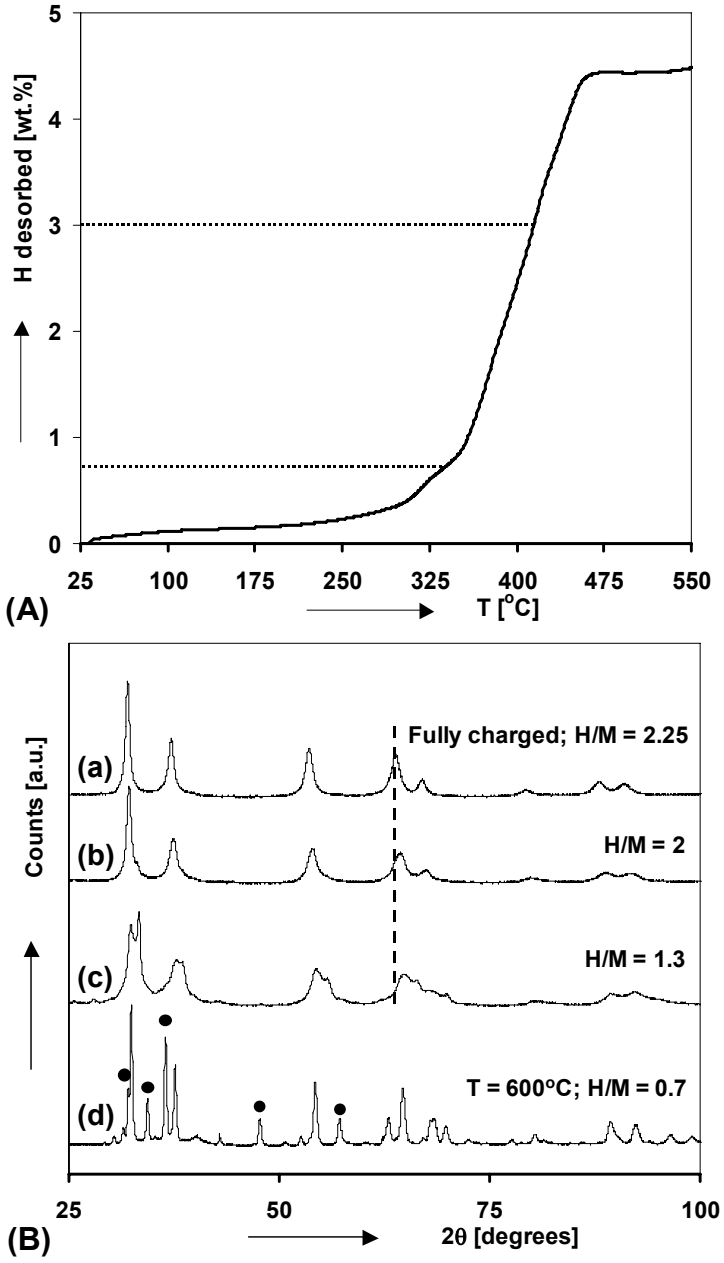

Fig. 46 (A): Thermal desorption curve of fully hydrided $Mg_{0.65}Sc_{0.35}$ between room temperature and 600°C. The dashed lines correspond to the temperatures where heating was stopped to obtain partially desorbed samples. (B): Diffraction patterns of fully hydrided material (a), sample heated to 350°C (b), 425°C (c) and 600°C (d).

At H/M ~2 the material is still single-phase and the lattice constant has slightly decreased from 4.84 Å to 4.80 Å as indicated by the dashed line. Curve (c) represents the diffraction pattern of a hydride from which 3 wt.% H has been desorbed. 3 wt.% corresponds to approximately 800 mAh/g, which means the material should be in a 2-phase region at this point. This is indeed the case, as can be seen from the splitting of all the diffraction peaks into 2 distinct fcc patterns. The lattice constants that were found for the two structures are 4.80 Å for the hydrogen-rich structure and 4.68 Å for the hydrogen-depleted structure. 4.80 Å is still slightly larger than pure ScH_2, the 4.68 Å for the hydrogen-poor phase is clearly smaller. The discrete lattice expansion/contraction, *i.e.* the relative volume change associated with the phase transformation, that can be calculated from the lattice constants in Fig. 46 (B) is (V_β-

$V_\alpha)/V_\alpha = (4.80^3\text{-}4.68^3)/4.68^3 \approx 8\%$, which is significantly smaller than *e.g* the 21 % determined for AB_5 type materials such as $LaNi_5$[49].

Fully desorbing the hydrogen by heating the material to more than 500°C finally results in decomposition of the material and free Mg metal is detected in the diffraction pattern. The lattice constant of the remaining fcc structure changes back accordingly to the value of 4.78 Å of pure ScH_2.

4.4 Discussion

Like all rare-earth dihydrides, ScH_2 has a so-called fluorite structure where the metal atoms are in an fcc arrangement, as was also found for the ternary hydrides. The H-atoms completely fill the tetrahedral sites. This structure is shown in Fig. 47 (left), where the location of an empty octahedral site is also indicated.

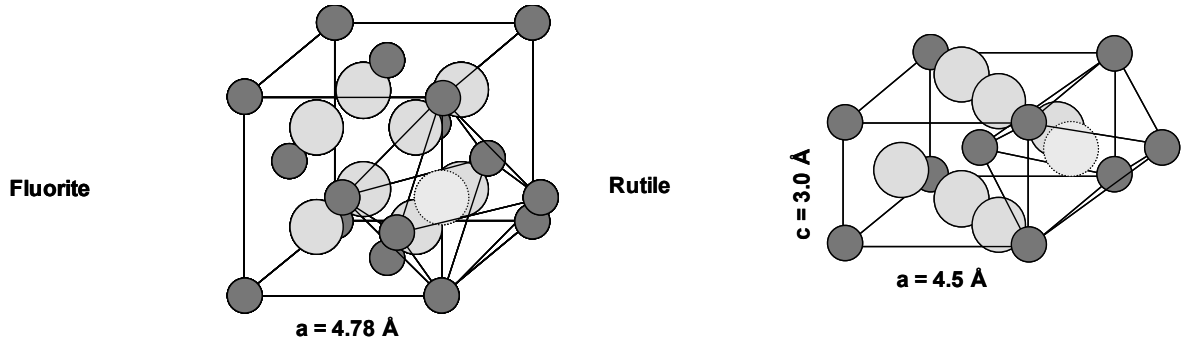

Fig. 47: Fluorite (left) and rutile (right) unit cell with an additional hydrogen atom in an 'octahedral' site.

According to the Westlake criterion[101], the distance between neighboring H-atoms should be at least 2.1 Å. This 'criterion' is based on an extensive review of available experimental data on interstitial hydrides of which the crystal structures, available interstitial sites and maximum hydrogen content were known at the time. It was found that the radius of the interstitial site was always larger than 0.4 Å and that the H-H distance was never smaller than 2.1 Å. Therefore, it may be regarded as an empirical rule, rather than a 'rigid' criterion. Quantum-mechanical calculations have shown that 2.1 Å is the optimum separation in LiH[102], below which electrostatic repulsions become stronger, but as this is a strongly ionic hydride, (small) deviations should be possible in other types of hydrides.

The Tetrahedral-Octahedral distance in pure ScH_2 with a = 4.78 Å is equal to ¼ * √3*a = 2.07 Å. This is, in principle, too small to allow simultaneous occupation of T and O-sites, and cubic ScH_2 indeed does not transform to the trihydride phase at atmospheric pressures. Contrary to, for instance, YH_2 and LaH_2, which have T-O distances of 2.252 Å and 2.455 Å, respectively and readily form a trihydride. There are two ways to try and synthesize ScH_3. Firstly, increasing the chemical potential of hydrogen gas by increasing the pressure as was done by Bashkin *et al.* [107, 108]. A second possibility is expanding the ScH_2 lattice by making a solid solution with another hydride. Pure MgH_2 has a rutile structure, which is also shown in Fig. 47 (right). Both representations show 1 unit cell, containing 4 formula units in the case of ScH_2 and 2 formula units for MgH_2. The molar volume of MgH_2 (30.38 $Å^3$/f.u.) is more than 10% larger than that of ScH_2 (27.30 $Å^3$/f.u.) so dissolving MgH_2 in ScH_2 will increase the molar volume and the T-O distance, allowing the O-sites to be occupied.

As can be seen in Fig. 36, the measured capacities, especially for the thin films, match the theoretical predictions based on the uptake of 3 H/Sc and 2 H/Mg very well. As was shown in Fig. 44, a cubic single-phase hydride with H/M ratio higher than 2 is formed upon fully charging with hydrogen and the lattice constant of the bulk material has indeed increased

considerably compared to pure ScH_2. The thin films seem to have expanded more strongly than the bulk materials, but the bulk materials were measured ex-situ, so some hydrogen may have been lost there between loading and measuring. The hydrogen-rich phase in the 2-phase region of the bulk material (Fig. 46 (B)) is, with a lattice constant of 4.80 Å, still larger than ScH_2, so even though the T-O distance in the fully charged compound is still somewhat smaller than 2.1 Å (2.092 Å), it is clear that a solid solution of Sc hydride and MgH_2 has been formed and that above H/M = 2 the octahedral sites are partly filled.

The structural model discussed above also explains why the first solid-solution part of the discharge curves is heavily influenced by the amount of scandium in the alloy. If the material absorbs 3 H/Sc and 2 H/Mg, the total H/M ratio in the fully hydrogenated state increases with increasing Sc-content. Therefore, more octahedral sites must be occupied in the fully charged material and the amount of hydrogen extracted before the onset of the plateau increases.

For the bulk material, see Fig. 46 (B), the hydrogen-poor phase has retained its fcc structure. The lattice constant is now smaller than that of pure ScH_2, but since the H/M ratio is now much smaller than 2, this is to be expected. The fact that the fcc structure of the metal sublattice is retained upon discharging leads to the assumption that the plateau region in the discharge curves of the bulk alloys and thin films corresponds to a phase transition from fluorite, where all the tetrahedral sites are occupied by hydrogen, to sphalerite, where only half of the tetrahedral sites are filled. Note that this is only an assumption at this point, because X-Ray diffraction only gives the position of the metal atoms; hydrogen can not be detected. The sphalerite arrangement is commonly found in ionic 1:1 compounds such as ZnS and other metal chalcogenides, but since pure ScH_2 is metallic, the ternary hydride is unlikely to behave as a fully ionic compound.

Fig. 48 depicts the entire discharge process going from high to low H/M ratio. However, assuming H/M = 3-x in the fully charged state, the point where H/M = 2 does not exactly coincide with the onset of the plateau region as becomes clear from the upper x-axis in Fig. 37. Particularly for the Sc-richer compositions the deviation is substantial. In the next chapter, the results of neutron diffraction measurements on $Mg_{0.65}Sc_{0.35}D_x$ are presented. The site occupancies of the hydrogen interstitials in the materials are derived as a function of deuterium content and this will refine the picture sketched in Fig. 48.

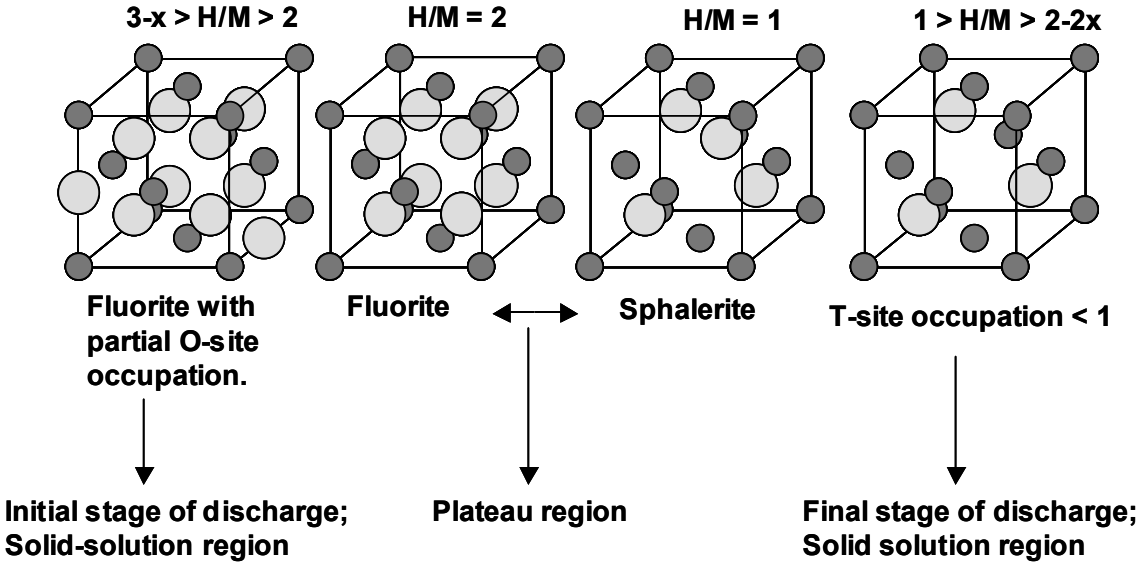

Fig. 48 : Visualization of most likely discharge mechanism, based upon the information presented until now.

It is interesting to look at how the hydriding behavior of the MgSc alloys presented in this study compares to previous investigations on Mg-RE systems. Isidorsson *et al.*[103] investigated

how the optical properties of MgLa thin layers changed upon loading them with hydrogen. A so-called 'black state' was observed which was attributed to the coexistence of nanocrystalline Mg and MgH_2. This implied that these films disproportionated upon hydriding and although structure determinations are always difficult to carry out on thin film samples because of very small grain size and preferential orientation, XRD on fully hydrogenated $La_{0.6}Mg_{0.4}$ confirmed the coexistence of LaH_3 and MgH_2. Giebels *et al*. also performed measurements on MgSc thin films[104]. Based on the observation of a black state, the same as in MgLa, and the fact that the enthalpy change calculated from the GITT curves in [11] is almost the same as the formation enthalpy of MgH_2, it was concluded that these materials also segregated into MgH_2 and ScH_3. Any conclusive evidence for the presence of rutile-structured MgH_2 in the fully charged material, as in the MgLa case[103] was, however, not found. Since the MgSc bulk materials in this form single-phase hydrides and the electrochemical responses of thin films and bulk materials are so similar, there seems to be no reason to assume that MgSc thin films disproportionate into the binary hydrides based on the data presented so far.

Bulk studies on other Mg-RE alloys give a similar picture. Mg_2La and Mg_2Ce, which are both cubic Laves phases were shown by Gingl *et al.* to form slightly tetragonally distorted, single-phase hydrides at room temperature and 100 bars of hydrogen pressure[105]. A composition of Mg_2LnH_7 was reached, which corresponds to 2 H/Mg and 3 H/La,Ce, the same as for the MgSc materials discussed here. For MgY it was shown by Goto *et al.* that cubic $MgY_2H_{7.8}$ can be formed at 1073 K and 3 GPa hydrogen pressure. The resulting compound was found to retain its fcc structure upon dehydrogenation to $MgY_2H_{4.9}$ at 600-800 K and atmospheric pressures[106], analogous to the Mg-Sc material presented here.

It may seem rather amazing that compounds that are not isostructural, ScH_3 is hexagonal[107], ScH_2 is cubic and MgH_2 is rutile, have such an extensive solid solubility region, up to at least 80 at%. However, both ScH_3 and MgH_2 have a cubic high-pressure modification that is stable above 1 GPa, 350 ^oC[108] and 3.8 GPa[109], respectively, which makes it a lot less surprising that the a cubic modification is formed upon making a mixed, ternary hydride.

As was already stated, and could also be seen in Fig. 36, there is a limit to the solid solubility of ScH_2 and MgH_2. The sudden drop in the discharge capacity for $x > 0.8$ indicates that there is a change in the crystal structure of the hydride beyond this composition. Pure MgH_2 has a rutile-structure, which is known to exhibit very poor hydrogen sorption kinetics. A study by Vigeholm *et al*. showed that hydriding of pure Mg metal ceases when there no longer is a metal/hydride interface present at the surface[110]. This implies that hydrogen diffusion *through* rutile-structured MgH_2 is almost infinitely slow and acts as a blocking layer. Because of the short diffusion distances of only 0.2 μm in the thin films, compared to 20 μm for the bulk materials, it is still possible to extract a considerable amount of hydrogen at low current density, even for pure Mg films. For the bulk materials, however, the discharge capacity almost drops to 0.

Although it has long been known that MgH_2 effectively blocks hydrogen diffusion, a reason for this is almost never given. However, it can easily be understood by considering the distances between the H-atoms and the empty interstitial sites in the crystal lattice. In Fig. 47 an Octahedral site has also been indicated for the rutile structure. The distance between the indicated O-site and the neighboring H-atom is only 1.27 Å, which is much less than the 2.1 Å prescribed by the Westlake criterion. This shows that during hydrogenation, diffusion *through* rutile structured MgH_2 can only take place via vacancies on the hydrogen sublattice, which is a very slow process. Even though the T-O distance in the observed cubic structures is also less than 2.1 Å, it has been shown that simultaneous occupation of T and O-sites is possible. This means that the, mostly empty, octahedral sites provide a very rapid diffusion path for the hydrogen atoms enabling much faster diffusion compared to the rutile structure.

4.5 Conclusions

The electrochemical and structural properties of MgSc alloys were studied, both in thin film and bulk form. The electrochemical properties of MgSc thin films and bulk materials are very similar. Both materials show similar trends in storage capacity and the shape of the discharge curves with composition. The maximum capacity reached for a composition with 80 at.% Mg was 1740 mAh/g for the thin films, corresponding to 6.5 wt.% H and 1495 mAh/g (5.6 wt.%) for the bulk materials, using a low discharge current. The rate capability of the thin films is much better than that of the bulk materials due to shorter diffusion lengths and complete coverage by the Pd-layer in the thin film case and the alloying of the Pd catalyst in the bulk materials. The plateau pressure is not a function of composition and almost equal to the equilibrium pressure of pure MgH_2.

Diffraction data obtained from the bulk system showed that the fully charged hydride is a single-phase fcc-structured hydride and segregation into MgH_2 and ScH_3, to an extent detectable with diffraction techniques, has not taken place. Two co-existing fcc-structures were found in the plateau region. The hydrogen-rich phase is slightly expanded compared to pure ScH_2, whereas the hydrogen-poor phase has a smaller volume than ScH_2, all in agreement with Vegards' law. The thin films showed a drop in both rate capability and, to a lesser extent, storage capacity at the same composition as the bulk systems, so despite the lack of accurate structural data it is reasonable to assume that the crystal structure of the thin films is the same as that of the bulk materials.

Impedance spectroscopy showed that the charge transfer kinetics of the thin films are completely dominated by the Pd topcoat and are about a factor 5 faster than in the bulk system. This shows that the alloying of Pd with Mg and Sc has a large influence on its catalytic power. A ball-milled bulk alloy catalyzed with pure Pd showed the same dependencies of the exchange current density on the state-of-charge and potential as the thin films. Overall, the thin films can be regarded as a suitable model system for bulk alloys. Both the electrochemical responses and the trends in storage capacity and kinetics with composition and hydrogen content are quite similar, showing that thin films can provide a better insight in the electrochemical processes taking place in bulk systems.

5

Fundamental properties of Mg_xSc_{1-x} hydrides: Neutron diffraction, Nuclear Magnetic Resonance and Density Functional Theory

Abstract

A Neutron Diffraction study on $Mg_{0.65}Sc_{0.35}$ is presented as a function of hydrogen content. Additional information regarding the hydrogen site occupancies is extracted from the neutron diffraction data. Partial occupation of octahedral sites, besides tetrahedral ones, is found for the fully loaded deuteride and the concentration boundaries of the 2-phase region were found to be ~1.6 and 0.85 D/M. The material was also studied *in-situ* during electrochemical loading. Deviating behaviour was found in the first hydrogen loading compared to the first unloading. During charging, a transformation from a bcc to a single fcc structure was found, as opposed to a co-existence of 2 fcc phases during discharge. The materials were also studied with Nuclear Magnetic Resonance (NMR). Using data on relaxation times, greatly improved hydrogen motion rates by 9 orders of magnitude were found for $Mg_{0.65}Sc_{0.35}H_{2.20}$ compared to MgH_2. NMR spectroscopy showed three distinct hydrogen sites with hydrogen rapidly exchanging between them. Furthermore, indications for deviations from a statistical distribution of the metal atoms were found, as the fraction with pure Mg co-ordination was found to be much larger than expected. DFT calculations were performed on $Mg_{1-x}Sc_xH_2$, to elucidate the structure preference of the hydrided material as a function of Mg/Sc ratio. The fluorite/rutile transition point was found at exactly the same composition, ~80 at.% Mg, as that inferred from electrochemical measurements. The site preference of the hydrogen atoms as a function of H/M ratio was also studied. At H/M = 1, the sphalerite arrangement of the H atoms turned out to be the least stable configuration, contrary to what is generally found in ionic solids. Instead, of maximizing the H-H distance, the hydrogen atoms tended to cluster together as close as possible.

5.1 Introduction

This chapter presents a more fundamental study on the material properties of the Mg_xSc_{1-x} alloys and their hydrides (deuterides). The X-Ray diffraction results presented in the previous chapter do not provide a complete picture of the crystallographic properties of the hydride because the positions of the hydrogen atoms can not be resolved. Because the heavier hydrogen isotope, deuterium, has a high scattering power for neutrons, neutron powder diffraction on a deuterated alloy can be used to determine which interstitial sites are occupied by hydrogen. This has been investigated in two ways, by fully loading a $Mg_{0.65}Sc_{0.35}$ alloy with deuterium at high pressure and temperature followed by stepwise desorption at 300°C and during *in-situ* deuterium loading/unloading in an electrochemical setup at room temperature. The phase evolution as a function of deuterium content is investigated and the results at elevated temperature and room temperature are compared.

Nuclear magnetic resonance has been used to study both the chemical environment of the deuterium atoms on nearest-neighbor level and the dynamics of hydrogen motion through the crystal lattice. Hydrogen diffusion rates can be determined by measuring the relaxation times as a function of temperature as was described in chapter 2. In this way, the vastly improved diffusion rates in the fluorite structure of the ternary hydride as compared to rutile MgH_2 have been quantified. NMR spectroscopy further supplements the information obtained from X-ray and neutron diffraction as short-range deviations from the average long-range order measured by diffraction can be detected. A significant deviation from a statistical distribution of the metal atoms is indeed found.

The rutile-to-fluorite transition point as was found from the electrochemical measurements presented in chapter 4 is exactly reproduced by Density Functional Theory calculations. At 75 at.% Mg, the equilibrium structure starts to deviate from a pure fluorite structure as the hydrogen atoms shift away from the tetrahedral positions. At lower hydrogen content, the hydrogen atoms are found to cluster together, which is another short-range deviation from the average long-range order that is not detected by diffraction. In general, it will be shown that only a combination of a number of all aforementioned characterization techniques can provide a complete picture of the material's behavior.

5.2 Experimental

5.2.1 Neutron Diffraction

Deuteration of a $Mg_{0.65}Sc_{0.35}Pd_{0.024}$ alloy was done in the same way as the gas-phase hydrogenation described in section 4.2.1.2. Stepwise desorption of this material was preformed at 300°C using the Sievert's method. Static Neutron Diffraction measurements were carried out at the Laboratoire Léon Brouillin in Saclay on the 3T2 instrument in the range $6^o<2\theta<120^o$, with a step size of 0.05^o. The wavelength used was 1.225 Å. All patterns were refined using the Rietveld method in the FULLPROF program.

In-situ measurements under dynamic conditions were done at the Institut Laue Langevin in Grenoble on the D1B instrument. The alloy powder was prepared by ball-milling as described in section 4.2.1.2. The particle fraction smaller than 60 microns was used to prepare the electrodes. The intermetallic powder was mixed with carbon black and PTFE in the weight ratio 90:5:5. This mixture was spread out in sheets of 1.5 mm thick and pressed onto 5 × 3.14 cm nickel grids, which play the role of current collector, at up to 12 tons of force. These electrode plates were then rolled up on themselves to form a cylinder of about 50 mm height and 10 mm diameter. Each working electrode was introduced in a specially designed silica cell (see Fig. 49). The electrode is sandwiched between inner (Ø 8 mm) and outer (Ø 12 mm)

counter-electrode cylinders made of nickel grid rolled on themselves, with silica sheaths as separators on each side of the working electrode. The electrodes were immersed in 6M NaOD electrolyte and pumped under primary vacuum in order to fully impregnate the working electrode with the liquid and to remove any gaseous species trapped in the material. The potential was monitored against a solid state $Cd/Cd(OH)_2$ reference electrode.

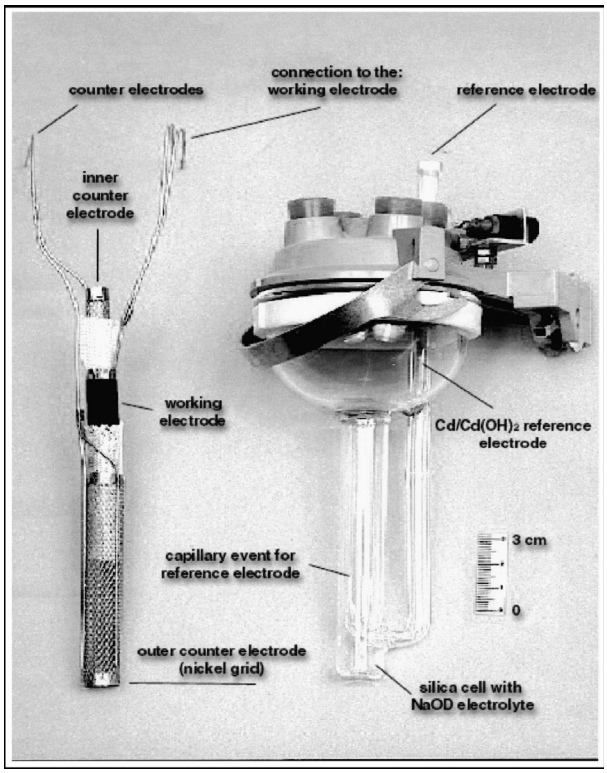

Fig. 49: Special electrochemical cell used for the in-situ neutron diffraction experiments. The electrode assembly consisting of 2 cylindrical Ni mesh counter electrodes and the working electrode separated by silica sheats is depicted on the left.

5.2.2 NMR relaxometry

Relaxation times were measured at Washington University St. Louis with a homebuilt pulsed, superheterodyne NMR spectrometer with four transmitter phases and quadrature-detected receiver. The transmitted power to the probe was about 80W peak. Pulse sequences were generated with a combination of TTL hardware and a Pulse Blaster card. T_1 was determined with inversion-recovery and repeated-saturation-recovery schemes. T_2 was measured from the decays of free induction signals (T_2^*), two-pulse (Hahn) echoes, and CPMG echo trains. Continuous spin-locking with $\gamma B_1/2\pi$ = 50 kHz was used to measure $T_{1\rho}$. The relaxation of the dipolar-ordered state (T_{1D}, essentially $T_{1\rho}$ in zero amplitude field) was measured using a phase-alternated version of the Jeener–Broekaert three-pulse method[111]. All measurements were made at 21.25 and 53.14 MHz at field strengths of 0.5 and 1.25 T, respectively.

5.2.3 NMR spectroscopy

Spectra were recorded on a Bruker DMX500 NMR spectrometer operating at ^1H and ^2H NMR frequencies of 500 and 77 MHz with TMS as an external reference compound. For ^2H spectra,

the natural abundance of deuterium in TMS was used for obtaining the reference frequency. Spectra were recorded using a Hahn-Echo sequence at a Magic Angle Spinning frequency of 8 kHz. Echo times were varied between 0.25 to 4 ms. For TRAPDOR measurements, ^{45}Sc was irradiated for half the echo time.

Two dimensional exchange ^2H NMR spectra were recorded with the p_1-t_1-p_1-t_{mix}-p_1-t_2 pulse sequence with a 90º pulse duration p_1 of 5 μs. Only interested in chemical exchange between NMR-distinct deuteron states, rotor-synchronous sampling was used in both time dimensions. (Dwell time equal to (multiples of) rotation time T_r = 125 μs.) As a result, the sidebands fold back onto the centerband in both frequency domains and the relative loss of diagonal intensity and increase of off-diagonal intensity in the resulting spectrum is only correlated with chemical exchange.

5.2.4 Density Functional Theory

The *ab-initio* calculations are based on Density Functional Theory. All calculations were performed using the Vienna *Ab-Initio* Simulation Package (VASP). The Kohn-Sham equations are solved using a basis of Projector Augmented Wave-functions with a plane-wave energy cut-off of 300 eV[112], using pseudopotentials to describe the core electrons. The Perdew-Wang '91 generalized gradient approximation was used for the electron exchange and correlation potential[23]. A total of 13x13x13 k-points was used to model the Brouillin zone for all investigated structures[113]. Beyond this number of k-points, the influence of the distribution of the k-points on the calculated total energies became less than 0.02% and therefore this number of k-points was deemed sufficiently large. All (hydride) structures were studied in terms of total energy minimization within symmetry restrictions, where only the lattice parameters and unit cell volume were allowed to change. When imaginary frequencies* were found after structure optimization within symmetry constraints, the symmetry condition was discarded and the structure re-optimized while allowing all atomic positions to change in every direction.

5.3 Results

5.3.1 Neutron Diffraction

5.3.1.1 Solid-gas desorption

A basic introduction to structure determination by diffraction methods was already given in Chapter 2 for electromagnetic (X-Ray) radiation. X-Rays are scattered by electrons, which means the diffracted intensity scales directly with atomic number (mass). This immediately pinpoints a practical limitation of X-Ray diffraction: hydrogen, with only one electron, will have almost zero diffraction intensity. It is therefore impossible to determine hydrogen positions by X-Ray Diffraction.

However, elementary particles, such as electrons and neutrons, also have wave-like character, expressed as the deBroglie wavelength $\lambda = \frac{h}{p}$, where p is the momentum of the particle. Contrary to X-rays, neutrons are scattered by atomic nuclei. The scattering strength

* A lowering of the total energy by displacing an atom in a certain direction can be viewed as a negative force-constant k and the resulting frequency $\omega = \sqrt{\frac{k}{m}}$ will therefore be imaginary.

depends strongly on the precise configuration of the protons and neutrons inside the nucleus, which makes it possible to distinguish between elements which are very close together in the periodic table and even between isotopes of the same element, as they can have vastly different neutron scattering strengths. The opposite is also true, elements readily distinguished in XRD because of a large difference in atomic mass may have quite similar neutron scattering strength.

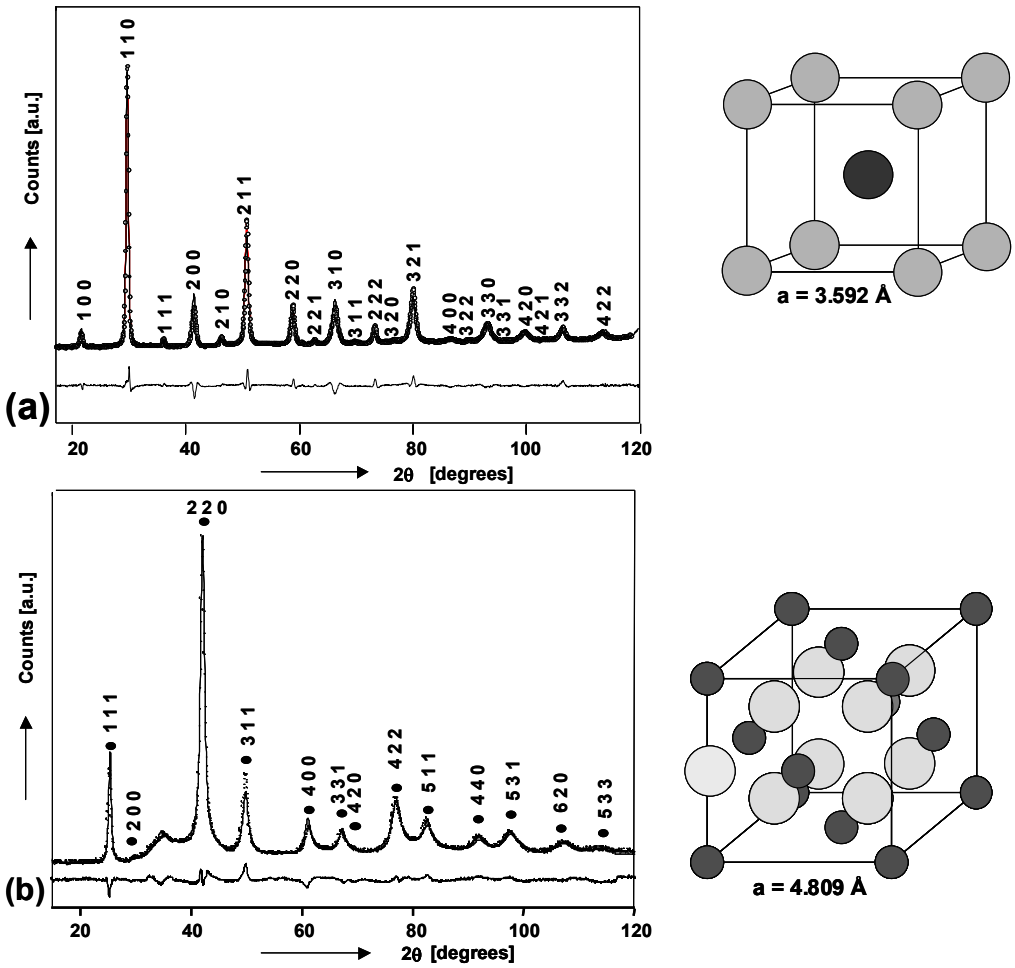

Fig. 50: Neutron diffraction patterns of $Mg_{0.65}Sc_{0.35}$ starting alloy (a) and fully deuterated $Mg_{0.65}Sc_{0.35}Pd_{0.024}D_{2.25}$ (b) The unit cells of each structure are shown on the right.

First an explanation will be given about the differences between Fig. 50 and the X-Ray diffraction patterns in Fig. 44 and Fig. 46 by elaborating the structure factor calculation for a bcc and a fluorite structure. Subsequently, the neutron diffraction results as a function of D/M ratio will be discussed further. From the equilibrium phase diagram of the MgSc system (see Fig. 32), it is known that $Mg_{0.65}Sc_{0.35}$ forms a single phase body-centered cubic (bcc) solid solution. From the positions of the diffraction lines in Fig. 50, it can be derived that the structure of the formed alloy is indeed cubic with a lattice constant of about 3.59 Å. However, as can be seen in Fig. 50, reflections for which the sum of the indices is odd are visible, which means the structure is not really bcc (see Eq. *(2.27)*), but primitive cubic. This indicates that both sites are preferentially occupied by either Mg or Sc, which can be taken into account as follows:

$$F_{hkl} = \begin{cases} N^{Mg}_{(0,0,0)} * b_{Mg} + N^{Sc}_{(0,0,0)} * b_{Sc} \text{ for } h+k+l = even \\ N^{Mg}_{(1/2,1/2,1/2)} * b_{Mg} - N^{Sc}_{(1/2,1/2,1/2)} b_{Sc} \text{ for } h+k+l = odd \end{cases} \quad (5.1)$$

where $N^{M}_{(u,v,w)}$ are the fractional occupancies of Mg and Sc on both atomic positions and the *neutron scattering length b,* rather than the form factor *f* is used to designate the scattering power of each element. The fractional occupancies of Mg and Sc on both metal sites are now adjusted to values for which the agreement between the observed and expected diffraction patterns (dotted and solid lines in Fig. 50, respectively) is as small as possible and the residual factor R given by:

$$R = \frac{\sum \left| |F_{obs}| - |F_{calc}| \right|}{\sum F_{obs}} \quad (5.2)$$

is minimized. The difference between the calculated diffraction pattern and the observed one is given by the lower line in Fig. 50. The agreement between the fitted and observed pattern is quite good. The results are summarized in Table 3:

Table 3: Structural parameters obtained from refinement of the neutron diffraction pattern of $Mg_{0.65}Sc_{0.35}$

Atom	position	N
Mg	(0, 0, 0)	0.916
Sc		0.084
Mg	(½, ½, ½)	0.384
Sc		0.616
a = 3.5921(2) Å; R_{Bragg} = 6.7%		

For the fluorite structure of the hydrided material, the structure factor calculation is elaborated once more, because it will clarify the differences between the neutron diffraction pattern in Fig. 50 and the X-Ray diffraction pattern in Fig. 44. The unit cell of a hydrided (deuterated) material is depicted in Fig. 50. The unit cell contains 4 metal atoms, 8 tetrahedral interstices and 4 octahedral interstices. All tetrahedral sites are indicated in the figure and all lie within the unit cell. The octahedral sites, on the other hand, are located on the cube´s vertices. As each of the 12 vertices is shared by 4 adjacent unit cells, these sites account for 12/4 = 3 octahedral positions. There is one more octahedral site exactly in the middle of the unit cell. The atomic co-ordinates are given by:

Tetrahedral sites:

$$(\tfrac{1}{4},\tfrac{1}{4},\tfrac{1}{4})\,(\tfrac{1}{4},\tfrac{1}{4},\tfrac{3}{4})\,(\tfrac{1}{4},\tfrac{3}{4},\tfrac{1}{4})\,(\tfrac{3}{4},\tfrac{1}{4},\tfrac{1}{4})$$
$$(\tfrac{3}{4},\tfrac{3}{4},\tfrac{1}{4})\,(\tfrac{3}{4},\tfrac{1}{4},\tfrac{3}{4})\,(\tfrac{1}{4},\tfrac{3}{4},\tfrac{3}{4})\,(\tfrac{3}{4},\tfrac{3}{4},\tfrac{3}{4})$$

Octahedral sites:

$$(\tfrac{1}{2},0,0)\,(0,\tfrac{1}{2},0)\,(0,0,\tfrac{1}{2})\,(\tfrac{1}{2},\tfrac{1}{2},\tfrac{1}{2})$$

The calculation of the structure factor is simplified by the fact that the fluorite unit-cell is centro-symmetric, which means the sine terms in Eq. *(2.26)* are equal to, or add up to 0. This is not immediately obvious for the T-sites, but can be easily checked. Substituting all the atomic coordinates into the structure factor equation gives the following result for the first 6 visible reflections:

$$\begin{aligned}
F_{111} &= 4b_{Metal} + N^H_{tetr} b_H [0 + ... + 0] + N^H_{oct} b_H [-1 .. -1] = 4b_{Metal} - 4N^H_{oct} b_H \\
F_{200} &= 4b_{Metal} + N^H_{tetr} b_H [-1 ..... -1] + N^H_{oct} b_H [1 + .. + 1] = 4b_{Metal} - 8N^H_{tetr} b_H + 4N^H_{oct} b_H \\
F_{220} &= 4b_{Metal} + N^H_{tetr} b_H [1 + ... + 1] + N^H_{oct} b_H [1 + .. + 1] = 4b_{Metal} + 8N^H_{tetr} b_H + 4N^H_{oct} b_H \\
F_{311} &= 4b_{Metal} + N^H_{tetr} b_H [0 + ... + 0] + N^H_{oct} b_H [-1 .. -1] = 4b_{Metal} - 4N^H_{oct} b_H \\
F_{222} &= 4b_{Metal} + N^H_{tetr} b_H [-1 ..... -1] + N^H_{oct} b_H [1 + .. + 1] = 4b_{Metal} - 8N^H_{tetr} b_H + 4N^H_{oct} b_H \\
F_{400} &= 4b_{Metal} + N^H_{tetr} b_H [1 + ... + 1] + N^H_{oct} b_H [1 + .. + 1] = 4b_{Metal} + 8N^H_{tetr} b_H + 4N^H_{oct} b_H
\end{aligned} \qquad (5.3)$$

where N^H_{tetr} and N^H_{oct} are the fractional hydrogen occupancies of the tetrahedral and octahedral sites, respectively. The neutron scattering length b of deuterium atoms is 6.674, whereas b_{Mg} and b_{Sc} are 5.371 and 12.1 respectively[114], so deuterium contributes considerably to the diffracted intensities, contrary to X-ray diffraction. From Eq. *(5.3)* it becomes clear that:

- Occupation of the octahedral sites contributes negatively to reflections with odd-numbered indices and contributes positively to all reflections with even-numbered indices.
- Occupation of tetrahedral sites contributes negatively to reflections with even-numbered indices where h+k+l is divisible by 2, not by 4.
- For h+k+l divisible by 4, all sites contribute positively.

The differences between the X-ray and Neutron diffraction patterns can now be qualitatively understood. The T-sites contribute negatively to reflections for which h+k+l is not divisible by 4 and as a consequence the (200), (222) and (420) are almost invisible in the neutron diffraction pattern, while their intensity in the X-ray pattern is considerable. The structure factors for which h+k+l = 4n are a summation of all individual scattering strengths of the atoms and are therefore much stronger in the neutron diffraction pattern as compared to the X-Ray diffraction pattern. This is most clearly illustrated by the (220) reflection, which is the strongest by far in the neutron diffraction pattern, contrary to the XRD pattern, where the (111) has the highest intensity.

The results of the refinement procedure on the fully deuterated material are summarized in Table 4:

Table 4: Results of the refinement of the diffraction pattern of the fully deuterated $Mg_{0.65}Sc_{0.35}$ alloy.

$Mg_{0.65}Sc_{0.35}Pd_{0.024}D_x$	Space Group: Fm3m	
Atom	position	N
Mg	(0, 0, 0)	0.65 (fixed)
Sc		0.35 (fixed)
D (O)	(¼, ¼, ¼)	0.243
D (T)	(½, ½, ½)	0.977
	a = 4.8087(7)	D/M ratio
	R_{Bragg} = 6.6%	2.197

The best fit to the observed diffraction pattern was obtained assuming 97.7% occupancy for the T-sites and 24.3% for the O-sites, in good agreement with the full T-site and partial O-site occupation in the fully charged state that has been assumed throughout the previous chapters. The resulting total D/M ratio is ~2.2 D/M, which is slightly less than the 2.35 that was theoretically expected and was also achieved electrochemically.

Note that the occupancy factors of Mg and Sc on the metal sites have been fixed and that no distinction is made between sites occupied by Mg and Sc and by Mg only. Indication for such ordering is no longer found in the diffraction pattern of the deuteride. However, ordering may be expected if the metal lattice does not undergo any major reorganization upon deuteration according to the scheme depicted in Fig. 51:

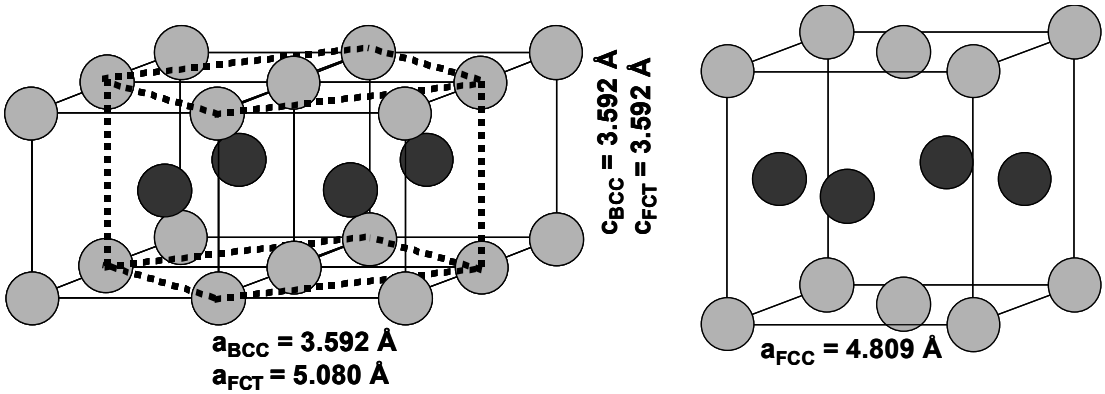

Fig. 51: graphical representation of the hydriding (deuteration) process showing only the metal sublattice. 4 bcc unit cells are shown on the left, where an alternative representation as a Face-Centered-Tetragonal cell is indicated by the dashed lines. Upon hydrogen l oading, the a-axis of the fct cell shrinks and the c-axis expands resulting in an fcc lattice (right).

On the left, 4 unit cells of the original CsCl-type structure are depicted. It is shown by the dashed lines that this structure can also be viewed as a face-centered tetragonal (fct) cell with $a = \sqrt{2} * 3.592 = 5.080$ Å and the body-centered atoms now in the middle of the side faces. Upon deuteration, the c axis expands to 4.809 Å and the a-axis effectively shrinks from 5.080 to 4.809 Å. The resulting metal sublattice is depicted on the right-hand side. This ordering of the structure could be evidenced by the appearance of additional reflections (*e.g.* a (001) peak) besides those of a pure fcc phase in the neutron diffraction pattern, but none are present. It is therefore possible that the ordering is destroyed upon deuteration. It is evident from Fig. 51 that the ordering would be present in only one direction, which makes it very doubtful whether any effect can be detected in a randomly oriented polycrystalline powder sample.

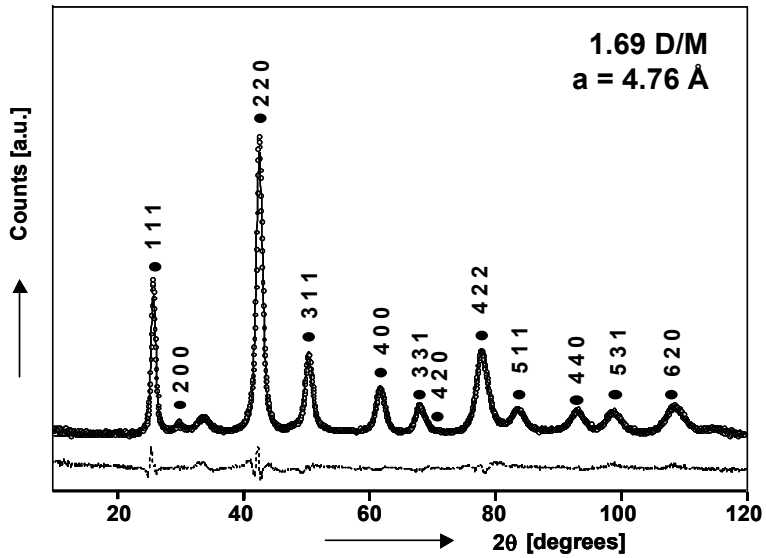

Fig. 52 : Neutron diffraction pattern of $Mg_{0.65}Sc_{0.35}Pd_{0.024}D_x$, x=1.69

Starting from the fully charged deuteride, the sample was first desorbed at 300°C and 0.65 bars of pressure down to a deuterium content of 1.69 D/M. The diffraction measurement was carried out at room-temperature. As can be seen in Fig. 52, the fcc structure is preserved, but the lowering of the D-content causes a shrinkage of the lattice parameter down to 4.7583[3] Å (standard deviation of the last decimal between brackets). The deuterium concentration that was derived from the refinement was somewhat lower with 1.55±0.02 D/M, almost exclusively in the tetrahedral sites. The accuracy of solid-gas measurements is about 5-6% (~0.10 D/M), so the agreement with the neutron refinement is reasonable. The fact that the octahedral sites are no longer occupied and the T-sites only partially is most clearly expressed in the diffraction pattern by the sharp decrease of the relative intensity of the (220) reflection with respect to *e.g.* the (111) and (311) reflections, as could be expected based on Eq. *(5.3)* .

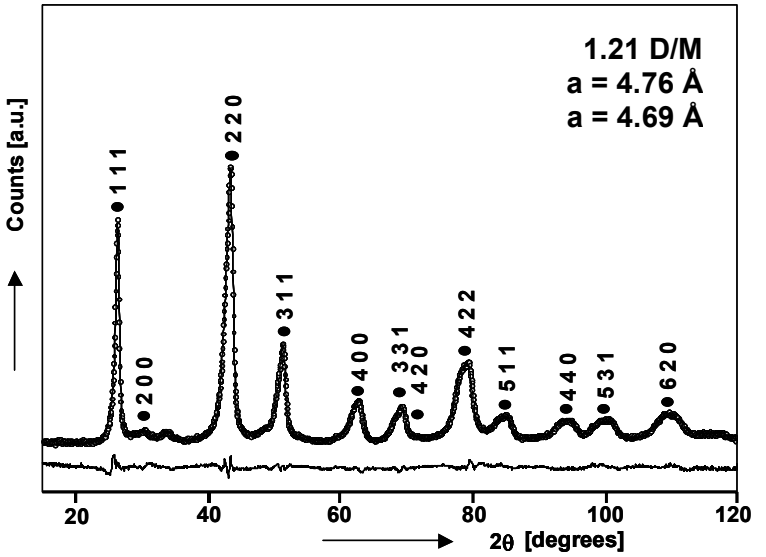

Fig. 53 : Neutron diffraction pattern of $Mg_{0.65}Sc_{0.35}Pd_{0.024}D_x$, x=1.21

Further desorption was carried out at 300°C and 0.005 MPa down to a deuterium content of 1.21 D/M. According to electrochemical (GITT) measurements, the material should now be in the two-phase region. As can be seen in Fig. 53, this is indeed true. Especially at higher 2θ values, a splitting of the diffraction peaks is evident, indicating that the material now consists

of 2 phases with a strongly similar structure. Indeed, the pattern could best be fitted using 2 fcc phases with lattice constants of 4.7598(5) and 4.6936(3) Å. The fractional occupancies of the tetrahedral sites are 1.55 D/M and 0.85 D/M for the phase with the larger and the smaller lattice constant respectively. From the relative amount of each phase, 42 and 58 wt.% respectively, a deuterium content of 1.25 D/M is obtained, which is in good agreement with the value of 1.21 D/M from the volumetric measurement.

5.3.2.2 In-situ electrochemical cycling

A cylindrical electrode was constructed from a $Mg_{65}Sc_{0.35}$ alloy ball-milled with 5 at.% of Pd and introduced into the special electrochemical cell shown in Fig. 49. The neutron diffraction pattern of the dry electrode is shown in Fig. 54.

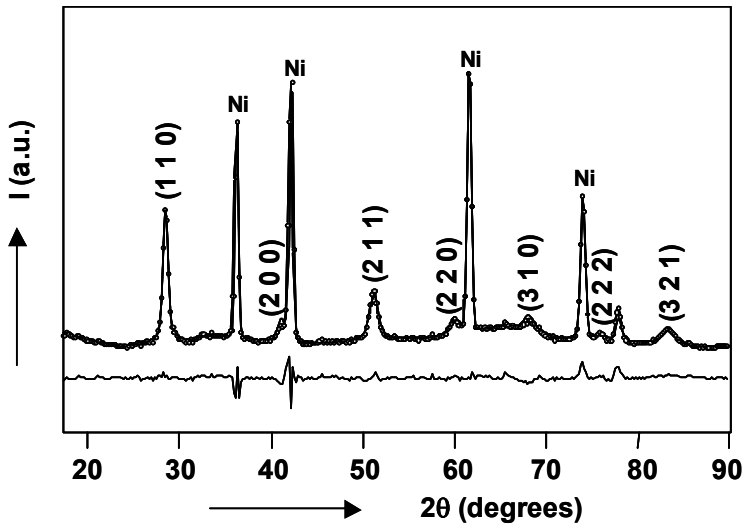

Fig. 54: Neutron diffraction pattern of $Mg_{0.65}Sc_{0.35}$ electrode in the dry state; before addition of the electrolyte. Reflections of the MgSc phase are indexed, reflections from the Ni mesh counter electrodes are also indicated.

Contrary to the starting material for the solid-gas experiment, see Fig. 50, no evidence for ordering of the Mg and Sc is found in this case. Apparently, ball-milling treatment with Pd destroys the ordering on the MgSc lattice. The reflections belonging to a pure bcc lattice are, however, clearly visible.

Subsequently, the electrode was charged at 150 mA/g. A 2-D plot of the diffraction patterns, as a function of angle and time, during the first charge of the electrode is shown in Fig. 55. After ~2 h, an fcc phase is first detected and after 6-7 h, the peaks of the bcc phase have completely disapeared. Remarkably enough, only 1 fcc phase is detected during charge, whereas solid-gas desorption showed a two-phase co-existence region of 2 fcc phases (see Fig. 53), although it has to be noted that the first *ab*sorption was not investigated in the soid-gas experiments. The octahedral sites are not found to be significantly occupied, but the T-site occupation is 1.24 +/- 0.31 D/M (note the large standard deviation!), when the fcc phase is first detected and increases gradually upon further charging.

After 9h 30 mins, the charging current was switched off, which is visible as an increase in the background in Fig. 55. During charging, 9.5*150 = 1425 mAh/g has been inserted into the material, which corresponds to 1.96 D/M. The diffraction pattern of the fully charged electrode is shown in Fig. 56.

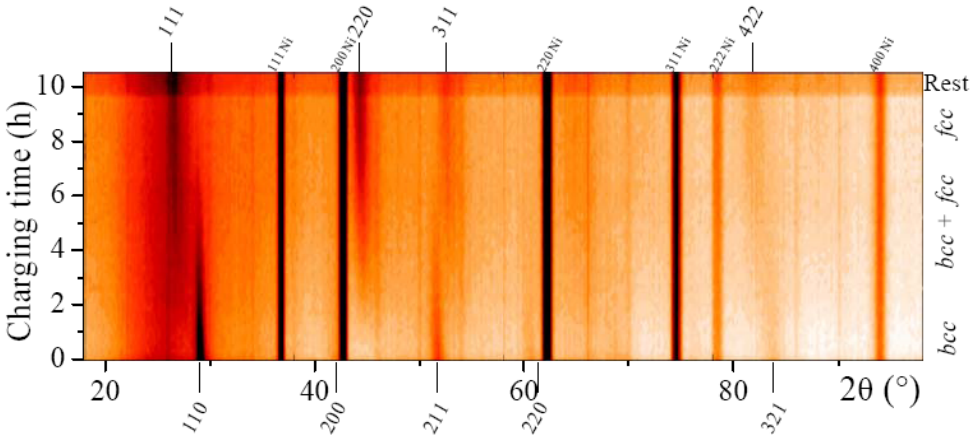

Fig. 55: 2-Dimensional plot of the neutron diffraction patterns obtained during charging of the electrode.

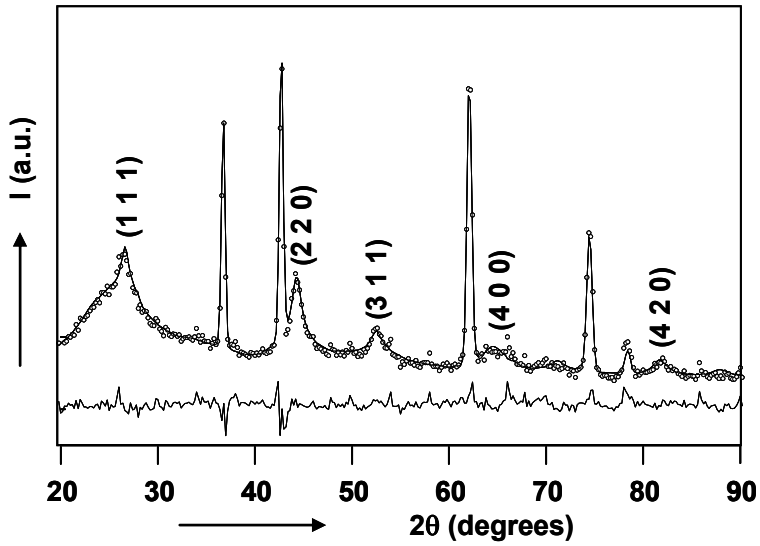

Fig. 56: Neutron diffraction pattern of fully charged $Mg_{0.65}Sc_{0.35}$ electrode collected during rest period.

Compared to the dry electrode in Fig. 54, there is a heavy background at lower angles arising from the heavy water. The fully charged electrode consists of a single fcc phase with a lattice constant of 4.81 Å. In principle, the deuterium content can also be refined from the intensities of the reflections, but the overlap with the Ni peaks and the large 'bump' from the heavy water make the determination of the D-content from the diffraction pattern a lot more difficult. Only the T-sites are found to be occupied and the deuterium content determined from the refinement is 1.50 +/- 0.12 D/M. The difference between the value obtained from the refinement and the total amount of charge inserted into the material is also rather large. However, it has to be moted that the reaction at the Ni-electrodes is simply the oxygen-evolution reaction:

$$4OH^- \rightarrow 2H_2O + O_2 + 4e^- \qquad (5.4)$$

and that the formed oxygen gas is partly recombined at the working electrode. The oxygen reduction reaction is simply the reverse of reaction *(5.4)* and consumes electrons, the same as the hydrogen storage reaction, leading to the observed discrepancy between the amount of current passed through the electrode and the amount of hydrogen derived from structure refinement.

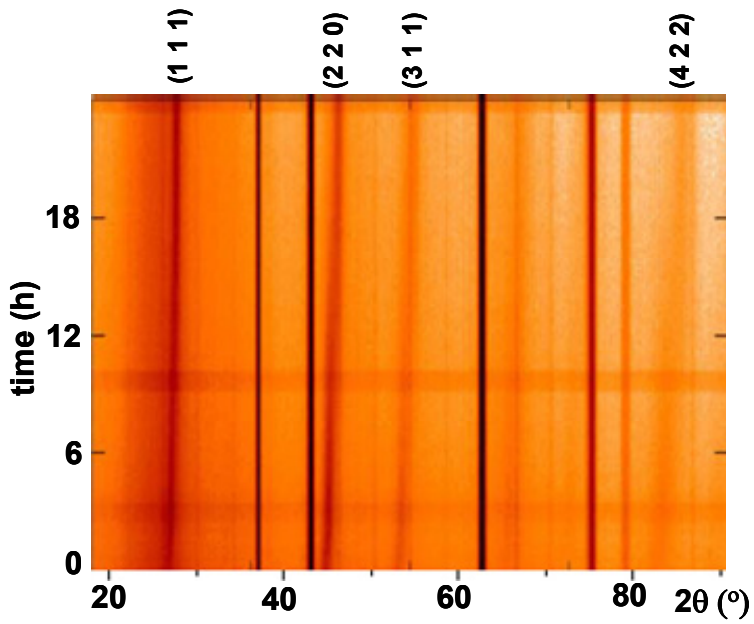

Fig. 57: 2-D plot of discharge of $Mg_{0.65}Sc_{0.35}$ electrode at 75 mA/g. An increase in the background signal during rest is clearly seen as darker stripes in the 2-D map.

The 2-D plot of the ND patterns during discharge with 75 mA/g is shown in. From the 2-D map, it can clearly be seen that the peak positions shift towards higher angles during discharge, indicating a decrease of the lattice constant. The occurrence of a two-phase region is not immediately evident from Fig. 57, but after ~9 h, a broadening of the diffraction lines is observed. A close-up of the (220) reflection in the pattern collected during the rest period after 9 h 15 min of discharging is shown in the inset in Fig. 58. The material now indeed consists of 2 fcc phases with different lattice constants:

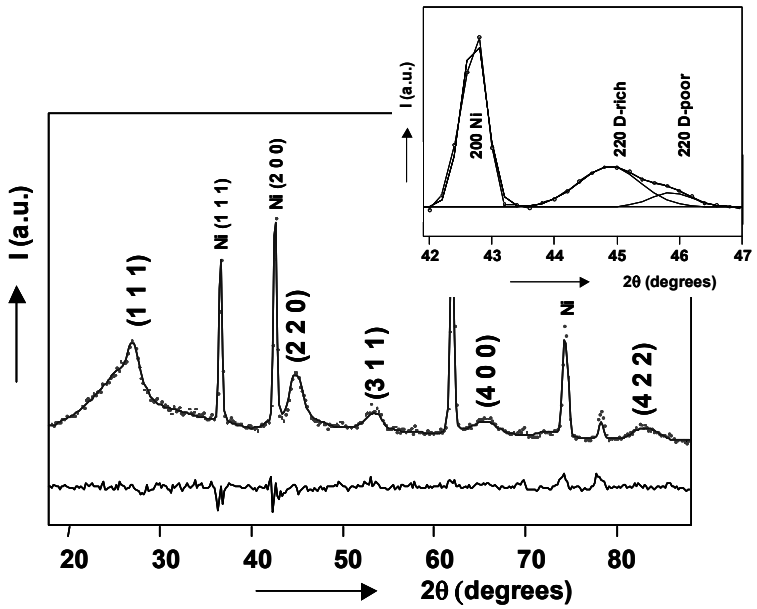

Fig. 58: Neutron Diffraction pattern of $Mg_{0.65}Sc_{0.35}Pd_5$ electrode in the two-phase region during discharge. A close-up of the (2 2 0) reflection is also shown.

The best fit to the observed pattern was obtained for a = 4.758 Å for the D-rich phase and 4.672 Å for the D-poor phase, with T-site occupancies of 1.55 D/M for the D-rich phase and 0.85 D/M for the D-poor phase, the same as in the solid-gas experiments. Note that the

discrete volume expansion, at 5.6%, is somewhat larger than in the solid-gas desorption, but still smaller than for the hydride. From the refinement, the phase amounts were determined as 70 wt.% of the D-rich phase and 30 wt.% of the D-poor phase, giving a D/M ratio of 1.34.

The amount of extracted charge, 9.25*75 = 694 mAh/g, corresponds to 0.94 D/M, which is considerably more than the difference in D/M derived from the diffraction patterns in Fig. 56 and Fig. 58, respectively. However, during discharge, deuterium gas is formed at the Ni counter-electrodes which can then be recombined with OD^- ions to from water at the working electrode:

$$D_2(g) + 2OD^- \rightarrow 2D_2O + 2e^- \qquad (5.5)$$

leading to a discrepancy between the measured amount of extracted charge and the actual amount of deuterium that has been removed from the material.

5.3.3 Nuclear Magnetic Resonance

In this section, results on $Mg_{0.65}Sc_{0.35}$ hydrides and deuterides obtained by Nuclear Magnetic Resonance (NMR) will be discussed. NMR is a technique that studies the behavior of atomic nuclei inside a magnetic field, which is directly influenced by the local electronic environment of the atom. As it probes the local environment around an atom down to the nearest-neighbor level, NMR provides structural information on a much smaller length scale compared to diffraction, yielding additional information on the properties of the hydride. Here, measurements of the relaxation times as described in section 2.5 are presented and correlated to diffusive hydrogen motion in MgH_2, ScH_2 and the ternary $Mg_{0.65}Sc_{0.35}H_{2.20}$. Furthermore, NMR spectroscopy is used to obtain more information on the local structure around the hydrogen (deuterium) atoms, further completing the picture obtained from diffraction measurements.

5.3.3.1 NMR relaxometry[115]

Fig. 59 shows the characteristic relaxation times measured as a function of temperature in $Mg_{0.65}Sc_{0.35}H_{2.20}$. It is clear from the figure that T_2 is indeed relatively constant at lower temperatures, but at T≈330 K T_2 starts to increase by several orders of magnitude from $5*10^{-6}$ s up to $5*10^{-4}$ s at 500 K. The onset of T_2 increase corresponds to a hydrogen hopping rate ω_H of 10^5 s^{-1}. The minimum in T_1 was not attainable for this material, as heating above 300°C caused irreversible changes in the sample. Therefore $T_{1\rho}$, rather than T_1, was used to determine the hydrogen motion rate. The $T_{1\rho}$ minimum corresponds to $\omega_H = 5*10^5$ s^{-1} and occurs around 400 K.

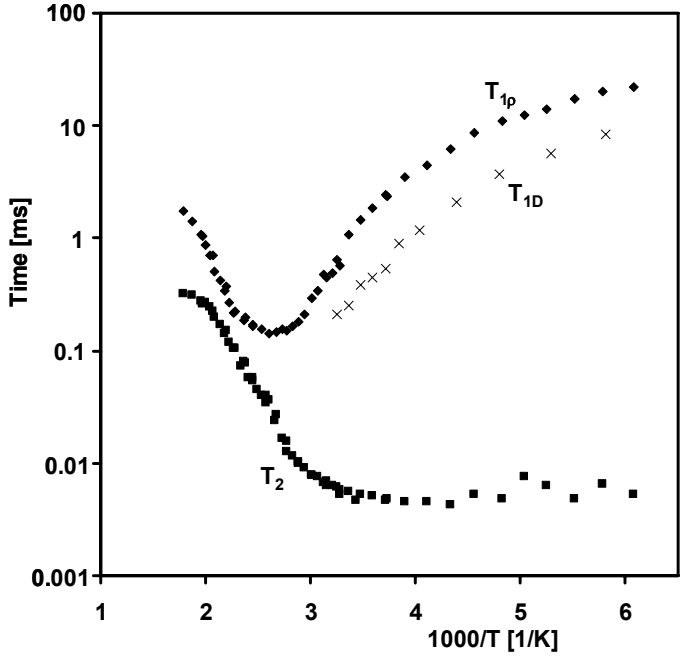

Fig. 59: Relaxation times $T_{1\rho}$, T_{1D} and T_2 as a function of reciprocal temperature for $Mg_{0.65}Sc_{0.35}H_{2.20}$

Fig. 59 also depicts T_{1D} as a function of temperature. T_{1D} is the relaxation time of the dipolar-ordered state, which is a small residual magnetization that remains after the B_1 field of the spin-locking pulse in a $T_{1\rho}$ measurement has slowly been reduced to zero[116]. This time constant is especially suited to study very slow motions and has been used to measure the hydrogen hopping rate in MgH_2. The hydrogen motion rate ω_H is, to within a factor 2, equal to $1/T_{1D}$.

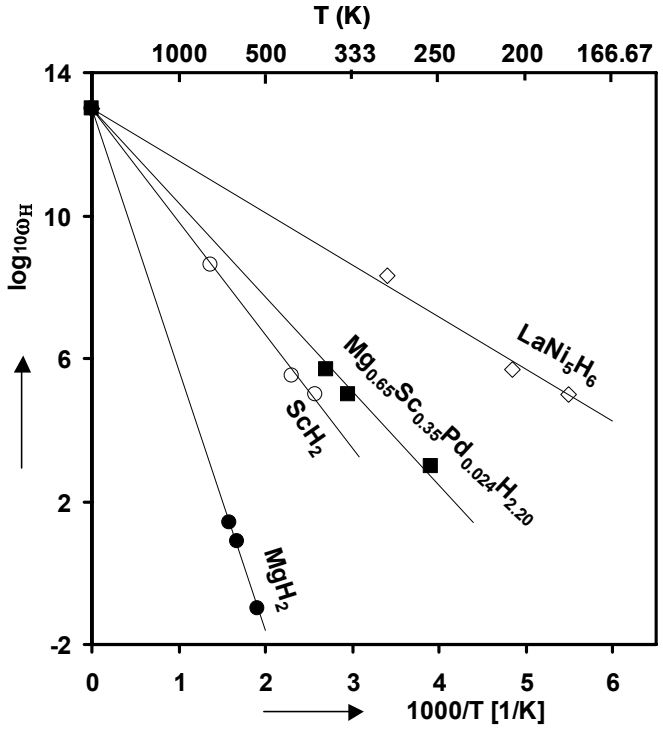

Fig. 60: Hydrogen hopping rates as determined from measurement of a number of characteristic relaxation times as a function of temperature for $LaNi_5H_6$, $Mg_{0.65}Sc_{0.35}Pd_{0.024}H_{2.20}$, ScH_2 and MgH_2

Fig. 60 shows the H-hopping rate as a function of temperature, determined by relaxation NMR measurements, for MgH_2, ScH_2 and $Mg_{0.65}Sc_{0.35}Pd_{0.024}H_{2.20}$. For comparison, $LaNi_5H_6$ is also included. The H-motion rates depicted in Fig. 60 were determined from T_{1D} for MgH_2, $T_{1\rho}$ minimum, T_2 increase and T_{1D} for $Mg_{0.65}Sc_{0.35}H_{2.20}$ and T_1 minimum, $T_{1\rho}$ minimum and T_2 increase for ScH_2 and $LaNi_5H_6$. As can be seen from Fig. 60, H-motion is indeed very slow in MgH_2, as was expected, and much faster for the cubic Sc and $Mg_{0.65}Sc_{0.35}$ hydrides. At 500 K, the average H-motion rate is 8 orders of magnitude faster in ScH_2 compared to MgH_2, while the ternary hydride is 1-2 orders of magnitude faster still. This finally quantifies the vast improvement of the hydrogen diffusion rate, which was already inferred from electrochemical measurements, upon going from a rutile structure (MgH_2) to a cubic structure (ScH_2 and $Mg_xSc_{1-x}H_y$). It should be noted, however, that the rate of H-motion in $Mg_{0.65}Sc_{0.35}H_{2.2}$ is still 4-5 orders of magnitude slower than in the 'classic' AB_5-type hydrides.

5.3.3.2 NMR spectroscopy

Where measurements of the relaxation times dealt with hydrogen mobility through the crystal lattice, NMR spectroscopy aims to distinguish between chemically distinct hydrogen atoms inside the crystal structure by resolving the different chemical shift components. The basic principles were already described in section 2.5, but there are some additional factors that have to be taken into account and they will be briefly discussed below.

Two NMR active nuclei that are in close proximity to one another will influence the magnetic field that each of the nuclei experiences by dipolar, or, in the case of deuterium, quadrupolar coupling. The field experienced by a nucleus as a result of dipolar coupling depends on the distance between the nuclei and the angle the vector connecting the two nuclei makes with the applied magnetic field. In a liquid, this effect would be averaged out by molecular tumbling but in a solid sample, the spins are fixed inside the crystal lattice and the angle each internuclear vector makes with B_0 is fixed over time. This leads to a broad distribution in the local field strength and hence a broad distribution in resonance frequencies around the central Larmor frequency. Another source of orientation dependent line broadening in solids is the so-called quadrupolar coupling of nuclei with spin > ½, such as deuterium, to local electric field gradients in the crystal. This is well illustrated by the static NMR spectrum of MgD_2, which is shown in Fig. 61 (a). The spread around the central resonance frequency is indeed very large, ranging between +350 and -350 ppm. For an isotropic microcrystalline powder with no preferential orientation with respect to the magnetic field, the number of quadrupolar-tensor orientations perpendicular to the applied field is relatively large, which explains the 'horns' on either side of the central resonance frequency.

The change in the local field caused by dipolar and quadrupolar coupling scales with the angle θ as $3\cos^2\theta - 1$. For a particular value of $\theta = \arccos(\sqrt{1/3})$ (54.7°), the dipole interactions vanish. 54.7° is also equal to the angle between a cube's vertices and space diagonal and is called the *magic angle* in geometry. By positioning the sample holder at an angle of 54.7° with respect to B_0 and rapidly spinning it, the time-averaged orientation angle between each dipole and B_0 becomes equal to the magic angle and line broadening as a result of quadrupolar coupling is reduced. This is called *Magic Angle Spinning* or MAS-NMR. The spinning frequency should be comparable to the static line width in Hz. The result is a typical sideband pattern such as the ones shown in Fig. 61. Compared to a static spectrum, the lines are narrower and occur at frequency intervals equal to the spinning frequency.

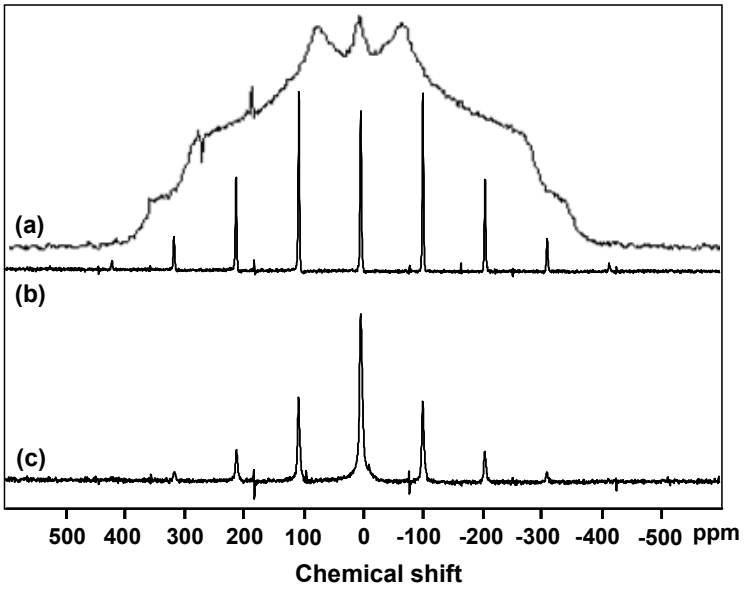

Fig. 61: Static spectrum (a) and 8 kHz MAS NMR sideband pattern (b) of MgD_2 and 8 kHz MAS NMR spectrum of $Mg_{0.65}Sc_{0.35}Pd_{0.024}D_{2.20}$ (c)

The ^{2}D MAS-NMR sideband spectrum of $Mg_{0.65}Sc_{0.35}Pd_{0.024}D_{2.20}$ at a rotation frequency of 8 kHz is also shown in Fig. 61 (c). The most notable difference with the spectrum of MgD_2 is that for the ternary deuteride, the sideband intensity decreases much more rapidly. This means the line-broadening by quadrupolar coupling is much less for the ternary deuteride, which indicates higher deuterium motion rates. This is once more in line with the expectation that the hydrogen (deuterium) atoms will have a higher mobility in a cubic host lattice than in a rutile structure, which was already found by the relaxation measurements on the hydrides.

Zooming in on the centerband region, more specific chemical information can be derived. Fig. 62 (a) shows the centerband of $Mg_{0.65}Sc_{0.35}Pd_{0.024}D_{2.20}$ measured at 213 K[117]. The lineshape can be decomposed into four distinct components at 4.5, 2.7, -2.0 and -11 ppm. This last component is ascribed to the deuterium fraction inside the secondary catalytic phase, which contains the Pd. The three main components were subsequently studied with a special spin-echo sequence called TRAPDOR (TRAnsfer of Populations in DOuble Resonance). After the 90^o pulse, the ^{45}Sc is irradiated on its own resonance frequency for half the echo time, which specifically shortens the T_2 of the deuterium spins with Sc in their nearest neighbor shell. This will result in a lower intensity of the Sc-sensitive components after the same echo-time, which is shown in Fig. 62 (b).

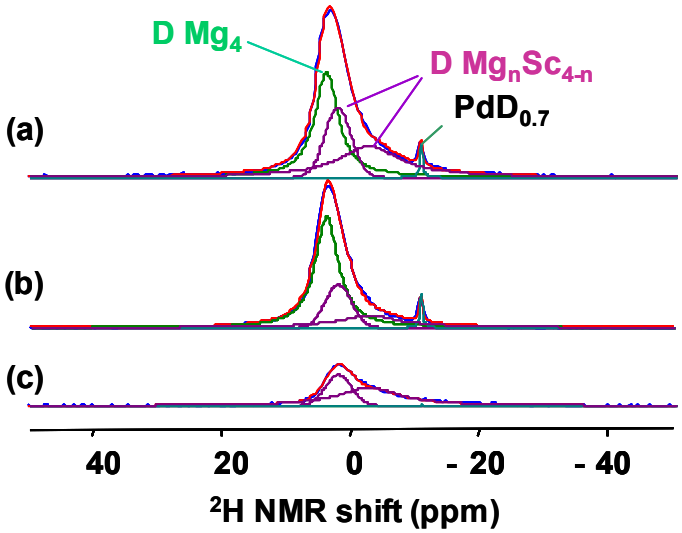

Fig. 62: Centerband region of 8 kHz MAS ^{2}D spectrum at 213 K of $Mg_{0.65}Sc_{0.35}Pd_{0.024}D_{2.20}$ without ^{45}Sc irradiation (a), with ^{45}Sc irradiation (b) and the difference between the two (c). The echo time is 4 ms in both cases. Note that only the components at 2.7 and –2.0 ppm are sensitive to Sc irradiation.

The difference between spectrum (a) and (b) is shown as curve (c) in Fig. 62. It becomes clear now that the 'green' component, at 4.5 ppm, is not sensitive to Sc irradiation as its intensity is equal in spectrum (a) and (b). The other two components are strongly affected by the ^{45}Sc irradiation, indicating that they originate from deuterium atoms with at least one Sc atom in their nearest-neighbor coordination shell.

The intensity ratio between the component at 4.5 ppm, corresponding to pure Mg coordination, and the sum of the components at 2.7 and -2.0 ppm is 1:1 and constant *vs.* echo time. This means that 50% of the deuterium atoms have a pure Mg coordination, which is significantly different from what would be expected from a statistical distribution of Mg and Sc over the metal sublattice. For a statistical distribution, the expected 'Mg_4'-fraction is equal to $(0.65)^4 = 0.17$, which is only one-third of the value that is found in the TRAPDOR experiment. These results suggest that there exist Sc-rich and Mg-rich domains inside the hydride (deuteride) structure, which still form a coherent, single-phase fcc lattice as measured by both XRD and ND.

2-D EXSY, or 2-Dimensional EXchange SpectroscopY, can be used to study diffusion processes between NMR-distinct sites in the crystal lattice. This is done by a pulse sequence consisting of three 90^o pulses, where the evolution time between the first two pulses, t_1, and the mixing time between the second and third, τ_{mix}, is varied and a FID signal is recorded after the third pulse. The pulse sequence and signals as a function of t_1 and t_2 are illustrated in Fig. 63.

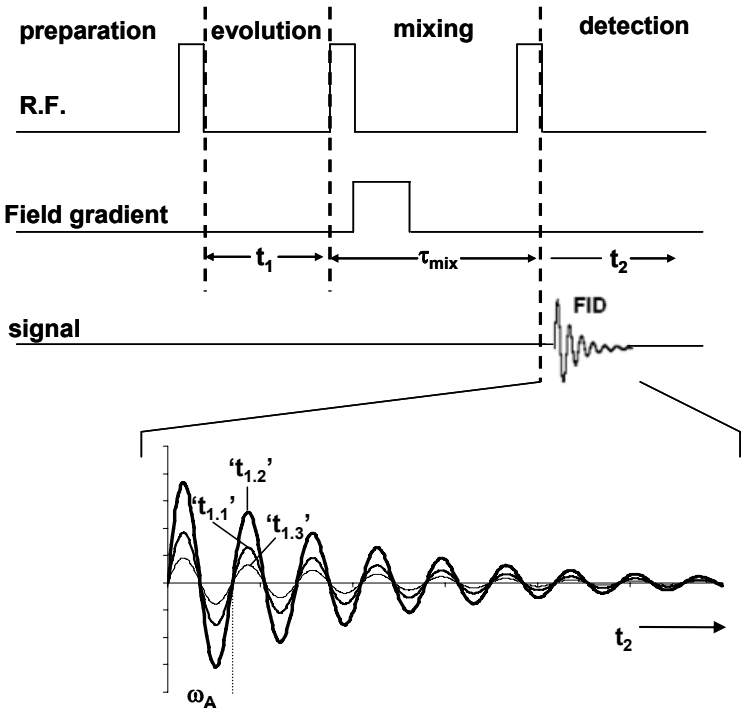

Fig. 63: The pulse sequence and recorded signals for a typical 2-D EXSY experiment. The pulse sequence consists of 3 90° pulses separated by an evolution time t_1 and mixing time τ_{mix}. 3 FID signals are depicted for a single-spin system for 3 different values of t_1.

The first 90° pulse puts the magnetization vector in the xy-plane. During the evolution time t_1, the spins precess at their own characteristic resonance frequencies. Subsequently, a second 90° pulse around the x-axis puts the magnetization vector in the xz-plane. The z-component of the magnetization vector is equal to the y-component at the moment the second pulse was applied and will therefore depend on t_1. During the mixing time, the exchange processes under investigation are allowed to take place for a certain time τ_{mix}. Subsequently, the magnetization is rotated back to the xy-plane by the third 90° pulse and the (new) resonance frequencies are obtained from a FID recorded during the acquisition time t_2.

The lower part of Fig. 63 schematically illustrates how the desired information is extracted from the signals for a single-spin system (A). The NMR frequency belonging to site A, is derived from the FID by Fourier transformation in the t_2-domain. The *amplitude* of the FID signal, at any given time during acquisition, *i.e.* a fixed t_2, depends on the magnitude of the magnetization vector after the second 90° pulse. A plot of the amplitude as a function of t_1 will also contain the frequency ω_A, which can be obtained by Fourier transformation in the t_1-domain.

Extension of this picture is now straightforward. Signals of multiple non-exchanging spins will each contain only their own seperate resonance frequency in the t_1 domain. However, when there is exchange, additional frequencies are found in the t_1 domain, equal to the resonance frequencies of the sites with which exchange has taken place. Graphically, hydrogen (deuterium) exchange between NMR distinct sites results in off-diagonal intensity on a plot such as the one shown in Fig. 64 for $Mg_{0.65}Sc_{0.35}Pd_{0.024}D_{2.20}$. By monitoring this intensity as a function of τ_{mix}, information on the exchange rates between different deuterium sites at a given temperature is obtained.

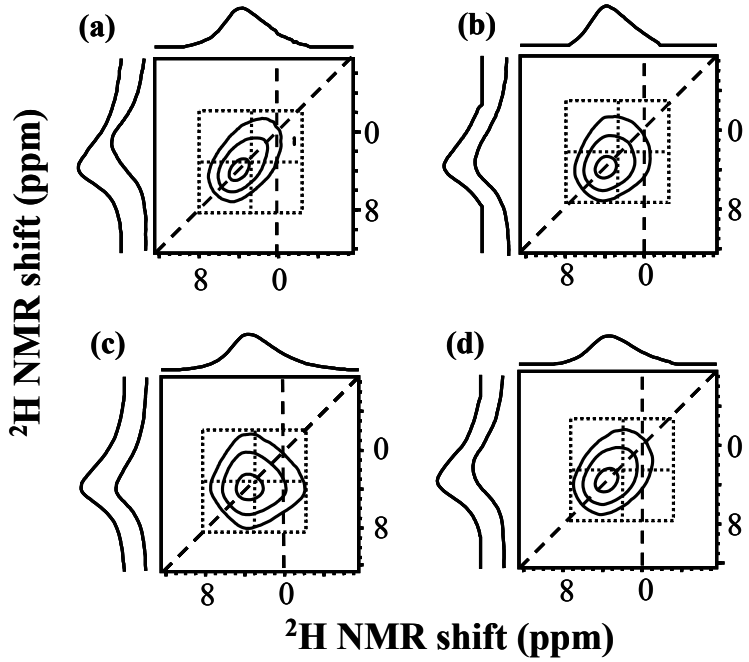

Fig. 64: 2-D EXSY spectra of $Mg_{0.65}Sc_{0.35}Pd_{0.024}D_{2.20}$ at 297K (a)-(c) for $t_m = 10^{-3}$s (a), 10^{-2}s (b) and 10^{-1}s (c) and at 213K for $t_m = 10^{-2}$s (d)

The TRAPDOR measurements already proved that there are indeed NMR-distinct deuterium sites in the lattice, where the MAS lineshape was rather broad and featureless. The EXSY-measurement provides additional evidence for this, but has an additional advantage over the measurements presented until now. The relaxation measurements presented in Fig. 59 and Fig. 60, only give information about the *average H-hopping rate*. Whether it concerns random motion throughout the entire crystal lattice or highly localized, or even concerted, motion between equivalent sites, as was found for *e.g.* Mg_2NiH_4[118, 119], can not be determined. In an exchange experiment, however, it is possible to pinpoint which sites, characterized by their chemical shift, do exchange hydrogen and which do not. It can be seen in Fig. 64 that the off-diagonal intensity is indeed considerable and strongly dependent on the mixing time τ_{mix}. 2-Dimensional plots are shown for mixing times of 10^{-3}, 10^{-2} and 10^{-1} s at T = 297 K (a)-(c) and 10^{-2} s at 213 K (d). Going from Fig. 64 (a) to (b), cross-intensity is found over an ever larger range of chemical shifts, until after 10^{-1} s, complete randomization of the deuterium atoms over the NMR-distinct sites has taken place (Fig. 64 (c)). This is further illustrated in Fig. 65, where the off-diagonal intensity is plotted as a function of the mixing time for three different temperatures. A gradual increase is observed from 10^{-3} to ~$5*10^{-2}$ s until the off-diagonal intensity levels off at $\tau_{mix} \approx 0.1$ s for all temperatures.

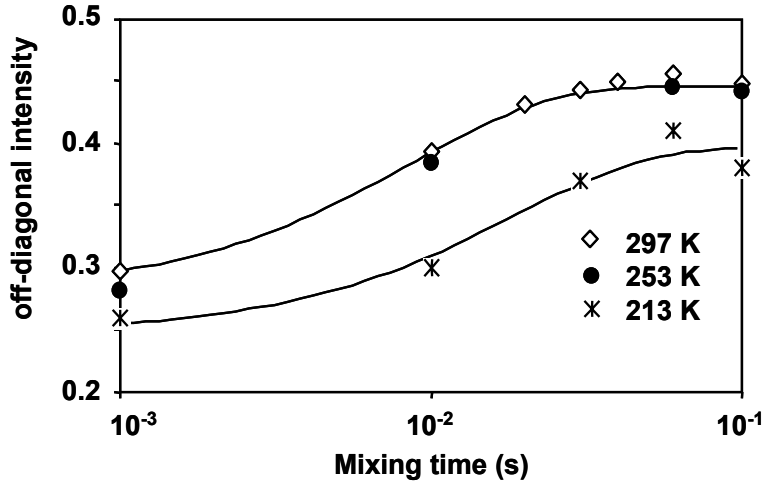

Fig. 65: Variation of the off-diagonal intensity as a function of the mixing time for three different temperatures. It can be seen that the off-diagonal intensity saturates between mixing times of 10^{-2} and 10^{-1} seconds for all temperatures, indicating full randomization of the deuterium atoms over the different sites within this time interval.

5.3.4 DFT calculations

A unit cell containing four metal atoms was used for both the fluorite and rutile structures (see Fig. 66), enabling calculation of an identical set of $Mg_{1-x}Sc_xH_2$ compositions in both structure types. The conventional rutile unit cell (dashed lines Fig. 66) was redefined so that it contains 4 metal atoms in a face-centered configuration, the same as for the fluorite structure.

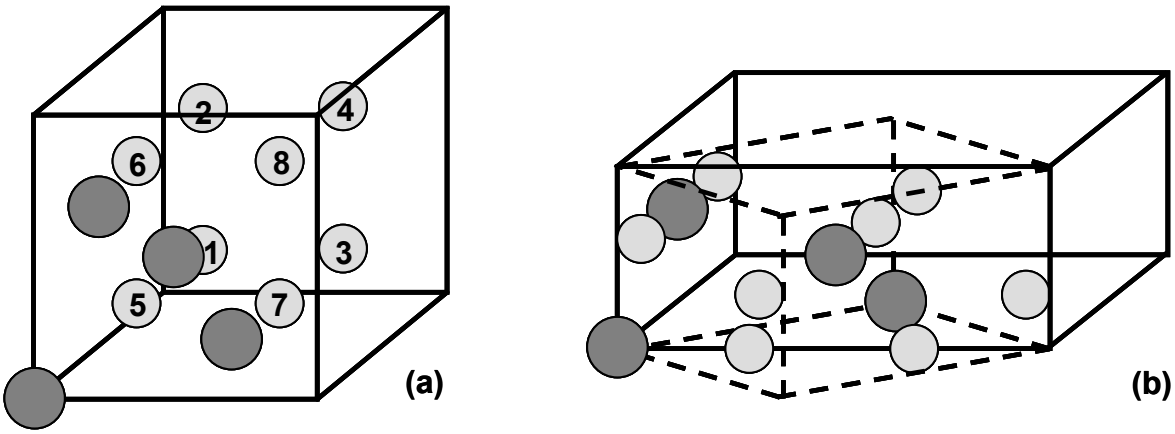

Fig. 66: Unit cell representations of the fluorite (a) and rutile (b) unit cells. The rutile structure is represented somewhat differently than usual in order to arrive at a face-centered arrangement of the metal atoms; as in the fluorite structure. The conventional body-centered tetragonal structure is indicated by the dashed lines.

The formation enthalpy of the ternary hydride can either be defined as

$$\Delta H_f = E_{Mg_{1-x}ScxH_2} - \left\lfloor (1-x)E_{Mg} + xE_{Sc} \right\rfloor - E_{H_2} \qquad (5.6)$$

or

$$\Delta H_f = E_{Mg_{1-x}Sc_xH_2} - E_{Mg_{1-x}Sc_x(alloy)} - E_{H_2} \qquad (5.7)$$

where $E_{Mg_{1-x}Sc_xH_2}$, E_{Mg} and E_{Sc} are the energies as obtained from their respective calculations, normalized to the number of metal atoms present in the unit cell. At H/M = 2, as is the case here, this is the same as normalization per H_2 molecule.

For the sake of simplicity, the same reference state has been used for the entire compositional range. The enthalpy of hydride formation was calculated both for formation from the elements (Eq. *(5.6)*), and from an empty face-centered lattice (Eq. *(5.7)*). For Mg-Sc, X-Ray and Neutron Diffraction showed that the plateau region in the desorption curve corresponds to an equilibrium between two face-centered cubic phases. Evidently, by subtracting Eq. *(5.6)* and *(5.7)*, the formation enthalpy of the empty fcc structure is obtained. When this value is small (<10 kJ/mol for the entire compositional range), the results obtained with Eq. *(5.6)* and Eq. *(5.7)* are very similar and only the results of Eq. *(5.6)* are presented.

Table 5: Enthalpies of formation and lattice parameters of metal compounds and binary hydrides in the Mg-Sc-H system. Literature values are between brackets.

alloy	Structure type	Lattice parameters (Å)	Enthalpy of formation [kJ/mol]
Mg	hcp	a = 3.19 (3.21) c = 5.20 (5.21)	
Mg	fcc	a = 4.52	+1.18
Sc	hcp	a = 3.31 (3.31) c = 5.13 (5.27)	
Sc	fcc	a = 4.58	+3.51
MgSc	bcc	a = 3.58 (3.59)	-3.57 (-6)
MgH_2	Rutile	a = 4.45 (4.50) c = 2.99 (3.01)	-63.3 (-77)
ScH_2	Fluorite	a = 4.74 (4.78)	-203.15 (-200)

5.3.4.1 Structure preference: fluorite vs. rutile

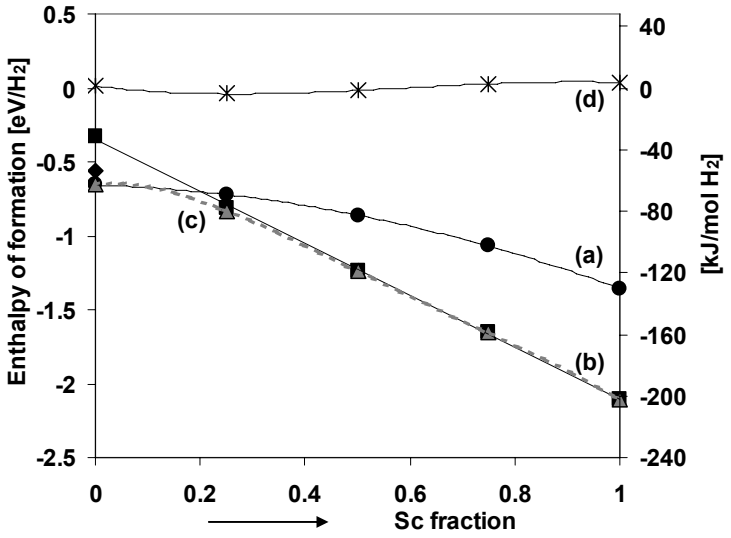

Fig. 67: Enthalpy of formation in eV/H_2 and kJ/mol H_2 of $Mg_{1-x}Sc_xH_2$ as a function of Mg/Sc ratio. (a): rutile energies. (b): fluorite energies, (c): energies after structure relaxation, (d): energy of empty fcc metal alloy. ◆: cubic MgH_2 according to Vajeeston *et al.*[109]

The formation enthalpies of $Mg_{1-x}Sc_xH_2$ are plotted as a function of the Sc content in Fig. 67. The formation enthalpy of an unhydrided intermetallic compound is almost zero for the entire compositional range, so only the hydride formation enthalpies obtained from Eq. *(5.6)*

are shown. In these calculations, no evidence for destabilization of the rutile structure by Sc is found. The formation enthalpy of the rutile structure decreases monotonously with increasing Sc content, going from –0.655 eV/metal atom for x = 0 to –1.356 eV/metal atom or –131 kJ/mol H_2 for x = 1. The formation enthalpy of the fluorite structure steeply decreases with increasing Sc content and quickly becomes more negative than that of the rutile structure. This is to be expected since it is well established by X-Ray and neutron diffraction measurements that a fluorite structure is formed for x = 0.35. The crossing point of the two curves is located around x = 0.20, which is the same composition at which electrochemical experiments showed the deterioration of the hydrogenation kinetics. The agreement between the calculations and experimental evidence is very gratifying.

However, some of the structures showed imaginary frequencies, indicating unstable structures, resulting from optimization while respecting the symmetry of the formal crystal structure. When the optimization is done without the symmetry constraints, significant changes occur. The dotted line in Fig. 67 represents the energies of the re-optimized structures. All rutile-structured hydrides with Sc-fractions 0.50-1 then revert back to a fluorite-type structure. This is interesting as it shows once more that the fluorite structures are preferred for these compositions. The fluorite structure of pure MgH_2, on the other hand, completely relaxes to the expected rutile structure. The cubic 'β-MgH_2' structure reported by Vajeeston *et al.* was also calculated and is depicted in Fig. 67 on the left y-axis. This structure was found to be 9.2 kJ/mole H_2 less stable than the rutile structure, reflecting the fact that this is not an equilibrium phase, but indeed a high-pressure modification.

When the symmetry restrictions are not applied, the fluorite structures of the alloys with Sc-contents of 0.25 and 0.5 show displacements of the hydrogen atoms within the unit cell and the metal lattice also undergoes a small distortion. The hydrogen displacements for x = 0.50 were very small, all well below 1%. However, for x = 0.25, the hydrogen atoms are significantly displaced. The results are summarized in Table 6. The atomic positions are expressed as fractional co-ordinates.

Table 6: Unit cell vectors and atomic positions of $Mg_{0.75}Sc_{0.25}H_2$ before and after structural relaxation.

vector/atom	undistorted cell			distorted cell		
a	4.71	0.00	0.00	4.73	0.00	0.00
b	0.00	4.71	0.00	0.00	4.71	0.00
c	0.00	0.00	4.71	0.00	0.00	4.75
Sc	0.5	0.5	0	0.5	0.5	0
Mg1	0.5	0	0.5	0.5	0	0.5
Mg2	0	0.5	0.5	0	0.5	0.5
Mg3	0	0	0	0	0	0
H1	0.25	0.25	0.25	0.276	0.213	0.231
H2	0.25	0.25	0.75	0.231	0.283	0.743
H3	0.25	0.75	0.25	0.231	0.717	0.257
H4	0.25	0.75	0.75	0.276	0.787	0.769
H5	0.75	0.25	0.25	0.769	0.283	0.256
H6	0.75	0.25	0.75	0.724	0.213	0.769
H7	0.75	0.75	0.25	0.724	0.787	0.230
H8	0.75	0.75	0.75	0.769	0.717	0.743

The unit cell undergoes a slight orthorombic distortion, the a and c-axes are slightly elongated compared to the undistorted cubic cell. The angles between the cell axes did not

significantly deviate from 90° in the distorted cell. The metal atoms retain their face-centered positions; displacements were less than 0.1% of the cell parameter.

For the hydrogen atoms, the situation is quite different. Displacements from the formal tetrahedral positions are quite clear with a maximum deviation of 14.8 % in the y-coordinate of H1 and H6 (see Fig. 66). This indicates that rather than a formal fluorite or rutile structure, it is, in practice, more likely that transition structures will be formed near the crossover point, with a tetragonal or orthorhombic distortion of the metal lattice and displacement of the hydrogen atoms from the tetrahedral positions.

5.3.4.2 Site preference of hydrogen at H/M ≠ 2

For H/M ratios other than 2, the site preference of the hydrogen atoms has been checked for $Mg_{0.75}Sc_{0.25}$. The energies in eV/metal were calculated for H/M ratios of 0.5 and 1 for all possible configurations of the H-atoms and the values are listed in Table 7:

Table 7: Energies of different H-atom configurations for $Mg_{0.75}Sc_{0.25}H_y$. H-atom positions based on Fig. 66

H/M	H-positions	Energies (eV/metal)
0.5	5, 4	-4.517
0.5	5, 2	-4.513
0.5	5, 7	-4.584
1	5, 3 8, 2	-6.162
1	5, 7, 3, 1	-6.472
1	5, 7 2, 4	-6.337
1	1, 5, 7 6	-6.387
1	1, 5, 7 2	-6.394
1	1, 5, 7 4	-6.321
1	1-8 (supercell)	-6.511

Surprisingly, the sphalerite arrangement (see Fig. 68 (a)) that is commonly found in ionic solids and which has been implicitly assumed for the MgSc hydrides until now, is the least stable one. From the energies of the different H-configurations for H/M ratios of 0.5 and 1, it can be seen that the lowest energy is obtained when the hydrogen atoms are placed as close together as possible. As a consequence, a planar configuration of the hydrogen atoms is most favorable for H/M = 1, as is shown in Fig. 68 (b). Calculations on a 1x1x2 supercell confirm this result. For 2 stacked unit cells with the H-atoms in a planar arrangement in each cell, as in Fig. 68 (b), the energy in eV/metal is exactly the same. However, completely filling one of the cells and leaving the other empty further lowers the energy by 3.8 kJ/mol H_2 (Fig. 68 (c)).

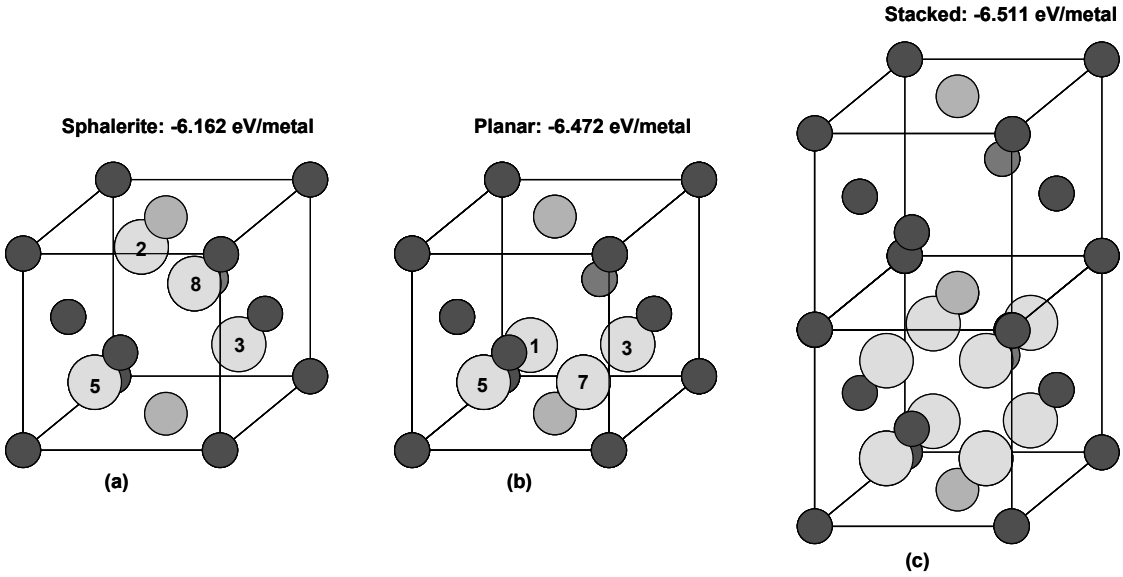

Fig. 68: $Mg_{0.75}Sc_{0.25}H_1$ in the sphalerite arrangement (a) and the planar arrangement (b). The planar arrangement with the H-atoms as close together as possible is the most favorable one. A 1x1x2 supercell (c) with the bottom cell completely filled is even more stable than (b).

5.3.5 Discussion

The ordering of the MgSc sublattice, which was present in the starting alloy, appears to be lost upon deuteration. This has also been observed for other types of cubic hydride-forming alloys such as $MgPd_3$. In its as-made form, this alloy has a tetragonal superstructure, but partially loses its ordering to form a primitive cubic structure upon hydriding. This primitive structure is then retained upon desorption. A mild grinding treatment even leads to a complete loss of ordering and results in the formation of a purely face-centered-cubic compound. Whether the $Mg_{0.65}Sc_{0.35}$ also shows this behavior can not be verified as an attempt at full desorption results in disproportionation into Mg and ScH_2 as was shown in Fig. 46 (B), but the initial ordering of the unhydrided metal was indeed lost upon deuteration. The Neutron Diffraction measurements allowed determination of the hydrogen (deuterium) positions and confirmed partial occupation of the octahedral interstices in the fully loaded state. Partial desorption showed conservation of the fcc structure and a co-existence region between 2 phases differing only in lattice constant and T-site occupation, the same as for the hydride (see Fig. 46 (B) pattern (c)).

The lattice constant for the fully charged deuteride is smaller than for the hydride (4.81 vs. 4.84 Å). This difference is observed more often for Mg-based materials in the fully hydrogenated state, such as the $LaMg_2$ and $CeMg_2$ alloys studied by Gingl *et al.*[105]. The discrete lattice expansion is, at only 4.3%, almost 50% smaller than for the hydride. This is different from what is commonly found for *e.g.* the AB_5-type compounds, where the discrete expansion for both $LaNi_5$-H and $LaNi_5$-D is ~22%. The most distinct difference, however, is the fact that the concentration boundaries for the plateau region deviate substantially from those derived from the electrochemically determined isotherms. Especially on the D-rich side, where single-phase behaviour is observed down to 1.6 D/M, whereas the H-concentration derived from the GITT curve is ~1.8 H/M (see Fig. 37). This may be due to the fact that the electrochemical measurements were done at room-temperature, while the solid-gas desorption was done at 300°C. Apparently, the partial Mg and Sc clustering that was observed by NMR and which may be enhanced by repeated exposures to elevated temperatures, influences the material's behavior in the plateau region.

The material's behavior during the first charging cycle was investigated during *in-situ* electrochemical loading at room-temperature. During charging, only one fcc phase was observed at deuterium loadings that correspond to the two-phase coexistence region during discharge. Such a discrepancy between the absorption and desorption behavior has not been reported for any other hydride-forming material. During discharge, the concentration boundaries, 1.55 and 0.85 D/M in the tetrahedral sites, were the same as for the solid-gas desorption. The discrepancies between the deuterium concentrations derived from the electrochemical measurements and those derived from the diffraction patterns is much larger than for the solid-gas measurements, but this is very likely cause by the recombination of oxygen and hydrogen gas that was formed at the Ni counter-electrodes. It has to be kept in mind that the electrochemical cell has been optimized for obtaining diffraction data, not for doing electrochemical measurements.

Based on the similarity in electrochemical properties between thin films and bulk materials found in Chapter 4 and the fact that the phase transition was shown to be between two fcc phases with different T-site occupation, phase segregation into MgH_2 and REH_2 that was inferred by others from optical measurements on thin films[89, 90, 91, 92] was initially assumed not to occur in bulk materials. However, results from NMR measurements and DFT calculations necessitate reconsideration on this point. NMR clearly showed clustering of the metal atoms as the number of D-atoms with pure Mg coordination was much larger than expected based on a statistically random distribution of the metal atoms. The fraction of deuterium atoms that will have pure Mg coordination in a completely phase segregated system is 130/220 = 59%. The value that was found from the NMR measurments, 50%, is already quite close to this value. Apparently, the Mg- and Sc clusters can grow reasonably large before diffraction will show any evidence for phase segregation. Indeed, neutron diffraction still showed a coherent fcc structure even after repeated exposures to 300°C followed by cooling to RT.

The results of the DFT calculations in Fig. 67 show that, at H/M = 2, the energy of a mixture of MgH_2 and ScH_2 would always be lower than that of a ternary hydride in either the rutile or the fluorite structure. Because of the large difference in hydrogen affinity between Mg and Sc; -200 kJ/mol *vs.*-77 kJ/mol H_2, disproportionation of the alloy will most likely take place by forming a mixture of ScH_2 and Mg first. Therefore, to evaluate the tendency of the system to disproportionate, the enthalpies of the following reactions:

$$Mg_xSc_{1-x} + (1-x)H_2 \rightarrow Mg_xSc_{1-x}H_{2-2x} \qquad (5.8)$$

$$Mg_xSc_{1-x} + (1-x)H_2 \rightarrow xMg + (1-x)ScH_2 \qquad (5.9)$$

should be compared. The calculations also showed that the hydrogen atoms tend to cluster together as closely as possible. This was a somewhat surprising finding, since the sphalerite arrangement is the one commonly found in ionic compounds such as metal chalcogenides.

With a unit cell of only 4 metal atoms, clustering of the Sc atoms can not be simulated, so whether the hydrogen atoms prefer to cluster not only as close together as possible, but also have a preference for a Sc-rich environment within a larger cubic structure unit could not be determined. However, the NMR and DFT results have yielded sufficient evidence to state that the barriers to phase segregation in MgSc hydrides are kinetic rather than thermodynamic. This can also explain why the plateau voltage (pressure) was virtually independent of the Mg/Sc ratio between 65 and 85 at.% Sc (see Fig. 37 (a)) and at a level equal to that of pure Mg. The plateau region of the isotherm would then correspond to the removal of hydrogen atoms from Mg-rich clusters.

The enthalpy of formation of a mixture of the binary hydrides could be represented in Fig. 67 as a straight line connecting the enthalpy of formation of rutile MgH_2 with that of fluorite ScH_2. It can be seen that the enthalpy difference between a segeregated mixture and the ternary fluorite-structured hydrides becomes ever smaller with increasing Sc-content, which means the driving force for phase separation is also reduced. Indeed, for $Mg_{0.50}Sc_{0.50}$ and $Mg_{50}Y_{50}$, the plateau pressures were reduced with respect to pure Mg by at least 1 and 3 orders of magnitude, respectively (see Fig. 37 and Fig. 30), which indicates that there were no Mg_4-clusters present in the hydrides.

It should be noted that entropy has not been taken into account in the calculations and that the material's behavior at finite temperatures can substantially deviate from that predicted by the calculations.

5.4 Conclusions and outlook

The positions of the hydrogen atoms were resolved by neutron diffraction measurements. Simultaneous T-and O-site occupation at D/M > 2 was confirmed. The ordering of the metal sublattice that was observed in the starting material was lost upon deuteration. Coexistence of 2 fcc phases with different lattice constants and T-site occupations was found in the plateau region, the same as for the hydride. *In-situ* measurements in an electrochemical setup showed different behavior during the first charging of the material, where only one fcc phase was observed. The concentration boundaries of the 2-phase region in the solid-gas desorption experiment were, at 1.55 and 0.85 D/M, substantially different from those found from the GITT curves. This is probably due to changes in the material induced by the elevated ab-and desorption temperatures.

NMR measurements confirmed and quantified the vast improvement of the hydrogen motion rate in the fluorite-type ternary hydride as compared to rutile MgH_2. The hydrogen diffusion rate was increased by 8 orders of magnitude, but still falls far short of the diffusion rates in AB_5-type materials.

NMR spectroscopy showed a much larger fraction of deuterium atoms with a pure Mg coordination than would be expected for a statistically ramdom distribution of the metal atoms in a deuteride synthesized at 300°C. DFT calculations yield a similar result as a mixture of the binary hydrides always appears to be lower in energy than a ternary hydride in either a rutile or a fluorite structure. The hydrogen atoms were also found to prefer cluster formation, even up to the point of completely filling one unit cell while leaving an adjacent one empty. These observations make it very likely that the phase segregation in Mg-RE thin films, as inferred from optical studies, does indeed take place as this effect has now been predicted (DFT) and measured (NMR) in bulk materials as well.

The high price of Sc will prevent practical application of this material in commercial batteries or hydrogen storage systems. However, there are many interesting routes for expanding the theoretical work on MgSc alloys and hydrides. The shift of the hydrogen atoms away from the tetrahedral positions that is predicted to take place for the 75/25 ratio can be verified by neutron diffraction. Using larger unit cells, the Mg/Sc ratio can be varied in smaller steps in the calculations and allow for a more accurate investigation of this effect for compositions other then $Mg_{0.75}Sc_{0.25}$ near the fluorite-rutile transition point.

Attempts to predict the (de)sorption isotherm by calculating the hydride formation enthalpy as a function of the H/M ratio have not been successful until now[120]. However, because the material appears to be stable as a metal alloy, but *meta*stable as a ternary hydride, it may be extremely difficult to reproduce the electrochemically measured isotherms. Experimentally well-studied stable (both as metal alloy and hydride) hydride-forming systems

such as $LaNi_5$ and TiV-based solid solutions can perhaps serve as a model system in this respect. $LaNi_5$ also represents an interesting case regarding the phase segregation issue as the difference in hydrogen affinity between the elements, -194 kJ/mol H_2 for La *vs.* only -5 kJ/mol H_2 for Ni[13], is even more extreme than for MgSc. Decomposition schemes similar to reactions *(5.8)* and *(5.9)* can be tested for AB_5-type compounds as well. Eventually, a way may be found to predict the (de)hydrogenation behavior of an alloy that is metastable both as a metal and as a ternary hydride, such as Mg-Ti, which will be the subject of the next chapter.

6

Hydrogen storage in Mg-Ti based materials synthesized by mechanical alloying

Abstract

In this chapter, results on Mg_xTi_{1-x} bulk materials synthesized by mechanical alloying are presented. The resulting Mg-Ti alloy is obtained as either a mixture of a cubic Mg-Ti phase and cubic Ti or a mixture of a hexagonal Mg-10 at.%Ti solid solution and amorphous Ti, depending on the Mg precursor. The hexagonal alloys have higher absorption capacity than the cubic ones (3.7 *vs.* 1.8 wt.%), whereas the rate capability is higher for the cubic alloys and, as a result, the total discharge capacities at 10 mA/g are comparable. Increasing the milling time resulted in an increase in the amount of the Ti-rich phase in the cubic alloy and a decrease in the electrochemical capacity, indicating that only one of the cubic phases is active. Addition of Ni improved the rate capability of both the cubic and hexagonal modification through the formation of a secondary Mg-Ni and Ti-Ni phase, respectively, which acts as a rapid diffusion path for hydrogen. The highest discharge capacities that were obtained were 520 mAh/g (~2 wt.%) for cubic $(Mg_{0.65}Ti_{0.35})_{0.95}Ni_{0.05}$ and 837 mAh/g (3.2 wt.%) for hexagonal $(Mg_{0.75}Ti_{0.25})_{0.90}Ni_{0.10}$. Electrochemically measured isotherms show only minor influences of Mg/Ti ratio and addition of a third element on the equilibrium pressure, confirming the XRD results that the alloying element does not dissolve in the Mg-Ti phase. X-ray diffraction seemingly detected no changes in the crystal structure or the lattice constants of cubic $Mg_{0.65}Ti_{0.35}$ upon deuterium absorption and subsequent thermal desorption. However, neutron diffraction measurements proved that this material completely segregates into the binary deuterides at a temperature and pressure of 175^{o}C and 75 bar, respectively. Despite this apparent phase separation, 2-D exchange NMR measurements showed that deuterium atoms exchange between Mg and Ti environments on ~1s time-scale. The rutile-to-fluorite transition point for the ternary hydride that was found in thin film studies is accurately reproduced by Density Functional Theory calculations at 80 at.% Mg.

6.1 Introduction

MgH_2 has a very high reversible storage capacity of 7.6 wt% hydrogen. A major disadvantage however, is its very slow desorption rate making its practical use very difficult. However, it was shown in the previous chapters, that alloying of Mg with Sc vastly improves the (de)sorption kinetics. A reversible capacity of 1500 mAh/g (5.5 wt.% H) was reached for $Mg_{0.80}Sc_{0.20}$. The improved discharge rate compared to pure Mg was ascribed to the more favorable crystal structure of the hydride as shown by means of ex-situ X-Ray and Neutron Diffraction for Mg-contents of 75 and 65 at.%[121, 122]. The presence of empty octahedral interstices in the fluorite lattice enables much faster hydrogen diffusion as compared to the rutile structure of pure MgH_2, as was quantified by solid state ^{1}H NMR measurements (see Chapter 5). The rate of H-motion in the ternary hydride was shown to be more than 8 orders of magnitude higher compared to pure MgH_2 and about 1-2 orders of magnitude higher compared to pure ScH_2[115].

However, a major disadvantage of using Sc is its high cost. Therefore, it is desirable to replace Sc with a cheaper metal. The most suitable replacements are expected to be found among the elements that, like Sc, form a dihydride with the fluorite structure. This, in principle, limits the options to Ti, V, Y, Zr, Nb, La and the rare-earths, Hf and Ta.

Previous investigations on MgTi, MgV and MgCr thin films showed that the electrochemical properties of MgTi films are comparable to those of MgSc, reaching a reversible capacity of 1750 mAh/g (~6.5 wt.%) for $Mg_{0.80}Ti_{0.20}$. The reversible storage capacities, both at high and low current density are summarized in Fig. 69, for all the Mg-TM systems studied[123]:

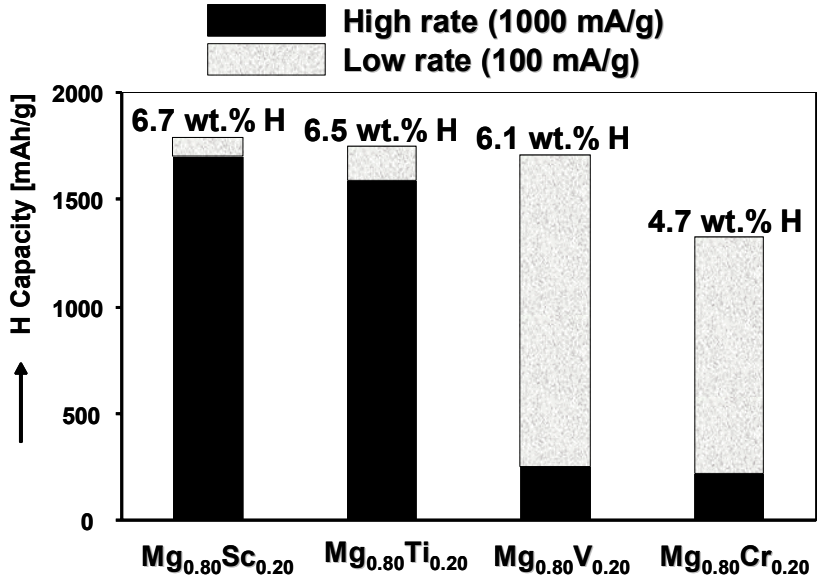

Fig. 69: Reversible storage capacities of $Mg_{0.80}TM_{0.20}$ (TM = Sc, Ti, V, Cr) thin films at 1000 and 100 mA/g. Notice how the relative capacity at high current suddenly drops going from Ti to V.

However, to make these materials in bulk form, there are some major problems to overcome as becomes obvious from the phase diagram presented in Fig. 70:

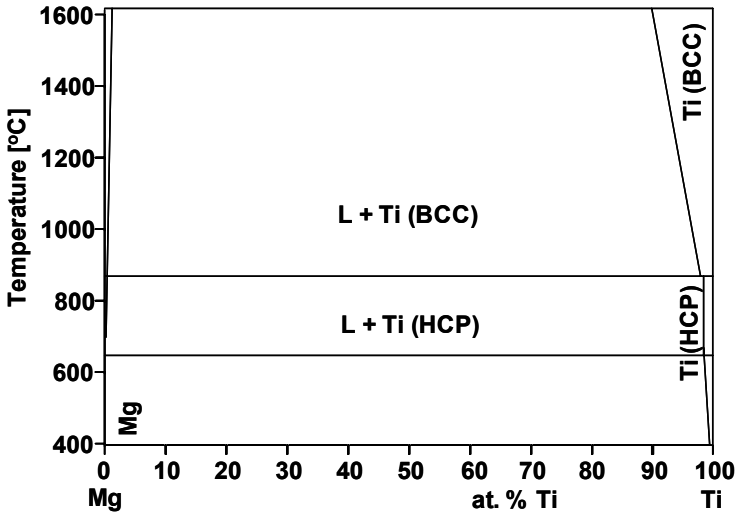

Fig. 70 : Equilibrium phase diagram of the Mg-Ti system.

The solid solubility of Ti in Mg is almost zero, even at elevated temperatures, and there are no known intermetallic compounds, ruling out any possibility of making bulk Mg-Ti alloys via the same metallurgical route as the one used for MgSc (see Chapter 4). Therefore, other ways have to be found to mix Mg and Ti at the atomic level. The boiling point of Mg (1090 ^{o}C) is below the melting point of Ti (1668^{o}C), ruling out melt-spinning and other rapid-solidification techniques for a binary mixture as they would involve pre-mixing of the molten metals.

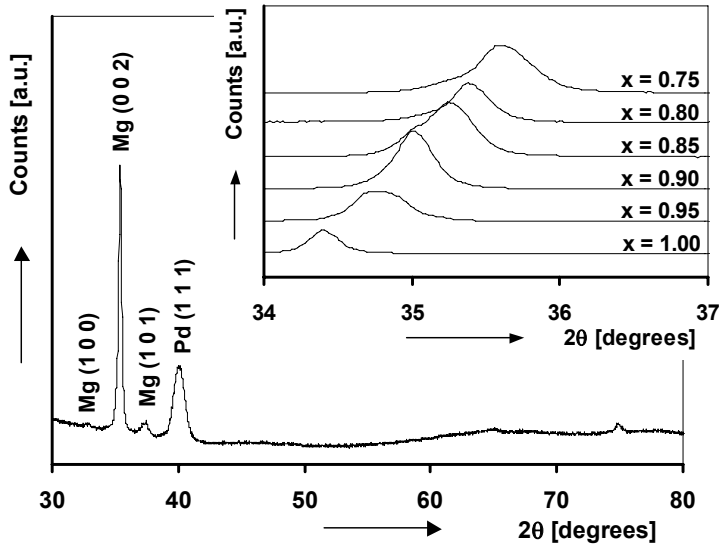

Fig. 71: XRD patterns of Pd capped Mg_xTi_{1-x} thin films for x = 0.75-1. Pattern for x = 0.80 is enlarged. The inset shows the (002) reflection as a function of x. Note how the peak position continuously shifts with composition indicating true alloying.

As is shown in Fig. 71, Mg-Ti thin films produced by e-beam deposition do exhibit extended solid solubility as is evidenced by the continuous shift in the position of the (002) reflection with changes in composition. Therefore, a way was sought to 'mimic' this behavior in a bulk material, despite the extremely low solid solubility in equilibrium (see Fig. 70). As the thin films are produced by e-beam deposition at room-temperature, which is not feasible for bulk materials of course, it can be assumed that a low-temperature technique is most likely to be successful for synthesizing bulk materials as well.

Mechanical alloying has long since been established as a very versatile way to produce non-equilibrium materials[124]. For instance, Co-Cu and Fe-Cu are virtually immiscible in thermodynamic equilibrium, but fully miscible by mechanical alloying[125]. Extending the solid solubility of Mg and Ti by mechanical alloying has been successfully attempted in the past. Sun and Froes reached a solubility of 24 at.% Mg in Ti by ball-milling of the elemental powders in a Spex 8000 mill[126]. Liang and Schulz reported a solid-solubility extension of Ti in Mg up to 12.5 at.%[127]. This shows that solid solubility extension occurs at both sides of the compositional range and the solubility of Mg in Ti seems to be larger than that of Ti in Mg, the same as for the equilibrium phase diagram. For Mg-rich mixtures, discrepancies between the nominal and dissolved amount of Ti were reported. For mixtures with 10 and 20 at.% Ti, the dissolved amount of Ti reached 8 and 12.5 at.%, respectively. On the Ti-rich side, higher Mg-contents than 24 at.% were not prepared so the saturation limits of Mg in Ti and Ti in Mg by mechanical alloying remain unknown. In both of the abovementioned studies, the hexagonal-close-packed (hcp) structure of pure Mg and Ti was retained.

When milling a mixture of ductile components, use of a Process-Control Agent (PCA) is often necessary to obtain a reasonable powder yield. The function of a PCA is to adsorb on the particles' surface to prevent cold-welding and lower the surface tension of the material, thereby reducing the energy needed to fracture the particles. An extensive overview of mechanical alloying and milling processes by Suryanarayana contains a listing of the most commonly used PCA's[124]. Most common are organic liquids such as ethanol, hexane, toluene or solid lubricants such as carbowax, graphite and stearic acid. For milling of ductile metals, stearic acid is by far the most commonly used.

From the work by Kyoi *et al.*[128] it is already known that ternary Mg-Ti *hydrides* can exist in bulk form. $Mg_7TiH_{\sim 13}$ was synthesized from MgH_2 and TiH_2 at 8 GPa and 873 K. However, upon desorption, the metal mixture decomposed into elemental Mg and Ti. From the work by Vermeulen *et al.*[129] it is known that the sorption kinetics of Mg-Ti thin films, which also retain the hcp-structure for a wide range of Ti contents, worsen significantly for Ti concentrations below 20 at.%. It is therefore desirable to achieve a Ti content that is larger than, or equal to, 20 at.%, which means that the 12.5 at.% Ti in Mg reached by Liang would be insufficient.

In the present study, an attempt was is to synthesize a bulk Mg-Ti hydrogen storage by mechanical alloying. Because the choice of PCA is known to affect the maximum achievable solubility levels in Cu-Fe[130], two different PCA's, graphite and stearic acid, are applied and the results are compared. Both high-and low-energy milling of binary Mg-Ti and ternary Mg-Ti-Ni mixtures was undertaken and the evolution of the phases formed during milling was studied with XRD. Transformation to cubic structures by mechanical alloying is reported for both the binary and ternary powder mixtures. Using a coarser Mg precursor, *i.e.* ribbon instead of powder, results in formation of hcp solid solutions. After activation by ball-milling with a Pd catalyst, the electrochemical characteristics were also investigated and will be reported in this chapter.

6.2 Experimental

6.2.1 Preparation

Mg powder (Goodfellow, particle size < 50 micron, 99.8% purity metal basis) or melt-spun ribbon (RSP Technologies Delfzijl, 60 micron thickness, 1.5 mm width), Ti powder (~325 mesh, Materials Research SA, Toulouse) and Ni powder (Johnson Mathey) were weighed and mixed manually in the appropriate ratios before loading into the milling-vial. High-energy milling was performed in a Spex 8000-230 ball-mill using tungsten-carbide-lined vials with

an nternal volume of 55 ml. The total powder load was around 5g for a ball-to-powder (BTP) ratio of 10 and 3g when the ratio was higher. Milling was done for intervals of 90 minutes or less to avoid overheating of the vials. After each interval, the vials were checked for cold-welding and scraped before continuing milling. The Spex 8000-230 ball mill was installed inside an Ar-flushed glove box and all powder handling was done under this inert atmosphere.

Low-energy milling was performed in an Uni-Ball-Mill-II from Australian Scientific Instruments (see Fig. 10). Six Cr-steel balls of 60 g each were used with a powder load of 30g. Milling was performed at 100 rpm for ~24 h intervals. The milling chamber was sealed with an O-ring to prevent air from leaking in. The apparatus as a whole was exposed to ambient atmosphere. This method was used only for sample III.

For the milling of powder mixtures, either graphite or stearic acid was added as PCA to prevent excessive cold-welding of the powders. When cold-welding was observed upon opening the vial, additional PCA was added, typically 0.5 wt.% at a time. X-Ray Diffraction analysis (XRD) was used to monitor the progress of the milling process.

Table 8: Compositions and experimental conditions of the samples described in the present chapter. SS stands for Stainless Steel, WC for Tungsten Carbide

Sample	Composition	Reactants	Balls, BTP ratio	PCA (wt.%)	XRD pattern in	Electrochem. measurements
I	$Mg_{0.80}Ti_{0.20}$	Mg, Ti powders	WC, 10	Graphite (5-10)	Fig. 72	
II	$Mg_{0.75}Ti_{0.25}$	Mg, Ti powders	WC, 10	Stearic acid (1.5-4.5)	Fig. 73	
III	$Mg_{0.75}Ti_{0.25}$	Mg, Ti powders	SS, 10	Stearic acid (1.5-4.5)	Fig. 74	
IV	$Mg_{0.65}Ti_{0.35}$	Mg, Ti powders	SS, 16	Stearic acid (1.5-4.5)	Fig. 75	Fig. 83
V	$Mg_{0.65}Ti_{0.35}$	Mg, Ti powders	SS, 16	Stearic acid (1.5-4.5)	Fig. 75	Fig. 83
VI	$Mg_{0.75}Ti_{0.25}$	Mg, Ti powders	SS, 16	Stearic acid (1.5-4.5)	Fig. 75	
VII	$Mg_{0.85}Ti_{0.15}$	Mg, Ti powders	SS, 16	None	Fig. 77	
VIII	$Mg_{0.65}Ti_{0.35}$	Mg ribbon, Ti powder	SS, 16	None	Fig. 78	Fig. 83
IX	$Mg_{0.75}Ti_{0.25}$	Mg ribbon, Ti powder	SS, 16	None	Fig. 78, 75	Fig. 84, Fig. 85
X	$(Mg_{0.80}Ti_{0.20})_{0.95}Ni_{0.05}$	Mg, Ti, Ni powders	WC, 10	Stearic acid (1.5-4.5)	Fig. 79	Fig. 86
XI	$(Mg_{0.80}Ti_{0.20})_{0.95}Ni_{0.05}$	Mg, Ti, Ni powders	WC, 10	Graphite (5-15)	Fig. 79	
XII	$(Mg_{0.65}Ti_{0.35})_{0.95}Ni_{0.05}$	Mg, Ti, Ni powders	WC, 10	Stearic acid (1.5-4.5)	Fig. 79	Fig. 87
XIII	$(Mg_{0.60}Ti_{040})_{0.95}Ni_{0.05}$	Mg, Ti, Ni powders	WC, 10	Stearic acid (1.5-7)	Fig. 80	Fig. 87
XIV	$(Mg_{0.75}Ti_{0.25})_{0.95}Al_{0.05}$	Mg ribbon, Ti, Al powders	SS, 16	None	Fig. 81	Fig. 88
XV	$(Mg_{0.75}Ti_{0.25})_{0.95}Ni_{0.05}$	Mg ribbon, Ti, Ni powders	SS, 16	None	Fig. 81	Fig. 88
XVI	$(Mg_{0.75}Ti_{0.25})_{0.90}Ni_{0.10}$	Mg ribbon, Ti, Ni powders	SS, 16	none	-	Fig. 88
XVII	$(Mg_{0.65}Ti_{0.35})_{0.95}Ni_{0.05}$	Mg ribbon, Ti, Ni powders	SS, 16	none	Fig. 81	

Table 8 summarizes the experimental conditions used for the alloys studied in this chapter. For samples prepared from Mg ribbon, addition of a PCA was found to be

unnecessary. In sample XIV, XV and XVI, the Ni or Al was added only *after* the $Mg_{0.75}Ti_{0.25}$ had been milled for 13h. The powder yield was determined prior to adding the third element so that the nominal composition was equal to that given in Table 8. Prior to electrochemical testing, the samples were activated by milling for 90 minutes with 5 at.% Pd powder, which acts as a catalyst.

6.2.2 Characterization

X-Ray Diffraction analysis (XRD) was used to monitor the progress of the milling process. Diffraction measurements were performed on a PANalytical X'Pert-Pro MPD Diffractometer using an X'Celerator detector or on a Rigaku D/MAX-B. Data was collected over a 2θ angular range of 10^o–100^o using Cu-K_α radiation at 40 kV and 40 mA.

For Transmission Electron Microscopy analysis, the sample powder was embedded in epoxy resin, polished and coated with a thin layer of Au, after which 1.5 μm of Pt was deposited onto the region of interest. The sample was then obtained by Focussed Ion Beam lift-out. TEM observations were performed on a TECNAI F30ST operated at 300 kV.

Electrochemical measurements were carried out in conventional thermostrated three-electrode cells at 25 ^{o}C. The cells contained 6M KOH aqueous electrolyte and the potential of the working electrode was measured versus a Pb-free Hg/HgO (6M KOH) reference electrode[18] from Koslow Scientific Company, USA. Unless stated otherwise, all potential values are given versus this reference. Galvanostatic measurements were performed using a Maccor M2300 battery tester (Maccor, Tulsa, USA).

Neutron Diffraction experiments were performed at the Institut Laue Langevin in Grenoble on the D1B instrument. The wavelength was set to 1.287 Å and the patterns were recorded every 10 min in the range 18° to 98° by the 400 cells of the Position Sensitive Detector (step=0.2° in 2θ). The alloy powder was prepared by ball-milling and ~4.5 g of material was brought into the beam inside a stainless steel sample holder connected to a calibrated volume through which deuterium gas could be introduced. An evacuated Vanadium metal furnace was used to heat the sample up to a temperature of 450^{o}C.

6.3 Results and discussion

6.3.1 Phase evolution during milling

6.3.1.1 Binary Mg-Ti mixtures with PCA

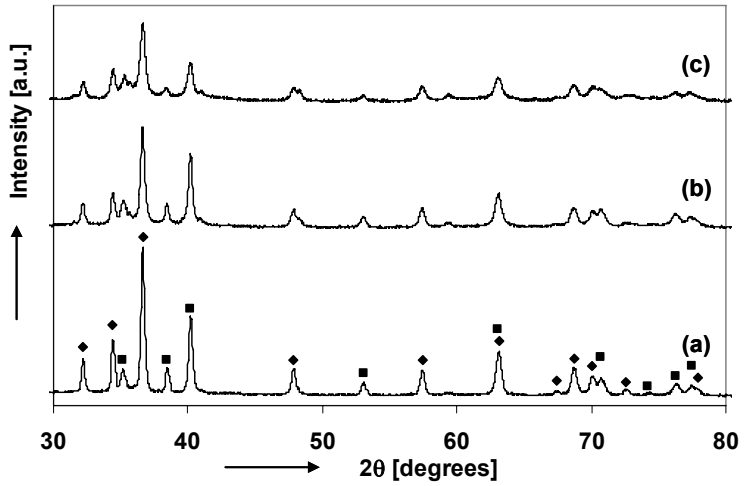

Fig. 72: XRD patterns of $Mg_{0.80}Ti_{0.20}$ milled with graphite (sample I), after 2.5 (a), 12 (b) and 16h (c) of milling. ♦: Mg, ■: Ti

Fig. 72 shows the X-Ray diffraction patterns of $Mg_{0.80}Ti_{0.20}$ milled with graphite (sample I) as a function of milling time. Apart from a broadening of the peaks and an increase in tungsten carbide contamination from the milling media during the course of the milling process, no changes occur. The size of the Mg crystallites has decreased to 38, 29 and 22 nm after 2.5, 8 and 16 hours of milling, respectively. The crystallite sizes for Ti are similar. No reflections of the graphite are found in the diffraction patterns, indicating that it has become amorphous. Additionaly, no evidence for the formation of a TiC phase is found, but only the reflections of the Mg and Ti starting materials, indicating that the carbon has not reacted with the metal. No shift of the Mg and Ti reflections is observed, which means that no alloying of the Mg and Ti is taking place. This is unexpected, since the work by Liang and Schulz clearly showed dissolution of the Ti in Mg after 12 hours of milling for similar Mg and Ti crystallite sizes.

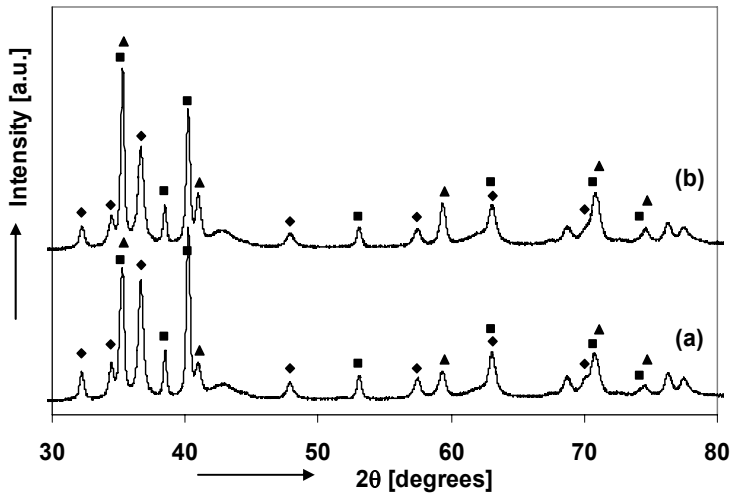

Fig. 73: XRD patterns of $Mg_{0.75}Ti_{0.25}$ (sample II) milled for 8 (a) and 12h (b). ♦: Mg, ■: Ti, ▲: fcc-structure with a = 4.40 Å.

When stearic acid is used instead of graphite, the situation is quite different. Fig. 73 shows the diffraction patterns of $Mg_{0.75}Ti_{0.25}$ (sample II) after milling for 8 (a) and 12 hours (b). Besides the reflections of pure Mg and Ti metal, two new reflections are clearly visible at 41^o and 59.4^o 2θ. The intensity of these reflections markedly increases between 8 and 12 hours milling time. Another remarkable feature is the sharp increase in intensity around 35.3^o. The Ti (100) reflection is also located around the same angle, but the theoretical intensity ratio between the (100), (002) and (101) reflections, at 35.12, 38.45 and 40.20^o, respectively, of 25:30:100 has drastically changed. This clearly indicates the emergence of a new reflection even if it cannot be fully resolved because of a large overlap with a peak of the starting material. Assuming the reflections at 41^o and 59.4^o are the (200) and (220) reflections of a face-centered-cubic structure, a lattice constant of ~ 4.40 Å can be calculated. All the peak positions of such a structure are indicated by the solid triangles in Fig. 73. It can be seen that, apart from the two aforementioned reflections, the overlap with the starting reactants is so large that a fully reacted sample is required to accurately determine the structure of the reaction products.

A $Mg_{0.75}Ti_{0.25}$ powder mixture was processed at low milling energies as well, using an Uni-ball Mill and stearic acid as PCA. Fig. 74 shows the diffraction patterns of sample III after 200 and 375 hours of milling. After 200 hours there are clear indications that a reaction has taken place. New reflections are emerging at the same 2θ as in sample II. When milling is continued for even longer times, the conversion of the material into the cubic phase continues:

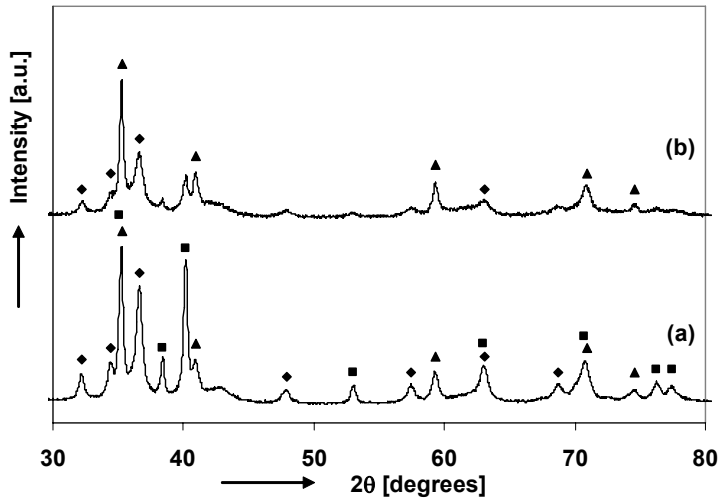

Fig. 74 : X-ray diffraction patterns of $Mg_{0.75}Ti_{0.25}$ processed in an Uni-ball Mill for (a) 200h and (b) 375h

After 375 hours, the Ti reflection at 40.2° has almost disappeared, whereas the peak at 35.3° has continued to increase in intensity. This confirms the result obtained at higher milling energies that the system is being converted into a mixture of 2 fcc phases.

Unfortunately, the powder processed in the Spex 8000 mill proved rather difficult to handle, showing a strong tendency to cold-weld onto the walls of the vial, despite the use of a relatively large amount of PCA. Due to a leak in the milling chamber, the powder in the Uni-ball mill started to oxidize after 400 h of milling, which is in itself already a rather unrealistically long reaction time of course. Therefore, a way was sought to improve the processability of the powder mixture in a high-energy milling process and/or speed up the reactions. It turned out that increasing the ball-to-powder weight ratio from 10 to 16, was effective in reducing the tendency for cold-welding and achieving quite short reaction times.

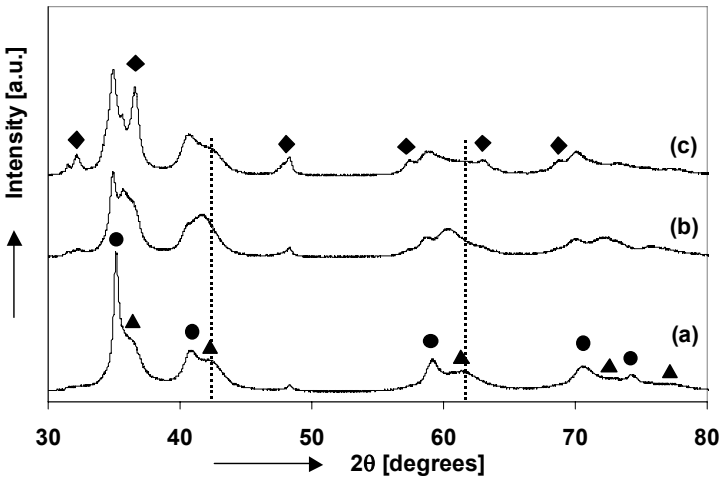

Fig. 75: XRD pattern (a): $Mg_{0.65}Ti_{0.35}$ milled for 5h using stainless steel balls (sample IV) , pattern (b): the same composition milled for 16h with WC balls (sample V), pattern (c): $Mg_{0.75}Ti_{0.25}$ milled for 28h (sample VI)

The X-Ray Diffraction pattern of $Mg_{0.65}Ti_{0.35}$ milled for 5 h (sample IV), is shown in Fig. 75 as pattern (a). The reaction is already completed after such relatively short time as almost no residual Mg is visible in the diffraction pattern. There are two cubic phases present in the sample with lattice constants of ~4.42 and ~4.25 Å. Based on a linear combination of the

molar volumes of Mg and Ti, a molar volume of 12.82 cm^3 is expected, which would correspond to a lattice constant of 4.40 Å. Therefore, the phase with larger lattice constant is likely very rich in Mg, whereas the phase with the smaller lattice parameter is more Ti-rich. Prolonged milling of the same composition (sample V) increases the relative abundance of the smaller fcc phase and the lattice parameter increases, indicating an increase in the Mg-content.

Unfortunately, determination of the relative abundances of the phases was very problematic due to a huge anisotropy in the peak widths of each of the crystallographic directions. The results are summarized in Table 9. As can be seen, the (111) reflection is relatively sharp for both phases, but all other reflections are considerably more broadened. The coherence length *L* was calculated by the Scherrer formula

$$L = \frac{\lambda}{B\cos\theta} \qquad (6.1)$$

, where λ is the wavelength of the X-rays (1.5405 Å) and B is the full-width-at-half-maximum of the diffraction peak in radians. Table 9 sums up the peak positions, FWHM in degrees and the coherence length *L* for the first three reflections of both fcc phases. The values for *L* range from almost 25 nm for the (111) direction to no more than 6 for the (200) of the largest fcc phase. The larger coherence length in the (111) direction could be expected, since this is the close-packed direction, with the same in-plane atomic packing as the hexagonal c-direction.

Table 9: Peak positions and coherence lengths for both fcc phases from Fig. 75 (a) (Sample IV)

(h k l)	***Peak position***	***B***	***L***
	[degrees 2θ]	[degrees]	[nm]
(1 1 1)	35.151	0.411	23
(1 1 1)	36.231	1.882	5
(2 0 0)	40.782	1.476	6
(2 0 0)	42.362	2.296	4
(2 2 0)	59.114	1.069	9
(2 2 0)	61.274	3.183	3

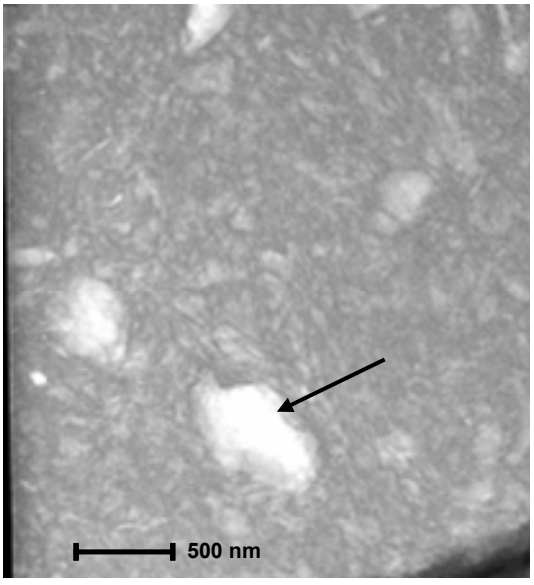

Fig. 76: TEM image of sample IV after 5h milling (see Fig. 75 (a)). The arrow points out a pure Ti particle.

Fig. 76 shows a TEM image of the same $Mg_{0.65}Ti_{0.35}$ sample the diffraction pattern of which was shown in Fig. 75. As was already clear from the XRD patterns, the material seems to consist of two phases with different compositions. The very bright white spot indicated by the arrow was found to be pure Ti by EDX analyses. The smaller bright spots inside the gray 'matrix' were found to be at least 80 wt.% Ti, which indicates they may also be pure Ti if these particles are thinner than the sample. A transformation from a hcp to a fcc structure has been reported for both elemental Ti and Zr and Ti-Zr solid solutions.[131, 132, 133, 134] Therefore, it is likely that the fcc phase with the smaller lattice constant is pure Ti, somehow transformed from hcp to an fcc structure and that the phase with the larger lattice constant is a mixed Mg-Ti phase.

When the Mg-content is increased from 65 to 75 at.% the result is somewhat surprising. Contrary to sample II, the higher BTP ratio enables processing of the powder until the reactions are at steady state. It would be expected that the relative amount of the Mg-rich phase would increase, but it is clear from Fig. 75 (pattern (b)) that this is not the case. After 16 h, when all the hcp Ti has been converted, some residual Mg remains, which is not converted anymore upon prolonged milling. Further milling up to 28 h showed no further progression of the reaction.

6.3.1.2 Binary mixtures without PCA

To investigate whether the addition of stearic acid plays a decisive role in the tranformation of the material to a cubic structure, processing of powder mixtures without stearic acid was attempted as well. $Mg_{0.65}Ti_{0.35}$ and $Mg_{0.75}Ti_{0.25}$ powder mixtures processed without the use of a PCA invariably resulted in an extremely hard and coarse-grained material after only a few hours, after which further milling no longer lead to any progress in the reaction. However, a Mg/Ti ratio of 85/15 (sample VII) allowed effective processing for longer times. The diffraction patterns are shown in Fig. 77.

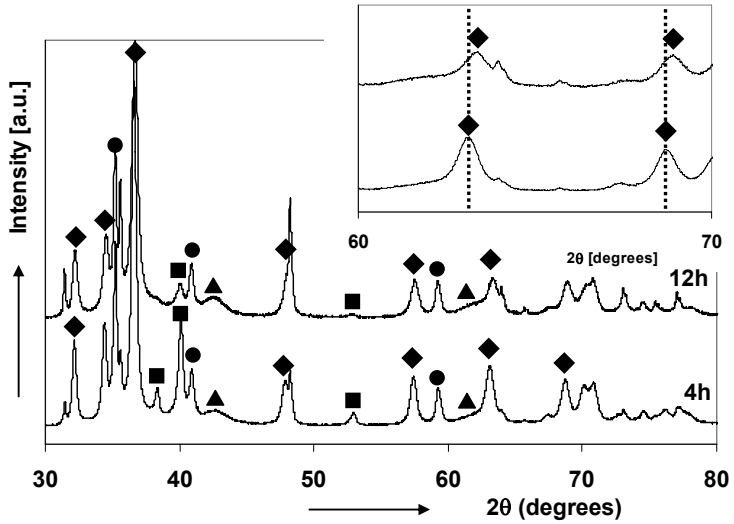

Fig. 77: $Mg_{0.85}Ti_{0.15}$ powder mixture milled without PCA for 4 and 12h. ♦: Mg, ■: Ti, ●: fcc structure with a = 4.40 Å, ▲: fcc-structure with a = 4.25 Å.

Once more, the same two cubic structures are observed after 4h of milling, proving that the use of a PCA by itself does not induce the transformation from hcp to cubic structures, although graphite did seem to prevent it (see sample I). From 4 to 12h of milling, the amount of the smaller fcc phase seems to increase, indicating that Ti is being converted from hcp to fcc. However, the reflections of Mg have shifted slightly towards higher angles, indicating

that dissolution of Ti is taking place simultaneously with the transformation to cubic phases. Table 10 lists the peak positions and corresponding d-spacings for the Mg patterns from Fig. 77. It can be seen that the Mg-pattern is significantly shifted after 12h of milling, by a few tenths of a degree. The values for the a-and c-axes that can be calculated from the patterns are 3.211 and 5.213 *vs.* 3.205 and 5.196 after 4 and 12h of milling respectively. The amount of Ti that is dissolved in the Mg phase can be estimated from the lattice constants to be ~2 at.%[127].

Table 10: Peak positions and d-spacings for the strongest Mg reflections after 4 and 12h of milling of a $Mg_{0.85}Ti_{0.15}$ (sample VII) powder mixture.

(h k l)	***Peak position***		***d-spacing***	
	degrees 2θ		Å	
	4h	12h	4h	12h
(1 0 0)	32.144	32.195	2.783	2.778
(0 0 2)	34.381	34.496	2.606	2.598
(1 0 1)	36.586	36.654	2.454	2.450
(1 0 2)	47.798	48.009	1.901	1.894
(1 1 0)	57.369	57.483	1.605	1.602
(1 0 3)	63.057	63.293	1.473	1.468
			a = 3.211 Å c = 5.213 Å	a = 3.205 Å c = 5.196 Å

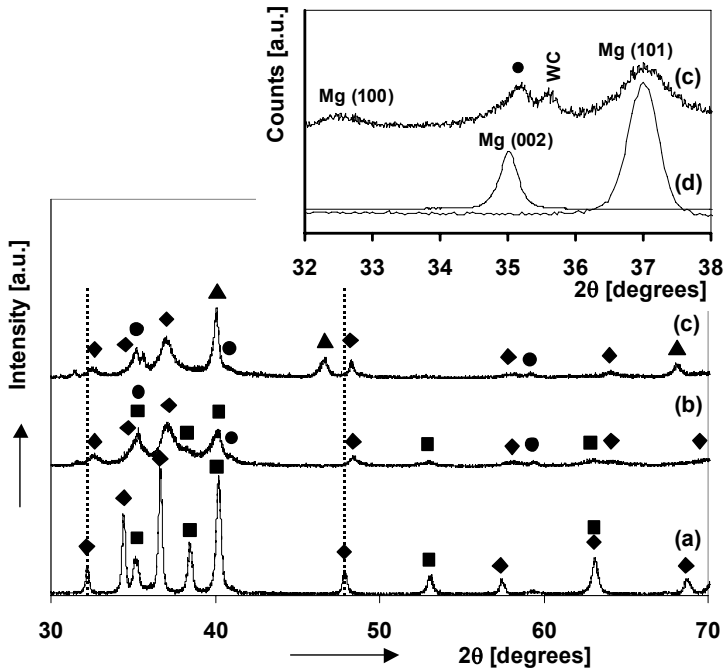

Fig. 78: XRD patterns of $Mg_{0.65}Ti_{0.35}$ using melt-spun Mg ribbon as starting material (Sample VIII), milled for 40 minutes (a) and 9 hours (b) and $Mg_{0.75}Ti_{0.25}$ (sample IX, curve (c)) activated with Pd (▲). There is a trace amount of the fcc phase (•) detected besides residual Ti (■) and a considerably shifted Mg-pattern (◆) further accentuated by the dotted lines at the original peak positions. The inset shows the (002) and (101) reflections of a $Mg_{0.9}Ti_{0.1}$ thin film (d) in comparison with pattern (c).

The X-Ray Diffraction patterns of $Mg_{0.65}Ti_{0.35}$ and $Mg_{0.75}Ti_{0.25}$ prepared from Mg-ribbon, samples VIII and IX, are depicted in Fig. 78. Contrary to the results obtained with powdered Mg and Ti milled with stearic acid, using Mg ribbon and no PCA retains the hexagonal

structure of Mg. The diffraction peaks do, however, undergo a significant shift towards higher 2θ values, indicating a decrease in volume resulting from (partial) dissolution of the Ti in Mg. This is in accordance with the results obtained previously by Liang and Schulz on a Mg-20% Ti mixture and by others on the Ti-rich side of the system. Although there are no longer any Ti reflections in pattern (c), the Ti-content in the Mg is estimated from the lattice parameters (a = 3.18 Å, c = 5.14 Å) is only 10 at.%[126, 127]. For comparison, the inset in Fig. 78 shows the (002) and (101) peaks of a $Mg_{0.90}Ti_{0.10}$ thin film. The peak positions coincide very nicely, further corroborating the estimate of the Ti-content of 10 at.%. However, this is considerably less than the 25 at.% that the material nominally contains. Apparently, a considerable amount of Ti is still converted to other compounds. A trace of fcc phase with a ~4.4 Å is again detected. The fcc Ti phase with a = 4.25 Å is not yet visible, but given the extremely small crystallite size of this phase (see Table 9), this is not surprising.

6.3.1.3 Ternary Mg-Ti-Ni mixtures with PCA

It was found by Vermeulen *et al.* that addition of a third element is effective in adjusting the thermodynamic properties of Mg-Ti thin films[135]. Addition of Al or Si was effective in shifting the equilibrium pressure of a considerable part of the isotherm towards near-atmospheric pressures. For the bulk system, the same was attempted by addition of small amounts of Al and Ni. Even though Ni was not tested in the study by Vermeulen *et al.*, a destabilizing effect would be expected according to the 'rule of reverse stability', which states that a more stable the metal alloy forms a less stable hydride[136], because Ni (as well as Al and Si) has a negative enthalpy of mixing with both Mg and Ti. The materials were prepared from metal powders with addition of stearic acid or graphite as PCA (samples X-XIII) or from Mg ribbon, Ti powder and Ni/Al powders (samples XIV-XVII).

The phase evolution as a function of milling time was essentially the same as for the binary system. Using Mg powder, 2 fcc structures are eventually formed, the same as for $Mg_{0.65}Ti_{0.35}$. The XRD patterns of $(Mg_{0.80}Ti_{0.20})_{0.95}Ni_{0.05}$ milled with stearic acid (sample X) and graphite (sample XI) and $(Mg_{0.65}Ti_{0.35})_{0.95}Ni_{0.05}$ (sample XII) are shown in Fig. 79:

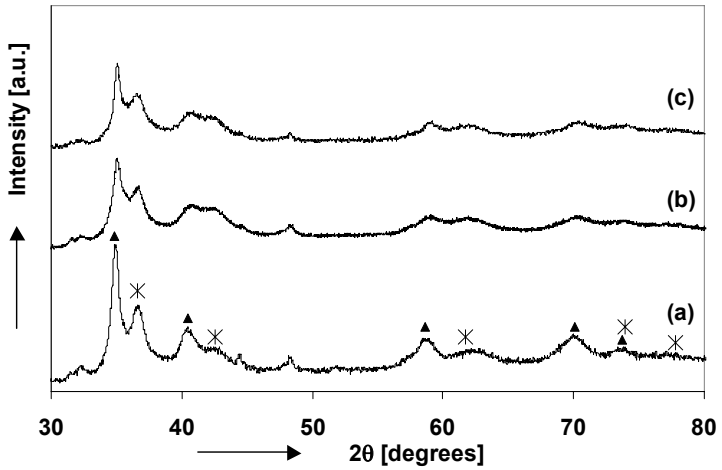

Fig. 79: XRD patterns of $(Mg_{0.80}Ti_{0.20})_{0.95}Ni_{0.05}$ (sample X) after 24h of milling (a), the same composition (sample XI) after 28h of milling with graphite (b) and $(Mg_{0.65}Ti_{0.35})_{0.95}Ni_{0.05}$ (sample XII) after 16h of milling (c).

Two fcc-structures are visible with lattice constants of 4.41-4.45 and 4.25-4.27 Å with a much larger peak-width for the latter phase. It is interesting to note here that also sample XI, which is a ternary mixture with 5 at.% Ni milled with graphite, is converted to the same two cubic

phases, while this was not possible for a binary Mg-Ti mixture (sample I). Also noteworthy is that the ternary mixture can be processed at the lower BTP ratio of 10 instead of 16 and that almost all the Mg is converted, even at a Mg/Ti ratio of 80/20. This is quite different from the binary system, where a signifcant amount of residual hcp Mg could be detected at a Mg/Ti ratio of 75/25 (see Fig. 75). Similar to the binary alloys, the peak width of the phase with the smaller lattice constant is considerably larger compared to the phase with the largest volume.

As can be seen in Fig. 79, and has been summarized for clarity in Table 11, changing the Mg/Ti ratio has only a small effect on the lattice constants of both phases, varying as little as 0.02 Å for both phases, which is, given the large peak width and overlap, not significant. However, contrary to the binary mixtures, changing the Mg/Ti ratio does affect the relative abundances of the phases, in accordance with mass-balance considerations. This is especially clear when one compares diffraction patterns (a) and (c) in Fig. 79 in the range between 40 and 45°.

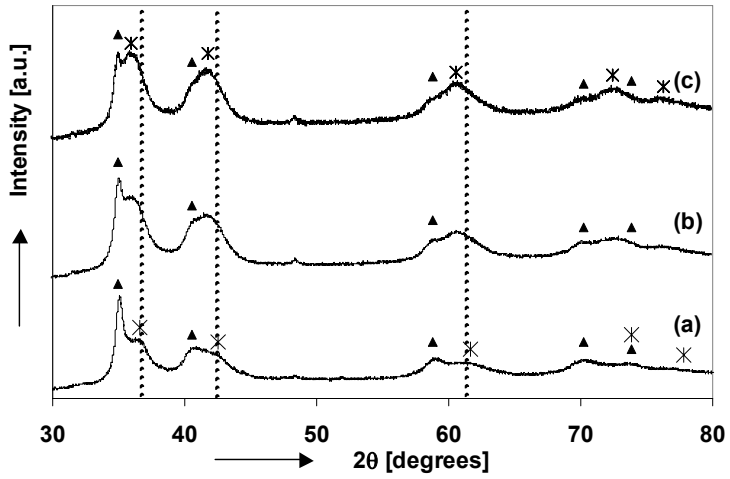

Fig. 80: XRD patterns of $(Mg_{0.60}Ti_{0.40})_{0.95}Ni_{0.05}$ (sample XIII) milled for 16 (a), 32 (b) and 46 h (c).

Fig. 80 depicts the diffraction patterns of $(Mg_{0.60}Ti_{0.40})_{0.95}Ni_{0.05}$ (sample XIII) after 16, 32 and 46 hours of milling. After 16h the starting reactants have disappeared. The fcc-phases have lattice constants of 4.44 Å and 4.25 Å the same as for x = 0.80 and x = 0.65. When milling is continued, the phase with a lattice constant of 4.44 Å remains essentially unaltered, regarding both the lattice constant and peak width. The smaller fcc-phase, however, starts to increase in both relative amount and lattice constant, which increases from 4.25 Å to 4.30 Å after 32 hours and eventually rises to 4.33 Å after 46 hours of milling. The fcc-phase with the larger lattice constant has by then almost disappeared. For clarity, a summary of all the lattice constants of the fcc-phases in Fig. 79 and 80 is given in Table 11.

Table 11: Lattice constants of both fcc phases for ternary Mg-Ti-Ni samples (X-XIII)

Sample	milling time (hours)	lattice constant fcc I (Å)	lattice constant fcc II (Å)
X	24	4.45	4.26
XI	28	4.44	4.25
XII	16	4.43	4.27
XIII	16	4.44	4.26
	32	4.44	4.30
	46	4.45	4.33

6.3.1.4 Ternary Mg-Ti-Ni,Al mixtures without PCA

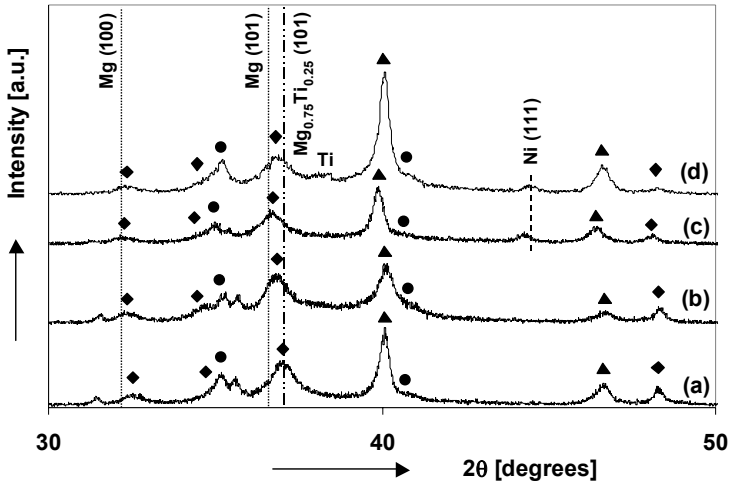

Fig. 81 XRD patterns of Pd-activated ternary mixtures. (a): $Mg_{0.75}Ti_{0.25}$ (sample IX), (b): $(Mg_{0.75}Ti_{0.25})_{0.95}Al_{0.05}$ (sample XIV), (c): $(Mg_{0.75}Ti_{0.25})_{0.95}Ni_{0.05}$ (sample XV) and (d): $(Mg_{0.65}Ti_{0.35})_{0.95}Ni_{0.05}$ (sample XVII). The original positions of the Mg (100) and (101) peaks are indicated in the figure (dotted lines) as well as the Mg (101) position (dash-dotted line) in the binary $Mg_{0.75}Ti_{0.25}$ mixture to illustrate the effects of Ni and Al addition. ◆: Mg, ●: fcc phase a = 4.42 Å, ▲: Pd

For ternary mixtures where Mg ribbon is used instead of powder, the results are quite different. For samples IX, XIV and XV, first a $Mg_{0.75}Ti_{0.25}$ mixture was milled for 13 hours, after which, in sample XIII and XIV, the alloying element Al or Ni was added and milling continued for 5h before activation with Pd. The X-ray diffraction pattern of sample IX was already shown in Fig. 78 and is included in Fig. 81 for comparison. In order to separate the effects of using a coarser Mg precursor (without PCA) and adding the third element at a later time, ($Mg_{0.65}Ti_{0.35}Ni_{0.05}$) where Ni was mixed in *at the beginning* of the milling process, was also synthesized as sample XVII and milled for the same duration as sample VIII (9h).

It can be seen that the addition of Al or Ni does not result in additional phases that can be detected with XRD. This means that if new phases are formed, they are either amorphous or nanocrystalline. However, there are other indications that the alloying elements are having an effect. The pattern of the binary mixture shows diffraction lines of a shifted hexagonal pattern, a trace of cubic phase and Pd. The dashed lines in Fig. 81 mark the peak positions of pure Mg. Clearly, addition of Al and Ni causes the hexagonal pattern to shift back towards these positions, suggesting that Ti is migrating back out of the Mg(Ti) solid solution and forms an

alloy with the Al or Ni. Indeed, from a comparison with the data presented by Liang and Schulz[127], a Ti-content below 5 at.% is found, where it was 10% for the binary alloy.

There is a small difference in the peak position of the Ni (111) reflection between patterns (c) and (d), which indicates that some Ti has dissolved in the fcc Ni in sample XV. The Ni (111) peak is found at its theoretical position in pattern (d), despite the longer mixing time of Ni with Ti for sample XVII (9h) compared to sample XV (5h). Apart from the absence of the shift in the Ni-peak, the moment of Ni addition has only minor influence on the result. Ti dissolves in Mg, the same as for the binary $Mg_{0.65}Ti_{0.35}$ mixture, but the amount of dissolved Ti is clearly less than in samples VIII and IX as derived from the peak positions in the diffraction pattern. This is, however, distinctly different from the result obtained from the powder mixtures milled with graphite (samples I and XI), where the addition of Ni was shown to trigger the conversion into a cubic structure.

Discussion I

Mg and Ti have almost zero solid solubility in thermodynamic equilibrium. This has been called rather surprising by some[137] as the so-called Hume-Rothery criteria are largely met by Mg and Ti:

1) the elements are isostructural
2) the electronegativities are similar
3) the atomic radii do not differ by more than 15%

However, the elements do have different valences, Ti is normally tetravalent whereas Mg is divalent, which was argued the 'only unfavourable factor for significant solid solubility to occur' by Zhou *et al.*[137]. However, rather than looking at the atomic radii, it is better to compare the molar volumes. The molar volume of Mg is 14.00 cm^3, whereas that of Ti is only 10.64 cm^3, which is more than 30% difference with respect to Ti. Furthermore, the covalent (or metallic) and ionic radii of an atom always strongly depend on the direct chemical environment and one should therefore be very careful when comparing atomic sizes of pure elements. However, the fact that Mg-Zr system also has almost zero solid solubility, while differing less than 0.15% in molar volume, indicates that the difference in valence is indeed a more important factor in preventing mutual solid solubility.

In the present study, milling of a binary Mg-Ti powder mixture did not result in the formation of a hexagonal solid solution when graphite was used as PCA. This is unexpected, since the work by Liang and Schulz[127] clearly showed dissolution of the Ti in Mg after 12 hours of milling for similar Mg and Ti crystallite sizes, but comparison of the results is a bit difficult, because no information about the use of a PCA was given in this particular study. However, using stearic acid as PCA did result in compound formation, but the resulting crystal structure is cubic.

The formation of the fcc high-pressure modification of normally hcp-structured metals upon mechanical milling has been reported previously for a variety of rare-earth metals by Alonso *et al.*[138] However, their results had to be rectified eventually when it turned out that this transformation was caused by contamination with oxygen, nitrogen and hydrogen due to poorly sealed vials[139]. The process control agent can also be a source of contamination for the metal phases. It is therefore important to consider whether the results obtained here are due to contamination or result from the intrinsic chemical properties of the metal powder mixture.

The Spex-mill is installed inside an Ar-flushed glove box, so gaseous contaminants can be ruled out. However, the PCA can act as a carbon source and lead to the formation of carbides. TiC has an fcc structure with a lattice constant of 4.37 Å. For a binary Mg-Ti mixture milled

with pure carbon (graphite) as a PCA no cubic phases were found in the diffraction patterns. For all samples the lattice constants of the cubic phases were always significantly different from 4.37 Å, which means that TiC was never formed, neither in the samples milled with graphite, nor in those milled with stearic acid.

Besides carbon, stearic acid also introduces a small amount of oxygen and a considerable amount of hydrogen into the metal powder mixture. A study by Wang *et al.* on mechanical alloying of Zr and Ti, similar to the study by Bera *et al.*[133], suggests that Zr can absorb hydrogen from stearic acid. Although the authors themselves concluded that Zr dissolved into Ti, the emergence of new reflections at 32.6 and 54.6°[140] is actually consistent with the formation of $ZrH_{2-\delta}$ with a = 4.76 Å. It is worthwhile to note here that during the present work, the formation of this fcc phase was also observed upon addition of Zr to compositions similar to sample XI. This phase evolved irrespective of the amount of Zr, which strongly suggests that it is a result of a reaction between Zr and the PCA. Even more pronounced was the case for a Mg-Sc mixture milled with stearic acid where a fcc phase with a = 4.78 Å, exactly the same as ScH_2, was found (see Fig. 82).

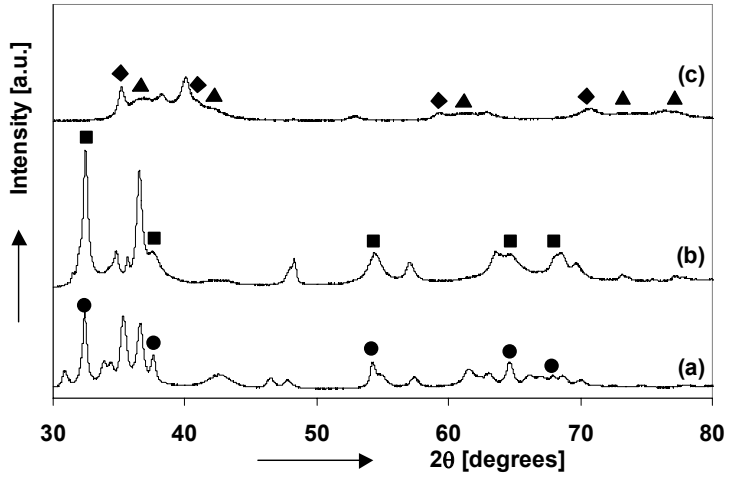

Fig. 82: XRD patterns of $Mg_{0.75}Sc_{0.25}$ metal mixture milled with 2 wt.% stearic acid for 4h (a), $Mg_{0.75}Zr_{0.25}$ powder mixture milled with 2 wt.% stearic acid for 4h (b), Ti 'blank' sample: Ti powder milled with 2.5 wt.% stearic acid for 10h (c). ●: ScH_2, ■: ZrH_2, ▲: fcc Ti, ♦: TiH_2

Especially the ScH_2 in pattern (a) shows up as a set of rather sharp diffraction lines, but also the $ZrH_{2-\delta}$ can be quite readily identified in pattern (b). This shows that one should be careful in choosing a PCA, as very stable hydride-formers can apparently dehydrogenate an organic compound during mechanical milling.

In view of these results, it is quite important to consider whether the fcc phase observed in the Mg-Ti mixtures with a lattice constant of up to 4.45 Å, is a TiH_2-like phase, as the lattice parameters are almost equal. Pattern (c), Ti powder milled for 10h with stearic acid, does show a small amount of TiH_2, but the major part of the material consists of hcp and fcc Ti. The $Mg_{0.85}Ti_{0.15}$ mixture milled *without* stearic acid (sample VII), also contains two cubic phases after 12h of milling (see Fig. 77); the same as in the other binary Mg-Ti and the ternary Mg-Ti-Ni mixtures. Therefore, it must be concluded that the largest of the two fcc phases is not a hydride phase, but a metallic phase consisting of Mg and Ti. The aforementioned studies by Manna *et al.* and Bera *et al.* used toluene as an additive[131, 133]. As this is a highly unsaturated hydrocarbon, it is unlikely that hydride formation occurred in these studies, which means their that the observed hcp-fcc transition is most likely an intrinsic property of Ti and Zr.

Besides formation of the two cubic phases, dissolution of Ti in hcp Mg is also taking place in sample VII as evidenced by a small shift of the Mg peak positions. This was never observed in any of the powder mixtures milled with stearic acid or graphite. These observations are in line with previous results obtained on Cu-Fe mixtures, where the final solute content was also significantly influenced by the use of a PCA[130]. Nevertheless, the final solute level that was achieved was quite low, only a few at.%, and the transformation into cubic structures was still the dominant reaction mechanism. It must therefore be concluded that the use of stearic acid prevents mutual dissolution of the hcp phases, but that it is not the most important factor in driving the hcp-to-cubic transformation. The latter is probably more heavily influenced by impurities already present in the starting powders such as oxygen. Chemical analysis typically shows the oxygen content to be ~4 wt.% for the Mg powder used in the present study.

The latter observation is further corroborated by the results obtained using Mg ribbon instead of fine powder. The dimensions of the ribbon; 60 micron thickness, 1.5 mm width and several meters length, are much larger and the specific surface area much smaller, compared to the powder and hence the oxygen content will be much lower. Indeed, in samples VIII and IX only a trace amount of cubic phase is found and the shift in the Mg lattice parameters is much larger compared to the $Mg_{0.85}Ti_{0.15}$ powder mixture.

Theoretical studies indicate that the early transition metals transform from hcp to bcc and eventually fcc, following the trend in the equilibrium structures across the periodic table from Sc to Ni, under the influence of very high pressures. This phenomenon has been ascribed to transfer of s-electrons to the d-band with increasing pressure[141, 142]. The particular case for Ti has never been experimentally elucidated, but a study by Skriver[143] showed that the energy difference between fcc and hcp Ti is ~ 4 mRy, corresponding to only 5 kJ/mol.

It is important to note here that this theoretically and experimentally confirmed intrinsic tendency of Ti to transform to a cubic phase imposes limitations on the solute levels that can be achieved. As the hcp-fcc transformation of Ti will always take place during mechanical milling, the amount of Ti that will dissolve in Mg will always be less than the nominal composition. Indeed, the difference between the dissolved amount of Ti and the nominal amount is rather high; 10% *vs.* 25. Liang and Schulz also reported discrepancies between the nominal and dissolved Ti content, which reached 8 at.% for a Mg-10%Ti mixture and 12.5 at.% for a Mg-20%Ti mixture. The remainder of the Ti was present as pure Ti particles with an apparently amorphous structure as no evidence of a second phase was present in the diffraction patterns[127]. This is in agreement with the observations presented in this chapter, where no fcc Ti was detected in samples VIII and IX. Apparently, hcp Ti is first converted to an amorphous state and recrystallizes in a fcc structure after prolonged milling. The results obtained on $Mg_{0.65}Ti_{0.35}$ and $(Mg_{0.60}Ti_{0.40})_{0.95}Ni_{0.05}$ after prolonged milling (see Fig. 80) indicate that Mg can be dissolved in this fcc Ti as evidenced by an increase in the lattice constant. It was found by Suryanarayana *et al.* that ~6 at.% of Mg could be dissolved into fcc Ti by mechanical alloying, although it was not clear whether this was an upper solubility limit[144].

Contrary to the binary mixtures, it is possible to react all the Mg in a ternary mixture with more than 65 at.% Mg. The diffraction pattern of $(Mg_{0.80}Ti_{0.20})_{0.95}Ni_{0.05}$ (sample X, see Fig. 79) shows only very small amounts of residual Mg and free Ni. The lattice constant of the small fcc phase is the same as for the binary mixtures, which could be expected since this phase consists of pure fcc Ti. However, the lattice parameter of the larger fcc phase is slightly higher than that for the binary alloys (see Table 11), which means Ni, which has a much smaller molar volume than either Ti and Mg, is not dissolved into this phase either. This is a strong indication that the Ni reacts with part of the Mg, that would have remained unreacted in a binary mixture, to form an amorphous or nanocrystalline Mg-Ni phase. The formation of

binary and ternary amorphous Mg-Ni-(Ti) alloys is well known and these materials have also been intensively investigated for electrochemical hydrogen storage[145, 146, 147].

For the alloys prepared with Mg ribbon and no PCA, addition of Ni or Al, which both have a negative enthalpy of mixing with Ti and Mg, results in migration of Ti out of the hcp solid solution phase (see Fig. 81). No secondary phase was detected by XRD for the mixture with Al, which indicates that the resulting TiAl phase is amorphous. This is in agreement with an amorphization range between 10 and 75 at.% Al that was found for binary Ti-Al mixtures[124]. For Ti-Ni, an amorphization range between $Ti_{0.9}Ni_{0.1}$ and $Ti_{0.3}Ni_{0.7}$ has been established by Murty *et al.*, while for Ti-contents below 20 at.% a fcc solid solution was found by the same authors[148, 149]. In the present study, a crystalline fcc Ni phase was found in the $(Mg_{0.75}Ti_{0.25})_{0.95}Ni_{0.05}$ alloy although the amount was apparently very small. The amount of dissolved Ti, as estimated from the shift in the (111) peak, only a few at.% with respect to Ni, is much smaller than the amount of Ti that has been leached from the Mg-phase, so it is likely that an amorphous Ti-Ni phase has also been formed.

6.3.2 Electrochemical properties

6.3.2.1 Binary Mg_xTi_{1-x} mixtures

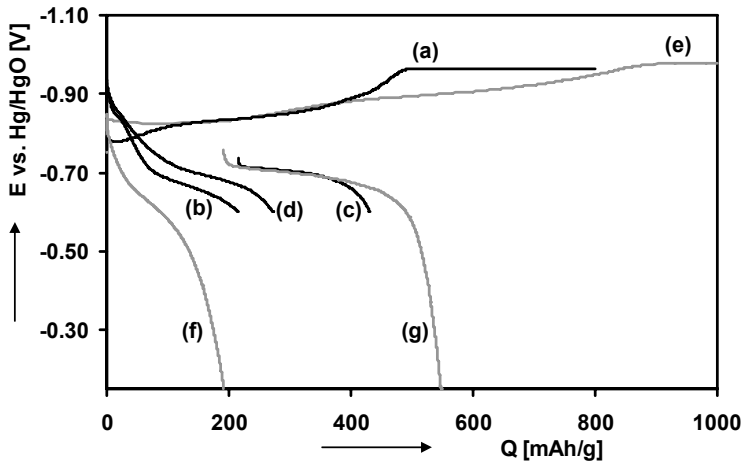

Fig. 83: Electrochemical response of binary cubic, (a)-(d), and hcp, (e)-(g), $Mg_{0.65}Ti_{0.35}$ mixtures. (a): Charging at 50 mA/g of sample IV activated after 5h, (b) and (c): discharge at 50 and 10 mA/g of sample IV, (d): discharge at 10 mA/g of sample V activated after 16h, (e): charging at 50 mA/g of sample VIII, (f) and (g): discharge at 50 and 10 mA/g of sample VIII

Fig. 83 depicts the electrochemical response of a $Mg_{0.65}Ti_{0.35}$ powder mixture in the cubic (curves (a)-(d)) and hexagonal structure (curves (d)-(f)). The largest difference between the two crystallographic modifications lies in the absorption capacity before the Hydrogen Evolution Reaction (HER) sets in, which is almost twice as large for the hexagonal compound as compared to the cubic one. The discharge capacity is not very strongly influenced and differs no more than 20% between the two alloys. The rate capability of the cubic modification is considerably higher; about 50% of the total discharge capacity can be extracted at 50 mA/g, whereas this is less than 35% for the hexagonal modification. Prolonged milling of the cubic material has a negative effect in the capacity. The total discharge capacity (10 mA/g) of sample V milled for 16h is only ~65% of that of the same sample activated after only 5h of milling. Longer milling times resulted in an increase in the amount of the Ti-rich fcc phase (see Fig. 75), which apparently has much poorer hydrogen absorption properties.

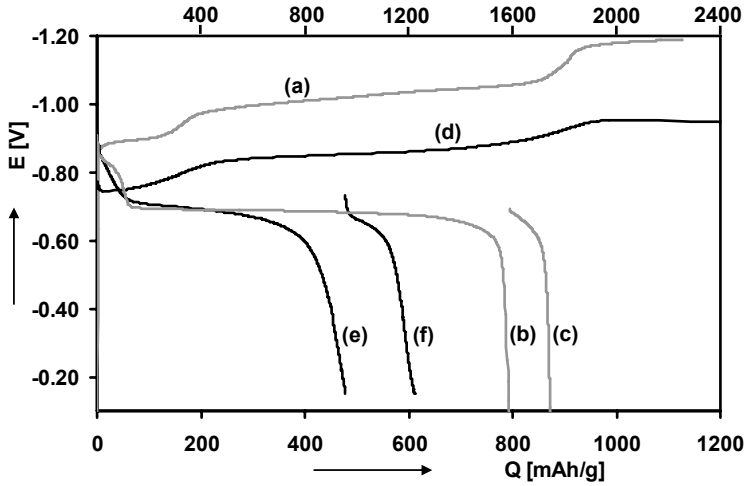

Fig. 84: Comparison of $Mg_{0.80}Ti_{0.20}$ thin film with $Mg_{75}Ti_{0.25}$ bulk material (sample IX). Curve (a)-(c), top x-axis: charging (5 A/g) and discharging (1 A/g and 100 mA/g) of thin film. Curve (d)-(f), bottom x-axis: charging with 10 mA/g and discharging with 10 and 5 mA/g of bulk material

The electrochemical response of Pd-activated $Mg_{0.75}Ti_{0.25}$ powder and a Pd-capped $Mg_{0.80}Ti_{0.20}$ thin film are depicted in Fig. 84. The thin film accepts ~1800 mAh/g at a rate of 5 A/g, which is almost twice as much as the bulk material (975 mAh/g) at 10 mA/g. The shape of the charging curves, however, is very similar in both cases. This is not surprising, because the structure of the starting materials is hexagonal in both cases and a similar behavior in the first charge/discharge cycle can, therefore, be expected. The discharge capacity of the bulk material is, however, much lower than the charge acceptance and the relative difference between charge and discharge capacity is also much larger than for the thin film. Even at a current rate of only 5 mA/g, the discharge capacity of the bulk material reaches only 600 mAh/g (or 2.25 wt.%).

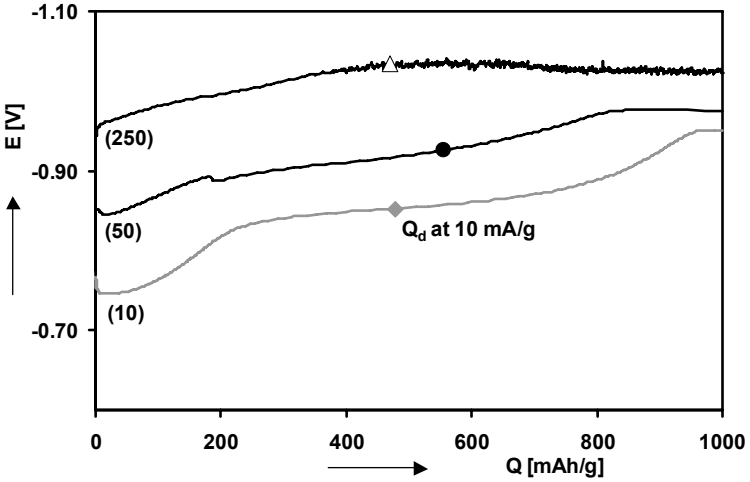

Fig. 85: Electrochemical response of sample IX as a function of the charge/discharge current. Charging current densities in mA/g are between brackets. The total discharge capacity at 10 mA/g is indicated in each curve.

Changing the charging current density also changes the behaviour of the material. The charging capacity until HER is ~975 mAh/g for a current rate of 10 mA/g and decreases to 825 and ~450 mAh/g when the current is increased to 50 and 250 mA/g, respectively. The total charge input was 1200 mAh/g in all cases. The total discharge capacities at 10 mA/g are

indicated by the markers in each of the curves. The discharge capacity is significantly influenced by the charging current and is 556 mAh/g for the electrode charged with 50 mA/g *vs.* 478 mAh/g for the electrode charged at 10 mA/g, which means the crystallite size has a clear influence on the discharge kinetics. Using lower currents will enable the hydride-crystals to grow larger, thereby increasing the effective diffusion length. The difference with the amount of absorbed hydrogen is, however, quite large. Charging with 250 mA/g does not increase the total discharge capacity further, but the amount the charge capacity until HER and the discharge capacity are approximately equal.

6.3.2.2 Ternary Mg-Ti-Ni,Al mixtures

For the alloys prepared from metal powders and using stearic acid as an additive, the electrochemical properties are similar to the binary mixtures prepared under the same conditions. Fig. 86 depicts the electrochemical characteristics of the Pd-activated $(Mg_{0.80}Ti_{0.20})_{0.95}Ni_{0.05}$ alloy (sample X).

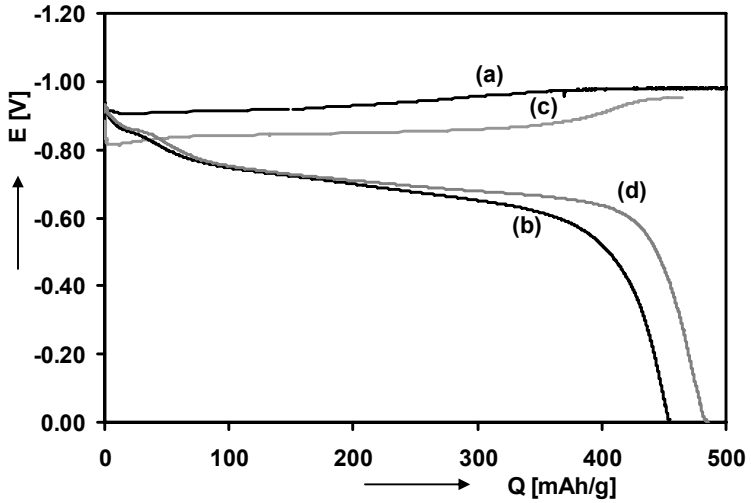

Fig. 86: Constant-current charging with 100 mA/g (a) and 5 mA/g (c) and discharging with 10 mA/g (b) and 5 mA/g (d) of $(Mg_{0.80}Ti_{0.20})_{0.95}Ni_{0.05}$ (sample X).

When the material is charged at 100 mA/g the Hydrogen Evolution Reaction (HER) starts to dominate when about 375 mAh/g (~1.4 wt.% H) has been inserted into the material (a). The discharge capacity at a current density of 10 mA/g is 455 mAh/g (~1.7 wt.% H), which is considerably higher. Therefore, charging was also done at a very low current density to determine the intrinsic storage capacity of the material. When charging at only 5 mA/g, the HER starts at around 450 mAh/g, which is about equal to the discharge capacity found with 10 mA/g. The discharge capacity at the same current density of 5 mA/g was still slightly higher with 485 mAh/g.

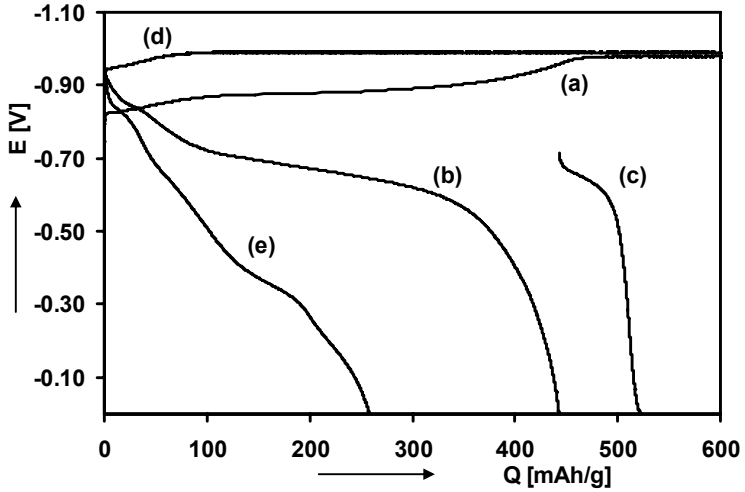

Fig. 87: Charge-discharge characteristics of cubic $(Mg_{0.65}Ti_{0.35})_{0.95}Ni_{0.05}$ (sample XII) and $(Mg_{0.60}Ti_{0.40})_{0.95}Ni_{0.05}$ (sample XIII). (a): charging of sample XII with 100 mA/g, (b) and (c): discharge of the same sample at 50 and 10 mA/g, respectively, (d): charging of sample XIII at 100 mA/g, (e): discharge of sample XIII at 10 mA/g.

The charge and discharge curves of the $(Mg_{0.65}Ti_{0.35})_{0.95}Ni_{0.05}$ alloy are depicted in Fig. 87. Sample XII was activated with Pd after 16h of milling. Charging it with 100 mA/g (a) reveals a capacity around 475 mAh/g which is in this case, contrary to the $(Mg_{0.80}Ti_{0.20})_{0.95}Ni_{0.05}$ alloy, about equal to the discharge capacity at 50 mA/g (b). Some additional charge can be extracted at a lower current density (c), giving a total capacity slightly above 520 mAh/g. When comparing these values with those obtained for cubic binary $Mg_{0.65}Ti_{0.35}$ (see Fig. 83), it can be seen that the rate capability is much higher for the Ni-containing alloy: over 85% of the total capacity can be discharged at 50 mA/g, compared to 50% for the binary alloy. Apparently, the formation of an amorphous secondary MgNi-phase, as was inferred from the XRD results, has a beneficial effect on the electrochemical properties. However, the same as for the binary cubic alloy (sample IV), both the charge-and total discharge capacity are far lower than those that were found for Mg-Ti thin films[123, 129].

The charge/discharge response of sample XIII, $(Mg_{0.60}Ti_{0.40})_{0.95}Ni_{0.05}$ activated after 46h, is also shown in Fig. 87. The effects of prolonged milling on the electrochemical properties are immediately evident. When charging with 100 mA/g (curve (d)), the hydrogen evolution reaction becomes dominant after less than 150 mAh/g has been charged into the material. The discharge capacity at 10 mA/g reaches ~250 mAh/g (e), at much more positive voltages compared to $(Mg_{0.65}Ti_{0.35})_{0.95}Ni_{0.05}$ at shorter milling times. Thus, an increase in milling time leading to an increase in the amount of the Ti-rich fcc phase (see Fig. 80), resulting in a decrease in the capacity. This is the same behavior as that found for sample V.

The XRD patterns of the ternary hcp alloys in Fig. 81 show no evidence for this 'inactive' fcc-Ti phase, although the amount of Ti dissolved in Mg was considerably smaller than the nominal amount. This means part of the Ti likely acts as 'dead weight' in the hcp alloys as well, but for $Mg_{0.65}Ti_{0.35}$ and $Mg_{0.75}Ti_{0.25}$ (samples VIII and IX) the *ab*sorption capacity was shown to increase considerably compared to the fcc modification (see Fig. 83 and Fig. 85). The addition of Ni and, as a consequence, the formation of a secondary Ti-Ni phase can be expected to improve the rate capability, and hence the total discharge capacity at a given current rate, as well, just as the a-MgNi phase was found to do for the cubic compounds. The charge-discharge curves of samples IX and XIV-XVI depicted in Fig. 88 show that this is indeed the case.

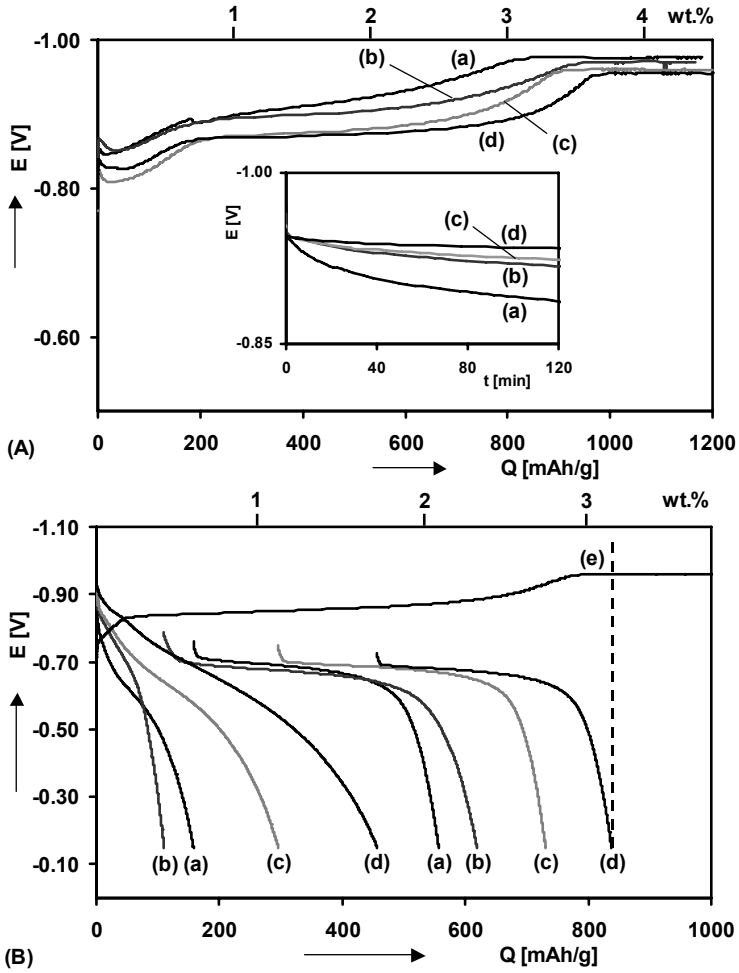

Fig. 88: Effects of Ni and Al addition on electrochemical response of hcp $Mg_{0.75}Ti_{0.25}$. (A): charging curves at 50 mA/g of (a): $Mg_{0.75}Ti_{0.25}$, (b): $(Mg_{0.75}Ti_{0.25})_{0.95}Al_{0.05}$, (c): $(Mg_{0.75}Ti_{0.25})_{0.95}Ni_{0.05}$, (d): $(Mg_{0.75}Ti_{0.25})_{0.90}Ni_{0.10}$. (B): Discharge curves at 50 and 10 mA/g of the same alloys as in (A). Curve (e) is the second electrochemical charging (50 mA/g) of $(Mg_{0.75}Ti_{0.25})_{0.90}Ni_{0.10}$ The evolution of the potential during 2h of relaxation is shown in the inset of (A).

Compared to the binary $Mg_{0.75}Ti_{0.25}$ mixture, the charging curves (Fig. 88 (A)) of the ternary systems have a much more well-defined plateau region. The absorption capacity until the HER becomes dominant is also higher for all the ternary mixtures. The most favorable properties are found for the $(Mg_{0.75}Ti_{0.25})_{0.9}Ni_{0.10}$ alloy (sample XVI, curve (d)) with a charging capacity until HER of 975 mAh/g, which is more than 75% of the theoretical capacity of 1260 mAh/g based on absorption of 2 H/M. Sample XVI is also the only alloy for which the equilibrium potential remains below -0.93V (*i.e.* an equilibrium pressure of 1 bar) after 2h of relaxation. This is quite remarkable as charging was continued well into the hydrogen-evolution regime in all 4 cases.

The discharge and deep-discharge curves, at 50 and 10 mA/g, respectively, of the same alloys are shown in Fig. 88 (B). The same as for the charging curves, addition of Ni has a very beneficial effect. Both the total reversible capacity and the rate capability are increased by the addition of Ni. The total discharge capacity increases from 550 mAh/g for $Mg_{0.75}Ti_{0.25}$ to 835 mAh/g for $(Mg_{0.75}Ti_{0.25})_{0.9}Ni_{0.10}$ and the fraction of the total capacity extracted at 50 mA/g from 28 to 54%. Because of the low current densities and, consequently, very long charge-discharge times, extensive cycle-life testing was not undertaken. However, as curve (e) shows, the second charging of sample XVI reaches 95% of the discharged capacity in the first cycle

before the HER starts, which means the (de)hydrogenation is fully reversible at room-temperature.

The effect of increasing the charging current on the elctrochemical response of the $(Mg_{0.75}Ti_{0.25})_{0.90}Ni_{0.10}$ alloy was investigated for comparison with the binary alloy. The results are depicted in Fig. 89.

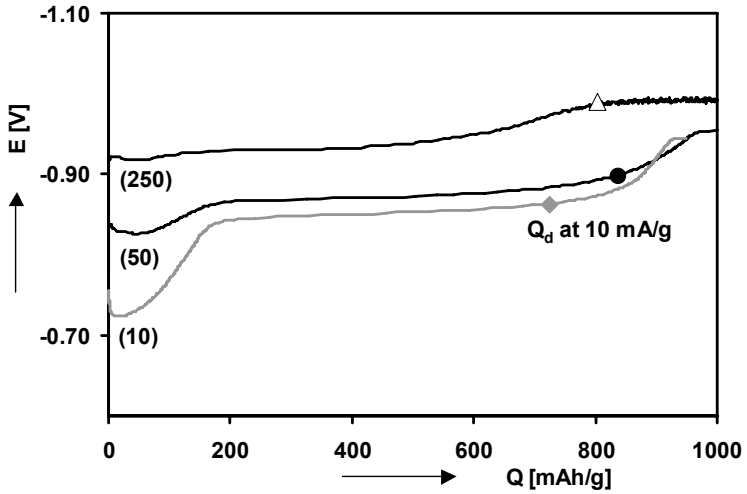

Fig. 89: Electrochemical response of $(Mg_{0.75}Ti_{0.25})_{0.90}Ni_{0.10}$ as a function of charging current. Charging current densities are between brackets. The total discharge capacity at 10 mA/g is indicated by a marker in each curve.

Compared to the binary $Mg_{0.75}Ti_{0.25}$ material (see Fig. 85), the influence of the charging current is much weaker. The absorption capacity before the onset of the hydrogen evolution plateau varies from 975 mAh/g when charging with 50 mA/g to ~800 mAh/g for a charging current of 250 mA/g. The discharge capacity of the electrode charged with 10 mA/g is clearly the smallest with 725 mAh/g *vs.* 837 and 800 mAh/g for the electrodes charged with 50 and 250 mA/g, respectively, pointing to a similar influence of crystallite size on the discharge kinetics as that found for the binary alloy.

6.3.3 Thermodynamic properties

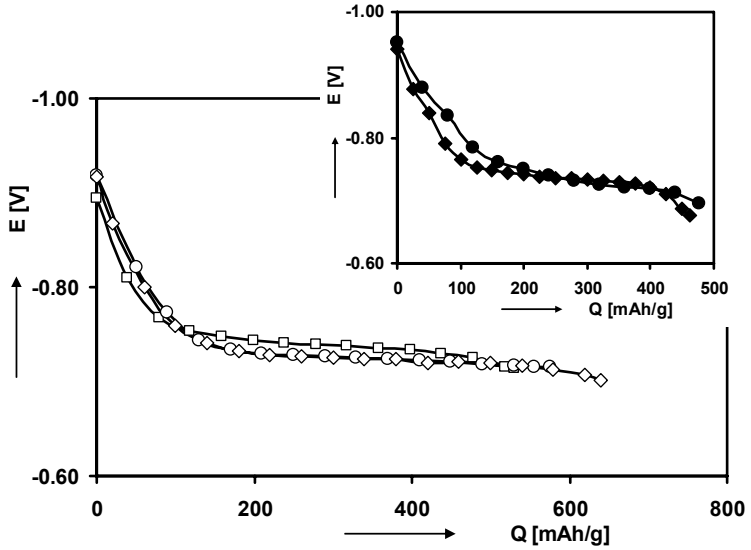

Fig. 90: GITT curves of binary and ternary Mg-Ti based materials. □: $Mg_{0.75}Ti_{0.25}$ (sample IX), ◊: $(Mg_{0.75}Ti_{0.25})_{0.95}Ni_{0.05}$ (sample XV), ○: $(Mg_{0.75}Ti_{0.25})_{0.95}Al_{0.05}$ (sample XIV), ♦: $Mg_{0.65}Ti_{0.35}$ (sample IV), ●: $(Mg_{0.65}Ti_{0.35})_{0.95}Ni_{0.05}$ (sample XII)

The GITT curves of both binary and ternary hexagonal compounds are shown in Fig. 90. The equilibrium curves of cubic $Mg_{0.65}Ti_{0.35}$ and $(Mg_{0.65}Ti_{0.35})_{0.95}Ni_{0.05}$ are shown in the inset. It can be seen that neither the Mg/Ti ratio, the same as for Mg-Sc, nor the addition of Al or Ni have a clear influence on the plateau pressure. In fact, the equilibrium potential of the binary $Mg_{0.75}Ti_{0.25}$ (open squares) is the most negative of all, by ~20 mV, but the equivalent pressure still falls within the same order of magnitude around 10^{-6}-10^{-7} bar. The shift to higher equivalent pressures of part of the isotherm that was found for Mg-Ti-Al and Mg-Ti-Si thin films[135] is absent here. This was to be expected since the XRD results proved that the Ni and Al do not enter the main Mg-Ti phase.

Discussion II

The electrochemical capacities found in the present study are only about one-third to one-half of those found for Mg-Ti thin films in the same compositional range. It was already stated that the fcc Ti phase appears to be inactive at room temperature, as evidenced by the strongly reduced capacity of $Mg_{0.65}Ti_{0.35}$ and $(Mg_{0.60}Ti_{0.40})_{0.95}Ni_{0.05}$ upon prolonged milling, turning a large part of the materials' mass into 'dead weight'. However, even counting only the absorption of 2 H/Mg, the theoretical charging capacity of $Mg_{0.65}Ti_{0.35}$ is >900 mAh/g, whereas for the cubic modification only 500 mAh/g is measured. This discrepancy is much smaller for the hcp modification. Based on the composition of the hcp Mg(Ti) solid solution of $Mg_{0.9}Ti_{0.1}$, 83 mol% of the $Mg_{0.75}Ti_{0.25}$ (sample IX) consists of the hcp solid solution phase, while the remaining 17% is amorphous Ti. The maximum absorption capacity based on 2H/hcpTi and 2H/Mg would then be 1250 mAh/g, where 975 mAh/g was achieved at 10 mA/g (see Fig. 85).

The rate capability is very poor both for hcp $Mg_{0.65}Ti_{0.35}$ and $Mg_{0.75}Ti_{0.25}$ (samples VIII and IX); 31 and 34%, respectively. From the lattice parameters of the resulting hcp solid solutions, it was derived that the amount of dissolved Ti is only 10%. It was shown by Borsa *et al.*[150] and Vermeulen *et al.*[151], that at the composition $Mg_{0.90}Ti_{0.10}$ a rutile structure is formed upon hydrogenation of a Mg-Ti thin film. This is the same structure as pure MgH_2,

which has extremely poor hydrogen transport properties. Therefore, it can be expected that here, a rutile structure was formed during electrochemical charging as well, resulting in poor discharge kinetics. Indeed, this was very nicely illustrated by the results obtained as a function of the charging current. The inverse relation between the applied current and the amount of inserted charge that was found, clearly showed that the material behaves similar to pure Mg, which was discussed in section 3.5.1.

Both for the cubic and hexagonal mixtures, addition of Ni as a third element markedly improves the electrochemical properties. For the cubic compounds (sample IV *vs.* XI), it is especially the rate capability that is increased. The initial charging capacity and total discharge capacity are only weakly influenced. Apparently, the secondary a-MgNi phase that has been formed during milling provides a more rapid diffusion path for hydrogen, leading to improved discharge kinetics. In fact, the rate capability of sample XII is comparable to that of bulk $Mg_{0.65}Sc_{0.35}P_{0.024}$ which has 90% *vs.* 85% for $(Mg_{0.65}Ti_{.35})_{0.95}Ni_{0.05}$.

The same is true for the hexagonal solid solutions, where both the rate capability as well as the total discharge capacity are much improved by the addition of Ni (sample IX vs. XVI, see Fig. 88) for the $Mg_{0.75}Ti_{0.25}$ composition. From the X-ray diffraction patterns, formation of a fcc and/or amorphous Ni(Ti) solid solution was found as a secondary phase. An (amorphous) TiNi phase is a hydride-forming material as well, although the reported electrochemical capacities are consistently very small[152, 153]. Such a TiNi phase finely dispersed throughout the Mg(Ti) matrix would provide a rapid diffusion path for hydrogen, effectively shortening the diffusion lengths *through* the rutile-type main phase, resulting in the observed improvements of the discharge kinetics. This was further illustrated by the electrochemical response as a function of the charging current. The self-limiting behavior that was clearly evident for binary $Mg_{0.75}Ti_{0.25}$ was much alleviated for ternary $(Mg_{0.75}Ti_{0.25})_{0.90}Ni_{0.10}$, which shows that the multi-phase structure not only enhances the (de)sorption kinetics, but also improves the materials' utilization.

6.3.4 Crystallographic properties of hydrided materials

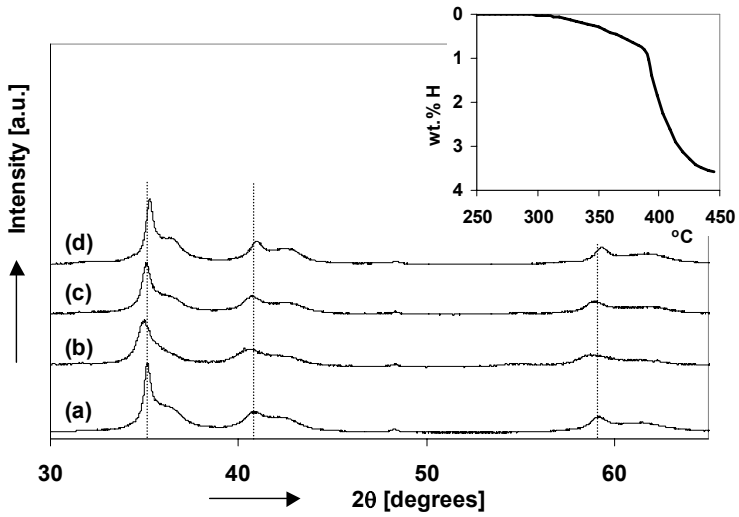

Fig. 91: XRD pattern of $Mg_{0.65}Ti_{0.35}$ (sample IV) in the as-milled state (a), deuterated at 75 bar and 175°C (b), partially desorbed up to 1.9 wt.% (c) and completely desorbed by heating to 450°C (d).

A fraction of sample IV was taken out of the milling vial before activation with Pd and exposed to 75 bars of deuterium gas at a maximum temperature of 175°C. Subsequent desorption was achieved by heating the sample to 450°C in a thermogravimetric analyzer. The

X-Ray diffraction patterns are depicted in Fig. 91. The as-milled powder (a) consists of two fcc phases as was already shown in Fig. 75. After deuterium absorption, very little seems to have changed, except for a small shift of the largest fcc phase towards lower angles. The second phase is hardly affected at all. The thermal desorption curve is shown in the inset of Fig. 91. The sample releases 3.6 wt.% of deuterium, equivalent to 1.8 wt.% H or 475 mAh/g, which is in good agreement with the electrochemical measurements. The XRD pattern after partial desorption (c) is slightly shifted to higher angles compared to the fully loaded material. After complete desorption, (d), the pattern has shifted to higher angles, slightly beyond that of the as-milled sample (a), but the patterns look otherwise identical.

Judging by the XRD results only, the material expands and contracts very little during hydrogen ab- and desorption, which would make it a very attractive option for practical hydrogen storage systems. However, as was repeatedly stated already, information on the positions of the hydrogen (deuterium) atoms is essential for obtaining a complete picture of the materials' behavior. For the neutron diffraction experiments, 2 fresh batches of cubic $Mg_{0.65}Ti_{0.35}$ were synthesized under the same conditions as sample IV.

At room temperature, the material absorbed deuterium only very slowly. By applying a pressure of 25 bars and gradually increasing the temperature to 175°C, identical to the conditions for the material used in X-Ray diffraction, the sample absorbed deuterium much more readily and the diffraction patterns started to change accordingly. The evolution of the neutron diffraction patterns is shown in Fig. 92. The very strong dark traces represent reflections from the stainless steel sample holder:

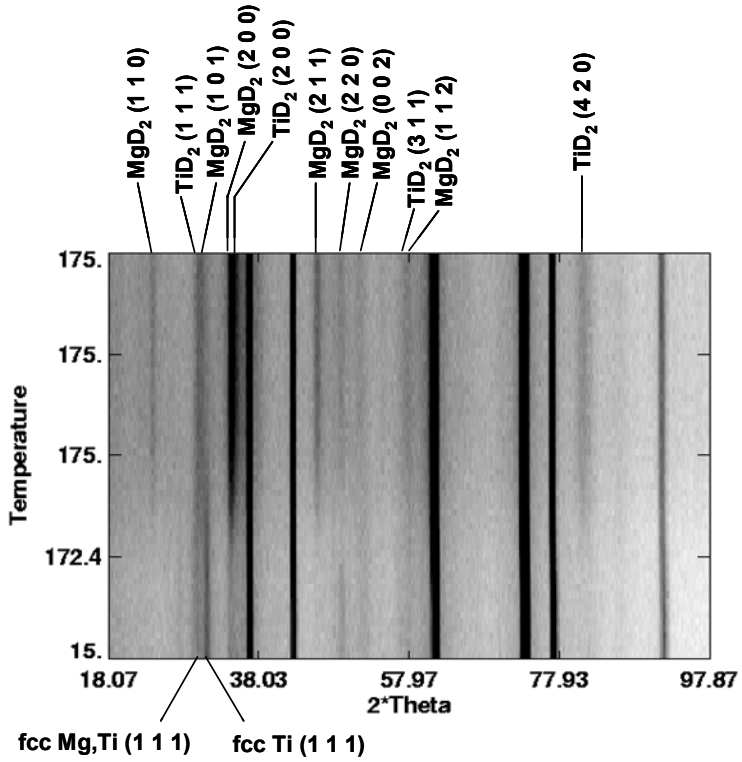

Fig. 92: Evolution of the neutron diffraction patterns during deuterium absorption.

The somewhat shorter wavelength of the neutrons compared to CuK_α-radiation, makes the detection of nanocrystalline phases easier as the peak width will be smaller. Contrary to the XRD results, the presence of MgD_2 is clearly detected at the end of the absorption half-cycle, as well as TiD_2. However, it can be seen that a number of these reflections are very close to the positions of the reflections of the starting phase, most particularly the TiD_2 (111) and

(200) and the MgD_2 (101) and (200) peaks, which explains why the XRD patterns in Fig. 91 changed so little upon deuterium absorption.

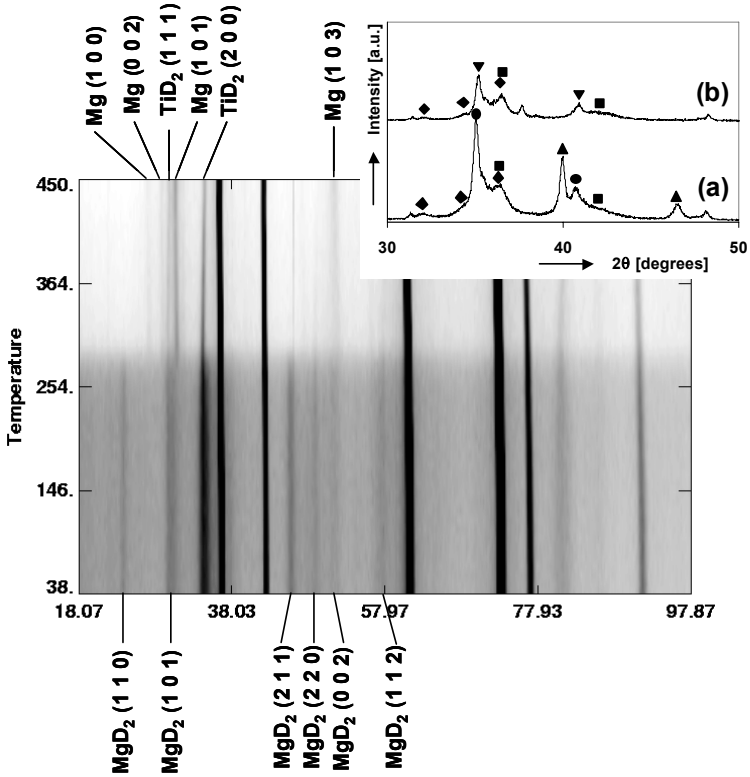

Fig. 93: Evolution of neutron diffraction pattern of $Mg_{0.65}Ti_{0.35}D_x$ during thermal desorption. The inset shows the XRD patterns of the material before starting the absorption (a) and after the desorption (b). ■: fcc phases, ◆: Mg, ▲: Pd, ▼: TiD_2

A 2-dimensional plot of the diffraction patterns during deuterium desorption is shown in Fig. 93. When the temperature has increased to ~275°C, the MgD_2 starts desorb, until at 450°C, a mixture of Mg metal and TiD_2 remains. When the desorption of MgD_2 starts, it becomes very hard to discern the diffraction lines as there is a concurrent sharp decrease in the overall signal intensity, but the strongest diffraction lines of Mg metal and TiD_2 are still visible. As stated earlier, the TiD_2 reflections strongly overlap with those of the initial fcc Mg(Ti) phase, but the fact that the (200) reflection is now stronger than the (111) clearly shows that TiD_2 is present. As Ti has a negative neutron scattering length[114], the presence of deuterium in tetrahedral sites now enhances the intensity of reflections for which h+k+l = 2n.

The inset in Fig. 93 shows the X-Ray diffraction patterns of the material used for the neutron experiments before (a) and after (b) the measurement. The small amount of free Mg that was present at the start has not noticeably increased and the diffraction pattern is still dominated by the (apparently) same two fcc phases. Apart from a small shift to higher angles of the larger fcc phase, which was already noted in Fig. 91, and the disappearance of the Pd reflections, there are no differences between the two patterns. The latter may be caused by neutron absorption by the Pd up to ^{109}Pd, which decays with a half-life of ~13 hours to ^{109}Ag or by the formation of Mg-Pd compounds at higher temperatures.

6.3.5 Nuclear Magnetic Resonance

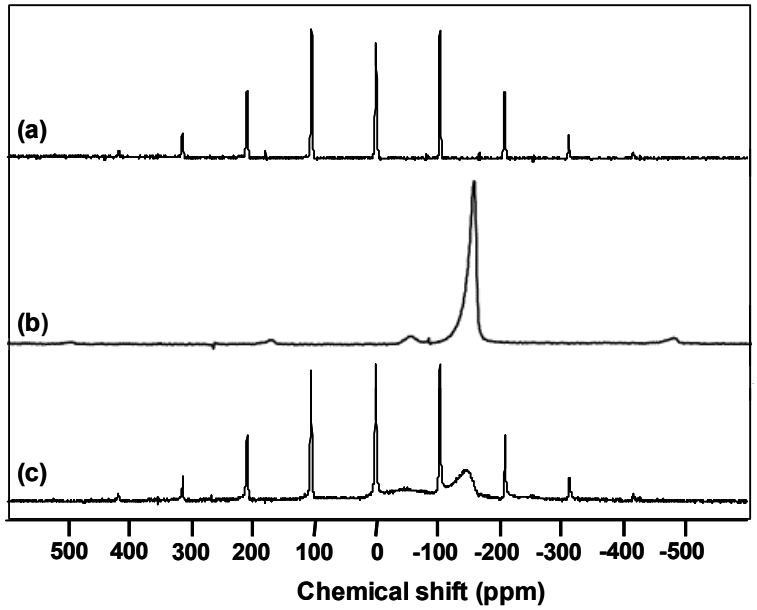

Fig. 94: 8 kHz MAS NMR sideband spectrum of MgD_2 (a), 25 kHz MAS sideband spectrum of TiD_2 (b) and 8 kHz MAS sideband spectrum of cubic $Mg_{0.65}Ti_{0.35}D_{\sim 1}$ (c)

The experimental details of the NMR measurements were essentially the same as for MgSc (see section 5.2.3). Fig. 94 (c) shows the 8 kHz MAS-NMR spectrum of the cubic $Mg_{0.65}Ti_{0.35}$ material (see Fig. 75 and Fig. 76) exposed to 75 bars of deuterium gas at a maximum temperature of 175°C, identical to the conditions used in the neutron diffraction experiments. The MgD_2 spectrum was already shown in Fig. 61 and is once more depicted here as spectrum (a). The TiD_2 spectrum (b) consists of two very broad bands; a small fraction of the deuterium atoms resonates at -50 ppm and the major component is located at -150 ppm. Contrary to the MgSc case, the MAS-NMR sideband spectrum of $Mg_{0.65}Ti_{0.35}D_x$ seems to be a simple superposition of the spectra of MgD_2 and TiD_2. The only clear difference is a change in the intensity ratio of the two TiD_2-related bands with respect to the spectrum of pure TiD_2. This may be related to the extremely small crystallite size, which was 3-23 nm for the metal alloy (see Table 9) and decreases even further upon deuteration. The peak width can clearly be seen to increase upon deuteration in Fig. 91.

To investigate whether, despite the apparent phase segregation that has taken place, there is still deuterium exchange between all the NMR-distinct sites, a 2-D EXSY measurement was carried out, similar to what was done for $Mg_{0.65}Sc_{0.35}$ (see Fig. 64). It can be seen in Fig. 95 that after a mixing time of 10 ms exchange is still very limited as most of the signal intensity is found on the diagonal. However, on a time scale of 1s, the TiD_2 component at –50 ppm can be seen to exchange deuterium atoms with the MgD_2-sites, whereas the major TiD_2-component at –150 ppm seems more or less isolated. This is quite different from the results obtained on $Mg_{0.65}Sc_{0.35}D_{2.20}$ where deuterium was shown to exchange between all NMR-distinct sites, but entirely consistent with the higher extent of phase separation for the Mg-Ti system as was measured with neutron diffraction. However, deuterium is clearly still able to move between Mg and Ti-environments.

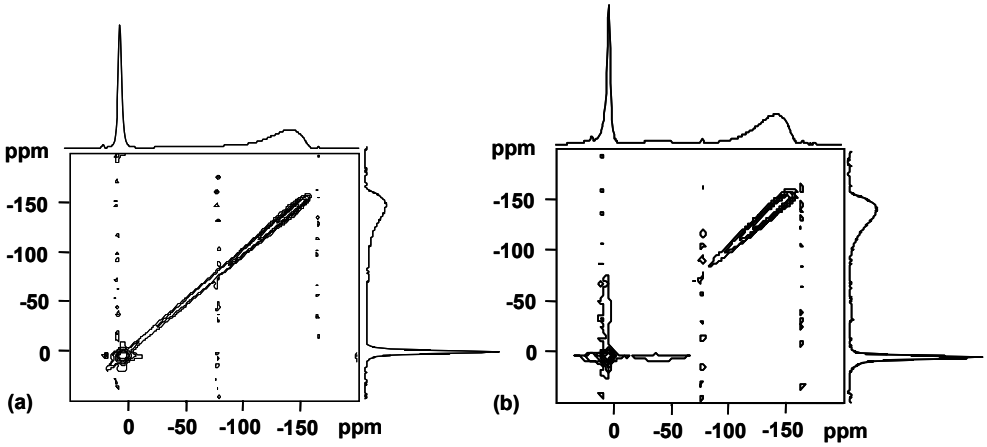

Fig. 95: 2-D EXSY spectra of $Mg_{0.65}Ti_{0.35}D_x$ (a): mixing time of 10 ms, (b): mixing time 1s

6.3.6 DFT calculations

The $Mg_{1-x}Ti_x$ system was also studied with DFT as a function of Mg/Ti ratio. The computational details were the same as for $Mg_{1-x}Sc_x$ (see section 5.2.4). The definitions of the formation enthalpies are:

$$\Delta H_f = E_{Mg_{1-x}TixH_2} - \left[(1-x)E_{Mg} + xE_{Ti}\right] - E_{H_2} \qquad (6.2)$$

or

$$\Delta H_f = E_{Mg_{1-x}Ti_xH_2} - E_{Mg_{1-x}Ti_x(alloy)} - E_{H_2} \qquad (6.3)$$

Table 12: Enthalpies of formation of metal alloys and hydrides in the Mg-Ti-H system. Literature values are between brackets.

Metal/alloy	Structure type	Lattice parameters (Å)	Enthalpy of formation [kJ/mol]
Mg	hcp	a = 3.19 (3.21) c = 5.20 (5.21)	
Mg	fcc	a = 4.52	+1.18
Ti	hcp	a = 2.93 (2.95) c = 4.65 (4.69)	
Ti	fcc	a = 4.10	+5.45
$Mg_{0.75}Ti_{0.25}$	fcc	a = 4.35	+14.07
MgH_2	Rutile	a = 4.45 (4.50) c = 2.99 (3.01)	-63.3 (-77)
TiH_2	Fluorite	a = 4.40 (4.45)	-149.2 (-145)

Table 12 lists the formation enthalpies of the metal alloys and binary hydrides. The energy difference between hcp and fcc Ti is quite small, as was already indicated by the transformation of pure Ti to fcc by ball-milling, although the lattice expansion that was observed in the ball-milling experiments is not reproduced. A fcc structure with the same unit cell volume as hcp would have lattice parameter a = 4.13 Å where 4.10 Å is calculated and 4.25 Å is found experimentally. The calculated transformation enthalpy of +5.5 kJ/mol is in excellent agreement with the value of +4 mRy (~ 5.2 kJ/mol) previously obtained by

Skriver[143]. The calculated lattice parameters as well as the enthalpy of formation of TiH_2 are in good agreement with the experimental values (-145 kJ/mol H_2)

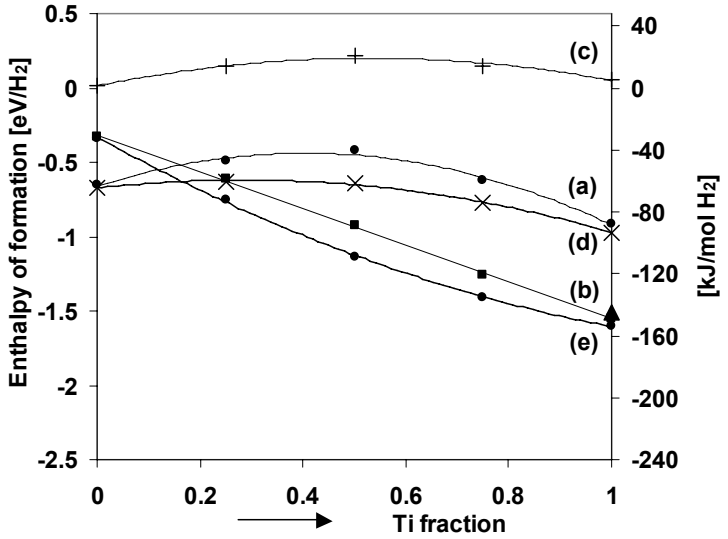

Fig. 96: Enthalpy of formation as a function of Ti-content of $Mg_xTi_{1-x}H_2$. (a): rutile eq. 6.1, (b): fluorite eq. 6.1, (c): hypothetical fcc alloy, (d): rutile eq. 6.2, (e): fluorite eq. 6.2

Fig. 96 depicts the formation enthalpies of an unhydrided metal alloy and of the ternary hydrides in the rutile and fluorite structure calculated by both Eq. *(6.2)* and *(6.3)*. Here, the rutile structure does show a considerable destabilization with respect to pure MgH_2. Maximum destabilisation occurs for x = 0.5. The formation enthalpy of rutile $Mg_{0.50}Ti_{0.50}H_2$ is –0.421 eV/H_2, which is 22.7 kJ/mol less negative than pure MgH_2. For $Mg_{0.75}Ti_{0.25}H_2$, the rutile structure is destabilized by only 16.0 kJ/mol, which is considerably less than the 22.9 kJ/mole reported by Song *et al.*[154] for $Mg_{0.80}Ti_{0.20}H_2$. The rutile structure with composition $Mg_{0.25}Ti_{0.75}H_2$ is also less stable than MgH_2, which means Ti destabilizes the rutile structure over almost the entire compositional range. The formation enthalpy of the fluorite structure (solid squares) shows a tendency towards more negative values for the entire compositional range, the same as for the MgSc system. The fluorite structure becomes the most stable one around x = 0.80, also similar to MgSc and once more in good agreement with experimental findings [129].

The formation enthalpy of the unhydrided alloys is quite positive, 20.8 kJ/mole for $Mg_{0.50}Ti_{0.50}$, which means that the values of the formation enthalpies calculated by Eq. *(6.2)* and *(6.3)* differ by a rather large amount, as can be seen in Fig. 96. However, the crossing point between the fluorite and rutile structure is not affected, remaining at approximately 20 at.% Ti. The maximum in the formation enthalpy, 20.8 kJ/mol for $Mg_{0.50}Ti_{0.50}$, is in good agreement with the value obtained from the Miedema model[155].

Discussion III

The neutron diffraction patterns drastically altered the picture that was obtained from X-ray diffraction. The contour plot in Fig. 92, clearly shows the presence of rutile MgD_2, as well as TiD_2. This means the material decomposes upon deuterium (hydrogen) absorption and subsequent desorption and that MgD_2 and Mg apparently have such small crystallite sizes that they are not detected by XRD. The tendency for phase segregation upon hydrogenation appears to be much stronger for Mg-Ti compared to Mg-Sc, since in the latter case, diffraction

showed only 1 phase in the fully loaded state despite the higher deuteration temperature for Mg-Sc compared to Mg-Ti (275 *vs.* 175°C). This is in agreement with the low rate capability compared to Mg-Sc that was found in the electrochemical experiments for the binary mixtures as the formation of rutile MgH_2 domains would strongly hinder hydrogen diffusion. However, it should be noted that the electrochemical measurements were carried out at room-temperature, whereas the solid-gas ab-and desorption were performed at elevated temperatures.

The NMR measurements are in very good agreement with the neutron diffraction results. Contrary to the MgSc deuteride, the MAS-spectrum of the ternary $Mg_{0.65}Ti_{0.35}D_x$ deuteride looks like a simple superposition of the spectra of the binary deuterides. From the 2-D EX SY experiment it was found that there is exchange between the Mg-coordinated deuterium atoms and the broad component at -50 ppm of the TiD_2 sites. Despite the fact that the material seems to be completely decomposed, hydrogen can still move throughout the crystal lattice. This is rather surprising given the extremely poor transport properties of rutile MgH_2. Apparently, the crystallite size of MgD_2 is so small that the transport limitations are, partly, overcome. At room temperature, the picture may be even more favorable in that the material does not completely disproportionate. From in-situ XRD on gas-phase loaded thin films, a coherent single-phase structure was found, but simulations of the optical properties show that the amount of Mg-H-like clusters should be much higher than expected in a statistically random alloy to explain the measured electrical and optical response upon hydrogenation[150].

The transition point from rutile to fluorite that was found for thin films at x = 0.80 was reproduced very well in the DFT calculations. For the hcp $Mg_{0.90}T_{0.10}$ solid solution that was formed in ball-milled $Mg_{0.65}Ti_{0.35}$ and $Mg_{0.75}Ti_{0.25}$, a rutile structure is expected upon hydrogenation. This was verified by the materials' behavior as a function of charging current, which strongly resembles that of pure Mg.

Regarding phase separation one can argue that, according to the calculations, a mixture of the binary hydrides is always lower in energy than the ternary compounds, the same as for MgSc. Contrary to MgSc, evidence for phase segregation was found both by neutron diffraction and NMR, which indicates that the tendency for decomposition into the binary hydrides is larger for the Mg-Ti system. This is probably related to the strongly positive enthalpy of mixing of Mg and Ti. In the initial stage of hydrogen absorption, it is energetically favorable to form TiH_2 clusters, because Mg-Ti bonds are broken in the process. It also requires diffusion of metal atoms, which is quite slow at room-temperature, but may be increased by the build-up of stress in the material as a consequence of lattice expansion upon hydrogenation.

In-situ XRD measurements on a $Mg_{0.90}Ti_{0.10}$ thin film showed formation of a contracted rutile structure, where the (110) reflection was shifted by ~0.3° with respect to pure MgH_2[151], which indicates that Ti is incorporated in the rutile structure. However, mobility of the metal atoms may be reduced by clamping effects from the substrate. The calculations show that a Ti-doped rutile structure is less stable than pure MgH_2, which should induce the system to separate into the binary hydrides. It can be argued that, compared to the fluorite-forming region, in the rutile-forming region the driving force for phase separation is higher and the kinetic barriers are lower, because the formation of MgH_2 does not require a crystallographic transformation. Bulk hcp solid solutions with >20 at.% Ti may therefore be less sensitive to decomposition, although this remains speculative as long as the Ti-content in Mg can not be accurately controlled.

6.4. Conclusions and outlook

Binary Mg_xTi_{1-x} alloys were prepared by mechanical alloying in two different crystallographic forms; a mixture of fcc Mg(Ti) and fcc Ti or a hexagonal-close-packed solid solution of Ti in Mg with traces of cubic phase. Which one of the two was obtained was determined by the Mg-precursor that was used. Using Mg powder resulted in cubic materials, whereas the use of Mg-ribbon, with much lower specific surface area, results in hcp solid solutions. The reason for this difference is most likely the higher specific area and, as a consequence, higher oxygen-content of the powder compared to the ribbon. Complete conversion of powder mixtures with more than 65 at.% Mg is not possible; after all the hcp Ti has been converted, the amount of residual Mg remains unchanged upon further milling. In mixtures which were primarily hexagonal after milling, partial transformation of the Ti from a hexagonal to a cubic or amorphous structure can not be avoided leading to a discrepancy between the amount of Ti dissolved in the Mg and the nominal composition. The amount of dissolved Ti was found to be at most 10 at.% from comparison of the lattice constants with literature data and a $Mg_{0.90}Ti_{0.10}$ thin film.

Ternary Mg-Ti-Ni mixtures prepared from powders are transformed to the same cubic structures as the binary system. The addition of Ni results in the formation of some amorphous MgNi-type phase, as evidenced by the minimal influence of the Ni-addition on the lattice constants of the cubic structures, the decrease in the relative intensity of the largest cubic phase and the response of the material in a GITT experiment. The diffraction patterns of the Mg-Ti-Al/Ni materials prepared from Mg ribbon exhibit a shift of the hcp phase back towards higher angles, which indicates that a part of the Ti from the hcp solid solution reacts with the Ni (or Al) to form a TiNi secondary phase.

The absorption capacity of the binary cubic materials is much lower than that of the hcp compounds. From the decrease of the electrochemical capacity upon prolonged milling (see samples V and XIII) and the simultaneous increase in the amount of Ti-rich phase, it is concluded that fcc/amorphous Ti is not electrochemically active at room-temperature. However, the charging capacity of cubic $Mg_{0.65}Ti_{0.35}$ is even much lower than expected based on absorption of 2 H/Mg. The reason for this is not entirely clear, but it is possibly the same self-limiting effect that was observed for hcp $Mg_{0.75}Ti_{0.25}$ when the charging current was increased.

For both the cubic and hexagonal compounds, the electrochemical properties are much improved by the addition of Ni. For the cubic compounds, the influence is mainly on the rate capability, which rises from ~50 to 85%. For the hexagonal mixtures the charge acceptance, discharge capacity at 50 mA/g and total discharge capacity are increased as a result of formation of a multi-phase structure. The maximum reversible electrochemical storage capacities that were found were 520 mAh/g for cubic $(Mg_{0.65}Ti_{0.35})_{0.95}Ni_{0.05}$ and 837 mAh/g (3.2 wt.%) for hcp $(Mg_{0.75}Ti_{0.25})_{0.90}Ni_{0.10}$. These capacities are much lower than for the thin films, although the hcp $(Mg_{0.75}Ti_{0.25})_{0.90}Ni_{0.10}$ almost reaches its theoretical *ab*sorption capacity (3.7 wt.% H) if the inactive amorphous Ti fraction is taken into account. Contrary to the binary $Mg_{0.75}Ti_{0.25}$, the absorption capacity is much less sensitive to increases in the charging current, once more underlining the beneficial effect of the formation of a multi-phase structure upon Ni addition.

Cubic $Mg_{0.65}Ti_{0.35}$ deuterated at 175°C completely segregates into the binary deuterides, as was shown by both neutron diffraction and NMR. The X-Ray Diffraction patterns before and after deuterium absorption subsequent desorption are virtually identical, which means the MgD_2 crystals are extremely small. This alleviates the inherent transport limitations of the rutile structure to some extent as 2-D Exchange NMR gave clear evidence for deuterium exchange between Mg and Ti environments.

The rutile/fluorite transition point that was found for thin films at 80 at.% Mg is reproduced very well by DFT calculations. The expected formation of a rutile structure for a bulk $Mg_{0.90}Ti_{0.10}$ solid slution was also, though indirectly, verified. A mixture of the binary hydrides is, in principle, always lower in energy than any ternary dihydride. This, together with the finding that Ti destabilizes the rutile structure with respect to pure MgH_2 and the strongly positive enthalpy of mixing of Mg and Ti, should make the tendency towards phase separation very large. For cubic $Mg_{0.65}Ti_{0.35}$ alloy this has indeed been verified as complete segregation was detected by neutron diffraction as well as NMR.

Future work should aim to optimize the milling conditions to prevent transformation of Ti to an amorphous or fcc structure and dissolve more Ti in Mg so that the fluorite-forming region is reached. This would improve hydrogen diffusion and likely reduce the tendency towards phase separation as well. Pre-alloying of the Ti may be a way to prevent the hcp-to-cubic transformation. Dissolution of a small amount of Si into hcp Ti to form a crystalline $Ti_{92}Si_8$ solid solution together with a small amount of Si-rich amorphous phase can be achieved by mechanical alloying of Ti and Si powders. The milling conditions were comparable to those where fcc Ti is formed when milling pure Ti powder[156]. If such a hcp Ti-Si solid solution would react with Mg as readily as pure Ti, it might simultaneously achieve destabilization of the hydride, as incorporation of Si has already been shown to do in Mg-Ti thin films[135].

Formation of a multiphase structure has been shown to greatly improve the discharge capacity and kinetics even when the hydride phase assumes a rutile structure. Further optimization of the dispersion of the secondary phase into the Mg phase can further improve the discharge kinetics of the material by further reduction of the size of the rutile domains. To this end, the milling duration and milling conditions such as energy, BTP ratio, ball diameter etc. must be optimized further. Instead of forming a composite *in-situ* by adding an alloying element during the course of the milling process, another option would be to synthesize a, for instance, Ti-Ni or Ti-V phase and subsequently mix it with the Mg-Ti phase. This has the advantage that it allows separate optimization of the main storage phase and the secondary phase(s).

Insight into the hydrogen diffusion processes has, until now, been obtained only on hydrides (deuterides) that were synthesized at elevated temperatures, which were shown by ND to induce phase separation. However, characterization of the storage capacity, kinetics and equilibrium voltage (pressure) have been carried out at room-temperature, where the segregation behavior of the material may be different. Therefore, future NMR studies should include hydrides and deuterides that have been loaded at room-temperature in order to gain more insight in hydrogen transport processes when the materials are used as electrodes. In order to learn more about the influences of phase separation and crystallite size on hydrogen diffusion, ball-milled mixtures of the binary hydrides are an interesting option. By varying the milling time and Mg/Ti ratio, the crystallite size of MgH_2 and TiH_2 can be controlled. 2-D exchange measurements can then be used to determine whether there exists a 'critical' dimension below which there is exchange of hydrogen between Mg and Ti environments, as was shown for cubic $Mg_{0.65}Ti_{0.35}D_x$.

Besides determining the preferred crystal structure of the hydride phase, DFT calculations can be used in the search for suitable substitution elements to destabilize the hydride. Although the initial successes in this area on Mg-Ti-Si and Mg-Ti-Al thin films were based on the Miedema Model and van Mal's 'rule of reversed stability', DFT calculations are more sophisticated and could prove very useful in the future.

Summary

Nowadays, the use of portable electronic devices is increasing tremendously. The continuous rise in the amount of built-in functionality, *e.g* in mobile phones, makes the power consumption of these devices ever higher. This puts very high demands on the portable energy source that is used for a particular application with regard to the operating time of the equipment, cycle life *etc.*

On a larger scale, the availability of energy is also becoming an increasingly important issue. Traditional energy sources such as fossil fuels are not infinitely available and the resulting emissions are environmentally unfriendly. The use of hydrogen produced in a sustainable manner, such as from solar or wind power, has been proposed as an alternative, environmentally friendly, energy carrier. Stored hydrogen can be used in two forms; as a gas in *e.g.* PEM fuel cells or electrochemically in rechargeable Nickel-MetalHydride (NiMH) batteries, which can be used in portable electronic devices or in Hybrid Electric Vehicles (HEVs).

At present, a number of different technologies to store gaseous hydrogen are under intense investigation. It can be stored under very high pressures in containers, as a liquid at cryogenic temperatures, physisorbed on large surface area materials such as activated carbons and Metal-Organic-Frameworks or in the form of reversible metal hydrides (MHs). For a hydrogen storage technology to be viable, it must store at least 6 wt.% of hydrogen as stated in the U.S. Department of Energy (DoE) target for 2010. The present-day AB_5 type storage materials that are used as the negative electrode in NiMH batteries can store only 1.2 wt.%, which makes them unsuitable for use in fuel cell applications. Therefore, materials that can store a substantially higher amount of hydrogen, both as a gas and electrochemically, are intensively being investigated. Magnesium-based alloys have been identified as a promising class of materials, as the capacity of pure MgH_2 is 7.6 wt.%

Electrochemistry is used as the main tool to investigate the hydrogen storage properties of the alloys. The basic principles of electrochemistry are discussed in Chapter 2. The electrochemical hydrogen storage reactions as well as a numerous different measurement techniques such as constant-current (CC) measurements, galvanostatic intermittent titration technique (GITT) and electrochemical impedance spectroscopy (EIS) and the experimental electrochemical setup are described. The preparative methods used to synthesize the Mg-based alloys and hydrides by casting and ball-milling are also discussed in Chapter 2. The remainder of this chapter is devoted to theoretical introductions on X-ray Diffraction (XRD), Nuclear Magnetic Resonance (NMR) and Density Functional Theory (DFT) calculations. XRD, as well as neutron diffraction, is extensively used to study the crystallographic properties of the alloys and hydrides. NMR gives insight into the direct chemical environment of the hydrogen atoms on nearest-neighbor level and in this way complements the information obtained from diffraction measurements. Using DFT, it is possible to predict hydrogenation enthalpies of metals and alloys and to compare the relative stabilities of different crystallographic modifications of the hydride. XRD, NMR and DFT are introduced to a level that is sufficient to understand how the results presented in subsequent chapters are obtained and how the conclusions drawn from those results are reached.

Chapter 3 is an overview of the state-of-the-art in hydrogen storage materials. Some general properties of metal hydrides as well as a number of interesting application areas are highlighted in this chapter. Four classes of hydrogen storage materials are discussed, complex hydrides, nitride-based materials, interstitial metal hydrides and Mg-based alloys. The complex hydrides, in particular the borohydrides, have very high hydrogen storage capacities.

Limiting factors for their practical application are the rather extreme conditions, several tens of bars hydrogen pressure and high temperatures, required for their rehydrogenation. For $NaAlH_4$, use of Ti as a catalyst has lead to significant improvements in this respect, but this material has a reversible capacity of only 5.5 wt.%, which is not high enough for application in fuel-cell powered vehicles. Li_3N can, potentially, store more than 10 wt.% hydrogen. However, the temperatures required for desorption are too high due to the low equilibrium gas pressure of this material. Addition of Mg was found to increase the equilibrium pressure by more than an order of magnitude and it is therefore likely that the properties of these materials can be tuned towards accessible working pressures at ambient temperatures.

Of the interstitial hydrides, four different classes of Transition Metal based alloys are described. The AB_5 and AB_2-type materials as well as superlattice alloys and Vanadium-based solid solutions are reviewed based on their crystallographic properties, hydrogen storage capacity and the optimization of their composition for application as solid-gas or electrochemical hydrogen storage media. The AB_5-type materials, where A is a Rare-Earth metal or a mixture of RE metals and B is a (mixture of) transition metal(s) are widely applied nowadays in rechargeable NiMH batteries. These materials have a hexagonal $CaCu_5$-type structure, which is retained upon hydrogenation. The initial shortcomings of the original $LaNi_5$ compound, an equilibrium pressure substantially above 1 bar and a large discrete lattice expansion, leading to progressive pulverization and corrosion of the material, were successfully solved by substitution of part of the Ni by Co, Mn and Al. The capacity of these alloys is rather low; only 1.2 wt.% of hydrogen can be stored, which is not sufficient with respect to the DoE targets. The AB_2-type alloys, where A is Zr or Ti and B a mixture of other transition metals, have also been intensively studied for electrochemical applications. These materials can have a cubic (C15) or a hexagonal (C14) structure, depending on the overall composition, which is retained upon hydrogen loading, similar to the AB_5-type alloys. Although their intrinsic capacity is substantially higher than that of AB_5-type alloys, up to 1.96 and 2.8 wt.% for $ZrCr_2$ and ZrV_2, respectively, optimization of the corrosion resistance and activation behavior reduces the capacity to ~350 mAh/g (1.3 wt.%). The superlattice alloys have $AB_{3\text{-}4}$ stoichiometry and consist of a periodic stacking of AB_5 and AB_2 structure-units. The gravimetric capacity is increased with respect to the AB_5 and AB_2-type alloys by substituting part of the Rare-Earth metals (A-site) for lightweight Mg. For the composition $Mm_{0.83}Mg_{0.17}Ni_{3.1}Al_{0.2}$ a 10% higher capacity compared to AB_5 alloys has been reported for commercial AA-size batteries. The Vanadium-based solid solution alloys have the highest intrinsic storage capacity (~4 wt.%) of all the Transition Metal based systems and very interesting crystallographic properties. As the hydrogen content is increased, these alloys transform from a body-centered-cubic (bcc) to a face-centered-cubic (fcc) structure, sometimes via an intermediate tetragonal phase, depending on the exact composition. The total volume expansion often exceeds 35%, which is much higher than for the AB_5 and AB_2 type materials. The most favorable properties to date were reported for $(Ti_{0.355}V_{0.645})_{0.86}Fe_{0.14}$, which has a reversible capacity of 2.3 wt.% at 100°C and can be fully charged with hydrogen gas within 40 s at room-temperature.

Although significant improvements in storage capacity have been achieved, the V-based materials have almost twice the capacity of AB_5 alloys, the capacity needs to be more than doubled once again to reach the DoE target of 6 wt.%. MgH_2 has a very high storage capacity of 7.6 wt.%, but suffers from extremely slow (de)sorption kinetics. Hydrogen diffusion through rutile-structured MgH_2 is extremely slow and hydrogenation of Mg particles is effectively blocked once a closed layer of hydride has been formed at the surface. An inverse relation between the final hydrogenated fraction and the initial hydrogenation rate is consistently found throughout the literature, even for nanocrystalline/nanoparticulate Mg produced by ball-milling. Addition of catalysts does not entirely solve this problem either,

although more than 7 wt.% of hydrogen can be stored in a ball-milled mixture of Mg, Zr and Mn.

Mg-RE (RE = Gd, La, Y) thin films undergo drastic changes in their optical properties as a function of hydrogen content. The films are reflective in the as-deposited state, highly absorbing (black) at intermediate hydrogen content and transparent when fully loaded with hydrogen. The films can be very rapidly switched between these optical states up to quite high Mg content of more than 70 at.%. Although a phase segregation model has been used to explain the occurrence of the black state, the experimental findings on a bulk $Mg_{0.50}Y_{0.50}$ alloy and ball-milled $Mg_{0.65}Y_{0.35}$ hydrides indicate the formation of a cubic, ternary hydride.

Because Sc is directly above La and Y in the periodic table, Mg-Sc alloys can be expected to show the same improvements in (de)sorption rates as the Mg-RE and Mg-Y systems. Moreover, because Sc is much lighter than Y and La, Mg-Sc alloys will have the highest gravimetric capacity. In view of the results on Mg-Y bulk alloys and thin films, the Mg-Sc system presented an interesting case for a comparative study between bulk materials and thin films and the results are described in Chapter 4. The main aim of this work was to determine whether the electrochemical, crystallographic and thermodynamic properties of thin films give a good indication of the behavior of bulk materials. If this is indeed the case, then thin films can be used to quickly search for promising new compositions, as the preparation technique (e-beam deposition) is not restricted to thermodynamically stable alloys. The trends in the electrochemical capacity, the equilibrium hydrogen pressure and the crystallographic structure are shown to be virtually identical between the two systems.

With increasing Mg/Sc ratio, the reversible capacity first increases to a maximum of 1795 mAh/g (6.7 wt.%) for thin films and 1495 mAh/g (5.6 wt.%) for bulk materials at a composition $Mg_{0.80}Sc_{0.20}$. These values are very close to the theoretically expected ones based on the absorption of 3 H/Sc and 2 H/Mg and desorption of 2 H/Mg and approximately 1 H/Sc. For higher Mg content, the rate capability as well as the total capacity decreases sharply. This is ascribed to a change in crystal structure from the fluorite structure of ScH_2 to the rutile structure of MgH_2. The presence of large empty octahedral interstices in the fluorite structure facilitates much more rapid hydrogen motion compared to the rutile structure.

The plateau pressure determined by GITT measurements, is only very weakly dependent on the Mg/Sc ratio in the compositional range between 85 and 65 at.% Mg and almost equal to that of pure Mg at 10^{-6}-10^{-7} bar. The concentration boundaries of the plateau region are approximately 2 and 1 H/M. Only for a $Mg_{0.50}Sc_{0.50}Pd_{0.024}$ bulk material, the equilibrium pressure at the beginning of the plateau region was lowered by more than 1 order of magnitude, similar to what was observed for the $Mg_{0.50}Y_{0.50}$ alloy.

Impedance spectroscopy reveals that the surface kinetics of the thin films are completely dominated by the Pd topcoat. The dependence of the charge transfer rate on the hydrogen content is identical to that of a single Pd layer if the exchange current density is plotted as a function of the equilibrium potential. At low hydrogen concentrations, the overall kinetic response of the thin films is dominated by the transfer of hydrogen from the Pd layer to the MgSc phase. For a bulk $Mg_{0.65}Sc_{0.35}$ alloy ball-milled with Pd, the same behavior was found although the transfer of hydrogen across the Pd/MgSc interface never comes to dominate the kinetic response.

Formation of the fcc structure of ScH_2 upon hydrogenation is confirmed by *ex-situ* XRD measurements for $Mg_{0.65}Sc_{0.35}$ and $Mg_{0.75}Sc_{0.25}$ bulk materials. Partial desorption of a hydrogenated $Mg_{0.65}Sc_{0.35}$ alloy showed coexistence of 2 fcc structures at H/M ratios between 1 and 2. This shows that the metal host structure is retained upon crossing the plateau region, the same as for AB_5 and AB_2 type alloys. Although the strong preferential orientation of the

thin films puts severe limitations on the crystallographic information that can be obtained, their behavior seems strongly similar to that of bulk materials.

Overall, thin films seem to give a very good indication of the behavior of a bulk material regarding the storage capacity, thermodynamic properties and crystal structure and are therefore considered suitable as a model system.

In Chapter 5, the properties of MgSc alloys and hydrides are studied in more detail using Neutron Diffraction, NMR and DFT calculations. Contrary to X-ray diffraction, neutron diffraction enables direct determination of the positions of the hydrogen (deuterium) atoms. For a fully charged $Mg_{0.65}Sc_{0.35}$ alloy, simultaneous occupation of tetrahedral and octahedral sites was found at a D/M ratio of 2.25. Partial solid-gas desorption showed a single fcc phase down to a D/M ratio of 1.69. At 1.21 D/M, coexistence of two fcc phases was found, in accordance with the XRD results presented in Chapter 4. However, the concentration boundaries of the plateau region are, at 1.55 and 0.85 D/M, found to be substantially different from those derived from the GITT measurements. *In-situ* neutron diffraction measurements in a specially designed electrochemical cell yielded crystallographic information on the first hydrogen loading. Remerkably, no evidence of a two-phase coexistence region was found during charging. During discharge, the material's behavior was identical to what was found in the solid-gas experiments.

The hydrogen motion rates were quantified by determining NMR relaxation times as a function of temperature. Diffusional motion of hydrogen was found to be seven orders of magnitude higher in cubic ScH_2 compared to rutile MgH_2. For the ternary $Mg_{0.65}Sc_{0.35}H_{2.20}$ hydride, the hydrogen motion rate is increased by a further two orders of magnitude, although it is still far below that of $LaNi_5H_6$. These measurements provided quantitative evidence for the improved hydrogen transport properties in cubic hydrides compared to rutile MgH_2, which was already inferred from the electrochemical experiments in Chapter 4.

NMR spectroscopy showed clear evidence of clustering of the metal atoms and thus of partial phase segregation. So-called TRAPDOR measurements, which involve simultaneous excitation of the deuterium and scandium atoms, were used to determine the amount of D-atoms with pure Mg coordination. Based on a statistically random distribution of the metal atoms in a hydrided (deuterated) $Mg_{0.65}Sc_{0.35}$ alloy, 17% of the D-atoms is expected to have Mg_4 coordination. However, about 50% of the D-atoms was insensitive to Sc-irradiation, which means the material has a tendency to segregate into the binary hydrides. This is an intriguing result because diffraction measurements did not give any evidence for phase separation, but instead showed only one type of long-range order. From 2-D Exchange measurements, the deuterium atoms were found to exchange between all NMR-distinct sites. Full randomization took place within 100 ms.

The fluorite-to-rutile transition point, as derived from the electrochemical measurements, is exactly reproduced by DFT calculations at 80 at.% Mg. Around the transition point, a significant shift of the hydrogen atoms away from the tetrahedral positions is found, which should be detectable by neutron diffraction. At 1 H/M, the sphalerite structure that is commonly found in ionic solids was found to be the most unstable. Instead, the hydrogen atoms are found to cluster together as close as possible for any H/M ratio lower than 2. These results, together with the NMR measurements, show that MgSc hydrides indeed tend to segregate into the binary hydrides, although the tendency is not very strong for bulk materials, as even after repeated exposure to elevated temperatures during slid-gas desorption, diffraction still showed a coherent fcc structure.

Chapter 6 describes the synthesis and characterization of metastable Mg-Ti alloys and hydrides by mechanical alloying. Sc is a very expensive element (> 10 USD/g) and a suitable,

cheaper substitute had to be found. Because the cubic crystal structure had been found to be very important in obtaining favorable (de)sorption kinetics, suitable candidates were sought among elements that form a cubic dihydride. Previous studies on thin films had already shown that Ti is a promising alternative to Sc, and a reversible capacity of 6.5 wt.% had been reached for $Mg_{0.80}Ti_{0.20}$. Unfortunately, Mg and Ti are immiscible in thermodynamic equilibrium, although bulk Mg-Ti hydrides have been synthesized using ultra-high pressure 'anvil-cell' techniques.

The solid solubility of Ti in Mg can be extended by mechnical alloying, while retaining the hexagonal-close-packed (hcp) structure of Mg and Ti. A solute level of 12.5 at.% Ti in Mg had been reached in the past, but the resulting alloy was only studied at elevated temperatures and decomposed into MgH_2 and TiH_2. By milling Mg and Ti powders together with up to 4 wt.% of stearic acid as a process-control agent, a mixture of 65 at.% Mg and 35 at.% Ti can be completely reacted to form 2 fcc structured compounds with different lattice constants. The phase with a = 4.25 Å was identified as pure Ti, which is apparently transformed from hcp to fcc. This behavior was known from studies on high-energy ball milling of pure Ti. The second phase has a = 4.40-4.42 Å and is a cubic solid solution of Ti in Mg. At higher Mg content, some unreacted Mg always remained at the end of the milling process.

A $Mg_{0.85}Ti_{0.15}$ powder mixture can be processed without addition of stearic acid. In this case, dissolution of a few at.% of Ti in Mg is also observed, besides the formation of cubic compounds. When using Mg ribbon instead of powder, a hcp solid solution of Ti in Mg is formed with only trace amounts of the cubic MgTi phase. It is concluded that oxygen impurities, more abundant in a powder which has a much higher specific suface area compared to a ribbon, induce the transformation from hexagonal to cubic. From the shift in the lattice parameters, a Ti-content of 10 at.% could be determined. This is, however, much lower than the 25-35 at.% Ti that the mixtures nominally contained and in the compositional range where a rutile structure is formed upon hydrogenation.

The addition of 5-10 at.% of Ni powder does not drastically change the outcome of the milling process. The same two fcc phases are formed when Mg and Ti powders are used and the values of the lattice constants give no indication that Ni is dissolving in either of the fcc phases. It is therefore most likely than the Ni forms an amorphous secondary Mg-Ni-Ti phase, which has also been intensively investigated by others as a hydrogen storage medium. When Ni is added to a hexagonal Mg(Ti) solid solution, a shift of the Mg reflections is observed in the XRD patterns in the direction of pure Mg. This means that Ti is 'leaking' back out of the Mg to form a secondary phase. Formation of a nanocrystalline supersaturated solid solution of Ti in Ni is indeed observed.

The hydrogen storage capacity of the binary hexagonal compounds is much larger than that of their cubic counterparts. The hcp solid solutions absorb up to 975 mAh/g (3.7 wt.%) whereas the cubic compounds reach no more than 500 mAh/g. The influence on the discharge capacity is much smaller, reaching 420 mAh/g for the cubic *vs.* 550 mAh/g for the hexagonal compounds. The addition of Ni has a very favorable influence on the electrochemical properties for both the cubic and hexagonal materials. The discharge capacity increases to 520 mAh/g for the cubic compounds and to 837 mAh/g for the hexagonal solid solution. Moreover, 85% of the total capacity extracted at a current density of 10 mA/g can be extracted at 50 mA/g for the ternary cubic mixture compared to only 50% for the binary compound. For the hexagonal solid solutions, a similar improvement is observed from less than 30% for the binary to more than 50% for the ternary mixture.

Neutron diffraction and NMR on a deuterated cubic $Mg_{0.65}Ti_{0.35}$ mixture showed complete decomposition into the binary deuterides at 175°C and 75 bars of pressure. Remarkably, 2-D Exchange NMR did show that deuterium atoms exchange between Mg and Ti environments, despite the extremely poor transport properties of rutile MgD_2 and that a large part of the

deuterium atoms in a Ti environment are very tightly bound and isolated. The fluorite-to-rutile transition point derived from studies on Mg_xTi_{1-x} thin films is exactly reproduced by DFT calculations at x = 0.80, the same as for MgSc.

In conclusion, the research work described in this thesis clearly shows that the crystal structure of the hydride plays a very dominant role in determining the hydrogen storage properties of Mg-based alloys. Sc and Ti are proved to be suitable alloying elements to induce a transformation from a rutile to a much more favorable cubic structure. The high price of Sc makes Ti the preferred choice. Although much progress has been made in synthesizing metastable Mg-Ti bulk materials, their properties need to be improved further before their storage capacity is sufficient for practical application.

Samenvatting

Het gebruik van draagbare electronische apparatuur neemt de laatste jaren enorm toe. Tegelijkertijd zorgt de toename van het aantal ingebouwde functies, bijvoorbeeld in mobiele telefoons, voor een voortdurende toename van het energieverbruik van deze apparaten. Dit stelt hoge eisen aan de draagbare energiebron die in een bepaalde toepassing wordt gebruikt wat de opslagcapaciteit en de levensduur bij herhaaldelijk op-en ontladen betreft.

De wereldwijde beschikbaarheid van energie is eveneens een steeds belangrijker wordend probleem. Traditionele energiebronnen zoals fossiele brandstoffen zullen op den duur opraken en zorgen ook voor milieu-onvriendelijke emissies. Waterstof, op een duurzame manier geproduceerd, bijvoorbeeld uit wind-of zonne-energie, kan dienen als een alternatieve, milieuvriendelijke energiedrager. De opgeslagen waterstof kan op twee manieren gebruikt worden; als gas in bijvoorbeeld een brandstofcel of electrochemisch, zoals in oplaadbare Nikkel-MetaalHydride (Ni-MH) batterijen die gebruikt worden in draagbare electronica of hybride auto's.

Een aantal verschillende technologieën om gasvormig waterstof op te slaan worden intensief onderzocht. Het gas kan worden opgeslagen onder zeer hoge druk, als cryogene vloeistof, geadsorbeerd op een materiaal met een hoog actief oppervlak zoals actieve koolstof en Metal-Organic Frameworks of in de vorm van een reversible metaal hydride. Wil een waterstof opslag technologie levensvatbaar zijn, moet hij minstens 6 gew.% waterstof kunnen opslaan, zoals vermeld in de doelstellingen van het U.S. Department of Energy (DoE) voor 2010. De AB_5-type materialen die momenteel in Ni-MH batterijen gebruikt worden hebben een opslagcapaciteit van slechts 1.2 gew.%, wat ze ongeschikt maakt voor branstofcel toepassingen. Daarom wordt er momenteel intensief gezocht naar materialen die, zowel voor gasvormig waterstof als electrochemisch, een beduidend hogere capaciteit hebben. Legeringen op basis van Magnesium vormen een veelbelovende klasse materialen, omdat de capaciteit van puur MgH_2 maar liefst 7.6 gew.% bedraagt.

Electrochemie is de belangrijkste karakteriseringsmethode die wordt gebruikt om de waterstofopslageigenschappen van de legeringen te onderzoeken. De basisprincipes van electrochemie worden in Hoofdstuk 2 uiteengezet. De electrochemische reacties die een rol spelen, evenals de belangrijkste meettechnieken om ze te onderzoeken, zoals beladen en ontladen met constrante stroom (CC), het electrochemisch bepalen van de evenwichtsdruk (GITT) en impedantie spectroscopie (EIS) worden behandeld. De experimentele details van de electrochemische meetopstelling en de preparatie van Magnesium-gebaseerde legeringen en hydrides zijn eveneens in Hoofdstuk 2 te vinden. De rest van dit hoofdstuk bevat een theoretische inleiding in Röntgen diffractie (XRD), kernspinresonantie (NMR) en Dichtheidsfunctionaaltheorie (DFT). XRD en neutronen diffractie worden gebruikt om de kristallografische eigenschappen van legeringen en hydrides te bestuderen. NMR geeft inzicht in de atomaire omringing van de waterstofatomen en completeerd op die manier de informatie uit diffractiemetingen. Met DFT is het mogelijk om vormingenthalpieën van legeringen en hydrides te voorspellen en om de relatieve stabilitiet van verschillende kristalstructuren met elkaar te vergelijken. XRD, NMR en DFT worden in voldoende detail beschreven om de resultaten en conclusies uit de overige hoofdstukken begrijpelijk te maken voor de lezer.

Hoofdstuk 3 is een uitgebreid overzicht van de state-of-the-art in waterstofopslagmaterialen. De algemene eigenschappen, evenals een aantal interessante toepassingsgebieden worden in dit hoofdstuk besproken. Vier typen materialen, complexe hydrides, nitrides, interstitiële metaal-hydrides en Mg-gebaseerde legeringen worden beschreven. Complexe hydrides, met name de boorhydrides, hebben een zeer hoge capaciteit,

maar de extreme omstandigheden (tientallen atmosfeer aan druk en hoge tmperaturen) die nodig zijn voor rehydrogenering bemoeilijken toepassing van deze materialen. Toevoeging van Ti als katalysator, met name voor $NaAlH_4$, leidt tot een belangrijke verbetering, maar de totale reversibele ccpaciteit, 5.5 gew.%, is niet hoog genoeg voor praktische toepassing. Li_3N kan, in principe, meer dan 10 gew.% waterstof opslaan. De temperatuur benodigd voor desorptie is echter te hoog, doordat de evenwichtsdruk zeer laag is. Toevoeging van Magnesium verhoogt de evenwichtsdruk met meer dan een orde grootte en het lijkt waarschijnlijk dat de eigenschappen van deze materialen naar toegankelijke werkdrukken gebracht kunnen worden.

Van de interstitiële hydrides worden vier typen overgansmetaallegeringen behandeld. De AB_5 en AB_2-type materialen evenals de superstructuur-legeringen en Vanadium-gebaseerde materialen worden aan de hand van hun kristallografische eigenschappen, waterstofopslagcapaciteit en optimalisatie van hun samenstelling voor toepassing als (electrochemisch) opslagmedium besproken. De AB_5 type materialen, waar A een zeldzaam-aard (RE) metaal of een mengsel daarvan is en B een (mengsel van) overgangsmeta(a)l(en) worden toegepast in herlaadbare Ni-MH batterijen. Deze materialen hebben een hexagonale $CaCu_5$ structuur die behouden blijft na waterstofabsorptie. De tekortkomingen van het oorspronkelijke $LaNi_5$: een evenwichtsdruk van aanzienlijk meer dan 1 bar en een grote discrete expansie, wat tot verpulvering en progressieve corrosie van het materiaal leidt, werden succesvol opgelost door een deel van het Ni te vervangen door Co, Mn en Al. De capaciteit van deze materialen is echter vrij laag, 1.2 gew.%, wat niet voldoende is met het oog op de doelstellingen van het DoE. De AB_2 type legeringen, waar A Zr of Ti is en B een een mengsel van andere overgangsmetalen, zijn ook uitvoerig bestudeerd voor electrochemische toepassingen. Deze materialen kunnen een kubische (C15) of een hexagonale (C14) struktuur hebben, afhankelijk van de exacte samenstelling, die na waterstofabsorptie behouden blijft. Hoewel de intrinsieke capaciteit aanmerkelijk hoger is dan voor AB_5-type legeringen, tot wel 1.96 en 2.8 gew.% voor $ZrCr_2$ respectievelijk ZrV_2, verlaagt optimalisatie van de samenstelling met het oog op corrosiebestendigheid en activeringsgedrag de capaciteit tot ~350 mAh/g (1.3 gew.%). De superstructuur-legeringen hebben AB_{3-4} stoechiometry en bestaan uit een periodieke stapeling van AB_5 en AB_2 structuur-eenheden. De gravimetrische capaciteit wordt verhoogd door een deel van de RE-metalen (A-site) te vervangen door het lichtere Mg. Voor de samenstelling $Mm_{0.83}Mg_{0.17}Ni_{3.1}Al_{0.2}$ is een 10% hogere capaciteit dan AB_5 type legeringen gedemonstreerd voor een AA-type batterij. De Vanadium-gebaseerde legeringen hebben de hoogste intrinsieke capaciteit (~4 gew.%) van alle overgangsmetaallegeringen en ook zeer interessante kristallografische eigenschappen. Wanneer het waterstofgehalte toeneemt, transformeren deze legeringen van een lichaam-gecentreerd-kubische (bcc) naar een vlak-gecentreerd-kubische (fcc) struktuur, waarbij afhankelijk van de exacte samenstelling soms nog een tetragonale fase voor komt. De totale volume-expansie ligt daarbij vaak boven de 35%, veel meer dan bij de AB_5 en AB_2-type materialen. De meest gunstige eigenschappen tot nu toe zijn gevonden voor $(Ti_{0.355}V_{0.645})_{0.84}Fe_{0.14}$ met een reversibele capaciteit van 2.3 gew.% bij 100^oC en een absorptie-tijd van slechts 40 seconden bij kamertemperatuur.

Hoewel aanzienlijke verbeteringen in opslagcapaciteit zijn bereikt, de vanadium-legeringen hebben ruim twee maal zo veel capaciteit als de AB_5-type materialen, moet deze nog eens verdubbelen om de DoE-doelstelling van 6 gew.% te halen. MgH_2 heeft een zeer hoge capaciteit van 7.6 gew.%, maar heeft als belangrijk nadeel dat de (ab)sorptie kinetiek extreem traag is. Diffusie van waterstof door MgH_2 met de rutiel-structuur is extreem langzaam en hydrogenering van Mg poeder wordt effectief geblokkeerd zodra er een gesloten laag van het hydride is gevormd aan het oppervlak van een deeltje. Een omgekeerde relatie tussen de uiteindelijke gehydrogeneerde fractie en de initiële hydrogeneringssnelheid is

consequent in de literatuur terug te vinden, zelfs voor nanokristallijn Mg geproduceerd door ball-milling. Toevoeging van een katalysator lost deze problemen niet geheel op, hoewel meer dan 7 gew.% waterstof kan worden opgeslagen in een ball-milled mengsel van Mg, Zr en Mn.

Dunne films van Mg-RE (RE=Gd, La, Y) legeringen ondergaan drastische veranderingen in hun optische eigenschappen als functie van hun waterstofgehalte. De films zijn reflecterend in hun metallische vorm, hoog absorberend (zwart) bij tussenliggende waterstofconcentratie en transparant in volledig beladen toestand. De films kunnen zeer snel geschakeld worden tussen deze drie toestanden zelfs bij hoge gehaltes aan Mg van meer dan 70%. Hoewel in eerste instantie een fase-segregatie model is voorgesteld als verklaring voor de zwarte toestand, wijzen de experimentele resultaten voor een bulk legering van $Mg_{0.50}Y_{0.50}$ en ball-milled $Mg_{0.65}Y_{0.35}$ hydrides op de vorming van een ternair, kubisch hydride.

Omdat Sc direct boven La en Y in het periodiek systeem staat, is te verwachten dat Mg-Sc legeringen dezelfde verbetering van de (de)sorptie kinetiek laten zien als de Mg-RE en Mg-Y legeringen. Bovendien is Sc veel lichter dan Y en La en daarom zullen Mg-Sc legeringen een veel hogere gravimetrische capaciteit hebben. Gelet op de verkregen resultaten op Mg-Y bulk legeringen en dunne films leenden de Mg-Sc legeringen zich uitstekend voor een vergelijkende studie tussen bulk materialen en dunne films en dit is dan ook het onderwerp van Hoofdstuk 4. Hoofddoel van dit werk was om te bepalen of de electrochemische, kristallografische en thermodynamische eigenschappen van dunne films een goede indicatie geven van het gedrag van bulk materialen. Wanneer dit inderdad zo is, kunnen dunne films gebruikt worden als een snelle manier om naar veelbelovende samenstellingen te zoeken, omdat hun preparatiemethode (e-beam depositie) niet beperkt is tot thermodynamisch stabiele legeringen. De trends in de electrochemische capaciteit, evenwichtsdruk en kristalstruktuur blijken inderdad vrijwel identiek te zijn voor beide systemen.

Bij toenemende Mg/Sc verhouding neemt de reversibele capaciteit eerst toe tot een maximum van 1795 mAh/g (6.7 gew.%) voor dunne films en 1495 mAh/g (5.6 gew.%) voor bulk materialen voor de samenstelling $Mg_{0.80}Sc_{0.20}$. Deze waarden liggen zeer dicht tegen de theoretisch maximale waarden gebaseerd op de absorptie van 2 H/Mg en 3 H/Sc en de desorptie van 2 H/Mg en ongeveer 1 H/Sc. Bij nog hoger Mg gehalte nemen zowel het vermogen om hoge stromen te leveren als de totale reversibele capaciteit sterk af. Dit wordt toegeschreven aan een verandering van de kristalstruktuur van de fluoriet struktuur van ScH_2 naar de rutiel struktuur van MgH_2. De aanwezigheid van een groot aantal lege octaëdrische roosterplaatsen in de fluorietstruktuur zorgt voor een veel snellere diffusie van waterstof ion vergelijking met de rutielstruktuur.

De plateaudruk, zoals bepaald met GITT metingen, is zeer weinig afhankelijk van de van de Mg/Sc verhouding tussen 65 en 85 at.% Mg en vrijwel gelijk aan die van puur Mg bij 10^{-6}-10^{-7} bar. De waterstofconcentratiegrenzen van het druk-plateau zijn, bij benadering, 2 en 1 H/M. Alleen voor een bulk materiaal met samenstelling $Mg_{0.50}Sc_{0.50}Pd_{0.024}$ is de evenwichtsdruk aan het begin van het druk-plateau meer dan een orde grootte lager, wat eveneens werd waargenomen voor een $Mg_{0.50}Y_{0.50}$ legering.

Uit metingen met impedantiespectroscopie blijkt dat de oppervlaktekinetiek van de dunne films volledig wordt gedomineerd door de Pd toplaag. De relatie tussen de ladingsoverdrachtsweerstand en de waterstofconcentratie is identiek aan die van een enkele Pd laag, wanneer deze wordt uitgezet als functie van de evenwichtspotentiaal. Bij lage waterstofconcentraties wordt de totale kinetische respons van de films hoofdzakelijk bepaald door de overdracht van waterstof tussen de Pd toplaag en de onderliggende MgSc fase. Voor bulk $Mg_{0.65}Sc_{0.35}$ ball-milled met Pd werd hetzelfde gedrag van de ladingsoverdrachtsweerstand gevonden, hoewel de overdracht over het Pd/MgSc grensvlak nooit dominant wordt.

De vorming van de fcc structuur van ScH_2 wordt bevestigd door *ex-situ* XRD metingen voor $Mg_{0.65}Sc_{0.35}$ en $Mg_{0.75}Sc_{0.25}$ bulk materialen. Na gedeeltelijke desorptie van gehydreerd $Mg_{0.65}Sc_{0.35}$ bestaan 2 fcc fasen naast elkaar bij H/M verhoudingen tussen 1 en 2. De structuur van het metaalrooster is een weerszijden van het plateau dus identiek, net als bij de AB_5 en AB_2 materialen. Hoewel door de sterke voorkeursoriëntatie van de dunne films de hoeveelheid kristallografische informatie beperkt is, lijkt hun gedrag toch grotendeels hetzelfde als dat van de bulk materialen.

Al met al geven de dunne films een zeer goede indicatie van het gedrag van bulk materialen wat betreft de opslagcapaciteit, thermodynamische eigenschappen en kristalstruktuur en kunnen daarom als een geschikt modelsysteem worden beschouwd.

In hoofdstuk 5 worden de eigenschappen van MgSc legeringen en hydrides in detail bestudeerd met Neutronen Diffractie, NMR en DFT berekeningen. In tegenstelling tot XRD, maakt neutronen diffractie directe waarneming van de posities van de waterstof (deuterium) atomen mogelijk. $Mg_{0.65}Sc_{0.35}$. Voor een volledig beladen $Mg_{0.65}Sc_{0.35}$ legering wordt gelijktijdige bezetting van de tetraëdrische en octaëdrische roosterplaatsen waargenomen bij een D/M verhouding van 2.25. Tijdens stapsgewijze desorptie wordt tot D/M=1.69 één fcc structuur waargenomen. Bij 1.21 D/M worden, in overeenstemming met de XRD resultaten uit hoofdstuk 4, 2 fcc fasen waargenomen. De concentratiegrenzen van het druk-plateau, 1.55 en 0.85 D/M, zijn echter beduidend verschillend van de waarden die uit de GITT metingen komen. *In-situ* neutronen diffractie metingen in een speciaal ontworpen electrochemische cel leverde kristallografische informatie op over de eerste belading met waterstof. Tijdens de eerste belading werd geen 2-fasen gebied waargenomen. Bij ontladen gedroeg het materiaal zich op dezelfde manier als tijdens *ex-situ* desorptie van waterstof gas.

De diffusiesnelheid van waterstof is gekwantificeerd door het bepalen van NMR relaxatietijden als functie van de temperatuur. Waterstof bleek $\sim 10^7$ maal zo snel door kubisch ScH_2 te diffunderen dan door rutiel MgH_2. Voor het ternaire $Mg_{0.65}Sc_{0.35}H_{2.20}$ hydride was de diffusiesnelheid nog eens 2 orde groottes hoger, hoewel ze nog steeds bveel langzamer is dan in $LaNi_5H_6$. Deze metingen leverden het kwantitatieve bewijs van de verbeterde waterstoftransporteigenschappen van kubische hydrides in vergelijking met rutiel MgH_2, wat al werd afgeleid uit de electrochemische metingen in Hoofdstuk 4.

NMR spectroscopie gaf duidelijke aanwijzingen dat de metaalatomen clusters vormen en dat er toch gedeeltelijke fasescheiding optreedt. Zogeheten TRAPDOR metingen, waarbij deuterium en Scandium tegelijkertijd worden aangeslagen, zijn gebruikt om te bepalen hoeveel D-atomen enkel omringd zijn door Mg atomen. Een statistisch willekeurige verdeling van de metaalatomen in een gehydreerd (gedeutereerd) $Mg_{0.65}Sc_{0.35}$ geeft een verwachtingswaarde van 17% voor de fractie D-atomen met Mg_4 coordinatie. Echter, 50% van de D-atomen bleek ongevoelig te zijn voor aanslag van Sc, wat betekent dat het materiaal de neiging heeft om uiteen te vallen in de binaire hydrides. Dit is een zeer interessant resultaat, omdat diffractiemetingen geen enkele aanwijzing gaven voor fasescheiding, maar slechts 1 type lange-afstands-ordening lieten zien. Uit 2-D uitwisselingsmetingen bleek dat deuterium atomen tussen alle sites die met NMR onderscheiden kunnen worden kunnen bewegen. Volledige uitwisseling vind plaats binnen 100 ms.

De overgang van een fluoriet naar een rutiel structuur, zoals reeds afgeleid uit electrochemische metingen, wordt exact gereproduceerd door DFT berekeningen bij 80 at.% Mg. Rond het overgangspunt wordt een aanzienlijke verschuiving van de waterstofatomen weg van de tetraëdrische posities voorspeld, welke met neutronendiffractie detecteerbaar zou moeten zijn. Bij 1 H/M blijkt de sphaleriet structuur, die gewoonlijk in ionogene vast stoffen wordt gevonden, het minst stabiel te zijn. In plaats daarvan blijken de waterstofatomen bij elke H/M ratio lager dan 2 zo dicht mogelijk naar elkaar toe te trekken. Dit, samen met de

NMR resultaten, laat zien dat MgSc hydrides inderdaad uiteen vallen in de binaire hydrides, hoewel deze neiging voor bulk materialen niet heel sterk is. Zelfs na herhaaldelijke blootstelling aan hoge temperaturen liet neutronendiffractie nog steeds een coherente fcc structuur zien.

Hoofdstuk 6 beschrijft de preparatie en karakterisering van metastabiele Mg-Ti legeringen en hydrides door mechanisch legeren. Sc is een erg duur metaal (> 10 USD/g) en daarom dient er een geschikt, goedkoper alternatief gevonden te worden. Omdat de kubische kristalstructuur erg belangrijk bleek te zijn om gunstige ab-en desorptie snelheden te krijgen, werden de alternatieven gezocht in de elementen die zelf een kubisch dihydride vormen. Eerdere studies aan dunne films hadden reeds laten zien dat Ti een veelbelovend alternatief is voor Sc, waarbij een reversibele capaciteit van 6.5 gew.% voor $Mg_{0.80}Ti_{0.20}$ werd gevonden. Helaas zijn bulk Mg-Ti legeringen thermodynamisch niet stabiel, al kunnen bulk Mg-Ti hydrides wel gevormd worden bij ultrahoge drukken.

De vaste oplosbaarheid van Ti in Mg kan verhoogd worden door mechanisch legeren, waarbij de hexagonale structuur van puur Mg en Ti behouden blijft. Een verhoging van de oplosbaarheid tot 12.5 at.% Ti in Mg is uit de literatuur bekend, maar waterstofopslag werd alleen bestudeerd bij hoge temperatuur, waar het materiaal uiteen viel in MgH_2 en TiH_2. Malen van 65 % Mg en 35% Ti poeder met 4 gew.% stearinezuur als anti-plakmiddel resulteert in een mengsel van 2 fcc fasen met verschillende roosterconstantes. De fase met a = 4.25 Å bleek puur Ti te zijn, wat blijkbaar van hcp naar fcc kan worden omgezet. Dit gedrag was reeds bekend uit eerdere studies aan ball-milling van puur Ti. De tweede fase heeft a = 4.40-4.42 Å en is een kubische vaste oplossing van Ti in Mg. Bij hogere Mg concentraties blijft ongereageerd Mg over aan het einde van het maal-proces.

Een poedermengsel met samenstelling $Mg_{0.85}Ti_{0.15}$ kan zonder stearinezuur gemalen worden. In dit geval wordt ook een hexagonale vaste oplossing van enkele at.% Ti in Mg gevonden naast de kubische fasen. Wanneer Mg lint, in plaats van poeder, wordt gebruikt, wordt een hcp vaste oplossing van Ti in Mg gevormd, samen met een kleine hoeveelheid van de kubische fase(n). Het is daarom het meest waarschijnlijk dat oxidische verontreinigingen, waarvan een poeder, vanwege een hoger specifiek oppervlak, meer bevat dan een lint, de transformatie van hexagonaal naar kubisch induceren. Uit de verschuiving van de roosterconstanten blijkt dat de hoeveelheid opgelost Ti ongeveer 10 at.% bedraagt. Dit is echter veel minder dan de 25-35% Ti die de mengsels nominaal bevatten en in het samenstellingsgebied waar en rutielstructuur wordt gevormd na hydrogenering.

Toevoeging van 5-10 at.% Ni heeft geen sterke invloed op het resultaat van het maalproces. Uitgaande van een poedermengsel worden dezelfde 2 kubische fasen gevormd en de waarden van de roosterconstantes geven geen reden om aan te nemen dat Ni oplost in een van de twee fasen. Het is daarom het meest waarschijnlijk dat Ni een amorfe Mg-Ti-Ni fase vormt, welke door anderen ook intensief zijn onderzocht als waterstofopslagmedium. Wanneer Ni wordt toegevoegd aan een hcp Mg(Ti) vaste oplossing, wordt een verschuiving van het diffractiepatroon terug in de richting van puur Mg waargenomen. Dit betekent dat Ti terug uit het Mg ‘lekt’ en een nanokristallijne oververzadigde vast oplossing met Ni vormt.

De opslagcapaciteit van de binaire hexagonale verbindingen is veel groter dan die van de kubische. De absorptiecapaciteit die voor de hcp vaste oplossing gevonden wordt is 975 mAh/g (3.7 gew.%), waar die van de kubische verbindingen slechts 500 mAh/g bedraagt. De invloed op de desorptiecapacitiet is veel kleiner; deze verbetert van 420 mAh/g voor de kubische naar 550 mAh/g voor de hexagonale fase. De toevoeging van Ni heeft een zeer gunstige invloed op de electrochemische eigenschappen van zowel de hcp als de fcc fasen. Voor de kubische verbindingen verbetert de ontlaadcapaciteit tot 520 mAh/g en vor de hexagonale tot wel 837 mAh/g (3.2 gew.%). Bovendien kan 85% van de totale capaciteit bij

een stroomdichtheid van 10 mA/g al met 50 mA/g ontladen worden voor het ternaire kubische mengsel, waar dit voor het binaire systeem slechts 50% is. Voor de hexagonale fase verbetert de capaciteit bij 50 mA/g van 30% naar meer dan 50% van het totaal wanneer Ni is toegevoegd.

Neutronendiffractie en NMR aan een gedeutereerd kubisch $Mg_{0.65}Ti_{0.35}$ mengsel liet volledige segregatie in de binaire deuterides zien bij 175^{o}C en 75 bar. Merkwaardigerwijs lieten 2-D uitwisselingsmetingen zien dat er wel deuterium atomen tussen Mg en Ti omgevingen worden uitgewisseld, ondanks de slechte transporteigenschappen van rutiel MgD_2, en dat een groot deel van de deuterium atomen in een Ti omgeving erg sterk gebonden zijn. DFT reproduceert ook dit keer het fluoriet-rutiel overgangspunt uit studies aan dunne films exact bij 80 at.% Mg, hetzelfde als voor MgSc.

Het kan geconcludeerd worden dat het werk beschreven in dit proefschrift duidelijk bewijst dat de kristalstructuur een zeer dominante rol speelt in het bepalen van de waterstofopslageigenschappen van Mg legeringen. Van Sc en Ti is bewezen dat ze in een legering met Mg de transformatie van rutiel naar een veel gunstiger kubisch hydride kunnen bewerkstelligen. De hoge prijs van Sc maakt Ti de beste keus. Hoewel er aanzienlijke vooruitgang is geboekt in de synthese van metastabiele Mg-Ti bulk legeringen, moeten hun eigenschappen nog verder verbeteren voordat de capaciteit voldoende is voor praktische toepassing.

List of Publications

1. W.P. Kalisvaart, R.A.H. Niessen, P.H.L. Notten, Electrochemical hydrogen storage in MgSc alloys: a comparative study between thin films and bulk materials, *J. Alloys Comp.*, **417**, 280-291 (2006)

2. M. Latroche, W.P. Kalisvaart, P.H.L. Notten, Crystal structure of $Mg_{0.65}Sc_{0.35}D_x$ deuterides studied by X-Ray and Neutron powder diffraction, *J. Solid State Chemistry*, **179**, 3024-3032 (2006)

3. W.P.Kalisvaart, P. Vermeulen, A.V. Ledovskikh, D. Danilov, P.H.L. Notten, The electrochemistry and modeling of hydrogen storage materials, *J. Alloys Comp.*, **446-447**, 648-654 (2007)

4. W.P. Kalisvaart, H.J. Wondergem, F. Bakker, P.H.L. Notten, Mg-Ti based materials for electrochemical hydrogen storage, *J. Mat. Res.*, 22, 1640-1649 (2007)

5. M.S. Conradi, M. P. Mendenhall, T.M. Ivancic, E.A. Carl, C.D. Browning, P.H.L. Notten, W.P. Kalisvaart, P.C.M.M. Magusin, R.C. Bowman jr., S-J. Hwang and N.L. Adolphi, NMR to determine rates of motion and structures in Metal-Hydrides, *J. Alloys Comp.*, **446-447**, 499-503 (2007)

6. Cubic MgH_2 stabilized by Alloying with Transition Metals: A DFT study, B.R. Pauw, W.P. Kalisvaart, S.X. Tao, M.T.M. Koper, A.P.J. Jansen, P.H.L. Notten, *Acta Materialia*, **56**, 2848-2954 (2008)

7. W.P. Kalisvaart, M. Latroche, F. Cuevas, P.H.L. Notten, *In situ* Neutron Diffraction study on Pd-doped $Mg_{0.65}Sc_{0.35}$ electrode material, *J. Solid State Chemistry,* **181**, 1141-1148 (2008)

8. P.C.M.M. Magusin, W.P. Kalisvaart, P.H.L. Notten, R.A. van Santen, Hydrogen sites and dynamics in light-weight hydrogen-storage material Magnesium Scandium Hydride investigated with ^1H and ^2H NMR, *Chem. Phys. Lett.*, **456**, 55-58 (2008)

9. W.P. Kalisvaart, P.H.L. Notten, Mechanical Alloying and Hydrogen storage of Mg-based systems, *J. Mat. Res.*, **23**, 2179-2187 (2008)

Curriculum Vitae

Willem Peter Kalisvaart was born in Terneuzen, the Netherlands on June 16, 1980. In 1992 he finished his primary education at Basisschool Reuzenhoek. Following his secondary education (VWO) at the Zeldenrustcollege in Terneuzen (1992-1998) he started his Chemical Engineering studies at the Eindhoven University of Technology in 1998. During his studies he performed various research assignments ranging from synthesis of mesoporous, high surface area silicate materials (Inorganic Chemistry and Catalysis group) to the investigation of filtration materials for natural-draft spray towers in the production of urea pellets (Hydro Agri, Sluiskil, The Netherlands). The topic of his graduation work was the luminescence properties of nanocrystalline Manganese-doped Zinc Sulphide (Solid state and Materials chemistry group), for which he received his M.Sc. degree in 2003. In January 2004 he started his Ph.D. research at Eindhoven University of Technology (Inorganic Chemistry and Catalysis group) under supervision of prof. dr. P.H.L. Notten. The research was focused on the synthesis and (electrochemical) hydrogen storage properties of Mg-based alloys. Almost all the work has been performed within the System in Package Devices group at Philips Research Laboratories Eindhoven. In the course of the Ph.D. project he visited the neutron research facility Insitut Laue-Langevin (Grenoble, France) several times to perform diffraction experiments. He presented the work described in this thesis at numerous conferences, both in the Netherlands as well as overseas (Quebec City and Banff, Canada and Boston, USA).

References

1. R. McAllister, The solar hydrogen civilization: the future of energy is the future of our global economy, (American Hydrogen Association, New York, 2003)

2. F. Barbir, PEM fuel cells; theory and practice, (Elsevier Academic Press, London, 2005)

3. P.H.L. Notten, Rechargeable nickel-metalhydride batteries: a successful new concept, in: F. Grandjean, G.J. Long, K.H.J. Buschow (Eds.), "Interstitial Intermetallic Alloys," NATO ASI Series E, vol. 281, 1995.

4. R.F. Nelson, Power requirements for batteries in hybrid electric vehicles, *J. Power Sources*, **91**, 2 (2000)

5. L. Schlapbach and A Züttel: Hydrogen-storage materials for mobile applications, *Nature*, **414**, 353 (2001)

6. U.S. Department of Energy, Multi-Year Research, Development and Demonstration Plan: planned program activities for 2005-2015, http://www1.eere.energy.gov/hydrogenandfuelcells/mypp/pdfs/storage.pdf

7. T. Graham, On the absorption and dialytic separation of gases by colloid septa, Phil. Trans. R. Soc., **156**, 426 (1866)

8. W.M. Müller, J.P. Blackledge, J.J. Libowitz, Metal hydrides, *Academic press, New York* (1968)

9. F. Cuevas, J.M. Joubert, M. Latroche and A. Percheron-Guégan: Intermetallic Compounds as negative electrodes in Ni-MH batteries, *Appl. Phys. A,* **72**, 225 (2001)

10. J.M. Tarascon, M. Armand, Issues and challenges facing rechargeable Lithium batteries, *Nature*, **414**, 359 (2001)

11. http://www.fueleconomy.gov

12. K. Machida, M. Enyo, G. Adachi, J. Shiokawa, The hydrogen electrode reaction characteristics of thin film electrodes of Ni-based hydrogen storage alloys, *Electrochimica Acta,* **29**, 807 (1984)

13. R. Griessen, T. Riesteter, Topics in Applied Physics-Hydrogen in intermetallic compounds I, Springer, Berlin, Chapter 6 (1988)

14. P.W. Atkins, Physical Chemistry, Oxford University Press, Oxford, p. 258 (1998)

15. M. Pourbaix, Atlas of electrochemical equilibria in aqueous solutions, 2nd ed. (National Association of Corrosion Engineers, Houston, 1974) p. 425

16. M. Pourbaix, Atlas of electrochemical equilibria in aqueous solutions, 2nd ed. (National Association of Corrosion Engineers, Houston, 1974) p. 97

17. J.R. MacDonald, Impedance Spectroscopy, John Wiley&Sons NY (1987)

18. R.A.H. Niessen, P.H.L. Notten, Reference electrode induced surface poisoning of thin film electrodes, *J. Electrochem. Soc.*, **152**, A2051 (2005)

19. J.P. Hornak, "The basics of NMR", **www.cis.rit.edu/htbooks/nmr/inside.htm**, (1997)

20. P. Hohenberg, W. Kohn, Inhomogeneous electron gas, *Phys. Rev.,* **136**, B864 (1964)

21. W. Kohn, L.J. Sham, Self-consistent equations including exchange and correlation effects, *Phys. Rev.*, **140**, A1133 (1965)

22. G. Kresse, J. Fűrthműller, Efficient iterative schemes for ab initio total-energy calculations using a plane-wave basis set, *Phys. Rev. B*, **54**, 11169

23. Perdew JP. in *Electronic Structure of Solids 91* Akademie Verlag, Berlin, 1991.

24. B. Bogdanovic, R.A. Brand, A. Marjanovic, M. Swickardi, J. Tölle, Metal-doped sodium aluminium hydrides as potential new hydrogen storage materials, *J. Alloys Compd.,* **302**, 36 (2000)

25. A.G. Haiduc, H.A. Stil, M.A. Schwarz, P. Paulus, J.J.C. Geerlings, On the fate of the Ti catalyst during hydrogen cycling of sodium alanate, *J. All. Comp.,* **393**, 252 (2005)

26. Ç. Çakanyıldırım, M. Gürü, Processing of $LiBH_4$ from its elements by ball-milling method, *Renewable Energy*, in press (2008)

27. H.W. Li, K. Kikuchi, Y. Nakamori, N. Ohba, K. Miwa, S. Towata, S. Orimo, Dehydriding and rehydriding processes of well-crystallized $Mg(BH_4)_2$ accompanying with formation of intermediate compounds, *Acta Materialia*, **56**, 1342 (2008)

28. J.-H. Kim, J.-H. Shim, Y. W. Cho, On the reversibility of hydrogen storage in Ti and Nb-catalyzed $Ca(BH_4)_2$, *J. Power Sources*, in press (2008)

29. K. Ohoyma, Y. Nakamori, S.I. Orimo, K. Yamada, Revised crystal structure model for Li_2NH by Neutron Diffraction, *J. Phys. Soc. Jpn*., **74**, 483 (2005)

30. P. Chen, Z. Xiong, J. Luo, J. Lin, K.L. Tan, Interaction of hydrogen with metal nitrides and imides, *Nature*, **420**, 302 (2002)

31. Z. Xiong, G.Wu, J. Hu, P. Chen, W. Luo, J. Wang, Investigations on hydrogen storage over Li–Mg–N–H complex—the effect of compositional changes, *J. All. Comp.*, **417**, 190 (2006)

32. W. Luo, ($LiNH_2$-MgH_2): a viable hydrogen storage system, *J. All. Comp.*, **381**, 284 (2004)

33. F.E. Pinkerton, G.P. Meisner, M.S. Meyer, M.P. Balogh, M.D. Kundrat, *J. Phys. Chem. B*, **109**, 6 (2005)

34. L. Schlapbach (ed.), Springer Verlag, *Topics in Applied Physics Vol. 63 : Hydrogen in Intermetallic Compounds I*, p219-227

35. B. Bogdanovic, A. Ritter, B. Spliethof, Active MgH_2-Mg systems for reversible chemical energy storage, *Angewandte Chemie*, **29**, 223 (1990)

36. P. Kumar and L.K. Malhotra, Palladium capped samarium thin films as potential hydrogen sensors, *Materials Chemistry and Physics*, **88**, 106 (2004)

37. M. Slaman, B. Dam, M. Pasturel, D.M. Borsa, H. Schreuders, J.H. Rector and R. Griessen, Fiber optic hydrogen detectors containing Mg-based hydrides, *Sensors and Actuators B: Chemical*, **123**, 538 (2007)

38. R.F. Nelson, Power requirements for batteries in hybrid electric vehicles, *J. Power Sources,* **91**, 2 (2000)

39. J.H.N. van Vught, F.A.Kuijpers and H.C.A.M. Bruning, Reversible room-temperature absorption of large quantities of hydrogen by intermetallic compounds, Philips Res. Reports, 25, 133 (1970)

40. A. Percheron-Guégan, C. Lartigue, J. C. Achard, P. Germi, F. Tasset, Neutron and X-ray diffraction profile analyses and structure of $LaNi_5$, $LaNi_{5-x}Al_x$ and $LaNi_{5-x}Mn_x$ intermetallics and their hydrides (deuterides), J. Less Common Metals, **74,** 1 (1980)

41. A. Percheron-Guégan, C. Lartigue, Hydrogen locations in $LaNi_5$ and related hydrides, *Mat. Sci. Forum,* **31**, 125 (1988)

42. M. Latroche, J. Rodriguez-Carvajal, A. Percheron-Guégan, F. Bourée-Vingeron, Structural studies of $LaNi_4CoD_{6.11}$ and $LaNi_{3.55}Mn_{0.4}Al_{0.3}Co_{0.75}D_{5.57}$ by means of neutron powder diffraction, *J. All. Comp.*, **218**, 64 (1995)

43 A. Ayeb, W. M. Otten, A. J. G. Mank and P.H.L. Notten, *J. Electrochem. Soc.*, 153 (2006) A 2055.

44. F.A.Kuipers, *Philips Res. Rep. Suppl.*, No. 2 (1973) 1.

45. H.H. van Mal, *Philips Res. Rep. Suppl*., No. 1 (1976) 1

46. J.-C. Achard, A. Percheron-Guégan, H. Diaz, F. Briaucourt and F. Demany 2nd Int. Congress on Hydrogen in Metals Paris (1977) 1E12.

47. M. Latroche, A. Percheron-Guégan, F. Bourée-Vingeron, Investigation of the crystallographic structures of $LaNi_4CoD_{4.4}$ and $LaNi_{3.55}Mn_{0.4}Al_{0.3}Co_{0.75}D_x$ (x = 2.0-4.6 D/f.u.) by neutron powder diffraction, *J. All. Comp.,* **265**, 209 (1998)

48. P.H.L. Notten, R.E.F. Einerhand, J.L.C. Daams, On the nature of the electrochemical cycling stability of non-stoichiometric $LaNi_5$-based hydride-forming compounds Part I. Crystallography and electrochemistry, *J. All. Compounds,* **210**, 221 (1994)

49. P.H.L. Notten, J.L.C. Daams, R.E.F. Einerhand, On the nature of the electrochemical cycling stability of non-stoichiometric $LaNi_5$-based hydride-forming compounds Part II. *In-situ* X-Ray diffractometry., *J. All. Compounds,* **210**, 233 (1994)

50. M. Latroche, J. M. Joubert, A. Percheron-Guégan, F. Bourée-Vingeron, Neutron Diffraction study of the deuterides of the over-stoichiometric compounds $LaNi_{5+x}$, *J. Solid State Chem.,* **177**, 1219 (2004)

51. J. M. Joubert, R. Cerny, M. Latroche, E. Leroy, L. Guénée, A. Percheron-Guégan, K. Yvon, A structural study of the homogeneity domain of $LaNi_5$, *J. Solid State Chem*., **166**, 1 (2002)

52. M. Latroche, Y. Chabre, A. Percheron-Guégan, O. Isnard, B. Knosp, Influence of stoichiometry and composition on the structural and electrochemical properties of AB_{5+y} based alloys used as negative electrodes in Ni-MH batteries, *J. All. Comp.,* **330-332**, 787 (2002)

53. D. Linden (Edt.), Handbook of batteries 2nd ed., McGraw-Hill, New York (1995)

54. S. Fujitani, I. Yonezu, T. Saito, N. Furukawa, E. Akiba, H. Hayakawa, S. Ono, Relation between equilibrium hydrogen pressure and lattice parameters in pseudobinary Zr-Mn alloy systems, *J. Less Common Metals,* **172-174**, 220 (1991)

55. J-M Joubert , M. Latroche , A. Percheron-Guégan , F. Bourée-Vigneron, Neutron diffraction study of $Zr(Cr_{0.6}Ni_{0.4})_2D_{3.3}$, *J. All. Comp.*, **217**, 283 (1995)

56. D. Fruchart, A. Rouault, C.B. Shoemaker, D.P. Shoemaker, Neutron Diffraction study of the cubic $ZrCr_2D_x$ and ZrV_2D_x (H_x) phases, *J. Less Common Metals*, **73**, 363 (1980)

57. J.M. Joubert, M. Latroche, A. Percheron-Guégan, J. Bouet, Improvement of the electrochemical activity of Zr-Cr-Ni Laves phase hydride electrodes by secondary phase precipitation, *J. Alloys and Compounds,* **240**, 219 (1996)

58. K. Yang, D. Chen, L. Chen, Z. Xiao Guo, Microstructure, electrochemical performance and gas-phase hydrogen storage properties of $Zr_{0.9}Ti_{0.1}([Ni,V,Mn]_{0.95}Co_{0.05})_\alpha$ Laves phase alloys, *J. All. Compounds,* **333**, 184 (2002)

59. D. Sun, M. Latroche, A. Percheron-Guégan, Effects of Lanthanum and Cerium on the equilibrium of $ZrNi_{1.2}Mn_{0.6}V_{0.2}Cr_{0.1}$ and its related hydrogenation properties, *J. Alloys and Compounds,* **248**, 215 (1997)

60. M. Matsuoka, K, Tamura, Effect of mechanochemical modification on electrochemical performance of Zr-Ti based Laves phase alloy electrode, *J. Electrochem. Soc.*, **154**, A119 (2007)

61. M. Matsuoka, K, Tamura, Effects of mechanical grinding on initial activation and rate capability of Zr–Ti based Laves phase alloy electrode, *J. Appl. Electrochem*, **37**, 759 (2007)

62. K. Kadir, T. Sakai, I. Uehara, Structural investigation and hydrogen storage capacity of $LaMg_2Ni_9$ and $(La_{0.65}Ca_{0.35})(Mg_{1.32}Ca_{0.68})Ni_9$ of the AB_2C_9 type structure *J. All. Comp*, **302**, 112 (2000)

63. T. Ozaki, M. Kanemoto, T. Kekeya, Y. Kitano, M. Kuzuhara, M. Watada, T. Sakai, Stacking structures and electrode performances of rare earth–Mg–Ni-based alloys for advanced nickel–metal hydride battery, *J. All. Comp.*, **446-447**, 620 (2007)

64. T. Kohno, H. Yoshida, F. Kawashima, T. Inaba, I. Sakai, M. Yamamoto and M. Kanda, Hydrogen storage properties of new ternary system alloys: La_2MgNi_9, $La_5Mg_2Ni_{23}$, La_3MgNi_{14}, *J. All. Comp.*, **311***,* L5 (2000)

65 S. Yasuoka, *Development of high-capacity nickel-metal hydride batteries using superlattice hydrogen-absorbing alloys*, J. Power Sources, **156**, 662 (2006)

66. T. Ueda, S. Hayashi, Y. Nakai, S. Ikeda, Local structure in β-$Ti_{1-y}V_yH_x$ studied by inelastic neutron scattering, *Phys Rev. B,* **51**, 5725 (1995)

67. S. Ono, S. Nomura, Y. Ikeda, The reaction of hydrogen with alloys of Vanadium and Titanium, *J. Less Common Metals,* **72**, 159 (1980)

68. S. Challet, M. Latroche, S. Heurtaux, Hydrogenation properties and crystal structure of the single bcc $(Ti_{0.355}V_{0.635})_{100-x}M_x$ alloys with M=Mn, Fe, Co, Ni (x=7, 14 and 21), *J. All. Compounds, in press*

69. J.E. Kleiner, E.H. Sevilla, R.M. Cotts, Diffusion of Hydrogen in α'-VH_x, *Phys. Rev. B,* **33**, 6662 (1986)

70. A. Kagawa, E. Ono, T. Kusakabe, Y. Sakamoto, Absorption of hydrogen by Vanadium-rich V-Ti-based alloys, *J. Less Common Metals,* **172-174**, 64 (1991)

71. C. Iwakura, W-K. Choi, R. Miyauchi, H. Inoue, Electrochemical and structural characterization of Ti-V-Ni hydrogen storage alloys with bcc structure, *J. Electrochem. Soc.,* **147**, 2503 (2000)

72. M. Tsukahara, K. Takahashi, T. Mishima, T. Sakai, H. Miyamura, N. Kuriyama, I. Uehara, Phase structure of V-basedsolid solutions containing Ti and Ni and their hydrogen absorptioon-desorption properties, *J. All. Comp.*, **224**, 162 (1995)

73. Q.A. Zhang, Y.Q. Lei, X.G. Yang, Y.L. Du, Q.D. Wang, Effects of annealing treatment on phase structures, hydrogen absorption-desorption characteristics and electrochemical properties of $TiV_3Ni_{0.56}Hf_{0.24}Mn_{0.15}Cr_{0.1}$ alloy, *J. All. Comp.,* **305**, 125 (2000)

74. Q.A. Zhang, Y.Q. Lei, L.X. Chen, Q.D. Wang, Effects of annealing treatment on phase structures, hydrogen absorption-desorption characteristics and electrochemical properties of $TiV_3Ni_{0.56}Hf_{0.24}Co_{0.14}Ta_{0.047}Nb_{0.047}$ alloy, *Mat. Chem Phys.*, **69**, 241 (2001)

75. L. Chen, R. Guo, Y. Lei, L. Li, Q. Wang, Structural and Electrochemical characteristics of $V_{2.1}TiNi_{0.5}Hf_{0.05}M_{0.152}$ (=Co, Cr) hydrogen storage electrode alloys, *Mat. Chem Phys.*, **92**, 554 (2005)

76. W. Yin, M. Zhao, Structure and electrochemical characteristics of $TiV_{1.1}Mn_{0.9}Ni_x$ (x = 0.1–0.7) alloys, *Electrochimica Acta,* **52**, 2723 (2007)

77. B. Vigeholm, K. Jensen, B. Larsen, A. Schrøder-Pedersen, Elements of hydride formation mechanisms in nearly spherical Magnesium powder particles, *J. Less Common Metals*, **131**, 133 (1987)

78. A. Zaluska, L. Zaluski, J.O. Strom Olsen, Nanocrystalline Magnesium for hydrogen storage, *J. Alloys Compounds,* **288**, 217 (1999)

79. W. Oelerich, T. Klassen, R. Borman, Comparison of the catalytic effects of V, V O , VN, and VC on the hydrogen sorption of nanocrystalline Mg, *J. All. Comp.*, **322**, L5 (2001)

80. O. Friedrichs, T. Klassen, J.C. Sanchez-Lopez, R. Bormann , A. Fernandez, Hydrogen sorption improvement of nanocrystalline MgH_2 by Nb_2O_5 nanoparticles,

81. A. Borgschulte, J.H. Rector, B. Dam, R. Griessen, A. Zuttel, The role of niobium oxide as surface catalyst for hydrogen absorption, *Journal of Catalysis,* **235**, 353 (2005)

82. I. Saita, T. Toshima, S. Tanda, T. Akiyama, Hydrogen storage property of MgH_2 synthesized by hydriding chamical vapour deposition, *J. All. Comp.*, **446-447**, 80 (2007)

83. R.W.P. Wagemans, J.H. van Lenthe, P.E. de Jongh, A.J. van Dillen, K.P. de Jong, Hydrogen storage in Magnesium Clusters: Quantum Chemical Study, *JACS*, **127**, 16675 (2005)

84. R.W.P. Wagemans, Magnesium for Hydrogen Storage; from micrometer tot nanometer, PhD thesis Utrecht University (2006)

85. R.W.P. Wagemans, B.S. Dauvillier, A.J. van Dillen, K.P. de Jongh, P.E. de Jongh, Process for preparing carbon and magnesium comprising composites, carbon and magnesium composites thus prepared, use of such composites and a hydrogen storage system, *European patent request EP06116799*

86. J. N. Huiberts, R. Griessen, J. H. Rector, R. J. Wijngaarden, J. P. Dekker, D. G. de Groot, N. J. Koeman, Yttrium and lanthanum hydride films with switchable optical properties, *Nature*, **380**, 231 (1996)

87. J.N. Huiberts, On the road to dirty metallic atomic hydrogen, Ph.D. Thesis, Vrije Universiteit Amsterdam (1995)

88. P. van der Sluis, M. Ouwerkerk, P.A. Duine, Optical switches based on Magnesium Lanthanide alloy hydrides, *Appl Phys. Lett.*, **70**, 3356 (1997)

89. I.A.M.E. Giebels, J. Isidorsson, R. Griessen, Highly absorbing black Mg and rare-earth-Mg switchable mirrors, *Phys. Rev. B,* **69**, 205111 (2004)

90. J. Isidorson, I.A.M.E.Giebels, E.S. Kooij, J.H. Rector, A.T.M. van Gogh, R. Griessen, Structural, optical and electronic properties of $LaMgH_x$ switchable mirrors, *Electrochimica Acta,* **46**, 2179 (2001)

91. S.J. van der Molen, D.G. Nagengast, A.T.M. van Gogh, J. Kalkman, E.S. Kooij, J.H. Rector, R. Griessen, Insulating fcc $YH_{3-\delta}$ stabilized by MgH_2, *Phys Rev. B*, **63,** 235116 (2001)

92. I.A.M.E. Giebels, J. Isidorsson, E.S. Kooij, A. Remhof, N.J. Koeman, J.H. Rector, A.T.M. van Gogh, R. Griessen, Highly reflecting Y/Mg–H_x multilayered switchable mirrors, *J. All. Comp.*, **330-332**, 875 (2002)

93. M. Ouwerkerk, Electrochemically induced optical switching of $Sm_{0.3}Mg_{0.70}H_x$ thin layers, *Solid State Ionics,* **113-115**, 431 (1998)

94. P.H.L. Notten, M. Ouwerkerk, H. Van Hal, D. Beelen, W. Keur, J. Zhou, H. Feil, *J. Power Sources*, **129**, 45 (2004)

95. I.A.M.E. Giebels, Shining light on Magnesium based switchable mirrors, PhD thesis VU Amsterdam (2004)

96. B.J. Beaudry, A.H. Daane, A study of the Scandium-Magnesium system from 0 to 60 at.% scandium, *J. Less Common Metals*, **18**, 305 (1969)

97. R.A.H. Niessen, P. Vermeulen and P.H.L. Notten, The electrochemistry of Pd-coated $Mg_ySc_{(1-y)}$ thin film electrodes : a thermodynamic and kinetic study, *Electrochimica Acta*, **51**, 2427 (2005).

98. A.J. Bard, and L. R. Faulkner, Electrochemical Methods; Fundamentals and Applications, p. 100, John Wiley & Sons, New York (2001).

99. P.H.L. Notten, M. Ouwerkerk, A. Ledovskikh, H. Senoh and C. Iwakura, Hydride forming electrode materials seen from a kinetic perspective, *J. Alloys Comp*., **356-357**, 759 (2003).

100. P. Villars (Edt), *Pearson's Handbook Desk Edition*, Vol. 2, p. 2101, ASM International (1997)

101. D.G. Westlake, Site occupancies and stoichiometries in hydrides of intermetallic compounds: Geometric considerations, *J. Less Common Metals*, **90**, 251 (1983)

102. B.K. Rao, P. Jena, Switendick criterion for stable hydrides, *Phys. Rev. B*, **31**, 6726 (1985)

103. J. Isidorson, I.A.M.E.Giebels, E.S. Kooij, J.H. Rector, A.T.M. van Gogh, R. Griessen, Structural, optical and electronic properties of $LaMgH_x$ switchable mirrors, *Electrochimica Acta,* **46**, 2179 (2001)

104. I.A.M.E. Giebels, "Shining light on Mg-based shitchable mirrors", PhD thesis VU Amsterdam

105. F. Gingl, K. Yvon, T. Vogt, A. Hewat, $LnMg_2H_7$ (Ln=La,Ce) two Laves-phase hydride derivatives having ordered hydrogen distribution, *J. Alloys Compounds*, **253-254**, 313 (1997)

106. Y. Goto, H. Kakuta, A. Kamegawa, H. Takamura, M. Okada, Effect of synthesis pressure on hydride phases in Mg-M systems (M=Y, Mn), *Science and Technology of Advanced Materials,* **4**, 333 (2003)

107. I.O. Bashkin, E.G. Ponyatovski, M.E. Kost, p-T diagram of the system Sc-H at high hydrogen pressures, *Inorg. Mater. (USSR),* **14**, 1260 (1978)

108. I.O. Bashkin, E.G. Ponyatovski, M.E. Kost, Phase transformations in hydrides of rare-earth metals under pressure II. The Sc-H and Yb-H systems under high hydrogen pressure, *Physica Status Solidi B*, **87**, 369 (1978)

109. P. Vajeeston, P. Ravindran, A. Kjekshus, H. Fjellvåg, Pressure-Induced Structural Transitions in MgH_2, *Phys. Rev. Lett.,* **89**, 175506 (2002)

110. B. Vigeholm, K. Jensen, B. Larsen, A. Schrøder-Pedersen, Elements of hydride formation mechanisms in nearly spherical Magnesium powder particles, *J. Less Common Metals*, **131**, 133 (1987)

111. J. Jeener, P. Broekaart, Nuclear Magnetic Resonance in Solids: Thermodynamic Effects of a Pair of rf Pulses, *Phys Rev.,* **157**, 232 (1967)

112. G. Kresse, J. Joubert, From ultrasoft pseudopotentials to the projector augmented-wave method, *Phys. Rev. B*, **59**, 1758 (1999)

113. H.J. Monkhorst, J.D. Pack, Special points for Brillouin-zone integrations, *Phys. Rev. B* **13**, 5188 (1976)

114. ILL neutron data booklet, http://www.ill.eu/top-links/publications/

115. M.S. Conradi, M. P. Mendenhall, T.M. Ivancic, E.A. Carl, C.D. Browning, P.H.L. Notten, W.P. Kalisvaart, P.C.M.M. Magusin, R.C. Bowman jr., S-J. Hwang and N.L. Adolphi, NMR to determine rates of motion and structures in Metal-Hydrides, *J. Alloys Comp.*, in press (2007).

116 E. Fukushima, S.B.W. Roeder, "Experimental pulse NMR, a nuts and bolts approach",

Addison-Wesley Publishing Co. (1981)

117. P.C.M.M. Magusin, W.P. Kalisvaart, P.H.L. Notten, R.A. van Santen, Hydrogen sites and dynamics in light-weight hydrogen-storage material Magnesium Scandium Hydride investigated with ^{1}H and ^{2}H NMR, *Chem. Phys. Lett.*, **456**, 55-58 (2008)

118. G.N. Garcia, J.P. Abriata, J.O. Sofo, Hydrogen movement in Cubic Mg_2NiH_4, *Phys. Rev. B*, **65**, 64306 (2002)

119. D. Noréus, L.G. Ollson, The structure and dynamics of hydrogen in Mg_2NiH_4 studied by elastic and inelastic neutron scattering, *J. Chem. Phys,* **78**, 2419 (1983)

120. B.R. Pauw, "Going deeper into metal hydrides: an *ab initio* study", Master Thesis, TU/e (2006), Ch. 5

121. W.P. Kalisvaart, R.A.H. Niessen, P.H.L. Notten: Electrochemical hydrogen storage in MgSc alloys: a comparative study between thin films and bulk materials, *J. Alloys Comp.*, **417**, 280-291 (2006)

122. M. Latroche, W. P. Kalisvaart, P. H. L. Notten, Crystal structure of $Mg_{0.65}Sc_{0.35}D_x$ deuterides studied by X-ray and neutron powder diffraction, *J. Solid State Chemistry*, 179 (2006), 3024-3032

123. R.A.H. Niessen and P.H.L. Notten: Electrochemical Hydrogen Storage Characteristics of Thin Film MgX (X=Sc, Ti, V, Cr) Compounds, Electrochem. Solid-State Lett., 8, A534-A538 (2005)

124. C. Suryanarayana, Mechanical alloying and milling, *Progress in Materials Science*, **46**, 1-184 (2001)

125. C. Gente, M. Oehring, R. Bormann, Formation of thermodynamically unstable solid solutions in the Cu-Co system by mechanical alloying, *Phys. Rev. B,* **48**, 13244 (1993)

126. F. Sun, F. H. Froes, Synthesis and characterization of mechanical-alloyed Ti–*x*Mg alloys, *J. All. Comp.*, **340** 220 (2002)

127. G. Liang, R. Schulz, Synthesis of Mg-Ti alloy by mechanical alloying, J. Mat. Science, **38** 1179 (2003)

128. D. Kyoi, T. Sato, E. Rönnebro, N. Kitamura, A. Ueda, M. Ito, S. Katsuyama, S. Hara, D. Noréus, T. Sakai: A new ternary magnesium–titanium hydride Mg_7TiH_x with hydrogen desorption properties better than both binary magnesium and titanium hydrides, *J. Alloys Comp*., **372**, 213 (2004)

129. P. Vermeulen, R. A. H. Niessen and P.H.L. Notten, Hydrogen storage in metastable $Mg_yTi_{(1-y)}$ thin films, *Electrochem. Comm*., **8**, 27-32 (2006)

130. E. Gaffet, M. Harmelin, F. Faudot, Far-from-equilibrium phase transition induced by mechanical alloying in the Cu-Fe system, *J. All. Comp.,* **194,** 23 (1993)

131. I. Manna, P.P. Chattopadhyay, P. Nandi, F. Banhart, H-J. Fecht, Formation of face-centered-cubic titanium by mechanical attrition, *J. Appl. Phys.*, **93**, 1520 (2003)

132. I. Manna, P.P. Chattopadhyay, F. Banhart, H-J. Fecht, Formation of face-centered-cubic zirconium by mechanical attrition, *Appl. Phys. Lett.*, **81**, 4136 (2002)

133. S. Bera, I. Manna, Polymorphic phase transformation in $Ti_{50}Zr_{50}$ binary alloy by mechanical alloying, *Mat. Science & Eng. A*, **417**, 110 (2006)

134. S. Bera, I. Manna, Hexagonal close packed to face centered cubic polymorphic transformation in nanocrystalline titanium–zirconium system by mechanical alloying, *J. All. Comp.*, **417**, 104 (2006)

135. P. Vermeulen, E.F.M.J. v. Thiel, P.H.L. Notten, Ternary MgTiX-Alloys: A Promising Route towards Low-Temperature, High-Capacity, Hydrogen-Storage Materials, *Chemistry-A European Journal,* **13**, 9892 (2007)

136. H. H. van Mal, K. H. J. Buschow, A. R. Miedema, Hydrogen absorption in $LaNi_5$ and related compounds: experimental observations and their explanation, *J. Less-Common Met*. 1974, 35, 65 –76

137. E. Zhou, C. Suryanarayana, F.H. Froes: Effect of premilling elemental powders on solid solubility extension of magnesium in titanium by mechanical alloying, *Mat. Lett*., 23, 27-31 (1995)

138. T. Alonso, Y. Liu, T.C. Parks, P.G. McCormick: Synthesis of the high pressure fcc phase in lanthanide metals by mechanical milling, *Scripta Metall. Mater*., 25, 1607-1610 (1991)

139. T. Alonso, Y. Liu, T.C. Parks, P.G. McCormick: Correction to 'synthesis of the high pressure fcc phase in lanthanide metals by mechanical milling', *Scripta Metall. Mater*., 26, 1931-1932 (1992)

140. S. Wang, S. Li, B. Xu, F. Cai, L. Li, J. Lei, Synthesis of binary nano-composite of $Zr_{50}Ti_{50}$ and its characterization, *J. All. Comp.*, **429**, 227 (2007)

141. R. A. Deegan: On the structure of the transition metals, *J. Phys. C*, 1, 763-766 (1968)

142. N. W. Dalton, R. A. Deegan: On the structure of the transition metals II. Computed densities of states*, J. Phys. C*, 2, 2369-2372 (1969)

143. H.L. Skriver: Crystal structure from one-electron theory, *Phys. Rev. B*, 31, 1909-1923 (1985)

144. C. Suryanarayana, F.H. Froes, Nanocrystalline titanium-magnesium alloys by mechanical alloying, *J. Mater. Res.*, **5**, 1880-1886 (1990)

145. C. Rongeat, L. Roué: Effect of particle size on the electrode performance of MgNi hydrogen storage alloy, *J. Power Sources,* **132**, 302-308 (2004)

146. C. Rongeat, M. H. Grosjean, S. Ruggeri, M. Dehmas, S. Bourlot, S. Marcotte, L. Roué: Evaluation of different approaches for improving the cycle life of MgNi-based electrodes for Ni-MH batteries, *J. Power Sources,* **158**, 747-753 (2006)

147. M. Abdellaoui, S. Mokbli, F. Cuevas, M. Latroche, A. Percheron-Guégan, H. Zarrouk, Structural, solid–gas and electrochemical characterization of Mg_2Ni-rich and Mg_xNi_{100-x} amorphous-rich nanomaterials obtained by mechanical alloying, *Int. J. Hydrogen Energy*, **31**, 246-250 (2006)

148. B. S. Murty, S. Ranganathan, M. Mohan Rao, Solid state amorphization in binary Ti-Ni, Ti-Cu and ternary Ti-Ni-Cu system by mechanical alloying, Mat. Sci. Eng A, 149, 231-240 (1992)

149. B. S. Murty, M. Mohan, Rao S. Ranganathan, Nanocrystalline phase formation and extension of solid solubility by mechanical alloying in Ti-based systems, *Nanostructured Materials*, **3**, 459-467 (1993)

150. D.M. Borsa, R. Gremaud, A. Baldi, H. Schreuders, J.H. Rector, B. Kooij, P. Vermeulen, P.H.L. Notten, B. Dam, R. Griessen, Structural, optical and electrical properties of Mg_yTi_{1-y} thin films, *Phys. Rev. B*, **75**, 205408 (2007)

151. P. Vermeulen, H. J. Wondergem, P.C.J. Graat, D. M. Borsa, H. Schreuders, B. Dam, R. Griessen and P. H. L. Notten, In-situ XRD of (de)hydrogenation of Mg-Ti thin film alloys, *submitted to J. Mat. Chemistry*

152. E. Jankowska, M. Makowiecka, M. Jurczyk, Electrochemical performance of sealed Ni–MH batteries using nanocrystalline TiNi-type hydride electrodes, *Renewable Energy*, **33**, 211-215 (2008)

153. B. Drenchev, T. Spassov, Electrochemical hydriding of amorphous and nanocrystalline TiNi-based alloys, *J. All. Comp.*, **441**, 197-201 (2007)

154. Song Y, Guo ZX, Yang R., Influence of selected alloying elements on the stability of Magnesium dihydride for hydrogen storage applications: A first principles investigation, *Phys. Rev. B,* **69,** 94205 (2004)

155. F.R. de Boer, D.G. Pettifor (Eds.), R. Boom, W.C.M. Mattens, A.R. Miedema, A.K. Niessen AK, "Cohesion in Metals, Transition Metal Alloys"

156. Z.H. Yan, M. Oehring, R. Bormann, Metastable phase formation in mechanically alloyed and ball-milled Ti-Si, *J. Appl. Phys.*, **72**, 2478-2487 (1992)